Shape evolution in neutron-rich Zr, Mo and Ru isotopes around mass A=100

Saba Ansari

NNT : 2019SACLS384

Thèse de doctorat

Shape evolution in neutron-rich Zr, Mo and Ru isotopes around mass A=100

Thèse de doctorat de l'Université Paris-Saclay
préparée à l'Université Paris-Sud

Ecole doctorale n°576
Particules, Hadrons, Énergie et Noyau: Instrumentation, Imagerie, Cosmos et Simulation (PHENIICS)

Spécialité de doctorat : Structure et réactions nucléaires

Thèse présentée et soutenue à Gif-sur-Yvette, le 25 octobre 2019, par

SABA ANSARI

Composition du Jury :

M. David Verney Directeur de recherche, Institut de Physique Nucléaire, Orsay	Président
M. Andreas Görgen Professeur, Université d'Oslo	Rapporteur
Mme. Silvia Lenzi Professeur, Université de Padoue	Rapporteur
M. Jürgen Gerl Directeur de Recherche, GSI, Helmholtzzentrum für Schwerionenforschung	Examinateur
M. Wolfram Korten Directeur de Recherche, Irfu, CEA, Université Paris-Saclay	Directeur de thèse

Acknowledgements

I would like to thank the PHENIICS school for giving me the opportunity to pursue my PhD here. I would like to thank my PhD supervisor, Wolfram Korten, for supporting me during my thesis. I really appreciate all the help Wolfram provided me especially during the writing of this manuscript. I would like to thank Andreas Görgen, Silvia Lenzi, Jürgen Gerl and David Verney for accepting to be my jury members. I really appreciated the work done by Andreas and Silvia in reviewing my manuscript. I would like to thank Magda Zielińska for proof reading my manuscript as well as for all the AGATA discussions I had with her.

My thanks go to Barbarra Sulignano and Frank Gunsing for being there for me whenever I needed to complain about my PhD. You both are amazing, and I will cherish the moral support you have given me in these past three years.

I would like to show my love to my dearest friend Pika Gospodaric for all the Germany-France phone calls we made, sharing the similar stories from our own PhD bubble. You are a sweetheart and the fact that you nailed your PhD, inspired me to do the same with mine.

My deepest thank and love goes to my husband, Pierre Chauveau, for helping me both mentally and with my thesis, even in the middle of the night. I also want to thank him for bearing with my PhD tantrums and for those little celebrations we had every time I get a nice peak fit. I love him so much for being there with me during the difficult days of my PhD. Talking about the difficult days, I would like to cuddle my cat boy Ziggy for teaching me not to be selfish and taking care of another living being. I would like to give my sincere thanks to my friend and mother-in-law, Chloe, for providing me the best "one-line" advises during my PhD and for helping me to stay sane.

I don't even know where to begin thanking my dad, Hasan, and how lucky I feel to be his daughter. My dad always made sure that I get the best education possible while coming from a community where a girl with a high school is an over-achiever. I don't remember a single time in my life when I couldn't count on him to help me through pass any obstacle. If it was not for him my fate could have been very different and I would have never ended up pursuing higher education. I want him to know that he is my role model and that I love him the most.

I would like to show my love and appreciation for my mom, Ishrat, and my little brother, Faizan, for believing in me that I could survive being alone in Europe and that I am strong enough to deal with every problem. Finally, I would like to thank my Bachelor teacher, Raka Dabhade, for motivating me to pursue my career in Physics. All her inspirational talks will stay with me forever. ...

To my papa

Contents

List of Figures

List of Tables

Chapter 1

Introduction

Nuclei are composed of neutrons and positively charged protons bound together by the interplay of nuclear and Coulomb forces. The nuclear force is a strong, attractive, short-range interaction that can overcome the repulsive Coulomb force at short range. All nuclei are arranged into a nuclear chart according to their number of neutrons and protons, see for example Fig. 1.1. This kind of representation offers insight into the characteristics of nuclei such as their decay modes, binding energy, nuclear shape, etc. As shown in Fig. 1.1, there are several regions throughout the nuclear chart which exhibit a rich variety of nuclear shapes. The aim of this thesis is to explore one such region at N = 60, which shows evolution from spherical to strongly deformed prolate[1] shapes and where the shape coexistence phenomenon is prevalent.

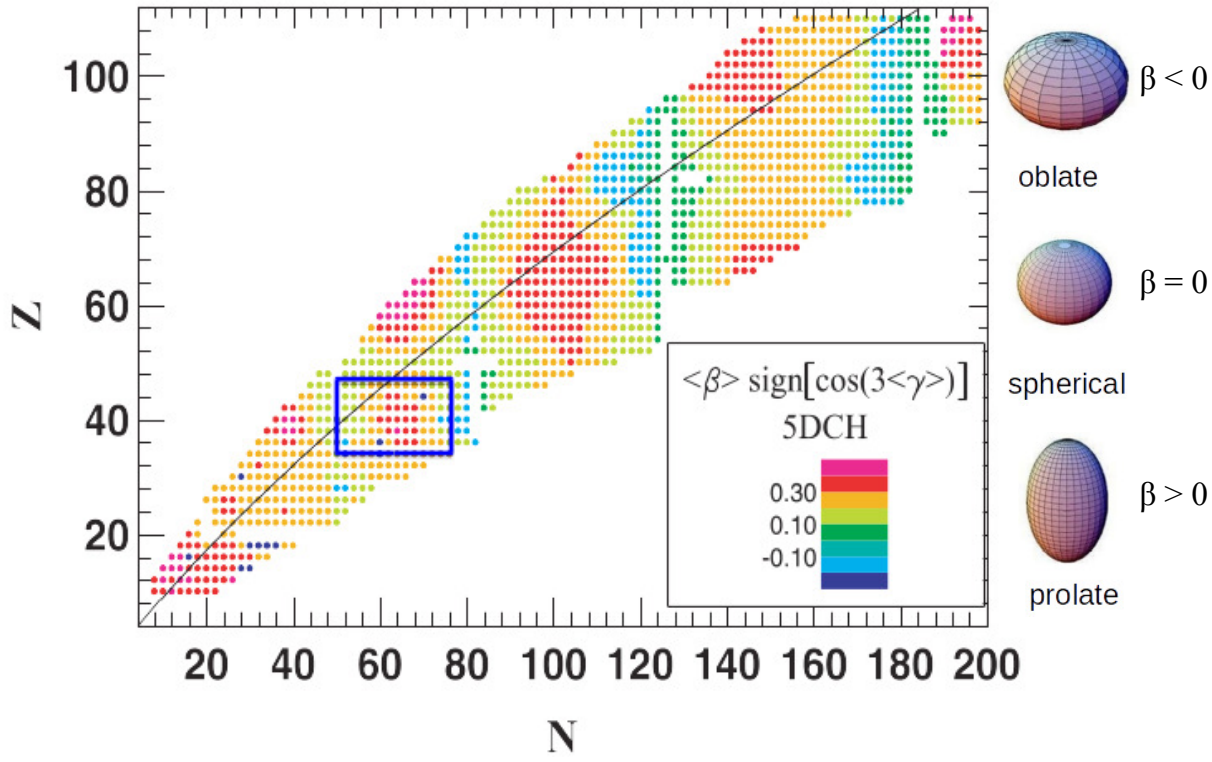

FIGURE 1.1: Nuclear chart showing the shape of the nuclear ground state predicted by the HFB+5DCH model (see section 2.6.1). Red colors indicate elongated (prolate) shapes and blue colors flattened (oblate) shapes. The HFB+5DCH calculations are performed with Gogny D1S force [Delaroche et al., 2010]

[1] represented by β in Fig.1.1 which will be described in section 2.3

In order to understand the phenomena observed throughout the nuclear chart, it was important to understand the basic nuclear structure. The invention of the nuclear shell model by Maria Goeppert Mayer was a breakthrough in the understanding of nuclear structure when she introduced the spin-orbit coupling to explain the high stability of nuclei with 28, 50, 82, or 126 neutrons or protons. The shell model describes the motion of a nucleon in a spherical potential well in a mean field created by all other nucleons. Goeppert-Mayer's nuclear shell model was backed up by experimental results on isomeric states, β decay schemes, magnetic moments and the observation of so-called magic numbers[2] at 2, 8, 20, 28, 50, 82, 126. Jensen was independently working on the same theory which led him and Mayer to share a Nobel prize for pioneering the theory of the nuclear shell model.

This model, although it served as an indispensable theoretical framework for understanding nuclear structure, could not predict the distortion of the nucleus from a spherical shape due to interactions between multiple valence nucleons far from the closed shells. This led Aage Bohr to lay the foundation of collectivity as he proposed that the nucleons outside of a closed shell do not move in a static mean field but rather in a varying field emerging from the collective oscillations, for which the frequency depends on the structure of the collective flow. This collective motion could have a great influence on the single particle energies and the deformation minimizing the sum of the energy of the occupied valence levels adopted by the nucleus. Bohr's idea was to have a unified collective model which could describe all nuclei in terms of a coupled system of particle and collective degrees of freedom.

As the nuclear shell model for single particles could not explain the complexity of nuclei related to the underlying many body problem, likewise, Bohr unified theory could not be applied to all the nuclei. However, the two models are often used complementarily in a microscopic-macroscopic combination that has proved to be very powerful.

This thesis presents new experimental results on lifetimes in neutron-rich Zr, Mo and Ru isotopes, which bring systematic information on evolution of nuclear deformation and collectivity in the vicinity of the N=60 shape transition. The measured transition strengths are compared to the results of Monte Carlo Shell Model, and beyond-mean-field calculations to interpret the data.

[2]The term was coined by [Wigner, 1937]

Chapter 2

Theoretical background

2.1 The shell model

Prior to the introduction of the shell model, experiments had shown that nuclei with certain "magic" numbers (2, 8, 20, 28, 50, 82, and 126) of proton and neutrons are more stable than other nuclei. A simple model of a nucleus considers the interaction of each nucleon with a mean field potential approximating its interaction with all other nucleons. If one considers such a single particle potential and fills the energy levels as per the Pauli exclusion principle[1] then one will obtain a shell structure analogous to the one in atoms. In order to derive the energy levels of nucleons inside the shells, it is necessary to solve the three-dimensional Schrödinger equation. One can start with a simple potential such as the infinite square well potential or a harmonic oscillator potential. The problem with both these potentials is that they can not reproduce the observed magic numbers beyond 20. For instance it can be seen in Fig. 2.1 that the harmonic oscillator potential, following the one at 20 produces a magic number at 40 which is not in agreement with the experimentally observed series of magic numbers. These potentials are unrealistic in the sense that they require an infinite amount of energy to free the bound nucleons. A more realistic approach can be achieved by using the Woods-Saxon potential to describe the energy levels of the nucleons inside the nucleus:

$$V_{ws}(r) = \frac{-V_o}{1 + exp(\frac{r-R}{a})} \tag{2.1}$$

where V_o represents the potential well depth, a is a parameter representing the surface diffuseness of the nucleus, $R = r_0 A^{1/3}$ is the nuclear radius with $r_o = 1.25$ fm and A is the mass number. Calculating the single particle energies using this potential leads to splitting the harmonic oscillator levels according to the orbital angular momentum "l" bringing down the energy levels with higher l values more strongly (see Fig. 2.1) but it can still not reproduce the magic numbers beyond 20. This problem was solved by Mayer and Jensen by introducing a strong spin-orbit splitting in the potential which had been previously ignored, considering its negligible effects on atomic shells. The spin-orbit interaction term is not strong enough to change the level ordering for light nuclei, however, it is significant beyond N,Z = 20 and can explain the shell closures beyond 20.

A nucleus being a complex quantum system cannot be fully described only by the single particle motion in a mean field potential. For nuclei having two or more valence nucleons (i.e. nucleons outside a closed shell) a residual two-body interaction must be added to the Hamiltonian:

$$H = H_o + H_{residual} \tag{2.2}$$

where

$$H_o = \sum_{i=1}^{A} (\frac{\vec{p_i}^2}{2m_i} + U(\vec{r_i})) \tag{2.3}$$

[1] Since the nucleons are fermions they will fill the energy levels according to Pauli exclusion principle

and

$$H_{residual} = \sum_{i<j=1}^{A} V(i,j) - \sum_{i=1}^{A} U(\overrightarrow{r_i})) \tag{2.4}$$

where p_i and m_i are the momentum and mass of the nucleon, $V(i,j)$ is a nucleon-nucleon interaction term and $U(\overrightarrow{r_i})$ is a one body potential.

The correlations generated by the residual interactions become more and more difficult to handle for heavier nuclei because of the enormous size of the matrices in which the residual interaction must be diagonalized.

The shell model simplifies this problem by separating the model space into an "inert" core and the valence space. In addition, the two body residual interaction is substituted with an effective interaction. Such an effective shell model interaction is adapted to a certain range of nuclei. The large number of degrees of freedom in a limited configuration space makes the shell model calculations rapidly intractable. The mean field models based on the Hartree-Fock formalism (see also section 2.6.1) follow the assumption that each nucleon moves in an average potential that is generated by all other nucleons. In this way the n-body problem is reduced to a one-body problem. The Hartree–Fock–Bogoliubov based models use Gogny [Dechargé and Gogny, 1980] or the Skyrme [Skyrme, 1958] interactions which are adapted to describe the ground-state properties of several different, often magic nuclei and are then fixed for all nuclei.

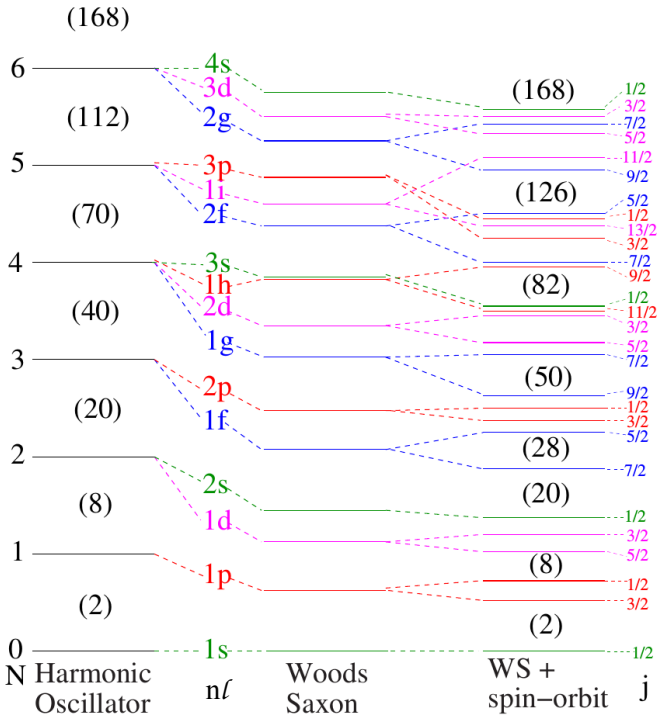

FIGURE 2.1: Comparison of the single-particle levels calculated using the harmonic oscillator (left), the Wood-Saxon potential (center) and with an additional spin-orbit term (right).

2.2 The deformed shell model

The shape of a nucleus is governed by both macroscopic and microscopic effects. The first ones are coming from the liquid-drop like properties of the nucleus while the second are a consequence of the underlying shell structure. The Nilsson model [Nilsson, 1955] is an independent particle model for non-spherical nuclei which describes the single-particle orbitals in a deformed potential. The deformation means that the nucleus is no longer spherical but is either elongated or flattened along one axis (see Fig. 2.3 for the coordinates). If the nucleus is deformed along the 'z' axis the resulting single particle Hamiltonian is given as:

$$H = -\frac{\hat{p}^2}{2M} + \frac{M}{2}\left[\omega_\perp^2(x^2+y^2) + \omega_z^2 z^2\right] - Cl\cdot s - D\left(l^2 - \langle l^2\rangle_N\right) \tag{2.5}$$

where $\hat{p}$ is the momentum operator, and C and D represent dimensionless parameters describing the strength of the spin-orbit and the l^2 term, respectively. The latter flattens the minimum of harmonic oscillator potential approximating it to the shape of the Woods-Saxon potential. The harmonic oscillator frequencies ω_z and $\omega_\perp$, along and perpendicular to the symmetry axis, respectively, are given as:

$$\omega_z = \omega_0(\epsilon)\left(1 - \frac{2}{3}\epsilon\right)$$
$$\omega_\perp = \omega_0(\epsilon)\left(1 + \frac{1}{3}\epsilon\right)$$

with

$$\epsilon = \frac{\omega_\perp - \omega_z}{\omega_0} \tag{2.6}$$

where ϵ is the Nilsson's elongation parameter and $\omega_0(\epsilon)$ is weakly dependent on ϵ. A nucleus is prolate for $\epsilon > 0$ and oblate for $\epsilon < 0$. The single particle energy as a function of ϵ is shown in Fig. 2.2, where the shell gaps at sphericity and large deformation are shown by circles. In the spherical case, the energy levels of each single-particle state have a degeneracy of $2j+1$, however if the potential has a deformed shape, the degeneracy of each single particle state is broken and their energy levels depends on the spatial orientation of the orbit. In addition to the spherical shell gaps new shell gaps appear at large deformation, for example at Z=38 and N=60.

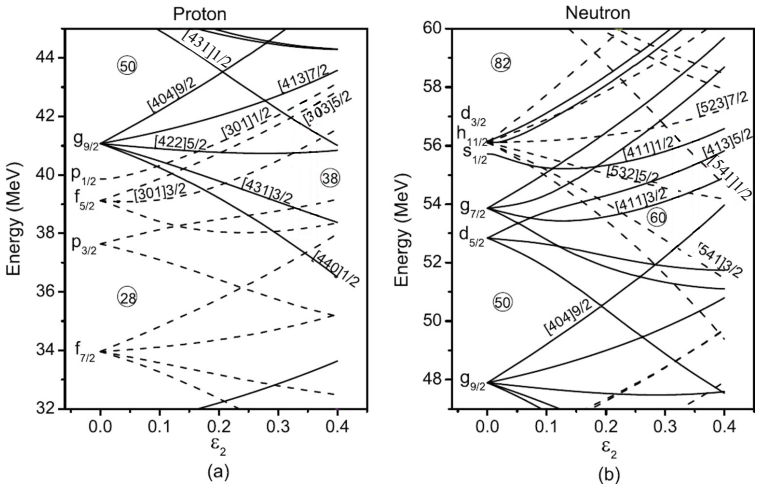

FIGURE 2.2: Nilsson diagram showing the proton and neutron single-particle energy levels relevant for the A$\sim$ 100 mass region. The figure is taken from Luo et al., 2014

2.3 Definition of nuclear shapes

In a nucleus with a fully occupied (closed) j shell all m states are equally populated leading to a spherical shape of the nucleus. However, if the shell is only partially filled the correlation between these valence nucleons may lead to a deformed shape. The most common deviation of the nuclear shape from sphericity is the quadrupole deformation. For such a nucleus its radius can be expressed as:

$$R = R_0[1 + \sum_{\mu} \alpha_\mu Y_{2\mu}(\theta, \phi)] \tag{2.7}$$

where $Y_{2\mu}$ are the spherical harmonics of order 2 and $\alpha_\mu, \mu = -2..2$ are the five expansion coefficients. The quadrupole deformation is associated with an ellipsoidal shape of the nucleus.

In the intrinsic reference frame of the nucleus, the expansion coefficients can be expressed as:

- $\alpha_{2,1} = \alpha_{2,-1} = 0$
- $\alpha_{2,0} = \beta cos(\gamma)$
- $\alpha_{2,2} = \alpha_{2,-2} = \frac{\beta sin(\gamma)}{\sqrt{2}}$

The two parameters called the quadrupole deformation parameter 'β' and the degree of axial symmetry 'γ' also referred to as Hill and Wheeler coordinates [Hill and Wheeler, 1953] are sufficient to describe all possible quadrupole shapes. The pictorial representation of different deformed shapes with respect to β and γ are shown in Fig. 2.3. The two axial symmetric shapes emerging from the Hill-Wheeler coordinates are prolate (Rugby-ball) and oblate (disk-like) shapes. As seen in Fig. 2.3, the prolate shape is extended in one direction and flattened in the other two directions whereas the oblate shape is flattened in one direction and extended in the other two directions. The axis along which the nucleus is stretched and squeezed depends on the value of γ. It is sufficient to study the γ=0° to 60° sextant to describe all quadrupole shapes. γ=0 corresponds to a pure prolate shape, γ=60 corresponds to an oblate shape and intermediate values corresponds to triaxial shapes for which a nucleus does not have a symmetry axis.

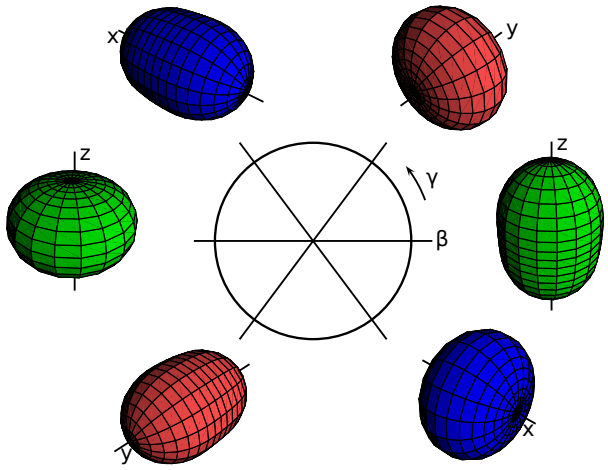

FIGURE 2.3: The quadrupole deformed shapes corresponding to $\beta = 0.4$ and $\gamma =$ 0°, 60°, 120°, 180°, 240°, 300° are shown for reference. Different colors represents different principal axes of symmetry (green for z, red for y and blue for x). Image is taken from Fortunato, 2005

The elongation parameter from Nilsson model can be related to the deformation parameter β using:

$$\epsilon \approx \frac{3}{2}\left(\frac{5}{4\pi}\right)^{1/2} \cdot \beta \tag{2.8}$$

2.4 Collective Hamiltonian

The theoretical explanation regarding the origin of nuclear deformation was provided by Bohr, Wheeler and Rainwater using the so called Bohr Hamiltonian [Bohr and Mottelson, 1953]. The collective Hamiltonian or the Bohr Hamiltonian introduces features of collective motion and describes the extent of deformation of the nuclear surface. The Bohr Hamiltonian is given as the sum of the collective kinetic energy T and potential energy E.

$$H = T + E \tag{2.9}$$

The kinetic energy T is expressed as a sum of vibrational energy T_{vib} and rotational energy T_{rot}. The idea of a collective Hamiltonian is to microscopically define the nuclear shape and its motion resulting from excitations. One of the simplest approaches to classify different types of macroscopic collective nuclear motion is through their energy ratios between the 4_1^+ state and the 2_1^+ state.

- axially symmetric rotor:
  The rotational energy of an axially symmetric rotor (rigid rotor) as per the Bohr formulation is given as:
  $$T_{\text{rigid rot.}} = \frac{\hbar^2}{2I}R^2 \tag{2.10}$$
  Where I is the moment of inertia and can be approximated in terms of the deformation parameter β as:
  $$I = \frac{2}{5}AMR_0^2(1 + 0.31\beta), \tag{2.11}$$
  and R is the collective angular momentum. The ratio $\frac{E(4_1^+)}{E(2_1^+)}$ for a rigid rotor is 3.3.

- γ-unstable:
  In this case the nucleus has a flat potential and oscillates back and forth from 0° to 60° and has $\gamma_{rms} = 30°$ [Casten, 2015]. The ratio $\frac{E(4_1^+)}{E(2_1^+)}$ for a γ unstable potential is 2.5.

- Spherical harmonic vibrator:
  The energy of the spherical harmonic vibrator as part of the Bohr Hamiltonian is given as:
  $$T_{vib} = -\frac{\hbar^2}{2B}\left[\frac{1}{\beta^4}\frac{\partial}{\partial\beta}\left(\beta^4\frac{\partial}{\partial\beta}\right) + \frac{1}{\beta^2}\frac{1}{sin(3\gamma)}\frac{\partial}{\partial\gamma}\left(sin(3\gamma)\frac{\partial}{\partial\gamma}\right)\right] \tag{2.12}$$
  where B is related to the mass density (ρ_0) and the radius of the nucleus by:
  $$B = \frac{1}{2}\rho_0 R_0^5 \tag{2.13}$$

with

$$R_o = r_o A^{1/3} \quad \left\{\text{with } r_o = 1.25 \text{ fm} \right. \tag{2.14}$$

The ratio $\frac{E(4_1^+)}{E(2_1^+)}$ for a vibrator is 2.0.

2.5 Electromagnetic transitions and quadrupole moments

An excited state of a nucleus can decay via the emission of electro-magnetic radiation having a certain multipolarity. The different multipole orders are called dipole, quadrupole, octupole and so on. In the case of an even-even nucleus where the ground state is 0^+, the first excited state has normally $J^\pi = 2^+$ and can only decay (to first order) by electric quadrupole or E2 radiation. The reduced E2 transition probability from an initial state of angular momentum J_i to a final state of angular momentum J_f is directly associated with electric quadrupole matrix element and is given as:

$$B(E2; J_i \longrightarrow J_f) = \frac{1}{2J_i + 1} \langle \psi_f \parallel E2 \parallel \psi_i \rangle^2 \tag{2.15}$$

where ψ_i and ψ_f corresponds to the wave-functions of the state with angular momentum J_i and J_f, respectively. If the energy of the state i is higher than that of state f, this reduced transition probability is called $B(E2;\downarrow)$ and one can calculate the reverse transition strength $B(E2;\uparrow)$ as:

$$B(E2; J_f \longrightarrow J_i) = \frac{1}{2J_f + 1} \langle \psi_i \parallel E2 \parallel \psi_f \rangle^2 \tag{2.16}$$

This reduced electromagnetic transition probability, B(E2), can be calculated directly from the measured nuclear lifetimes.

$$B(E2;\downarrow) = \frac{81.62 \cdot 10^{12} \cdot E^{-5}}{\tau(1+\alpha)} [e^2 b^2] \tag{2.17}$$

where τ is the lifetime in ps, E is the transition energy in keV and α is the total internal conversion coefficient. The B(E2) values can be expressed in Weisskopf units (W.u), where 1 W.u = $5.94 \times 10^{-6}(A^{4/3} e^2 b^2)$, with $e^2 b^2$ being 10^{-4} $\mathrm{e}^2 fm^4$. One Weisskopf unit (W.u) corresponds to a single particle transition of a single proton in an average central potential.

In the rotational model the reduced transitions probability can be related to the transition quadrupole moment Q_t using the following equation:

$$B(E2, KI_i \longrightarrow KI_f) = \frac{5}{16\pi} Q_t^2 (I_i, K, 2, 0 \mid I_f, K)^2 \tag{2.18}$$

where the Clebsch-Gordan coefficients remove the spin dependency.

Furthermore, B(E2) can be related to the nuclear deformation parameter β (assuming axial symmetry) using the following equations [Raman, Nestor, and Tikkanen, 2001]:

$$\begin{aligned} B(E2;\uparrow) &= \Big[\frac{\beta e}{(4\pi/3ZR_0^2)} \Big]^2, \\ R_0 &= 1.2A^{1/3}\ [fm] \end{aligned} \tag{2.19}$$

2.6 Nuclear models

2.6.1 Beyond mean field models

The Hartree-Fock-Bogoliubov (HFB) technique is a mean field approach that consists in restricting the many-body Hamiltonian to a special class of states called Hartree-Fock-Bogoliubov states (or quasi-free states), which are completely characterized by their one-particle density matrices [Lewin and Paul, 2014]. HFB calculations are commonly approached with Skyrme [Goriely, Chamel, and Pearson, 2013] and Gogny interactions [Libert, Girod, and Delaroche, 1999]. The mean-field approximation is able to describe basic nuclear properties such as binding energies or nuclear radii throughout the whole nuclear chart. However, in order to access the properties of individual states such as its excitation energy or electro-magnetic decay properties, one needs to go beyond the mean-field level by performing particle-number and angular-momentum projections and configuration mixing [Robledo, Rodríguez, and Rodríguez-Guzmán, 2018].

We compare the experimental results obtained in this thesis with the predictions of two beyond-mean-field models. The first one is the symmetry-conserving configuration mixing (SCCM) [Robledo, Rodríguez, and Rodríguez-Guzmán, 2018] method based on the HFB approach and using the parametrization D1S of the Gogny force [Libert, Girod, and Delaroche, 1999]. This method involves simultaneous particle number and angular momentum projection of different intrinsic HFB states and a subsequent mixing of these states performed within the generator coordinate method (GCM) framework [Rodríguez, Arzhanov, and Martínez-Pinedo, 2015]. When the calculation is restricted to parity and time-reversal symmetric intrinsic states, the method can be applied to the whole nuclear chart, however, the method can also be extended to other degrees of freedom such as octupole deformation. In the present work, calculations spanning the full β, γ plane including the triaxial degree of freedom have been considered.

As a second model we have compared our results with HFB calculations using the Gogny D1S interaction extended by using an approximation to the generator coordinate method mapping it onto a five-dimensional collective quadrupole Hamiltonian (5DCH) [Delaroche et al., 2010]. The 5DCH approach is a phenomenological approximation to the full GCM whereas the SCCM is a variant of the generic GCM framework. Both methods can predict ground-state properties such as charge radii, two-nucleon separation energies, but also spectroscopic properties and quadrupole shape parameters of even-even nuclei from Z =10-110.

2.6.2 Monte-Carlo Shell-Model

The conventional shell model could correctly describe the properties of the light (N<60) Zr isotopes [Sieja et al., 2009], however, it is constrained by the size of the configuration space for heavier isotopes. The MCSM allows the calculation in much larger configuration spaces which enables it to study deformation beyond N =60. In the present work it is quite relevant to use this model to predict the deformation in Zr isotopes. The main difference between the MCSM and the HFB based model is that the former still relies on empirical data to fit the effective interaction whereas the latter uses a global effective interaction for all nuclei.

The recent advances with the MCSM have made it possible to investigate the origin of the shape transition at N=60 [Togashi et al., 2016] and to relate the strong proton-neutron interaction between proton $\pi 1g_{9/2}$ and neutron $\nu 1g_{7/2}$ subshells. The so-called type-II shell evolution [Togashi et al., 2016], is invoked to be responsible for the appearance of deformed states in Zr isotopes. Since these specific particle-hole excitations lead to a significant reorganization of the effective single-particle energies, the mixing of normal states and those with deformation-optimized shell structure is suppressed, consistent with experimental results. The calculations of Togashi et

al., 2016 predict a dramatic shape change between the ground states of ^{98}Zr and ^{100}Zr. These calculation are used in the present work to interpret the experimental results in Zr chain.

2.7 Shape-phase transition in nuclei around A=100

The main emphasis of this work lies in measuring the lifetimes of the low-lying states of even-even Zr, Mo and Ru isotopes and to extract B(E2) values which can be compared with theoretical predictions. Neutron-rich nuclei in the A∼100 mass region have been a topic of research in nuclear structure physics for many years. Fig. 2.4a shows the excitation energy of the first 2_1^+ state as a function of the neutron number for even-even Sr, Mo, Zr, Ru, Pd and Cd isotopes. As we go from N = 58 to N = 60 there is a dramatic change in the excitation energy of the 2^+ state, predominately for Sr, Zr and Mo isotopes. This kind of dramatic behavior can be related to a change in the nuclear deformation, that is, the nuclei with N<60 are more spherical in shape whereas those beyond N = 60 are strongly deformed. A measurement of the reduced transition probability is a more direct measure of nuclear deformation. Fig. 2.4b shows the B(E2; $2_1^+ \longrightarrow 0_1^+$) values vs. the neutron number from Sr to Cd. The onset of collectivity is rather smooth from Ru to Cd whereas the collectivity sets in more rapidly beyond N = 58 for Sr, Zr and Mo isotopes.

This island of quadrupole deformation appearing beyond N=60 in the A∼100 mass region was first observed in the 1960s by Johansson, 1965 in a study of γ rays emitted by fission fragments. Shortly after, Cheifetz et al., 1970 identified excited states and measured lifetimes in A∼100 nuclei using spontaneous fission of ^{252}Cf, reporting a rotational-like behavior of neutron-rich even-even Zr, Mo, Ru and Pd isotopes, consistent with theoretical predictions of Arseniev, Sobiczewski, and Soloviev, 1969; Sheline, Ragnarsson, and Nilsson, 1972.

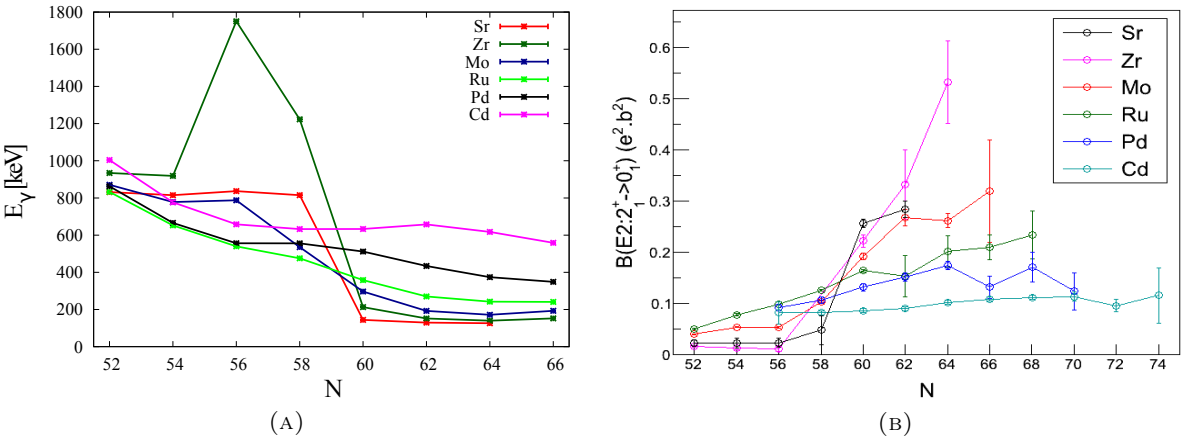

(A) (B)

FIGURE 2.4: (A) Evolution of the 2_1^+ excitation energy as a function of neutron number for even-even nuclei in the A∼100 region. (B) B(E2; $2_1^+ \longrightarrow 0_1^+$) transition probability as a function of neutron number.

2.7.1 Zr isotopes

In the Zr isotopes the energy of the 2_1^+ state decreases dramatically at the transition point N=60 (Fig. 2.4a). Experimental studies also show that for N ≥ 60, the E(4^+)/E(2^+) ratio is larger than 3 as seen in Fig. 2.5, which is characteristic for a well deformed rotor [Bettermann et al., 2010; Smith et al., 2004; Heyde and Wood, 2011]. These observations are corroborated by the sudden increase in absolute transition strength for $2_1^+ \longrightarrow 0_1^+$ from ^{98}Zr to ^{100}Zr. A recent study indicated a spherical-prolate-triaxial shape coexistence in ^{98}Zr [Singh et al., 2018]. More information is still

needed on low-lying states of ^{98}Zr to fully establish their properties.

The shape phase transition can be explained by the strong p-n interaction between protons in the $\pi 1g_{9/2}$ and neutrons in the $\nu 1g_{7/2}$ subshells. The protons are excited from the predominantly filled $\pi p_{1/2}$ shell to the predominantly empty $\pi g_{9/2}$ shell [Federman, Pittel, and Etchegoyen, 1984] which leads to a decrease of the spin-orbit splitting in the neutron sector and reduces the shell gap between $\nu g_{7/2}$ and $\nu d_{5/2}$. As the occupation of the $\nu g_{7/2}$ neutron orbital increases, the spin-orbit splitting increases in the proton sector, reducing the energy gap between $\pi p_{1/2}$ and $\pi g_{9/2}$. This self-stabilizing process is made responsible for the appearance of the deformation in Zr isotopes.

The monopole part of the p-n interaction causes the dramatic lowering of the 0_2^+ state (from 1.58 MeV to 0.85 MeV) as we go from ^{96}Zr (empty $\nu 2d_{5/2}$) to ^{98}Zr [Otsuka and Tsunoda, 2016] by adding two neutrons to the $\nu 2d_{5/2}$ orbital. The lowering of this configuration continues in ^{100}Zr where it becomes the 0_1^+ ground state of ^{100}Zr, while the spherical ground state of ^{98}Zr becomes the non-yrast 0_2^+ state (0.331 MeV) lying right above the 2_1^+ state of ^{100}Zr (0.212 MeV). This makes ^{100}Zr a perfect shape transitional point as beyond N≥60, the energy of the 0_2^+ state increases significantly and only one regular rotational band is observed for ^{102}Zr at low excitation energy. In the present work, we have performed new lifetime measurements up to spin 8^+ from ^{98}Zr to ^{104}Zr in order to understand the shape transition along the Zr chain. Such measurements are crucial to determine transition strengths, which gives systematic information on nuclear collectivity.

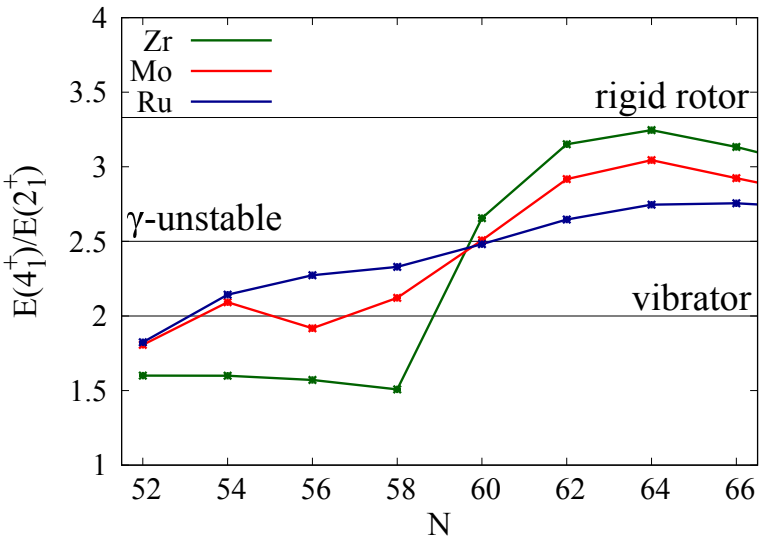

FIGURE 2.5: Evolution of the $E(4_1^+)/E(2_1^+)$ ratio in the Zr, Mo and Ru isotopic chains.

2.7.2 Mo isotopes

The Mo isotopic chain is particularly interesting since it lies in between the Zr isotopes, which exhibit strong onset of collectivity at N = 60 and the Ru isotopes where the shape evolution is rather smooth. The occupation of the neutron $1\nu h_{11/2}$ and proton $1\pi h_{9/2}$ intruder orbitals makes the Mo isotopes (around A = 100) candidates to display a triaxial behavior. The Mo isotopes were interpreted as an example of transitional nuclei between the limits known as γ-unstable and that of the rigid rotor [Hutter et al., 2003] (see Fig. 2.5). There is not yet sufficient experimental evidence to prove triaxiality in even-even Mo isotopes, however theoretical calculations

from Skalski, Mizutori, and Nazarewicz, 1997 predicted ground-state triaxial minima in several Mo isotopes around mass 100. The triaxial behavior in even-odd molybdenum isotopes has been studied experimentally. For instance in the work of Pinston et al., 2006, γ of $\approx 17°$ for ^{105,107}Mo was obtained. Electromagnetic properties of low-lying states in ^{100}Mo were studied in Wrzosek-Lipska et al., 2012 using the Coulomb excitation experiment. It was concluded that the 0_1^+ state in ^{100}Mo was less deformed than the excited 0_2^+ state and that the nucleus undergoes a shape transition from a triaxial shape of the 0_1^+ state to a prolate shape of the 0_2^+ state.

The main focus of this work is to measure reduced transition probabilities (B(E2)) values in Mo isotopes in order to verify the previous experimental as well as theoretical studies. This has been performed through lifetime measurement allowing to determine B(E2) values up to spin 8 for even-even ^{100}Mo-^{108}Mo isotopes.

2.7.3 Ru isotopes

Similar to the Mo isotopes, triaxiality at low spins has been a topic of discussion in the Ru isotopic chain, particularly for the isotopes from ^{106}Ru to ^{112}Ru as the ratio $E(4_1^+)/E(2_1^+)$ does not reach the limit for a rigid rotor and lies above the limit for a γ-unstable nucleus (Fig. 2.5). In $^{110-114}$Ru, the second 2^+ state lies energetically below the first 4^+ state which is a strong indication of triaxiality according to the model by Davydov and Filippov, 1958. The Density Functional Theory (DFT) calculations in Zhang et al., 2015 predicted triaxial ground state deformation in $^{108-112}$Ru and also the constrained Skyrme Hartree-Fock plus BCS calculations performed in Nomura, Shimizu, and Otsuka, 2010, predicted a weak triaxial deformation for N = 64-70. There were earlier experimental studies on ^{104}Ru using Coulomb excitation experiments listed in Cline, 1986, where the E2 properties were interpreted in terms of triaxial collective models having appreciable fluctuations in the β and γ degrees of freedom. Recent experimental support for triaxial deformation in ^{110}Ru came from Doherty et al., 2017 through a Coulomb excitation experiment. This was in agreement with beyond-mean-field and triaxial-rotor model calculations, which all predicted the triaxiality to be close to 30° for ^{110}Ru.

In this work we have measured the lifetimes up to 8^+ states in $^{106-112}$Ru isotopes. The B(E2) values are calculated and compared with the theoretical models up to 6^+ state.

Chapter 3

Experiment

This thesis describes the analysis and results of a γ-ray spectroscopy experiment, which was performed at *GANIL* in June 2017. The goal of the experiment was to create fission products which decay in flight in order to measure the lifetime of excited states. A beam of $^{238}_{92}$U was accelerated by a separated sector cyclotron (CSS1 [Lehérissier et al., 2004]) to 6.2 MeV/u and directed into a target of $^{9}_{4}$Be. In the fusion reaction, compound nuclei $^{247}_{96}$Cm at an excitation energy of 45 MeV were produced which then underwent fission. Thanks to the use of a sophisticated set of spectrometers, this experiment allowed measurement of nuclear lifetimes in a range from few to several hundreds of picoseconds.

Gamma-ray spectroscopy following fission is particularly interesting since fission reactions produce fragments on the neutron-rich side of the valley of stability. On the other hand it is also very challenging since many different fragments are produced that in turn decay by the emission of (contaminant) γ-ray transitions which are often entangled with the transitions of interest. The γ-ray transitions from the isotopes of interest could be separated from those corresponding to the decay of other reaction products thanks to the use of the high-precision mass spectrometer VAMOS, which allowed to identify the isotopes according to their atomic number Z, mass A, and atomic charge state Q. The AGATA array consisting in this experiment of 35 segmented germanium detectors were placed at backward angles with respect to the target. The target was placed inside a plunger mechanism which, in combination with AGATA and VAMOS, allowed the measurement of short-lived excited states. The inverse kinematics of the fusion-fission reaction produced recoiling fission fragments at a high velocity (≈10% of the speed of light) which in turn induced important Doppler shifts that proved crucial for lifetime measurements of short-lived states. The AGATA detectors were placed under backward direction (position from $\sim 135°$ to $175°$) in order to maximize the Doppler shift. The target was surrounded by 24 lanthanum bromide ($LaBr_3$) detectors[1] placed around $90°$ to measure the lifetimes of the longer-lived states from tens of ps to 100s of ps using the fast-timing method. Using different combinations of the spectrometers present in the setup, we could determine lifetimes in a range from $\sim$ 1 ps to $\sim$ 1 ns: by combining VAMOS, AGATA and the plunger device we could measure lifetimes down to a few ps, while the combination of VAMOS and FATIMA yields lifetimes of up to $\sim$ 1 ns. The schematics of the experimental setup is shown in Fig. 3.1. In this thesis we will only discuss the lifetime measurement of short-lived states using the plunger technique. In the following section each spectrometer used in the setup will be presented. Furthermore, both hardware and software aspects of AGATA array will be discussed.

[1] Commonly referred to Fast Timing (FATIMA) detectors in the community.

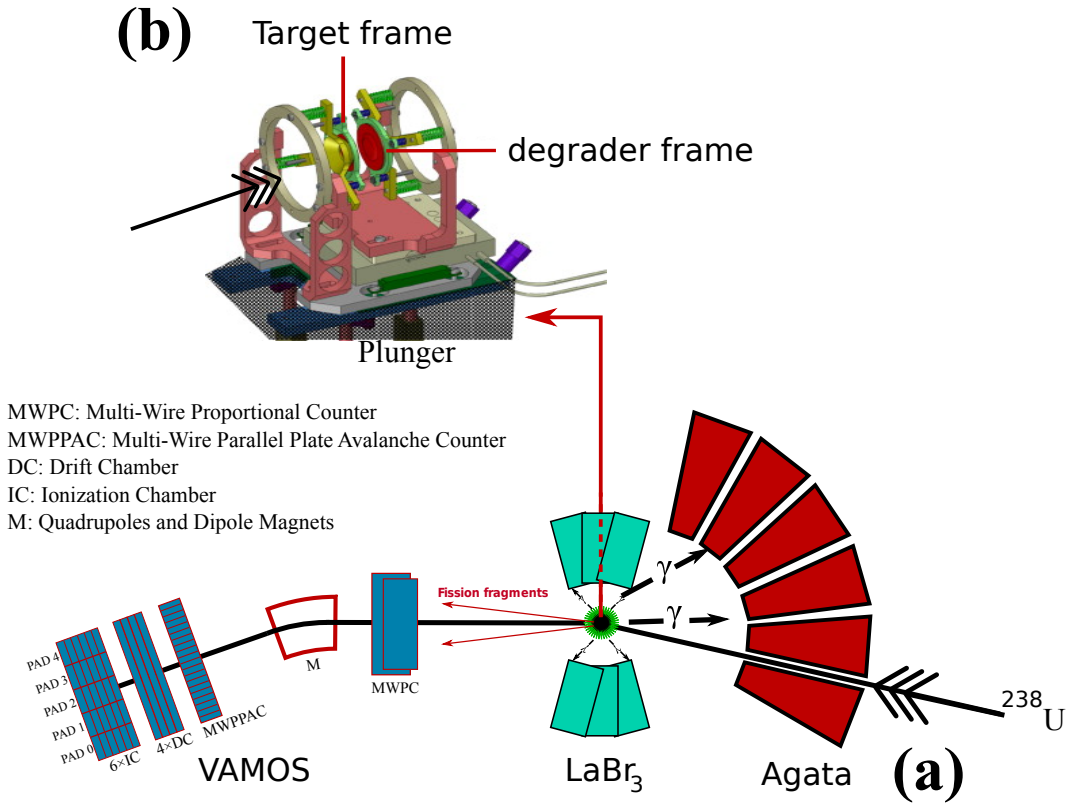

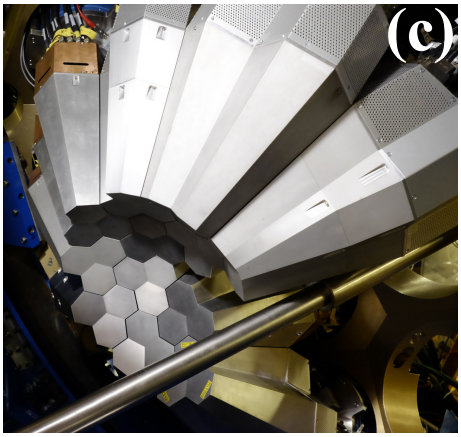

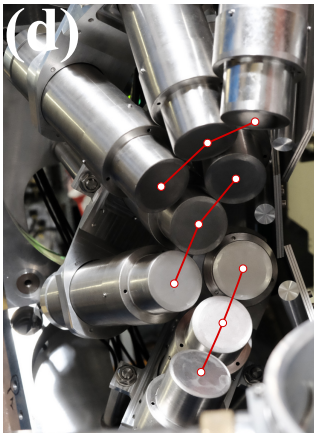

FIGURE 3.1: (a) Schematic diagram of the experimental setup at GANIL. The AGATA setup used during this experiment was placed at an angle of 180° with respect to the VAMOS axis. VAMOS was placed at an angle of 19° with respect to the beam axis in order to have the highest acceptance for the mass of interest (discussed in Sec. 3.1) (b) A plunger device was placed inside the target chamber with a Be foil mounted in the target position and Mg foil mounted in the degrader position. (c) Photo of the AGATA setup taken during the experiment showing all 35 detectors in a close-packed geometry. (d) $LaBr_3$ detectors were mounted under 90° clustered together by three detectors per frame (highlighted by red lines) for a total of 8 frames and 24 detectors. The $LaBr_3$ setup surrounded the target in a ring-like geometry perpendicular to the VAMOS axis.

3.1 VAMOS

The *VAriable MOde Spectrometer* (VAMOS++ [Rejmund et al., 2011])[2] is a large acceptance magnetic spectrometer which identifies the transmitted nuclei on the basis of Z, A and Q. The spectrometer is equipped with several components where each component plays a unique role in reconstructing the ion trajectory and in the identification. VAMOS comprises:

- a Dual Position-sensitive Multi-Wire Proportional Counter (DP-MWPC) entrance detector which measures the direction of the incoming fragments and their emission angle with respect to the target and gives a timing signal for the determination of the Time of Flight [Vandebrouck et al., 2016],
- two large aperture quadrupoles to focus the fragments as per the desired ion optical mode,
- a large magnetic dipole which separates the fission fragments according to their magnetic rigidity (Bρ) in the horizontal plane, perpendicular to the dipole axis,
- a Multi-Wire Parallel-Plate Avalanche Counter (MWPPAC) which together with the MWPC is used to obtain the time of flight,
- two Drift Chambers (DC) which measure the position of the particles at the focal plane,
- six ionization chambers (IC) segmented along the flight path out of which the first five measure the energy loss of the fragments, ΔE, whereas the total energy E deposited by the fragments is measured by the complete IC assembly.

All detectors located behind the dipole are mounted on a mobile rotating platform and will be called the focal-plane detection system as seen in Fig. 3.2. The ray-tracing technique uses the information from the focal plane and the target MWPC to reconstruct the trajectory of the fragments and to identify them in terms of their mass M, atomic number Z and charge state Q.

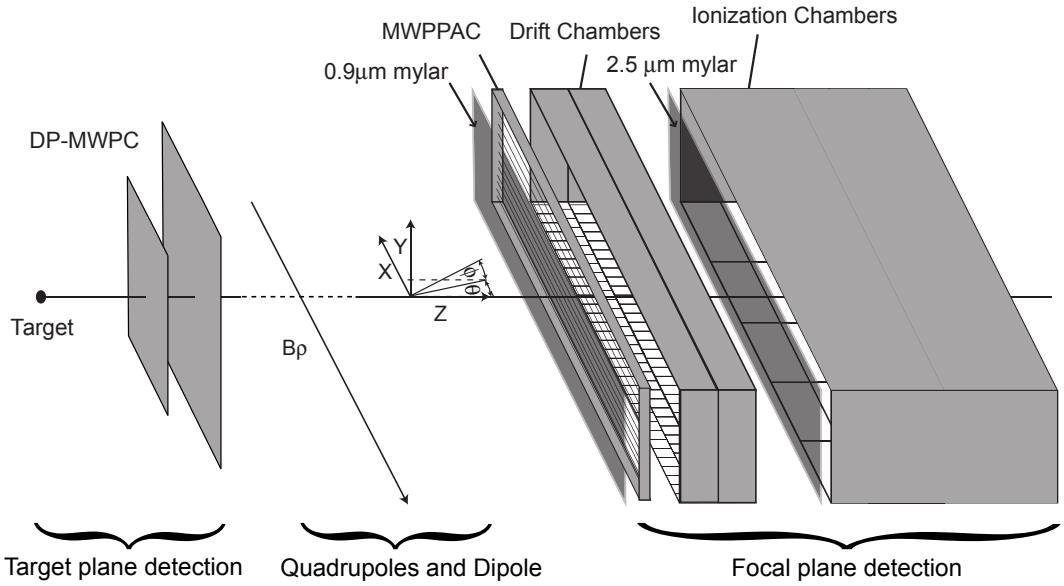

FIGURE 3.2: Vamos detection system. Image is adapted from Rejmund et al., 2011

VAMOS can be operated in either a zero-degree recoil-separator mode or a standard dispersive mode, depending on the kinematics requirement of the experiment [Rejmund et al., 2011]. The

[2]VAMOS++ will be referred as VAMOS for convenience

present experiment used the dispersive mode where the magnetic field created by the dipole along the y-axis separated the particles along the horizontal x axis on the basis of momentum over charge state. The VAMOS axis is rotated at 19° around the y-axis (see Fig. 3.2 for the coordinate system) in order to have maximum detection efficiency for the light fission fragment peak (A∼100). The circular trajectory of the particles inside the magnetic field is given by the Lorentz formula and the curvature radius ρ is given as:

$$B\rho = \gamma \cdot \frac{M \cdot v}{Q} \quad \left\{ \; \gamma = 1/\sqrt{1 - \frac{v^2}{c^2}} \right. \tag{3.1}$$

where γ is the Lorentz factor which is to be considered due to the relativistic velocities involved, B is the magnetic field of the dipole, M is the mass of the particle, Q is its charge and v is its velocity. The magnetic rigidity Bρ depends solely on the parameters of the fission fragments (M, v and Q). In order to access the isotopes around mass 100, the quadrupoles and dipole magnets of VAMOS were tuned to select a magnetic rigidity of Bρ_* = 1.11 Tm. This setting allows the maximum transmission for the fragments with Bρ_*. The further a fragment's Bρ is from Bρ_*, the less it will be transmitted through VAMOS with the acceptance of ≈ ±10%. Thanks to the inverse kinematics, the maximum scattering angle of the ^{238}U beam is very small (roughly 2° on the Be target and 6° on the Mg degrader, see section 5.2) and is outside of the angular acceptance of VAMOS (minimum angle is about 10°).

3.1.1 Trajectory reconstruction

The two parameters required to determine the velocity are the length of the fission fragments' path (D) and their Time of Flight (ToF). The ToF is given by the time difference between the delayed STOP signal from the MWPC at the entrance of VAMOS and the START signal from the MWPPAC at the focal plane. The MWPPAC was used for the start signal since its rate is much lower than that of the target MWPC avoiding random coincidences.

The length of the flight path can be determined by constraining the trajectory in two points along their path: immediately after the target and in the focal plane. The transverse position and angle of the incoming fragments are first determined by the DP-MWPC located between the reaction chamber and the entrance of the VAMOS spectrometer. The two MWPC are gas detectors with a common gas volume of isobutane $i-C_4H_{10}$. Each MWPC has a central cathode and two anodes that give the timing signal $t_{1,2}$ and the positions $X_{1,2}$, $Y_{1,2}$, respectively, as seen in Fig. 3.3. The gas in the detector is ionized by incoming particles resulting in the production of ionization electrons and positively charged ions. Owing to their high mobility, the electrons are quickly accelerated, giving rise to an avalanche effect. The electron cloud moves towards the cathode whereas the ions move towards the anodes. The cathode gives the timing signal which is used for the ToF determination. Since the charge cloud of the ions is deposited on several anode wires, the centroid of the charge distribution can be fitted [Lau and Pyrlik, 1995] to obtain the position with a resolution smaller than the wire spacing. The x and y positions measured with the two MWPC are used to extrapolate the position in the target plane (X_T, Y_T). The functioning and performance of the DP-MWPC is explained in detail in Vandebrouck et al., 2016.

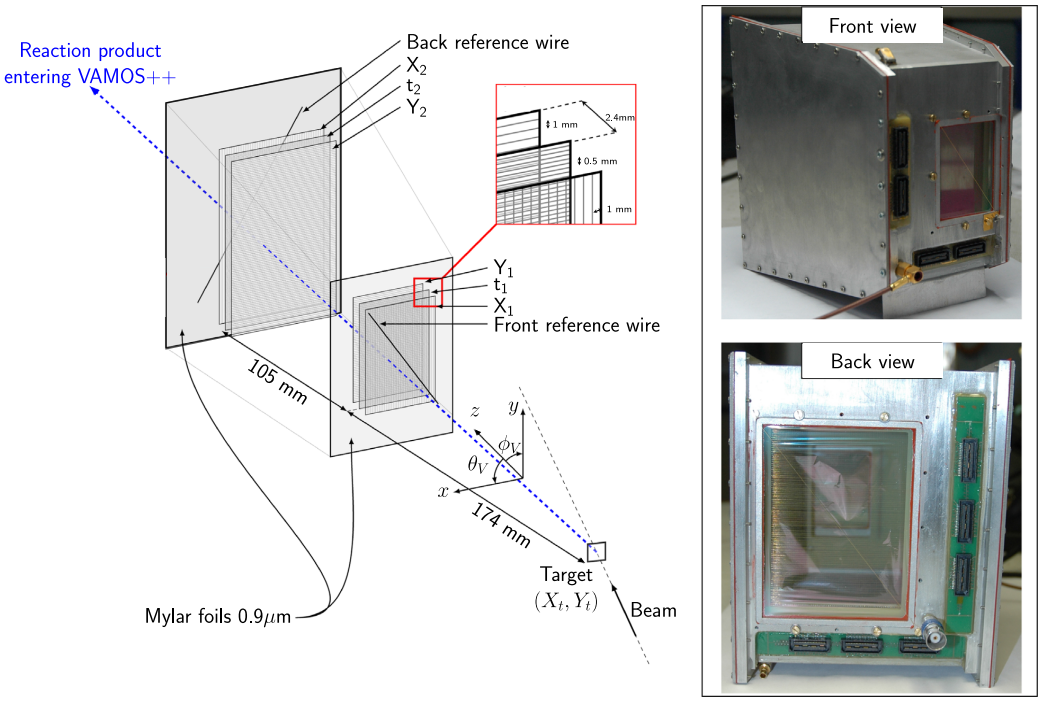

FIGURE 3.3: Schematics of the DP-MWPC. Image is adapted from Vandebrouck et al., 2016

The reconstruction of the trajectory is further constrained by the two drift chambers (DC). Similarly to the MWPC, the DC is a gas detector where the charges created by the passage of a fragment drift towards their respective electrodes. The electrons follow the electric field along the y-axis and are collected on a cathode which is 160-fold segmented in x direction (as shown in Fig. 3.2). The x position is determined from the centroid of the charge distribution on the cathode. The y position is deduced from the drift time i.e, the time it takes the electrons to drift to the cathode. The drift time is measured using a START signal from the MWPPAC and and a STOP signal from the DC charge collection time. The drift velocity can be considered constant and thus the y position is a linear function of the drift time. The two DCs are two-fold segmented along the beam axis (z-axis) giving four sets of position coordinates $([X_i, Y_i]_{i=1-4})$. These four coordinates are then used to determine the transverse position and angle at the focal plane $(x_f, y_f, \theta_f, \Phi_f)$. Using the position information at the target and the focal plane, the entire trajectory of the fragment can be reconstructed [Pullanhiotan et al., 2008].

Because of the complexity of the trajectories in the non-uniform magnetic field of the dipole and quadrupole magnets, this reconstruction procedure uses non-linear polynomials to relate the position information at the target plane to that at the focal plane. The polynomials to determine the complete particle trajectories can be defined as:

$$\begin{aligned} B\rho &= F_1(x_f, \theta_f, y_f, \phi_f) \\ \theta_T &= F_2(x_f, \theta_f, y_f, \phi_f) \\ \phi_T &= F_3(x_f, \theta_f, y_f, \phi_f) \\ D &= F_4(x_f, \theta_f, y_f, \phi_f) \end{aligned}$$

where x_f and y_f are the positions of the particle at the focal plane whereas θ_f and ϕ_f are the corresponding angles with respect to the axis of the reference trajectory. The trajectory of the reference (z axis in Fig. 3.2) is defined as the trajectory of a hypothetic particle traveling along

the beam axis before VAMOS with Bρ_*. θ_T and ϕ_T are the angles measured at the target as shown in Fig. 3.3[3]. The velocity (V) is finally calculated knowing the length of the trajectory (D) and the ToF.

3.1.2 Identification in atomic number Z

The six ionization chambers (ICs) placed at the end of the focal plane detection system of VAMOS measure the energy loss (ΔE) deposited in each of the first five chambers as well as the total energy (E) of the fragment. The ionization chambers are gas detectors filled with *carbon tetrafluoride (CF_4)* gas. Each segment is further sub-divided horizontally into five pads. A Frisch grid is placed in between the anode and the cathode (150 mm from the cathode and 20 mm from the anode). The Frisch grid is primarily used to improve the energy resolution of the ICs. The amplitude of the signal in each IC is directly proportional to the energy deposited in this chamber. After the calibration of the ICs, the energy loss as a function of total energy is obtained (shown in Fig. 3.4). The parallel curves corresponds to a given Z and follow the Bethe-Bloch formula [Leo, 1994] for high energies. For lower energies the individual lines converge towards the Bragg peak and cannot be separated any longer.

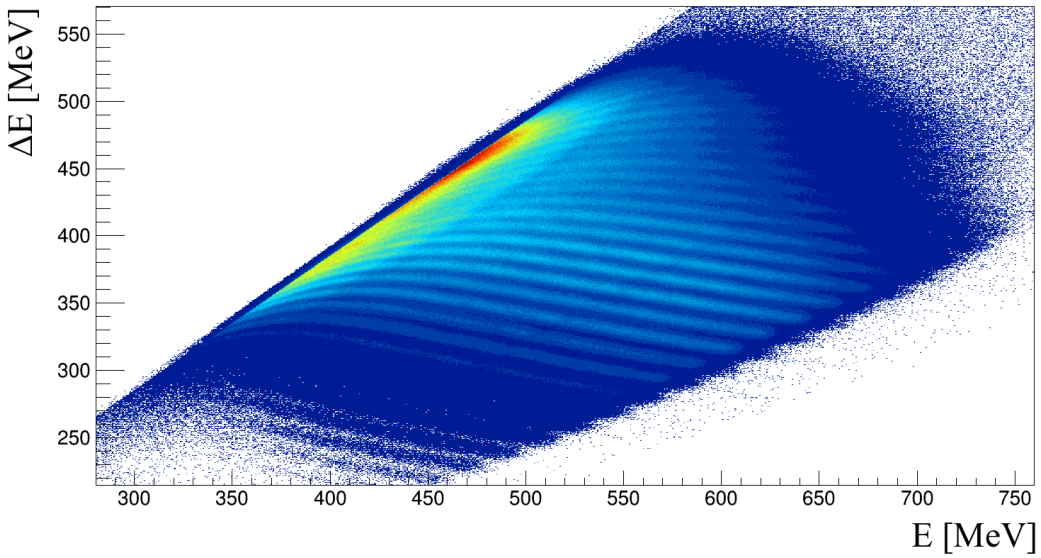

FIGURE 3.4: Energy loss in the first five ICs as a function of the total Energy.

3.1.3 Identification in mass M and charge state Q

The mass-over-charge ratio is calculated from the measured Bρ and velocity (V) using Eq. 3.1. Furthermore, a first mass estimate ($M_{\text{low res.}}$) can be obtained from the measured velocity and the total kinetic energy provided by the ionization chambers using equation 3.2:

$$M_{\text{low res.}} = \frac{E}{(\gamma - 1)c^2} \tag{3.2}$$

where γ is the Lorentz factor. Because of the energy resolution of the ionization chamber, this mass resolution is not sufficient to separate two neighboring isotopes. However, the resolution is sufficient to differentiate between two charge states of the same isotope and to calculate the

[3]The nomenclatures θ_T and ϕ_T are equivalent to θ_V and ϕ_V, respectively in Fig. 3.3 (taken from reference [Vandebrouck et al., 2016])

charge Q using mass-over-charge ratio as seen in Fig. 3.5. The bands in this figure corresponds to different charge states of the ions accepted by the spectrometer, where each locus represents one charge state of a given mass.

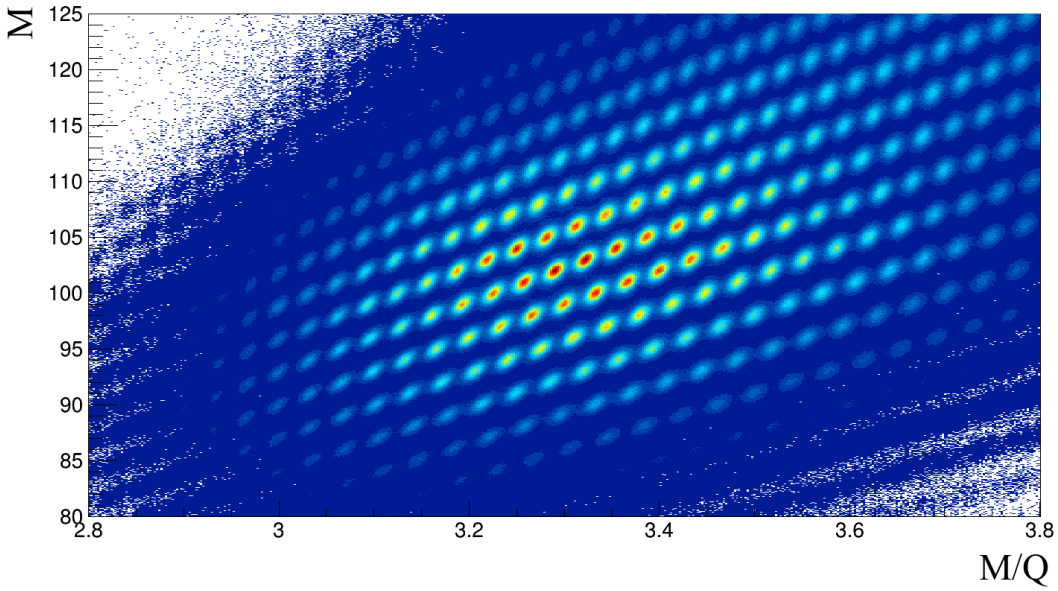

FIGURE 3.5: Correlation between the mass and mass over charge measured over the full focal plane.

A more accurate mass is finally calculated using the mass-over-charge ratio (or M/Q) and Q. The final mass spectrum summed over all the charge states can be seen in Fig. 3.6, showing mass 104 to be the strongest channel.

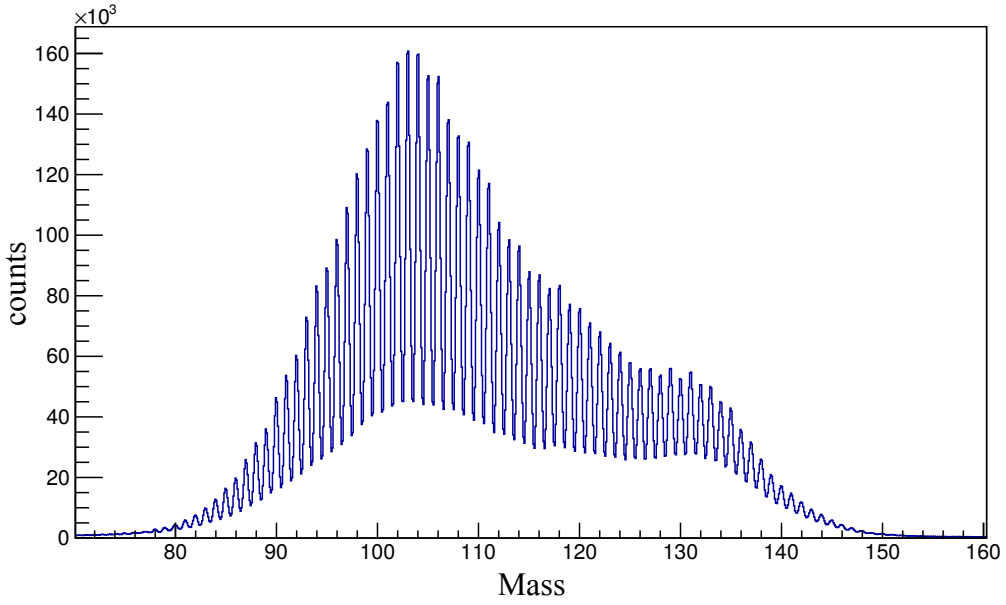

FIGURE 3.6: Mass spectrum summed over all the charge states.

The calibration of VAMOS was performed by *Purnima Singh*[4] and will not be detailed in the present work. The summary of the VAMOS analysis is illustrated in Fig. 3.7.

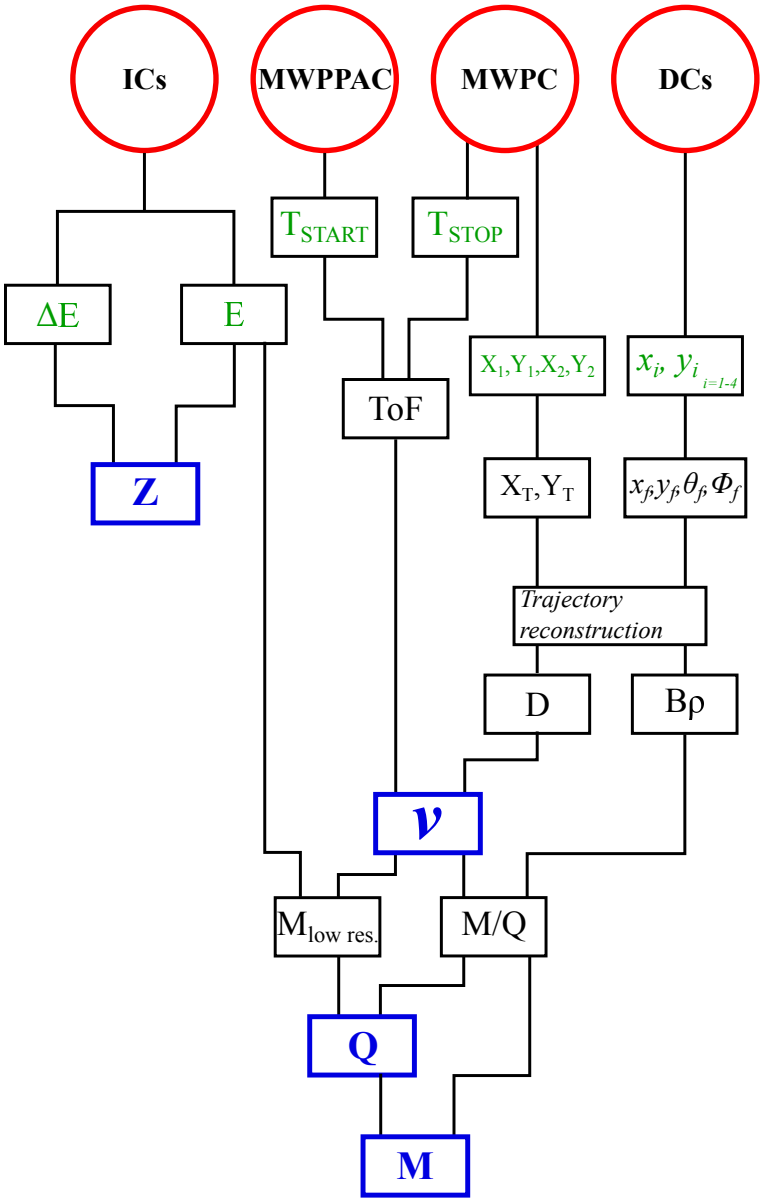

FIGURE 3.7: Schematic diagram of the steps required in VAMOS analysis. The red circles represents the detectors from which the green data is directly measured. The final relevant information for the present lifetime analysis is shown in blue.

[4] purnima.phy@gmail.com

3.2 AGATA

The *Advanced Gamma Tracking Array* (AGATA) [Akkoyun et al., 2012] is a collaborative project implemented by 40 institutions from 12 European countries [Simpson et al., 2008] which aims to construct the first γ-ray tracking spectrometer in Europe. AGATA is an array of position-sensitive high-purity Ge detectors where each detector is 36-fold segmented. The strength of the array lies in combining the excellent energy resolution of Ge detectors with unprecedented photo-peak efficiency through the use of the techniques of Pulse Shape Analysis (PSA) (see sec. (3.2.2) and γ-ray tracking (see section 3.2.3). These techniques allow determining the accurate position of all γ-ray interactions inside a Ge crystal as well as the reconstruction of Compton-scattered γ rays inside the array. In its final phase, AGATA is intended to have a 4π solid angle coverage to maximize its detection efficiency. The technology of encapsulated detectors developed for EUROBALL, where the crystals are hermetically sealed in an aluminum container with thin walls [Eberth and Simpson, 2008; Eberth et al., 1996], is also used in AGATA. To optimize the performance of the AGATA array, different geometric configurations (involving different number of crystals, crystal shapes, number of cluster types, covered solid angle etc) were tested and compared in Monte-Carlo simulations (see Fig. 3.9). Maximum solid angle coverage, full energy efficiency and P/T ratio were obtained for an array of 180 crystals regrouped in 60 AGATA triple clusters (ATC) (shown in Fig. 3.8) [Farnea et al., 2010].

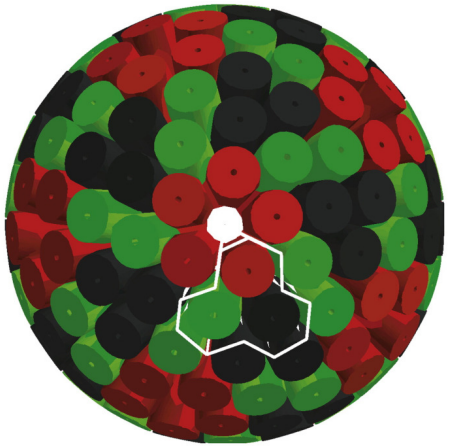

FIGURE 3.8: Schematic view of the 4π AGATA array with 180 Ge crystals. The white boundary corresponds to one triple cluster.

Currently, nearly a 1π configuration of the AGATA array with 13 triple and 1 double crystals forming a total of 41 Ge crystals is operational at GANIL. The AGATA array is extensively used in combination with the VAMOS++ spectrometer [Rejmund et al., 2011] and is positioned at backward angles around the VAMOS++ optical axis. This layout (shown in Fig. 3.10) provides the optimum peak-to-background ratio, Doppler-effect correction accuracy and improved efficiencies in lifetime measurements [Clément et al., 2017].

AGATA crystals

The AGATA crystals are manufactured by *Mirion* (the successor of *Canberra-Eurisys*), France, using high-purity n-type germanium crystals (with an impurity concentration ranging 0.4 - 1.8 $\times$ 10^{10} cm^{-3} [Akkoyun et al., 2012]) in a closed-end coaxial geometry. The use of high purity in Ge detectors is essential to minimize the loss of charge carriers due to *trapping* and *recombination*. Each crystal weighing $\approx$ 2 kg, due to its fragility is encapsulated in a hermetically sealed aluminium canister with 0.8 mm thick walls. The distance between the capsule walls and the crystal

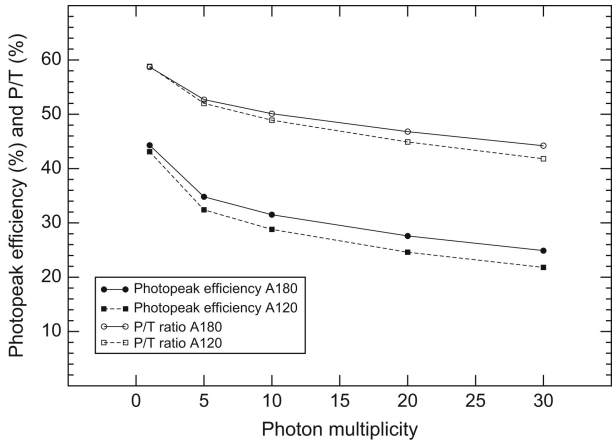

FIGURE 3.9: Simulation showing a comparison between 120 and 180 Agata crystals in terms of total energy efficiency and peak-to-total ratio of a 4π array [(Akkoyun et al., 2012)].

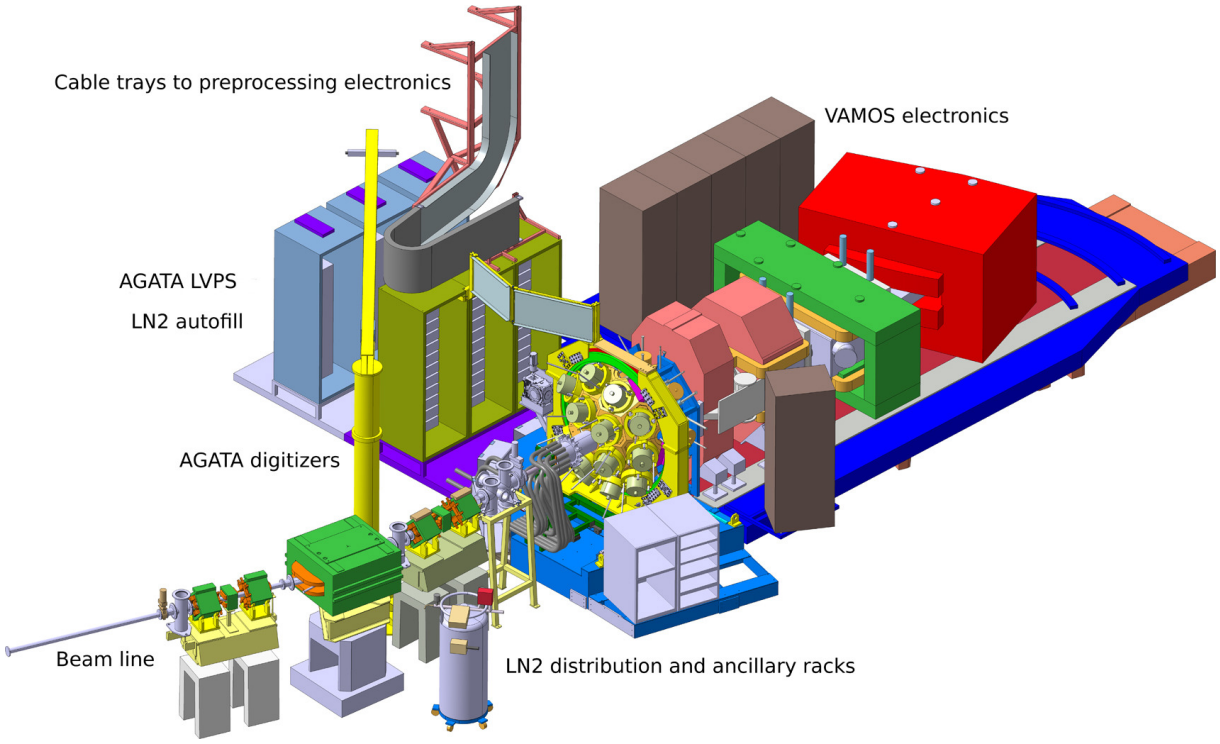

FIGURE 3.10: Layout of AGATA 1π array at G1 hall in GANIL [Clément et al., 2017]

side faces ranges from 0.4 mm to 0.7 mm. High voltage is applied to the central contact (core) isolated[5] with ceramic material. The central core is also used to obtain the full-energy signal, i.e. the total energy deposited in the crystal. The crystal surface is segmented into six electrically isolated rings and each ring is further divided into six segments, resulting in a total of 36 segments as seen in Fig. 3.11. There are in total 38 signals per crystal (the full energy collected in the core (amplified with two different, high gain, low gain) plus the 36 segments) bringing the total number of high-resolution spectroscopy channels per ATC to 114.

[5]The insulation is in the center of the lid of the capsule.

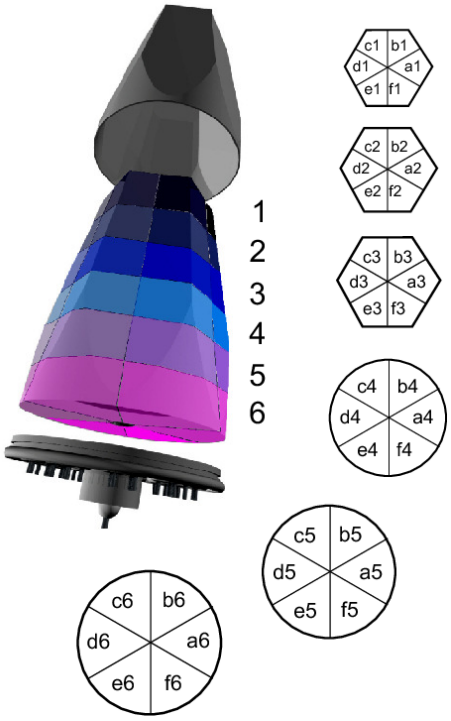

FIGURE 3.11: Schematic view of an AGATA crystal displaying central core contact and 6 pads with 6 segments each.

Each ATC includes three different crystals of distinct hexagonal shapes, displayed in Fig. 3.12. They are usually referred to by a letter or a color code: A- red, B- green and C- blue. Additionally a serial number is assigned to each crystal (nomenclature: A001, A002, etc..) [(Akkoyun et al., 2012)]. The segments are also labeled as shown in Fig. 3.11. This nomenclature is used in the following sections describing the treatment of the AGATA data.

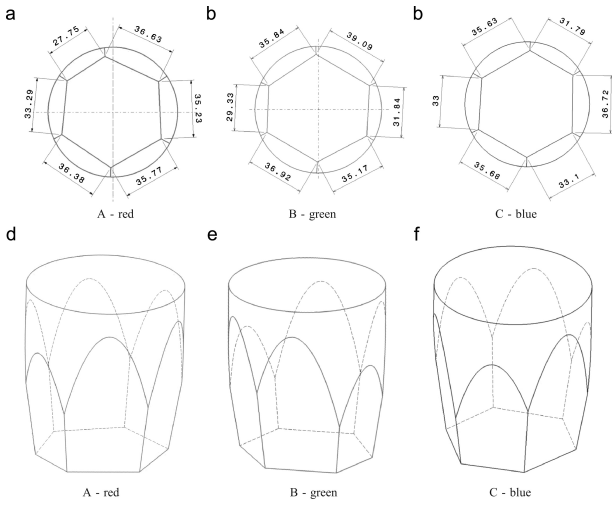

FIGURE 3.12: Geometry and nomenclature of AGATA crystals forming on ATC (image adapted from Wiens et al., 2010)

AGATA electronics

For a detector array with more than 1300 high resolution channels such as AGATA, high-speed digital sampling electronics is required to extract time and amplitude information for each signal in order to efficiently implement the PSA and tracking techniques. AGATA's Front-End Electronics (FEE) is a digital data-processing electronics that comprises:

- Advanced charge-sensitive resistive feed-back preamplifiers which read the 38 signals from each crystal.
- Digitizer modules along with broad-band digital data transmission lines which digitize the 38 signals from each crystal.
- Pre-processing electronics' which receives the digitized signals from all AGATA detectors and processes them through Global Trigger System (GTS) before routing them to the dedicated PC for the Local Level Processing (LLP). Pre-processing electronics extract the energy information via a digital trapezoidal filter or a Moving Window Deconvolution (MWD) algorithm [Georgiev, Gast, and Lieder, 1994]. Henceforth, the pre-processing electronics provide the γ-ray energy deposited in each segment, total energy deposited in the core, and a time-stamp per crystal [Pullia et al., 2012].

The three Ge crystals of each ATC are placed in a common cryostat keeping them at a temperature of $\sim$90 K. The pre-amplification of each energy signal, both for the core and the segments is done in two stages. First, the cold part of the preamplifiers uses low-noise silicon Field-Effect Transistors (FET) and a passive feedback network (located in close proximity to the Ge crystals) to optimize bandwidth and reduce noise at a temperature of 130 $\pm$ 20K [Barrientos et al., 2015]. The input channels of the cold part are electronically shielded to avoid crosstalk between them. Second, the warm (room temperature) part of the pre-amplifier comprises a low-noise amplifier, a pole-zero stage, a differential output buffer, and fast-reset circuitry and is located outside the cryostat for better access [Akkoyun et al., 2012]. The fast-reset circuitry is a time-variant device to reset high-energy signals (caused by energetic charged particles such as muons from cosmic radiation) above a certain threshold, hence reducing the dead time [Pascovici et al., 2008]. The inside of the cryostat is maintained at a pressure of 10^{-6} mbar, and the cold and warm parts are coupled through low thermal conductivity wires [Wiens et al., 2010]. An AGATA triple cryostat is visualized in Fig. 3.13.

In the first phase of the AGATA project individual rack-based digitizer modules were used for each AGATA crystal as well as pre-processing electronics using the Advanced Telecommunications Computing Architecture (ATCA) format. However, with the addition of more detectors over the years, new electronics modules were implemented representing an upgrade of the previous modules. The additional detectors are presently employing compact digitizers (Digi-Opt12) with lower power consumption to be able to handle the increasing number of detectors when going towards a 1π array.

Instead of using the ATCA format, the new digitizers are connected to the GGP (Global Gigabit Processor) Peripheral Component Interconnect Express (PCIe) cards for fast data transfer towards the PSA farms. The update of the AGATA electronics is detailed in [Pullia et al., 2012; Barrientos et al., 2015; Zocca et al., 2009; Pascovici et al., 2008; Grave et al., 2005]. The detectors equipped with the new electronics are listed in Fig. 3.14.

AGATA data flow

The core signal, which is the total charge released within the crystal by all γ-ray interactions acts as a local trigger. As soon as there is a signal in the core, a trigger request is sent to the GTS

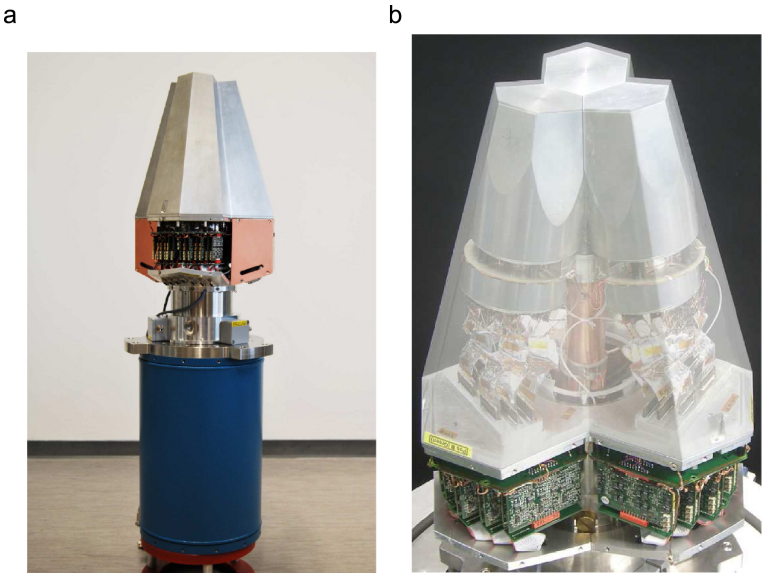

FIGURE 3.13: Image showing an AGATA triple cryostat (ATC). a) The blue cylindrical part is the liquid nitrogen dewar and the structure beneath the copper shielding is the warm part of the pre-amplifiers. b) The cold part of the preamplifier is visible through the semi-transparent cap and the green boards at the bottom are the warm part of the pre-amplifiers. The image is adapted from Wiens et al., 2010.

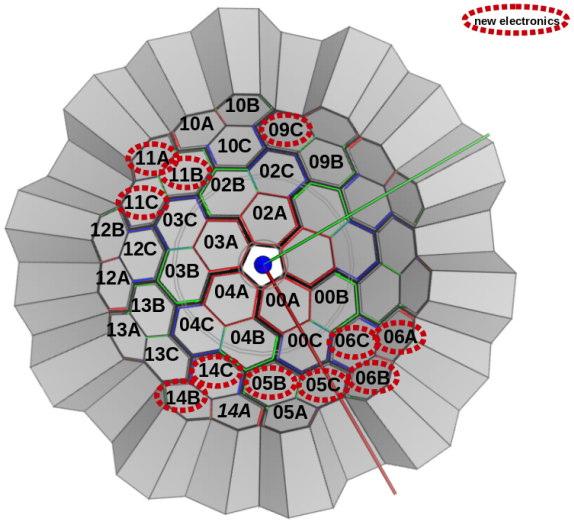

FIGURE 3.14: Nomenclature of the AGATA detectors; those equipped with new electronics are marked in red.

and the trigger processor. The validation of the request is controlled through the trigger processor according to the experiment's multiplicity or coincidence requirements. When the required conditions are met, a 'validation signal' with an event number and time stamp is sent back to the individual detectors in order to carry out the data transmission. When the conditions are not met a rejection request is sent. All tasks of the pre-processing electronics are implemented in real time by user-defined logics in Field Programmable Gate Arrays (FPGAs) [Barrientos et al., 2015].

AGATA uses the NARVAL data acquisition system that manages the data flow by user-defined tasks and is based on an abstract class called 'Actor' from an object-oriented language 'Ada 95' [Grave et al., 2005]. The three main actors inherited from the abstract class level are a) producer: collects data from each crystal, b) intermediate: builds data events, performs calibration and PSA, c) consumer: write the data on the disk. The data-flow is summarized in Fig. 3.15. The Narval actors at the global level are the Event Builder and the Tracking Filter. The VAMOS data is processed independently in the GANIL format called Multiframe metaformat (mfm) before being coverted into ADF (by mfm to adf converter). The processed VAMOS data together with the AGATA data from the Event Builder is dispatched towards the Event Merger.

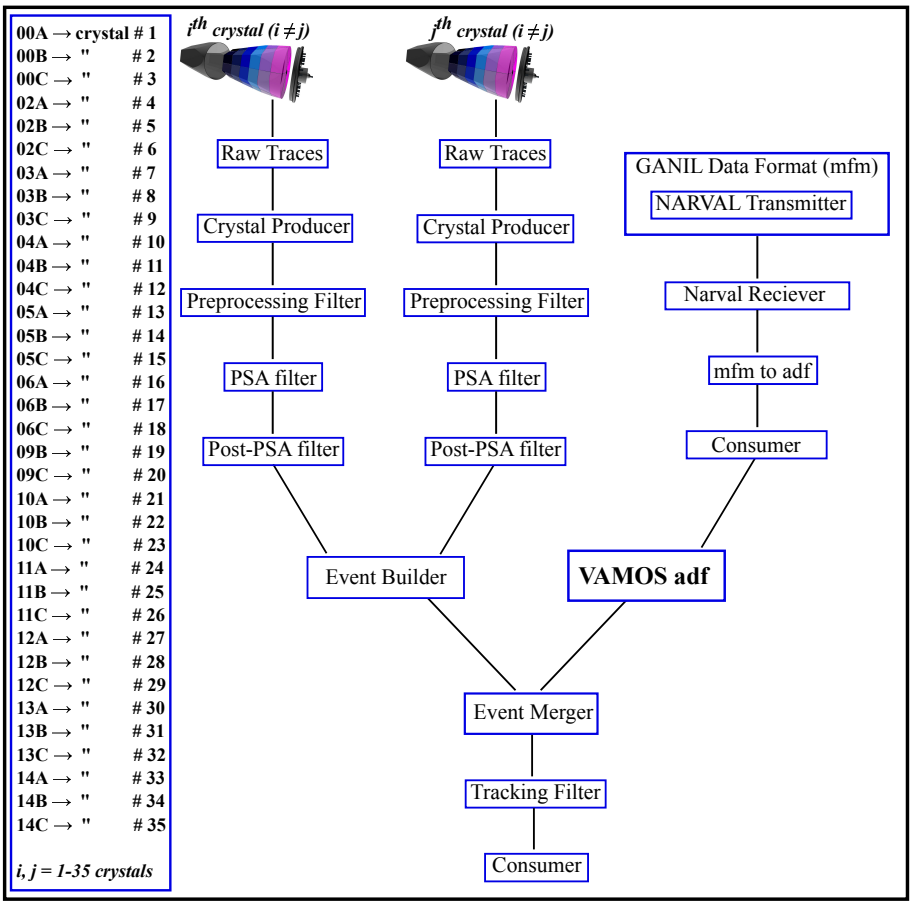

FIGURE 3.15: Data flow of AGATA analysis.

3.2.1 γ-ray detection with semiconductor detectors

When a γ-ray interacts with the Ge material (or other semiconductor detector) it can loose its energy via three main processes which depend on its initial energy.

- Photoelectric effect: This effect is likely to occur for a photon with energy below 250 keV and is the dominant process below 100 keV. In this process the energy of the photon is completely absorbed by an atomic electron resulting in the ionization of the atom through a single interaction.

- Compton scattering: This process occurs when the photon scatters and loses a part of its energy to an atomic electron. Depending on the energy of the incoming photon, Compton scattering can occur multiple times along the photon's path. The process of multiple

scattering will continue until the energy is sufficiently small to undergo a photoelectric absorption of the scattered photon. In the 100 keV - 250 keV energy range, the photoelectric absorption and the Compton scattering have similar cross-section [Marel and Cederwall, 1999]. Compton scattering strongly dominates above 250 keV and up to $\sim$ 10 MeV. This was established in the work of Roth, Primbsch, and Lin, 1984 where Monte Carlo simulations of photon interactions with a 6cm $\times$ 6cm Ge detector were performed (Fig. 3.17).

- $e^- - e^+$ pair production: The production of an electron and positron pair at the site of the first γ-ray interaction can occur at energies above 1022 keV. The kinetic energies of both electron and positron are spent in creating charge carriers with the latter eventually annihilating into two 511 keV photons, which may or may not be absorbed in the crystal.

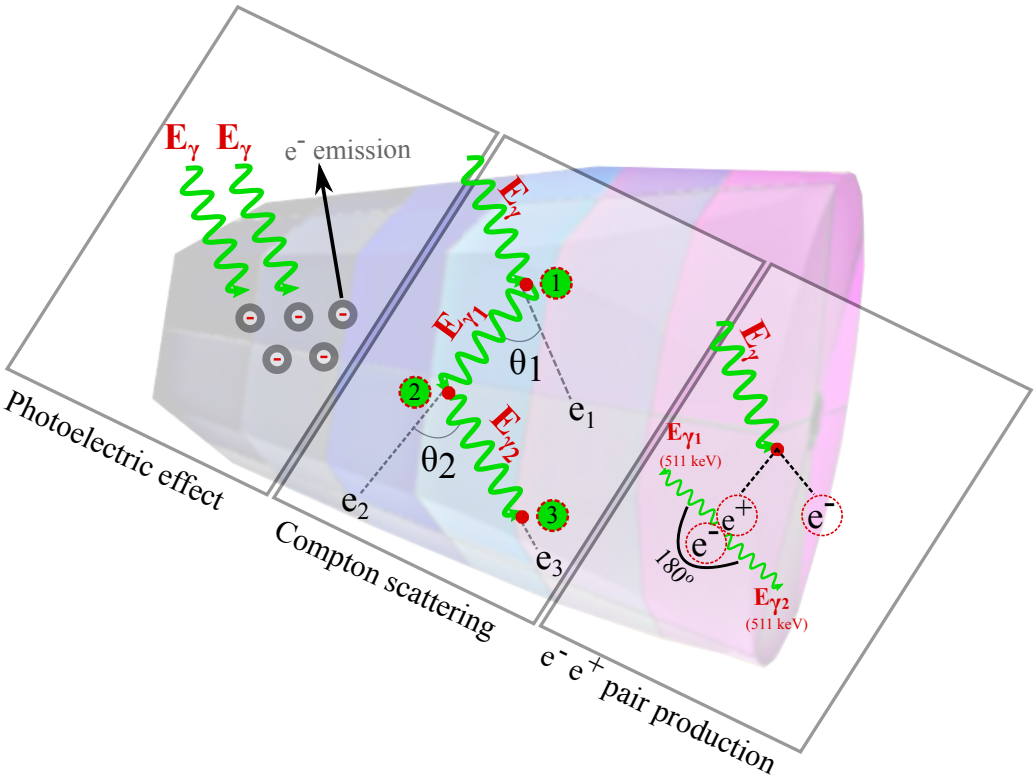

FIGURE 3.16: Schematics of three main γ-ray mechanism in matter.

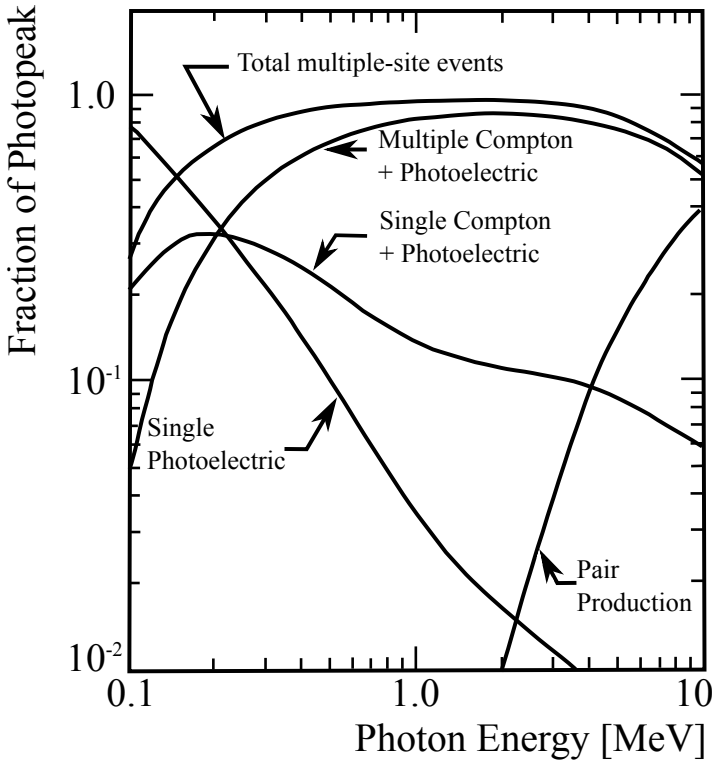

FIGURE 3.17: Fraction of Photopeak for different energy loss mechanism inside Ge (adapted from Roth, Primbsch, and Lin, 1984)

In a semiconductor detector, the basic charge carriers are electrons and holes. Electron-hole pairs can be created due to thermal agitation[6] or through the interaction of incoming particles with the semiconductor bulk material. In the presence of sufficient thermal energy, an electron can leave the valence band to occupy the conduction band hence leaving a vacancy (or hole) in the valence band. Electron-hole pairs drifting in a semiconductor can be trapped in lattice impurities which immobilizes the electron/hole hence contributing to the loss of charge carriers. In order to increase the conductivity, the tetravalent Ge/Si semiconductor lattice is doped with either pentavelent impurity or trivalent impurity making the semiconductor n-type or p-type, respectively. In a n-type semiconductor, pentavalent impurities (eg, Bismuth) are added to the lattice which after forming a covalent bond with four electrons, always leaves one "free" electron in the valence shell. Since this electron is loosely bound in the atom, it takes little energy to excite it to the conduction band. This process of n-type doping substantially increases the number of electrons as compare to the number of holes, thereby making electrons the primary charge carriers inside the lattice. In a p-type semiconductor the concentration of holes is much larger than that of electrons. This also makes n-type detectors more suited for in-beam spectroscopy. Indeed, the holes being more likely to be trapped in dislocations created by radiation damage, ensures a slow deterioration of the core energy resolution [Korichi and Lauritsen, 2019].

Without an electric field the free electrons and holes have a random thermal velocity, however, in the presence of an electric field both electrons and holes start to migrate with an average drift velocity parallel to the direction of the field. In a standard semiconductor detector, the electrons have higher mobility than the holes. For a low electric field the associated drift velocities (ν_e for electrons and ν_h for holes) increase linearly:

[6] Cooling a Ge-based semiconductor detector allows to reduce thermal noise

$$\begin{aligned} \nu_h &= \mu_h \xi \\ \nu_e &= \mu_e \xi \end{aligned} \tag{3.3}$$

where, μ_h and μ_e are the mobility of holes and electrons, respectively and ξ is the electric field magnitude. The drift velocity of electrons and holes is anisotropic and depends on the direction of the applied electric field with respect to the direction of the lattice vectors, making it a critical parameter for the pulse shape rise time, charge collection and signal generation process [Ottaviani, Canali, and Quaranta, 1975; Canali, Ottaviani, and Majni, 1974; Reggiani et al., 1977]. The crystal orientation can influence the mobility of the carriers by up to 30 % [Korichi and Lauritsen, 2019]. Thus, this orientation must be known or measured for each crystal for accurate pulse shape analysis and tracking [Bruyneel, Birkenbach, and Reiter, 2016].

3.2.2 Pulse Shape Analysis

The role of the PSA is to determine the precise position of the γ-ray interaction inside the array through algorithms that compare the shape of the signal with a set of position-dependent, single-interaction "Reference Pulse Shapes" (RPS) corresponding to well-defined positions.

The RPS are obtained by simulating the response of an AGATA crystal to the γ-ray interaction. The simulation takes into account the mobility of electrons and holes, and net and induced "mirror" charges in the electrodes. These reference signals can also be measured by using scanning tables (located in Liverpool [Nelson et al., 2007; Boston et al., 2009], Orsay [Ha et al., 2013], Salamanca and Strasbourg [Akkoyun et al., 2012]). Several of these devices use a highly collimated source (e.g. a strong ^{137}Cs source with less than 1 mm aperture) in coincidence with a collimated ring of scintillation detectors to map the response of the germanium detector as a function of the position of the γ-ray interaction in all three x, y and z directions [Akkoyun et al., 2012]. Scanning the entire array using this technique with a pencil-like γ-ray beam is time consuming[7] as it yields very low coincidence rate between the germanium detector and the scintillators. Therefore the direct measurement could not be performed yet for the entire array. The experimental results from the scanning are, however, used to optimize the simulations. For instance, it has been shown that a precise anisotropic characterization of electron and holes mobility can bring the error between the experiment and simulations of the signal shapes to less than 2% [Bruyneel, Reiter, and Pascovici, 2006].

There are several simulation programs being used, JASS (a Java based Simulation Software by Schlarb et al., 2011) and ADL (the AGATA Detector Library by Bruyneel, Birkenbach, and Reiter, 2016) that are developed within the AGATA collaboration to characterize the AGATA detectors in order to produce RPS for the entire array. PSA is performed in the present work using ADL bases. ADL bases are unique for each detector and need to be implemented while running the PSA algorithm. Ideally the ADL bases would only be developed for the three shapes (shape A, B and C), however in reality each AGATA crystal slightly differs from the nominal shapes due to the limitations of the manufacturers in reproducing the exact shape.

PSA implementation in AGATA

In an n-type germanium detector roughly 340000 electron-positron pairs are produced for an incident gamma ray with an energy of 1 MeV. This charge carrier cloud has a size of 0.5mm and a velocity of the order of 10^7 cm/s [Schlarb et al., 2011]. Under the influence of an electric field these charge carriers drift to their respective electrodes. The core electrode (anode) attracts electrons while the segment electrode (cathode) attracts holes (as discussed in section 3.2.1). The

[7] A full characterization of a crystal with a grid of 1 mm takes 2–3 months.

rise time of the signal depends on the distance between the position of the γ-ray interaction and the electrode collecting the charge. An interaction is ascribed to the segment whose electrode is collecting holes and displays an induced net charge. Since the AGATA crystals are electrically segmented, the electrodes of the neighboring segments experience a transient signal due to the motion of charges. The net-charge of this transient signal is zero.

The space charge distribution is defined by the Shockley-Ramo theorem which states that for a set of electrodes (1-n), the charge Q_i induced on electrode 'i' by a moving point charge 'q' at an arbitrary point r is given by:

$$Q_i = -q \cdot \phi_i(r) \tag{3.4}$$

where ϕ_i(r) is a weighting potential that depends only on the geometry. With the knowledge of the induced charge in an electrode, the corresponding current ($i = \xi q \nu$, where ξ is the Ramo field (not homogeneous with an electric field) [Ramo, 1939], ν is the velocity which can be calculated as a function of position and time. An example of the signal shapes resulting from a γ-ray interacting in a single segment is presented in Fig. 3.18. In this case, the shape of the signal implies that the segment B4 carries the net charge i.e the primary γ-ray interaction took place in this segment. The neighboring segments such as B3, A4, B5 and C4 experience only *transient* signals with no charge collection. The precise position information is drawn from the rise time of the net-charge signal and the transient signals as well as from a comparison of these signal shapes with the reference pulse shapes [Michelagnoli, 2013]. The energy of the γ-ray is proportional to the amplitude of the net charge signal. The comparison between the pulse shapes of the measured signals and the reference signals demands a sophisticated algorithm to identify the signal shape, compare it with the reference data-base and effectively provide the information on the position and energy of the γ-ray with least amount of CPU power. Out of several PSA algorithm tested for AGATA [Recchia et al., 2009] the *Adaptive Grid Search* provides the best results. This algorithm can be used to compare the signal shape for any number of firing segments in the crystal, however it cannot distinguish between the two signal firing in the same segment. In case of multiple segment firing in an event, the algorithm sums up all those signals before comparing the net signal to the PSA database. The primary concept of the algorithm is to evaluate the residue 'R' (given by Eq. 3.5) corresponding to well-defined points in the segment and assign a three dimensional coordinate to the position where R is minimum.

$$R = (Signal_{measured})^2 - (Signal_{calculated(RPS)})^2 \tag{3.5}$$

where the first term corresponds to the measured signals in the in-beam experiment and the second term is the calculated (simulated) signal corresponding to Reference Pulse Shapes. This procedure is applied on a coarsely-spaced grid followed by a search on a finer grid with limits identified by the coarsely spaced grid. A full fine grid search has 1000 points with 2 mm spacing in between [Michelagnoli, 2013]. This algorithm is more precise for a single interaction than for multiple interactions within one segment for which the algorithm assumes a pseudo single point interaction that is leaning towards the center of gravity of the real interaction [Recchia et al., 2009]. This algorithm provides an average resolution of 4 mm at 1.4 MeV [Venturelli and Bazzacco, 2004].

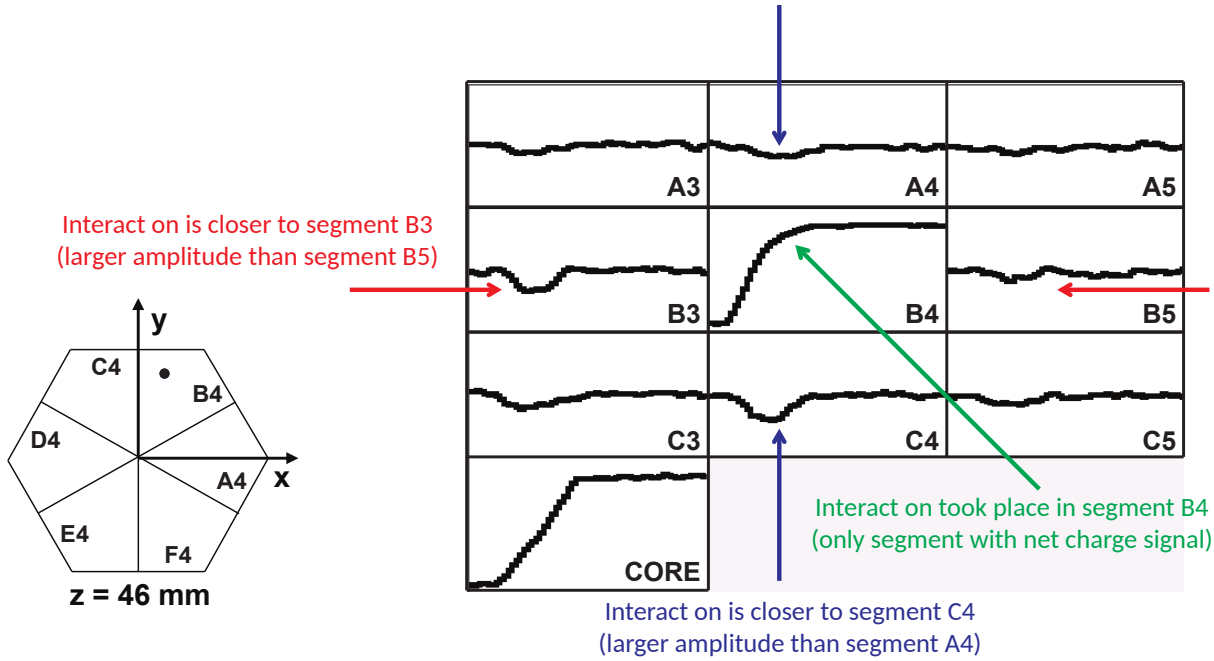

FIGURE 3.18: An example of PSA implementation. The net charge is deposited in segment B4 whereas the transient signals are induced in the neighboring segments. Image taken from Michelagnoli, 2013

3.2.3 Gamma-ray tracking with AGATA

Compton scattering is the dominant process of γ-ray interaction for energies between 100 keV and 10 MeV, relevant for nuclear spectroscopy. Various approaches to deal with Compton scattering can be applied in order to improve the ratio of the photo-peak to the Compton scattering background:

- In previous generation Ge arrays, the detectors enclosed in a Compton shield that rejects events if a Compton-scattered γ-ray leaves the detector. Such shielding strongly reduces the solid angle covered by the detectors and impacts the γ-ray detection efficiency.
- The add-back method can be used in Ge arrays using composite (clover or cluster) detectors, such as EXOGAM [Simpson et al., 2000]. If a γ-ray deposits its energy in more than one Ge crystal of a clover detector, the add-back procedure sums up the energies collected by all the Ge crystals in order to recover the full energy.
- AGATA combines an array of closely-packed Ge detectors with γ-ray tracking capability allowing for local addback even in the case of high γ-ray multiplicity. In a segmented array like AGATA the individual interactions corresponding to the same event are identified and the scattering sequence of the γ-ray within the array is reconstructed using the deposited energy and spatial distribution of the individual interaction points.

Fig. 3.16 shows an example of a Compton scattering event with two successive γ-ray interactions ($E_{\gamma 1}$ and $E_{\gamma 2}$) that transfer energies e_1 and e_2 to the electrons at positions 1 and 2, respectively, before the γ-ray is fully absorbed at position 3 by producing a photo electron of energy e_3. The relationship between the energy of the scattered photon and the emitted electrons is linked to the angle between them at each interaction position (θ_1 and θ_2 in this case) and is given by the following equation for the i^{th} Compton interaction.

$$E_{\gamma i} = \frac{E_{\gamma i-1}}{1 + \frac{E_{\gamma i-1}}{m_e c^2}(1 - cos\theta_i)} \tag{3.6}$$

where the electron energy is given as: $e_i = E_{\gamma i-1} - E_{\gamma i}$. This formula is used to determine the expected energy of the scattered γ ray. Tracking in AGATA is performed using the Orsay Forward Tracking (OFT) [Lopez-Martens et al., 2004] algorithm which is developed using the Geant4 AGATA code [Farnea et al., 2010]. The first task of OFT is to identify all γ-ray interaction points that are close to each other and assign them in a cluster of interactions. Two or more hits are ascribed to the same cluster if the angular separation between the hits is below a certain threshold. The algorithm searches for every interaction point fulfilling the aforementioned condition. A figure of merit is attributed to each permutation of the interaction sequence for each cluster. This figure of merit takes into account the cross sections for Compton scattering and photo-electric absorption at a given energy, the likelihood of a γ-ray traveling a certain distance between two interaction points, and compares the measured scattering energies with those predicted by Eq. 3.6. The permutation that maximizes the figure of merit is considered to be the correct sequence of the clusters. An example of the cluster representation of γ-ray Compton scattering points is shown in Fig. 3.19. The principle of OFT is detailed in Lopez-Martens et al., 2004.

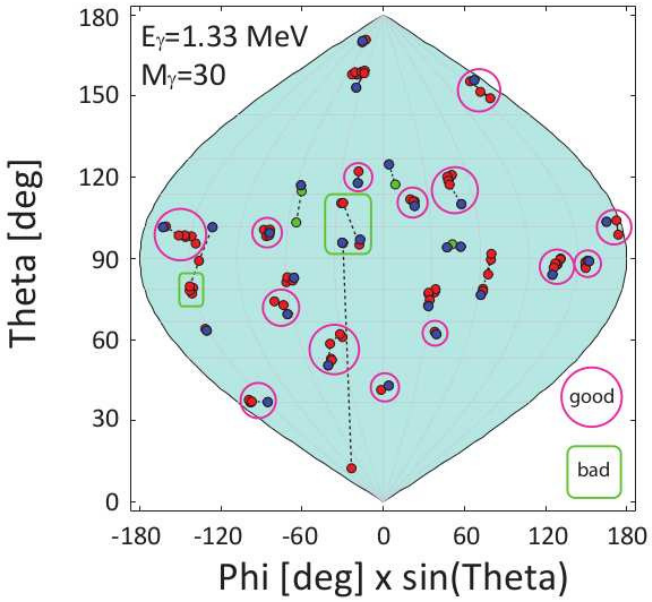

FIGURE 3.19: Illustration of the performance of the tracking algorithm showing the assignment of good and bad clusters on the basis of figure of merit (detailed in Lopez-Martens et al., 2004).

Fig. 3.20 compares a spectrum taken from the present AGATA experiment with the one taken from EXOGAM in a similar experiment under similar conditions [Singh et al., 2018]. It can be seen that AGATA has a better efficiency, energy resolution and peak-to-background ratio than EXOGAM. The gain in photo-peak efficiency in AGATA over EXOGAM is resulting from an improved solid angle in AGATA due to the absence of Compton shields in AGATA as compare to EXOGAM. Also, the gain in efficiency comes from the fact that the AGATA detectors are closely packed and (almost fully) covering the solid angle from 135° to 175°, while for the EXOGAM experiment (spectrum shown in Fig 3.20b) only 3 Clover detectors under backward angles centered

around 135° were used for the lifetime analysis.

In Compton-suppressed Ge detectors, as used in EXOGAM, events where the γ-ray is not completely absorbed in the Ge crystal, but scattered into the anti-Compton shield are rejected which influences the energy efficiency. On the other hand, the tracking procedure performed in AGATA allows to trace back such events and recover the full energy of these events.

The improved energy resolution in AGATA as compared to EXOGAM (as seen in Fig. 3.20) is due to the position sensitive Ge detectors used in AGATA as well as the tracking procedure which takes the information provided by PSA to reconstruct the full energy of a Compton-scattered γ-ray. The better position resolution in AGATA ultimately impacts the Doppler correction procedure and also improves the lifetime results.

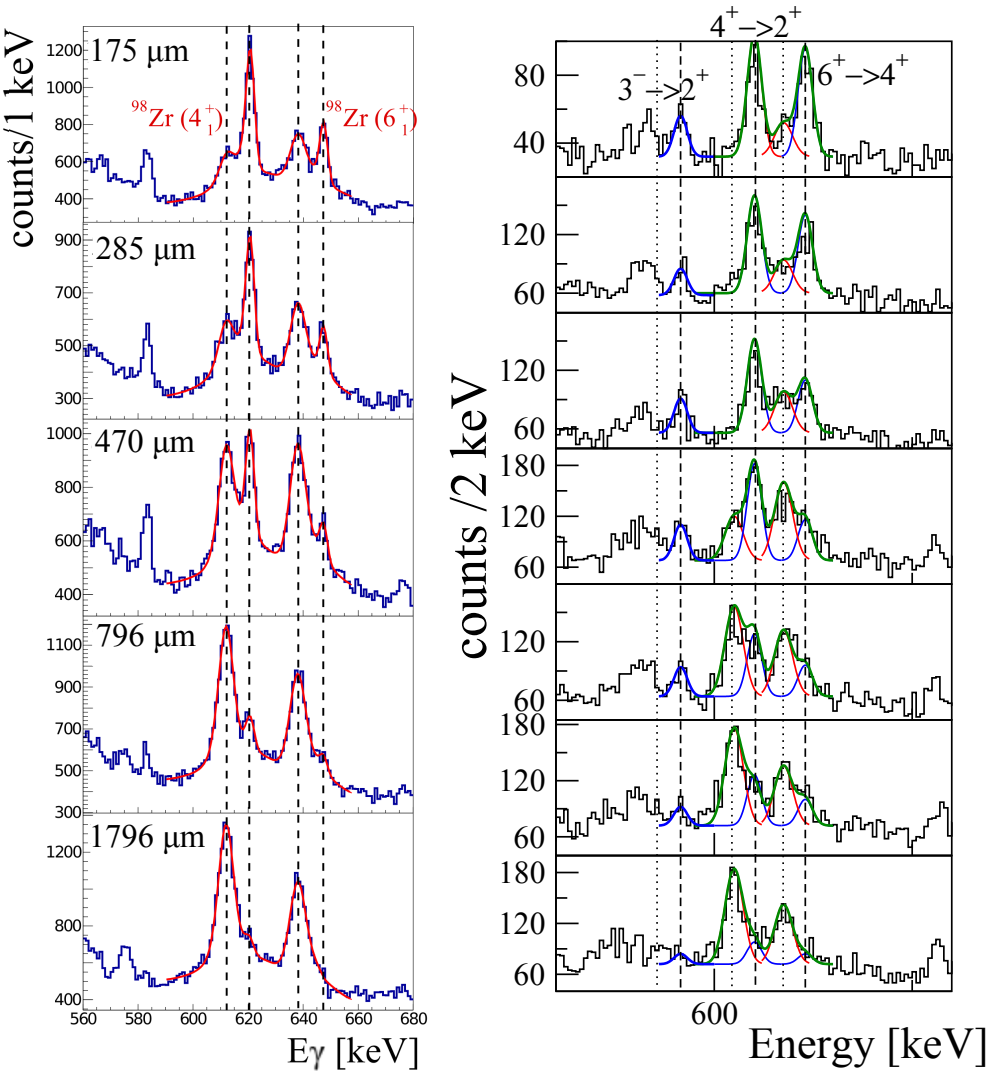

(A) AGATA (B) EXOGAM

FIGURE 3.20: Energy spectra in (a) and (b) are showing the $4^+_1 \longrightarrow 2^+_1$ and the $6^+_1 \longrightarrow 4^+_1$ transitions in ^{98}Zr measured with AGATA and EXOGAM, respectively, for different plunger distances (see section 6.1 for more details).

Chapter 4

Data Analysis

The aim of the experiment was to measure the lifetimes of low-lying excited states of neutron-rich nuclei around mass 100. In order to determine lifetimes using the Recoil Distance Doppler Shift method, AGATA needs to be carefully calibrated in energy and time which is described in this chapter.

4.1 Presorting

AGATA's software suite allows to reprocess offline the raw data (energy, traces and time stamps) to improve the energy and time calibrations and the cross-talk correction as well as to test different preprocessing options. One of the data replay option that has been tested is the pile-up rejection which is performed with the preprocessing filter (See block diagram 4.1). The energy, which is normally calculated through the MWD algorithm, can also be estimated from the traces albeit with a lower resolution (∼8 keV). If this energy is not compatible with the one provided by the MWD filter, the event is rejected as a pile-up event. This option slightly improves the peak-to-background ratio of the energy spectra.

4.2 AGATA Calibration

The raw data from AGATA and the corresponding time stamps are treated by a series of Narval actors, as depicted in the block diagram (Fig. 3.15). Each AGATA crystal produces 38 signals: 36 signals from the individual segments and 2 signals from the core corresponding to two different gains (low gain up to 20 MeV, high gain up to 6 MeV). The calibration of AGATA was performed using standard calibration sources of ^{60}Co and ^{152}Eu during two calibration runs taken at the beginning and at the end of the experiment. The beam time of the experiment was 10 days with two extra days devoted to these calibration runs. Energy, time calibration, cross-talk correction, neutron damage correction and global time calibration are performed using the ^{60}Co source data. For the final precise energy recalibration ^{152}Eu source data were used, because the recalibration is a polynomial function for which more than two points are needed for fitting, while ^{60}Co emits only 2 γ rays. Each calibration stage listed in the block diagram of Fig. 4.1 will be explained in the following part.

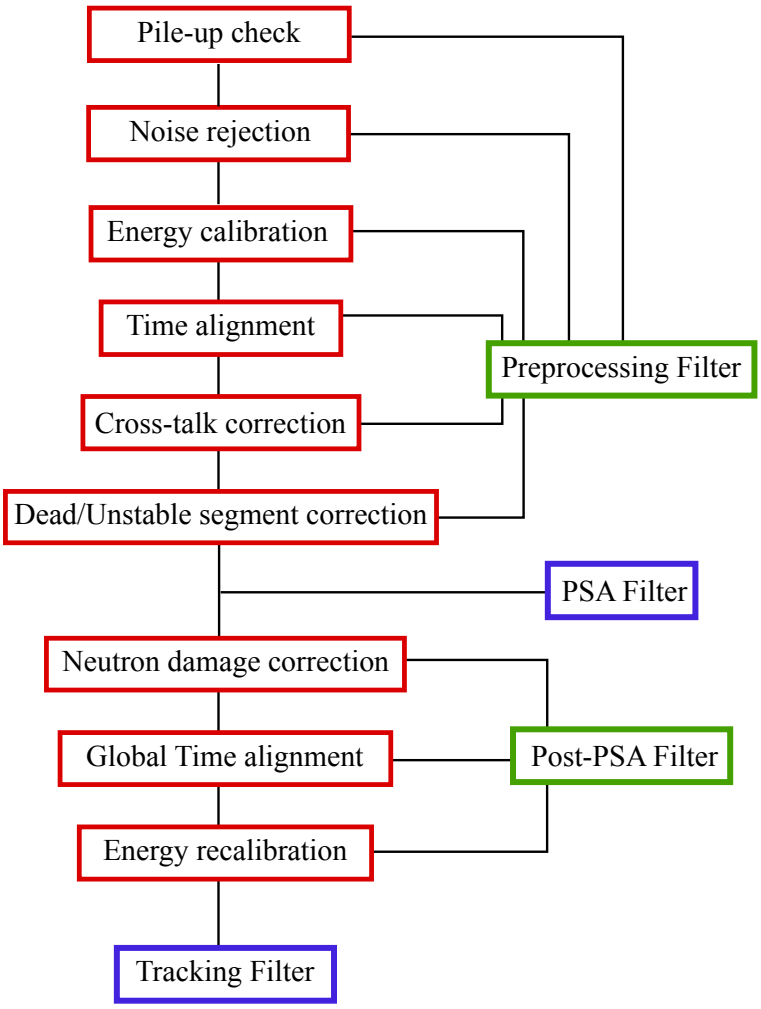

FIGURE 4.1: Block diagram highlighting the AGATA analysis tasks in red and the filter used for those tasks in green. The two main filters used for data replay are in blue.

Time alignment

The time calibration has an impact on the PSA, tracking and data merging with the VAMOS spectrometer. It is performed in three stages.

- Coarse time alignment between each segment and the core signal.
- Time alignment of the measured signal with the PSA database: performed during PSA, also known as T_{zero} alignment.
- Time alignment between individual AGATA detectors at a global level: performed at Post-PSA level.

In order to have a fast timing response, the time signals are generated using a leading-edge discriminator/Constant Fraction discriminator which is triggered by the central contact (core) of the crystal. Fig. 4.2a (top) shows a sketch of a signal trace from AGATA, where the leading edge discriminator is triggered when the rising signal from the core crosses a certain threshold. The timing of the core is arbitrarily set to 500 ns (50 TS) with respect to the time stamp or start of the traces and the time signals of all the segments are aligned to this value. The alignment parameters were produced by fitting and aligning the centroid of each peak of each segment using

^{60}Co data. These peaks were aligned to the reference value (500 ns) of the core and were stored in a configuration file processed at the pre-processing level. The timing signals of the detectors are misaligned with the *base pulse* signals of the PSA database. Fig. 4.2a (bottom) illustrates the PSA database signal with a baseline of 8 Time Stamp (TS)[1] which needs to be compatible with the trigger point at 50 TS (Fig. 4.2a (top)), hence the need to perform T_{zero} alignment. In this stage, the PSA is replayed[2] for a short period of time ($\approx$ 10 mins) and the alignment of the segment signals is performed simultaneously.

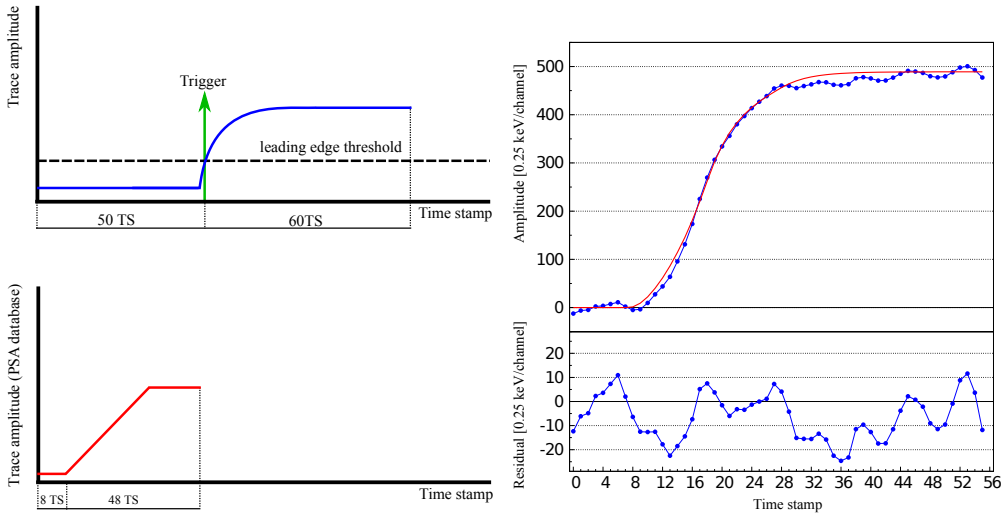

(A) Schematic view of traces timing

(B) Amplitude traces

FIGURE 4.2: Explanation of the AGATA timing properties. a) Schematics of an experimental signal trace of 1100 ns for core/segment with net charge (above) and a trace of 560 ns from the PSA database (below). b) Comparison between the PSA trace (red) from the database and an experimental signal trace (blue) for a γ-ray of energy $\approx$ 120 keV[3].

Energy calibration

In the present experiment a precise energy calibration is vital for three main reasons. Firstly, the PSA relies on the energy calibration of the segments to produce precise position information. Precise energy calibration of the high-gain core traces is extremely important for PSA performance, however a shift of 0.5-1 keV in the energy of the segment is tolerated by the PSA algorithm. Secondly, the tracking algorithm relies on the energy of the incoming γ ray, since the sum of the energies released in the segments is used for the reconstruction of the Compton scattering events (see section 3.2.3). Thirdly, the Doppler-shift techniques used to obtain lifetimes of short-lived states are impacted by the γ-ray emission angle determined from the first interaction point of a γ ray in the Ge crystal whose precision depends on the PSA performance. The energy calibration performed online was not precise enough and most of the segments of several detectors required a more careful offline analysis with the source data. An offline calibration was performed from scratch for all the detectors through a series of actions listed in Narval actor's *Topology* using a Narval emulator *femul* [Birkenbach et al., 2010] (Figs 3.15,4.1). The energy calibration was performed automatically using the *Recal* program [by D. Bazzacco] which performs peak search

[1] 1 TS = 10 ns
[2] The processing of PSA is called "replay" in AGATA terminologies.
[3] Plot credits: M. Siciliano

in energy spectra and a Gaussian fit of identified peaks, although it was frequently necessary to perform a manual calibration. Fig. 4.3 presents a comparison of raw and calibrated energy spectra of 36 segments for one of the AGATA detectors using ^{60}Co data.

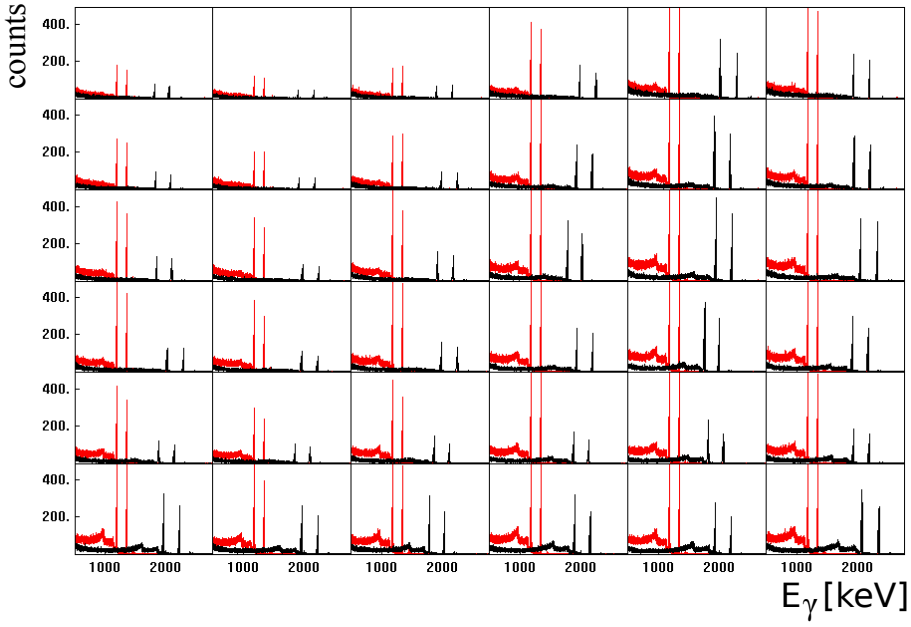

FIGURE 4.3: ^{60}Co spectra for 36 segments of crystal 00B before (black) and after (red) energy calibration.

Cross-talk correction

In an electrically segmented Ge detector the γ-ray energy can be completely absorbed in one segment or it can be distributed among multiple segments. In the latter case a deficit in the total deposited energy is often observed due to crosstalk effects. These are generated by capacitive coupling between the preamplifier FET signals of the segments and the core through the bulk of Ge material [Akkoyun et al., 2012], as well as by inductance of a large number of wires [Bruyneel et al., 2009a]. The effect of the cross-talk is shown in Fig. 4.4. Ideally, the energy deposited in the core should be equal to the energy of the sum of segments, however, as can be seen in Fig. 4.4a, the energy of the sum of the segments (blue plot) is shifted to lower values as compared to the core signal (black plot). A procedure has been developed to correct for this effect to recover the sum of hit energies for segment multiplicities up to 4 or 5, hence improving the energy resolution [Bruyneel et al., 2009a]. The cross-talk effect is linearly proportional to the segment multiplicity (number of firing segments) as illustrated in Fig. 4.4b [Bruyneel et al., 2009a; Bruyneel et al., 2009b]. There is a significant loss in energy of up to 10 keV (for multiplicity 5) before the cross-talk correction, which is improved to less than 0.5 keV after the corrections. An imprecise measurement of the cross-talk factor can lead to an overestimation of transient signals during PSA. Cross-talk matrices are generated with the *Xtalk* code by sorting the γ energies recorded for each segment with respect to the number of firing segments and comparing them with the nominal energies of ^{60}Co to calculate the energy shifts. The energy shifts in the segments are inversely proportional to the core decoupling capacitance as verified for MINIBALL detectors in Warr et al., 2003; Eberth et al., 2003. In the present case, it was necessary to apply the cross-talk procedure in the offline analysis. For instance, for detector 14A, the red (offline) and green curve (online) in Fig. 4.4a highlight the importance of offline analysis, which improved the statistics by 9.4% while keeping the same resolution.

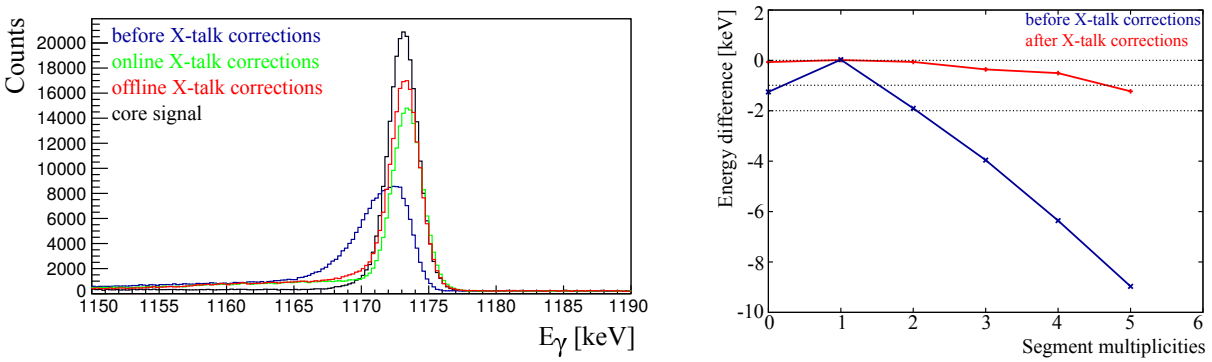

(A) cross-talk effects

(B) Energy loss before and after X-talk

FIGURE 4.4: Cross-talk effect resulting in a deficit in the sum of the energies of the segments. a) sum of segment energy (for segment multiplicities from 1 to 10) shown for the 1173.2 keV transition in ^{60}Co for detector 14A. Black histogram shows the core signal. b) Difference between the absolute energy and measured energy plotted against the segment multiplicity. M=1: total energy absorbed in 1 segment, M=2: total energy distributed between two segments and so on. M=0: sum of all multiplicities.

Faulty segments

Some of the AGATA crystals had faulty segments. These can be classified as follows:

- Broken segments: This is due to broken FETs. In this scenario the charge is not collected from the segment electrode and the corresponding charge appears in the energy spectra of neighboring segments as satellite peaks. This also affects the signal of the core by producing a left flank (step-like shape) on the core energy spectrum.
- Unstable segments: Unstable gain of a segment may either lead to multiple peaks or distorted peaks in segment energy spectra.
- Missing segments: This is due to a broken part of the electronics (preamplifier, or digitizer channel or ATCA channels). This can happen due to a poor connection, for example, between the digitizers and the preamplifiers. Here, the charge is collected by the FET, but not transmitted due to electronic issues.

When there is only one faulty segment in a detector, a correction to the cross-talk coefficients can be implemented using the features of the program *xTalkSort*. This program calculates the energy missing in the faulty segment by comparing it with the core energy using:

$$\sum E_{SEG} = E_{CORE} \tag{4.1}$$

where, $\sum E_{SEG}$ is the sum of energy for all segments and E_{CORE} is the energy deposited in the core. Table 4.1 summarizes the issues with the AGATA detectors in this experiment.

Faulty segments		Description
04A	All	Segments at low energy have double peaks therefore the detector is removed completely from the analysis
12A	-	This detector was removed from ≈ 85% of the data runs due to the core preamplifier being broken. The detector was a bit noisy from the beginning of the experiment showing counting rates of up to 180 kHz (compared to other detectors at ≈ 21 kHz).
12BC	-	These detectors were removed from ≈ 3% of the data runs due to high counting rates.
14B	-	Detector was removed from 13% of the data run due to the problem with digitizer power supplies. The digitizer were not working for longer than 2 hours even after connecting them to several different low voltage power supplies.
05C	8 & 9	These segments had double peaks in the low energy region, however the detector was still considered in the data flow by forcing the E_{SSeg} to E_{core} (*forceSegtoCore*[4]). It was observed that after *forceSegtoCore*, the double peaks had negligible influence on the final energy spectrum.
14A	16	This segment was missing from the detector and was restored by following the energy recovery procedure for faulty segments. The effect before and after the segment recovery is illustrated in Fig. 4.5.
11B	13	The segment was missing and was dealt with in the same way as 14A.

TABLE 4.1: Summary of faulty segments and detectors in the present experiment

[4]abbreviation used in the data sorting code *genconf*

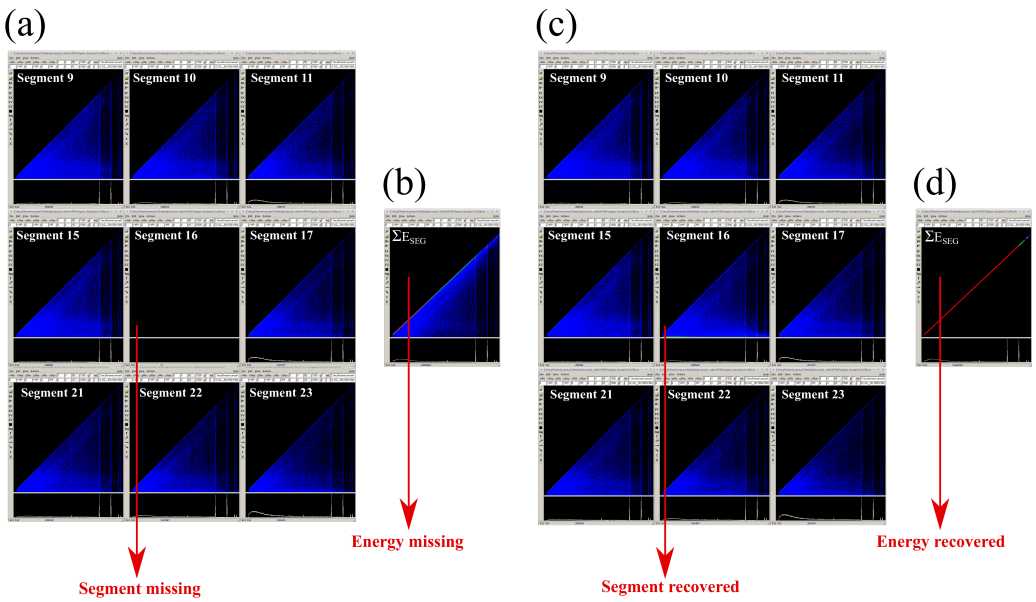

FIGURE 4.5: In (a) and (c), each distribution in the subplots is a correlation matrix of E_{SEG} vs the E_{CORE}. The behavior in (b) shows non correlation between energy of the sum of all segments ($\sum E_{SEG}$) and the energy of the core (E_{CORE}) due to the missing energy, whereas in (d) it can be seen that $\sum E_{SEG}$ vs E_{CORE} are nicely correlated shown by a diagonal line.

Neutron damage correction

The interaction of a high neutron flux with a Ge crystal can cause defects in the crystal lattice. This causes an appearance of a tail on the left side of the energy peak (see the blue plot in Fig. 4.6b) formed due to incomplete charge collection. Due to the large size of the AGATA crystals, the probability of the charge carrier being trapped is high. A prolonged exposure of the AGATA crystals to fast neutrons causes the segment energy signal to deteriorate faster since the holes are more likely to be trapped than the electrons collected on the central contact. The cores signals are only mildly affected because the electron trapping is less pronounced in n-type detectors. Ideally, neutron-damaged AGATA crystals should be annealed, however, this procedure is time consuming (especially during an experimental campaign) and often results in damaging the passivation layer between the segment electrodes causing a leakage current (noticed in $\sim 1/3^{rd}$ of the annealed AGATA crystals. The repair involves a costly task of opening the capsule and can only be performed by the manufacturer. Nonetheless, the γ-ray interaction position and energy loss corresponding to each hit can however be used to calculate the holes path and to correct approximately for the charge loss according to the path length. Information from the PSA plays a vital role in developing neutron damage algorithms for improving the performance of a neutron-damaged detector as shown by the corrected full energy peak (red) in Fig. 4.6b. Details on the correction for hole trapping in AGATA using PSA is explained in Bruyneel et al., 2013.

Global time alignment

The final time alignment is performed to re-align the time stamp of the core of each detector. The time stamp from the Global time alignment is required for the event building and event merging and a good time stamp alignment allows narrow time window in the builder and the merger. This procedure involves the construction of a 35 $\times$ 35 matrix by extracting the T_{zero} centroid of each

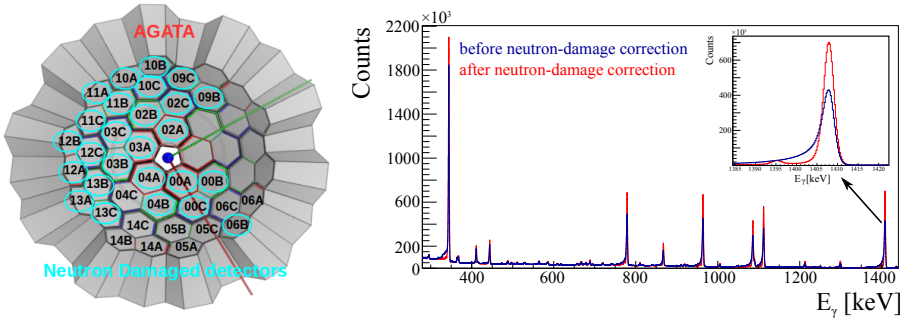

(A) (B)

FIGURE 4.6: Detector 00A corrected for neutron damage are highlighted in blue in (A). Performance recovery after neutron damage correction shown in (B) for detector 00A using ^{152}Eu source.

detector with respect to another detector, leading to 35 × 35 combinations and aligning them all at t= 500 ns (see Fig. 4.7).

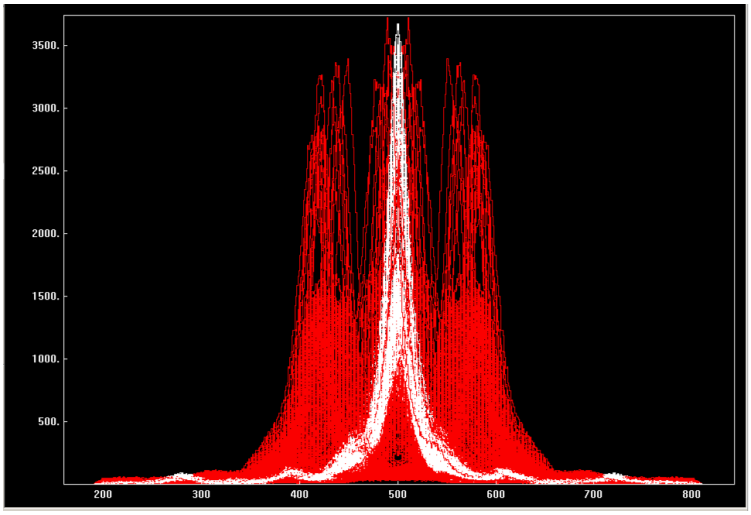

FIGURE 4.7: Time spectra before (red) and after (white) the global time alignment procedure for ^{60}Co source data.

Recalibration

Energy re-calibration is the final calibration stage. The algorithm used for neutron-damage correction can cause a shift in the energy calibration due to incorrect determination of the peak centroid caused by the distorted peak shape. The realignment of full-energy peaks requires the calibration coefficients both in terms of gain and offset over a wide energy range and therefore ^{152}Eu source is employed. Fig. 4.8 highlights the importance of re-calibration for detector 00A especially for segments 26 and 31 for which the observed energy shift was more than 1 keV. Similar shifts are observed for several segments of other detectors. Fig. 4.9 illustrates the energy difference between the true energy and the measured energy before and after re-calibration, which allowed to reduced the difference to less than 0.2 keV.

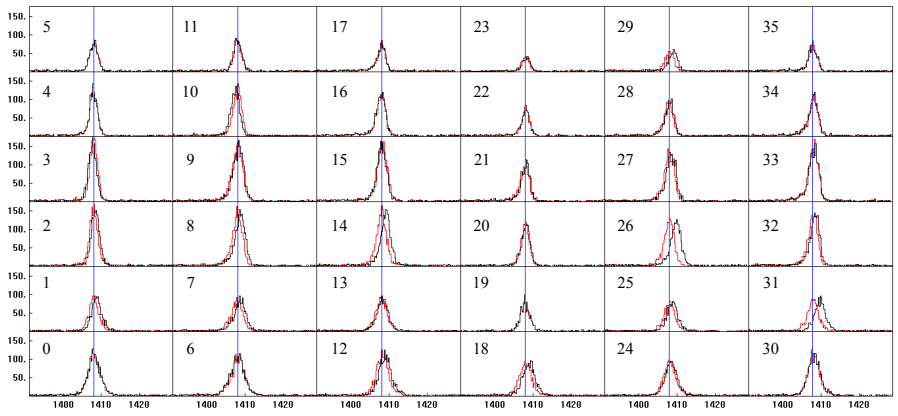

FIGURE 4.8: Before and after re-calibration procedure for 36 segments of detector 00A showing 1408 keV peak in ^{152}Eu

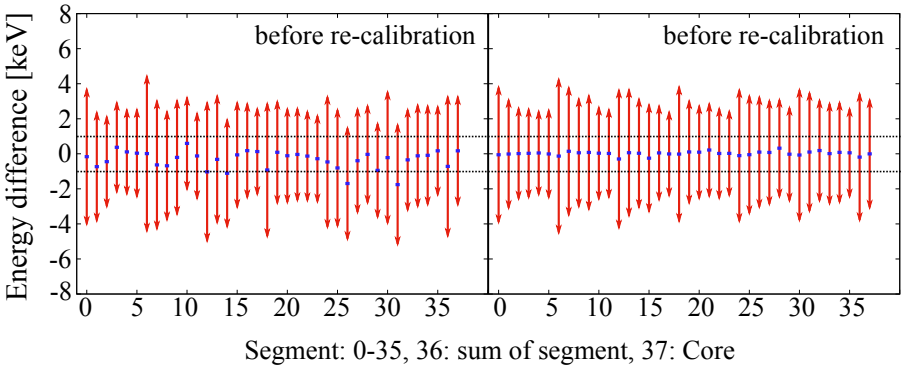

FIGURE 4.9: Energy difference = $E_{\gamma_{true}}$ - $E_{\gamma_{measured}}$ at 1408 keV (^{152}Eu) for crystal 00A. Red bars represent the energy resolution (FWHM) and blue points represent the centroid of the peak.

Relative Efficiency

The efficiency calibration was performed using a ^{152}Eu source. The obtained efficiency curve (Fig. 4.10) is used to correct the measured γ-ray intensities for different energies. The function used to fit the efficiency curve (Eq. 4.2) was adapted from "Radware".

$$Y = Exp\left(\left[A + B\cdot\frac{Log(E_\gamma)}{100}\right]^{-C} + \left[D + E\cdot\frac{Log(E_\gamma)}{1000} + F\cdot\left[\frac{Log(E_\gamma)}{1000}\right]^2\right]^{-C}\right)^{\frac{-1}{C}} \tag{4.2}$$

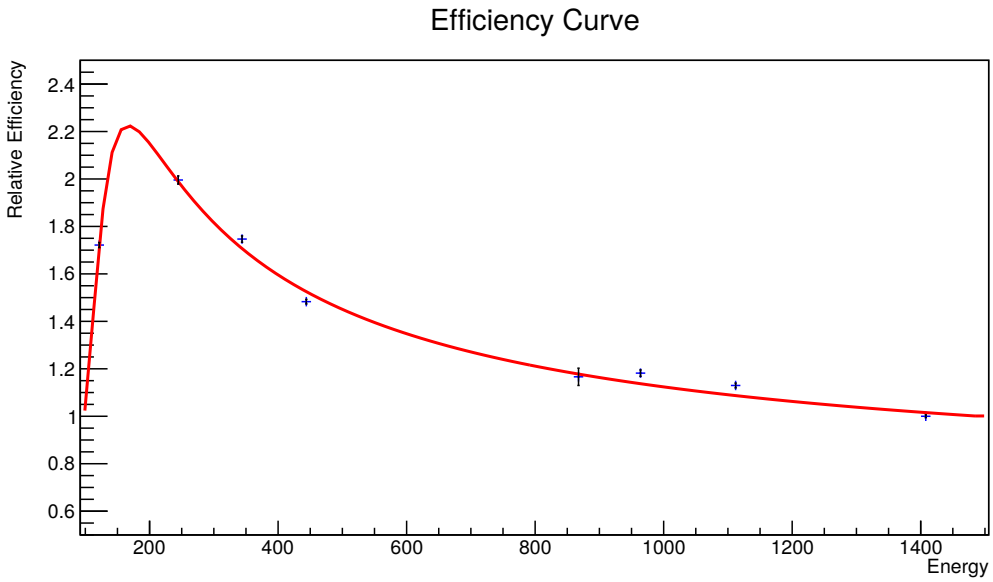

FIGURE 4.10: Efficiency curve normalized to 1 for 1408 keV.

Chapter 5

Lifetime measurement

This chapter details the lifetime measurement of short-lived states using the Recoil Distance Doppler Shift Method (RDDS) with a plunger mechanism. A plunger is a mechanical device used for lifetime measurements of short-lived states in the 10^{-12} –10^{-9} s range. The two main procedures of the RDDS data analysis are discussed here: the Decay Curve Method (DCM) and the Differential Decay Curve Method (DDCM). The $\gamma - \gamma$ coincidence method using both the DCM and DDCM procedures is also reviewed. Finally the practical implementation of the aforementioned procedures is illustrated using the case of ^{104}Mo.

5.1 Lifetime measurements in the picosecond range

The lifetimes of the excited states in a nucleus can be as short as a few femtoseconds, therefore, the lifetimes of most excited nuclear states cannot be measured directly. Even the fast-timing technique [Régis et al., 2013] is limited to lifetimes larger than few tens of ps. It is possible to circumvent this problem by measuring instead the position of a recoiling nucleus at the time of decay and then calculating the decay time knowing its velocity. However, measuring precisely the position of emission of a γ ray is also challenging. It can be inferred from the Doppler shift of the γ-ray transition energy due to the movement of the recoiling nuclei. All methods exploiting this idea are commonly referred to as Doppler-shift techniques. Using thick targets, the recoils slow down continuously with a velocity depending on the target material. The velocity at the decay time can be used to estimate the decay position. This is at the basis of the Doppler Shift Attenuation Method (DSAM), which can be used for very short lifetimes ($\leq$1ps), but requires the knowledge of the stopping powers as a function of the energy/velocity of the recoil nucleus in the target. For longer lifetimes in the picosecond range it was then proposed to use a sandwich of a thin target followed by a layer of a light material, and then by a heavy backing material [Devons, Manning, and Bunbury, 1955], making the measurement independent from the range in the backing material. At this time the poor energy resolution of the NaI detectors used for γ-ray detection allowed only to measure the shift of the mean of the energy distribution. Significant improvement of the method was introduced by Alexander and Allen, 1965 using:

- higher energy of the recoiling nuclei
- high-resolution germanium detectors
- a plunger device improving the "sandwich" concept by replacing the light material by vacuum and by making the distance between target and backing material tunable.

The energy resolution of Ge detectors, being highly superior to that of NaI detectors, makes it possible to observe two separate peaks in the energy spectrum: a shifted component corresponding to γ rays emitted in flight and an unshifted one for γ rays emitted from a nucleus at rest in the backing. The lifetime is then determined from the evolution of the intensity ratio of shifted and un-shifted components as a function of the distance between the target and the backing using

methods described in section 5.4.1. The first plunger devices consisted of a target frame and a stopper with either a solid target material or even a gas target [Bizzeti et al., 1967]. The target frame can be moved along the beam axis, hence the name "plunger".

5.2 Differential Plunger device

The idea of a differential plunger with a movable degrader between the fixed target and stopper was proposed by Ward et al., 1979 and implemented by Dewald, Harissopulos, and Brentano, 1989 where it was used to enable the DDCM analysis (described in section 5.4.2). The present experiment required the identification of the recoiling nucleus in VAMOS and therefore a standard two-foil type differential plunger without a stopper foil was used.

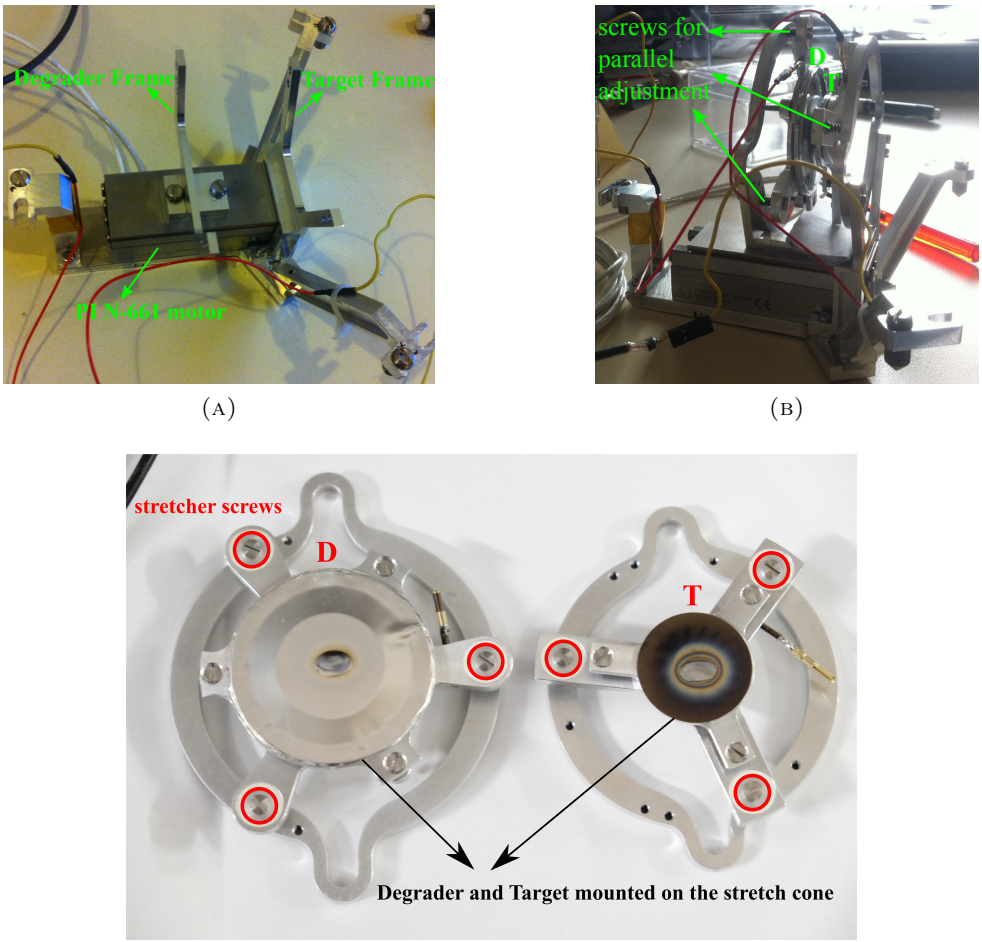

(A) (B)

(C)

FIGURE 5.1: Components of the plunger device. (A) Degrader and target frames with the plunger motor. (B) Target and the degrader mounted on their frames. The position of their screws used for parallel alignment is shown. (C) The degrader and target foils photo is taken after the experiment and the blackening of the target foil is due to carbon deposition.[1]

[1] Image courtesy of Victor Modamio

We have used the Orsay Universal Plunger System (OUPS) developed by Ljungvall et al., 2012 to perform the Recoil Distance Doppler Shift measurements (see section 5.3). The OUPS plunger has three important features:

- Target and degrader frames, which use a stretching mechanism where the target and degrader foils are attached to metallic cones (see Fig. 5.1b and 5.1c) that are machined with sub-micrometer precision to allow the positioning of the degrader at a distance from the target that ranges from tens of millimeter down to $\sim$ tens of micrometer[2],
- a piezo-electric linear motor (PI N-661) used to move the degrader frame, mounted on an aluminum support plate, which is also holding the target frame (see Fig. 5.1a),
- an electronic feedback mechanism to account for the variations of the distance between the target and degrader foils due to the beam heating the foils. Feedback is performed by correlating the distance between the foils with the capacitance measured between them. More details on the OUPS plunger can be found in Ljungvall et al., 2012.

5.3 Recoil Distance Doppler Shift Method

The principle of the Recoil Distance Doppler Shift method (RDDS) is illustrated in Fig. 5.2. If a nucleus is recoiling out of the target, it can decay in flight. The advantage of the plunger device is that the distance between the target and the degrader can be varied in order to change the number of nuclei decaying either before or after the degrader (Fig. 5.2b). In either case the energy of the γ rays emitted in flight will be Doppler shifted as follows:

$$E_\gamma = E_{\gamma_o} \frac{\sqrt{1-\beta^2}}{1-\beta cos\theta} \tag{5.1}$$

where E_γ and E_{γ_o} are the measured and the absolute energy of the γ-ray transition, respectively, $\beta = \frac{v}{c}$ is the recoil velocity and θ is the angle between the direction of the recoil and the γ-ray. Relativistic effects start to play a role when the velocity of the recoiling nucleus is equal or higher than 3%-4% of the speed of light [Dewald, Möller, and Petkov, 2012] (It was approximately 10% of the speed of light in the present experiment). The magnitude of the Doppler shift is correlated with θ as illustrated in Fig. 5.3. Therefore the Doppler correction relies on accurate determination of θ. This highlights the importance of PSA, which determines the accuracy of the position, and the γ-ray tracking in AGATA, which determines the first interaction position.

The velocity of a recoil decaying after the degrader is measured at the focal plane of VAMOS (as discussed in section 3.1). This velocity is used to correct for the Doppler effect (Eq. 5.1) on an event-by-event basis. Therefore, the energy of the γ rays emitted by the recoiling nucleus can be determined accurately when the decay occurs after the degrader.

[2]The minimum distance is limited by the surface quality of the foils

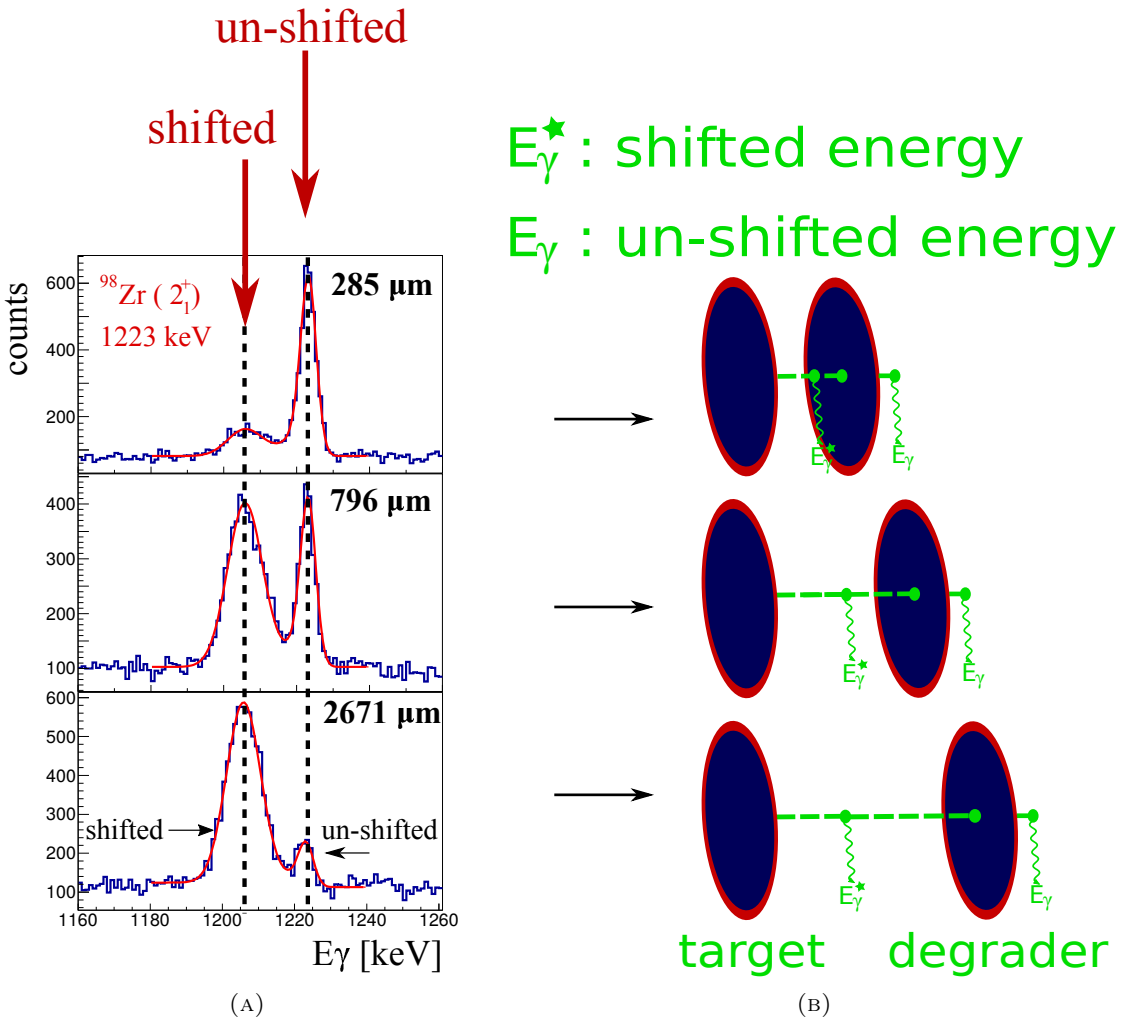

(A) (B)

FIGURE 5.2: Principle of the RDDS technique. The energy spectra (A) show the evolution of intensities of the shifted and unshifted peaks (terminology explained in text) as a function of the plunger distance (B).

After Doppler correction, γ rays emitted after the degrader are located in the energy spectrum at the original/absolute energy of the γ-ray transition, E_{γ_o} (unshifted position). However, when the nucleus decays before the degrader, the energy is shifted from the original value due to the energy loss in the degrader, as represented by the left peak in Fig. 5.2a (shifted position). From here onwards E_S and E_U will be referred to as shifted and unshifted energies, respectively. The velocities of the nuclei decaying before and after the degrader is related to the velocity loss inside the degrader by:

$$v_{in} = v_{out} + \delta v \tag{5.2}$$

where v_{in} is the velocity before the degrader, v_{out} is the velocity after the degrader and δv is the velocity loss inside the degrader which can in principle be determined from the thickness of the degrader. Before Doppler correction, there is a strong dependence of the measured γ-ray energies on θ (Fig. 5.3a), whereas after Doppler correction there is still a slight dependence of the shifted peak position on θ (Fig. 5.3b), which is responsible for the observed broadening of the shifted peak in Fig. 5.2a. This slight dependence is due to v_{out} being used to correct the Doppler shift on γ rays emitted before the degrader.

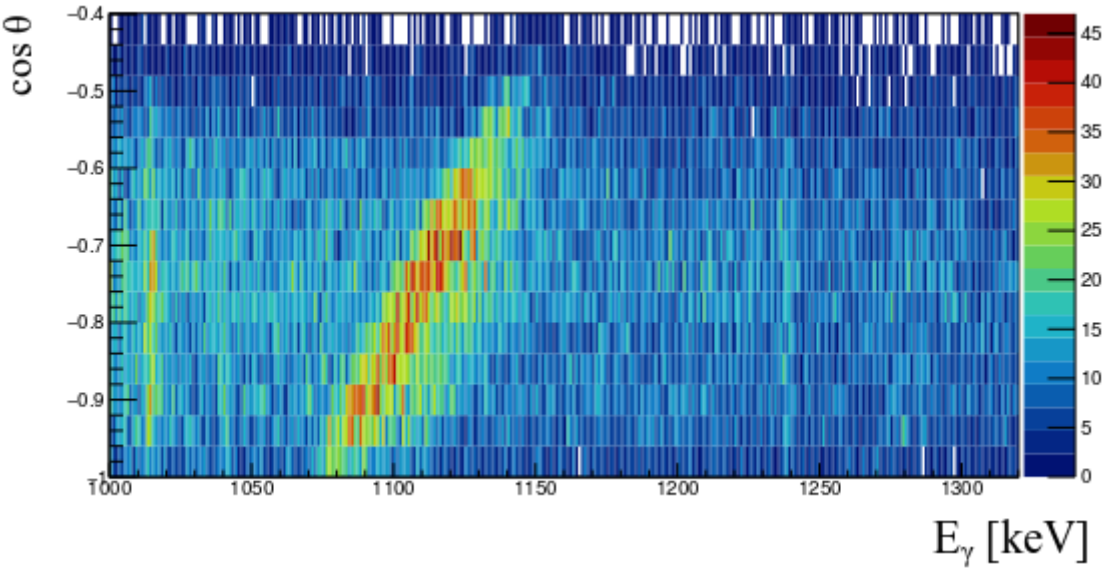

(A)

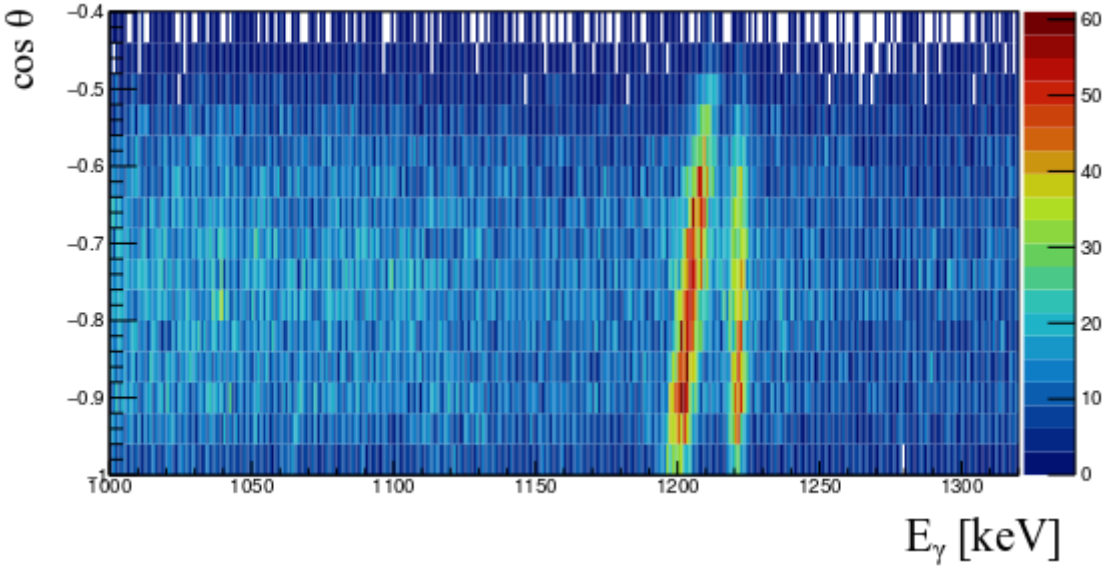

(B)

FIGURE 5.3: (A) Correlation of the γ-ray energy E_γ with the emission angle θ (A) before and (B) after Doppler correction using data from the plunger distance of 780 μm.

5.3.1 Implementation of the RDDS technique

In the RDDS analysis the evolution of Q_i, given by Eq. 5.3, is studied as a function of the plunger distance.

$$Q_i(x) = \frac{I_U(x)}{I_U(x) + I_S(x)} \tag{5.3}$$

where I_S and I_U are the intensities of the shifted and unshifted peak, respectively and x is the distance between the target and the degrader foils. Q_i, being the proportion of γ rays emitted after the degrader to the total number of γ rays, is expected to decrease as a function of x. The corresponding decay curve can be fitted using Bateman equations [Bateman, 1843] or with an appropriate user-defined function. In order to obtain $Q_i(x)$ the shifted and un-shifted peaks need to be well separated. Their separation depends on the energy resolution of the γ-ray detectors as well as on their position resolution, which influences the precise determination of the emission angle. The separation also depends on the velocity spread due to the energy loss in the target and the degrader. In the present experiment, the cross-talk correction and neutron-damage correction discussed in chapter 4 were crucial to achieve good energy resolution and thus to separate the two peaks.

5.3.2 Velocity distribution of the fission fragments

The fission fragments detected in the VAMOS spectrometer have a velocity distribution centered around the mean velocity $< v >$ which depends on the beam energy, the reaction mechanism and the target and degrader thicknesses. Beam energy and target thickness are the same for all reaction products, but the fission kinematics leads to a broad velocity distribution of the fission fragments. Due to the angular and momentum acceptance of VAMOS a certain fraction of this distribution is selected, which is different for each fragment. The velocity measured by VAMOS is v_{out} (Eq. 5.2), however the RDDS measurement requires the initial recoil velocity (v_{in}) (velocity of the nuclei before they enter the degrader) for a precise lifetime determination. The transmission of nuclei through the VAMOS spectrometer depends on the momentum acceptance of VAMOS in terms of magnetic rigidity Bρ (discussed in section 3.1). It is possible to estimate v_{in} by simulating the energy loss in the degrader, however it requires the knowledge of the reaction kinematics, energy losses in target and degrader and the acceptance of the spectrometer. Therefore in the present experiment we have used different Doppler shifts for the emission before and after the degrader to estimate the change in velocity due to slowing down in the degrader, i.e. to calculate v_{in} from the energies of the shifted and unshifted components (E_S and E_U, respectively). Eq. 5.1 can be extended to obtain a relation between δv and $\frac{E_S}{E_U}$ in order to calculate the v_{in} distribution. The ratio $\frac{E_S}{E_U}$ was calculated for all the strong transitions in Zr, Mo and Ru isotopes. When plotting these ratios as a function of v_{out} (Fig. 5.4), no correlation is observed between them and v_{out}. Therefore, the weighted mean of $\langle \frac{E_S}{E_U} \rangle = 0.986(1)$ for the ratio was chosen to correct the velocity of all nuclei.

The energies E_{γ_1} and E_{γ_2} of γ rays emitted after and before the degrader, respectively, are given as:

$$E_{\gamma_1} = E_{\gamma_o} \frac{\sqrt{1-\beta_{out}^2}}{1-\beta_{out} cos\theta}$$

$$E_{\gamma_2} = E_{\gamma_o} \frac{\sqrt{1-\beta_{in}^2}}{1-\beta_{in} cos\theta}$$

The Doppler correction for the unshifted peak can be obtained as:

$$E_{\gamma_o} = E_U = E_{\gamma_1} \cdot \frac{1 - \beta_{out} cos\theta}{\sqrt{1 - \beta_{out}^2}}$$

While the same Doppler correction applied to the shifted peak results in:

$$\begin{aligned} E_S &= E_{\gamma_2} \cdot \frac{1 - \beta_{out} cos\theta}{\sqrt{1 - \beta_{out}^2}} \\ &= E_{\gamma_o} \cdot \sqrt{\frac{1 - \beta_{in}^2}{1 - \beta_{out}^2}} \cdot \frac{1 - \beta_{out} cos\theta}{1 - \beta_{in} cos\theta} \\ &= E_{\gamma_o} \cdot \sqrt{\frac{1 - \beta_{out}^2 - 2\beta_{out}\delta\beta - \delta\beta^2}{1 - \beta_{out}^2}} \cdot \frac{1 - \beta_{out} cos\theta}{1 - (\beta_{out} + \delta\beta) cos\theta} \\ &= E_{\gamma_o} \cdot \sqrt{1 - \frac{\delta\beta}{1 - \beta_{out}^2}(2\beta_{out} + \delta\beta)} \cdot \frac{1}{1 - \frac{\delta\beta cos\theta}{1 - \beta_{out} cos\theta}} \quad \Big\{ \text{where } \beta_{in} = \beta_{out} + \delta\beta \end{aligned}$$

which can be approximated by Taylor expansion as:

$$E_S \approx E_{\gamma_o} \left(1 - \frac{\beta_{out}\delta\beta}{1 - \beta_{out}^2}\right) \cdot \left(1 + \frac{\delta\beta cos\theta}{1 - \beta_{out} cos\theta}\right)$$

therefore,

$$\frac{E_S}{E_U} \approx 1 - \frac{\beta_{out}\delta\beta}{1 - \beta_{out}^2} + \frac{\delta\beta cos\theta}{1 - \beta_{out} cos\theta}$$

Finally, $\delta\beta$, which was used to determine v_{in}, can be expressed in terms of $\frac{E_S}{E_U}$ as:

$$\delta\beta \approx \left(\langle \frac{E_S}{E_U} \rangle - 1\right) \frac{(1 - \beta_{out} cos\theta)(1 - \beta_{out}^2)}{cos\theta - \beta_{out}} \tag{5.4}$$

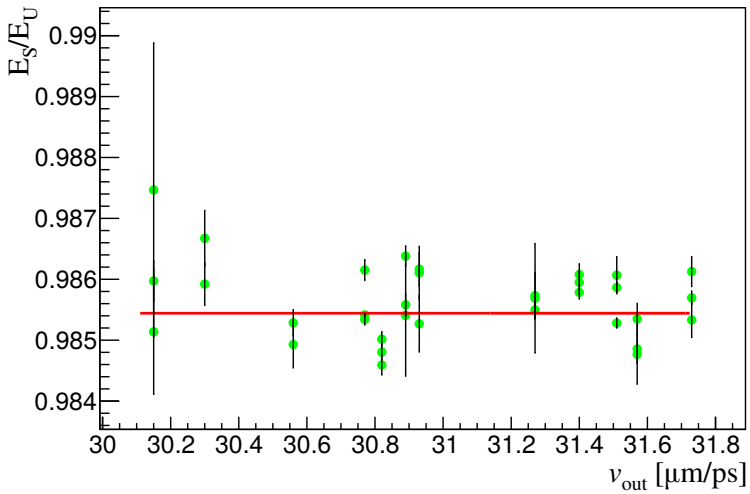

FIGURE 5.4: Values of $\frac{E_S}{E_U}$ for individual states as a function of v_{out}. No correlation of $\frac{E_S}{E_U}$ with v_{out} is observed.

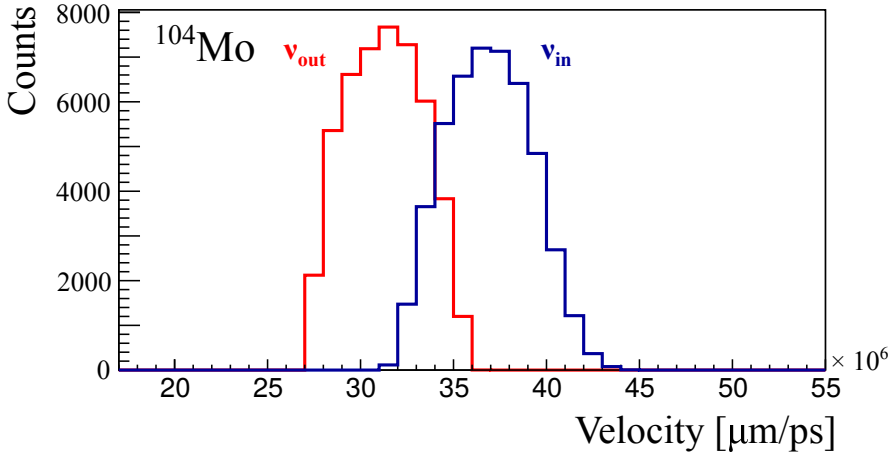

FIGURE 5.5: Comparison of velocity distribution for ^{104}Mo nuclei decaying before (v_{in}) and after the degrader (v_{out})

It was observed that the difference between v_{in} and v_{out} for all isotopes was $\approx 15\%$ as illustrated in Fig. 5.5 for ^{104}Mo. The velocities for each isotope before and after the degrader are given in Table 5.1.

Isotopes	v_{out}	v_{in}
^{98}Zr	31.8(20)	37.4(23)
^{100}Zr	31.4(21)	37.0(23)
^{102}Zr	30.8(22)	36.3(24)
^{104}Zr	29.6(23)	35.2(25)
^{100}Mo	31.7(19)	37.3(22)
^{102}Mo	31.6(19)	37.2(22)
^{104}Mo	31.2(20)	36.9(22)
^{106}Mo	30.8(20)	36.4(23)
^{108}Mo	30.0(21)	35.6(23)
^{106}Ru	30.9(18)	36.6(20)
^{108}Ru	30.8(19)	36.4(21)
^{110}Ru	30.5(19)	36.1(22)
^{112}Ru	29.9(20)	35.5(22)

TABLE 5.1: Comparison between the velocities before (v_{in}) and after the degrader (v_{out}) for even-even nuclei considered in the present analysis. The values in the brackets correspond to the standard deviation of the velocity distribution.

5.3.3 Thickness of target and degrader foils

The thickness of the degrader and target foils is chosen to accommodate the following requirements:

- The Be target should be thick enough to sufficiently slow down the beam in order to avoid the reaction between the beam (^{238}U) and the degrader (^{24}Mg). The purpose is to minimize the fusion-fission cross section of ^{238}U on ^{24}Mg.

- The degrader thickness should allow sufficient slowing down to have enough difference between v_{in} and v_{out} for the two peaks (shifted and unshifted) to be well distinguished. However, increasing the degrader thickness also leads to a larger Doppler broadening.
- The degrader thickness influences the mass resolution in VAMOS. A large degrader thickness will result in large velocity spread and impact the time-of-flight of the fission fragments in VAMOS, resulting in worsening of the mass resolution.

The target and degrader thicknesses were chosen to be 1.85 mg/cm^2 and 4.5 mg/cm^2, respectively as an optimal compromise.

5.3.4 Choice of target-degrader distances

The present experiment aimed to measure lifetimes of yrast states ranging from a few ps to 100 ps in a wide range of fission fragments. In most fission fragments the transition energies were ranging from 300 keV to 800 keV, with the exception of the 1223 keV transition from the 2_1^+ state of ^{98}Zr. Measurements were performed for 10 different plunger distances that were chosen according to the expected recoil velocities and level lifetimes. The plunger distances where only one component (shifted or unshifted) is observed cannot be used for a lifetime determination because $Q_i(x)$ saturates to 0 (1) when only shifted (unshifted) component is observed (see Eq. 5.3). Since the decays follow an exponential law, the plunger distances were chosen equidistantly on a logarithmic distance scale. The highest precision is obtained when both peaks show a similar intensity.

Table[3] 5.2 shows the plunger distances, run numbers and the hours of beam time for each distance. The fluctuations observed at the distance of 776 μm are due to turning off and on of the plunger feedback.

Distance [μm]	RMS spread [μm]	RMS spread [%]	Start run	Stop run	Run time (min)
29.8	0.5	1.67	113	126	992
51.6	0.3	0.58	128	144	1308
89.9	0.6	0.66	145	156	976
155	2	1.29	188	197	1067
264	5	1.89	157	170	1027
449	4	0.89	175	178	849
776	40	5.15	171	174	1195
1170	5	0.42	179	179	955
1776	5	0.28	180	183	1042
2651	5	0.18	184	187	772

TABLE 5.2: Summary of all plunger measurement distances with the statistical error and the corresponding run.

5.3.5 Determination of zero offset

The zero offset point is the point of electrical contact between the target and the degrader, ideally when the target foil is perfectly aligned parallel to the degrader foil. However, in reality the target and the degrader materials are not fully stretched or the two foils are not parallel to each other, which can lead to an uneven electrical contact between them (see Fig. 5.6). This unevenness gives an offset in the degrader position, which means that the electrical contact of the target and the degrader does not correspond to zero distance between the two foils.

[3]Table provided by Joa Ljungvall during the experiment

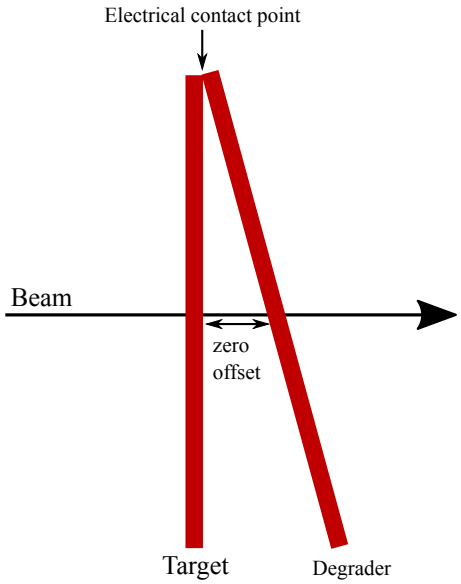

FIGURE 5.6: Schematic illustration of the source of zero offset in the case of two foils being not parallel to each other.

The plunger distance is changed during the experiment relatively to the position of the degrader. However, for the lifetime analysis it is necessary to know the absolute distance. Therefore, the zero offset of the degrader is measured and the remaining distances are corrected using this value. The zero offset determination is crucial for the DCM analysis because the fitted decay curves are sensitive to the absolute target-degrader distance. The correction of distances for the zero offset has a negligible influence in the DDCM analysis, since DDCM relies only on the relative plunger position.

The tuning of the target-degrader distance is performed using the capacitance method, where the capacitance between the target and degrader is inversely proportional to the distance between them. This capacitance (C) is related to the output voltage (induced charge: ($Q(x)$)) through:

$$Q(x) = CV_i \sim \frac{A}{x} \tag{5.5}$$

where V_i is the input voltage applied to the capacitor and A is the area of the target foil [Alexander and Bell, 1970]. A first calibration was performed to determine the relation between the measured voltage and the plunger distance. A second calibration was performed at the end of the experiment to check the stability of the plunger system during the experiment. It was observed that the calibration taken after the experiment was different from the one obtained before the experiment for distances below 85 μm. This difference is probably related to the carbon build up on the target (see Fig. 5.1c), but proved to be insignificant since the shortest target-degrader distances were all measured in the beginning of the experiment. In addition, we could well reproduce several known lifetimes of some short and long-lived states (discussed in section 5.5).

Therefore, the zero offset was determined using the calibration data taken before the experiment since it was more suitable for smaller distances (see the calibration curve in Fig 5.7). As shown in Fig. 5.8, $1/Q(x)$ behaves linearly with respect to x for small distances (< 10 μm). Extrapolating this curve to $1/Q(x) = 0$ (at the target-degrader contact point) gives the contact distance of the plunger to be $|20.3(5)|$ μm, where the error is from the linear fit. The error on each plunger distance is then determined by linearly adding the systematic error on zero offset and the

statistical error due to the spread of capacitive measurements throughout the experiment. Table 5.2 summarizes the statistical errors for each distance and the corresponding run numbers.

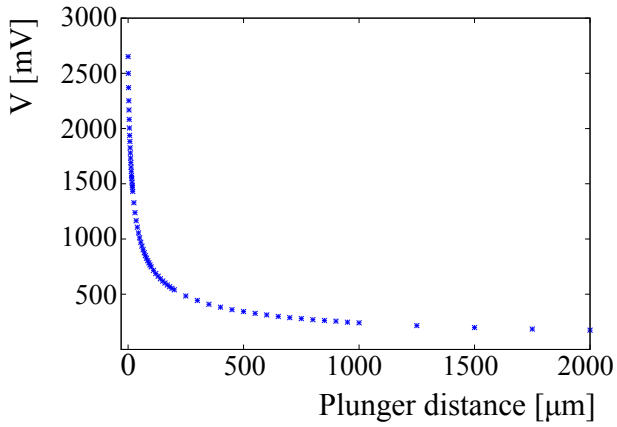

FIGURE 5.7: Correlation of the voltage signal induced on the plunger foils as a function of the plunger distance.

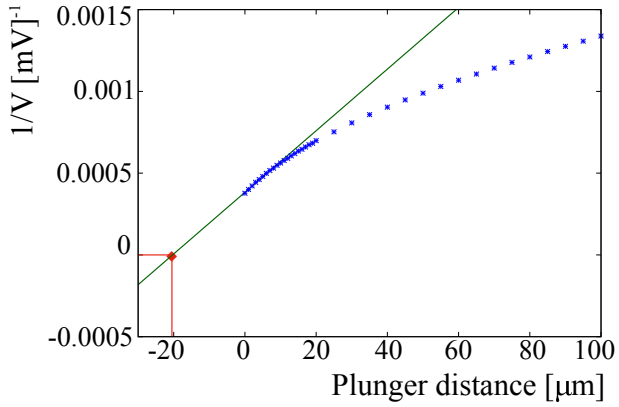

FIGURE 5.8: Inverse of the induced charge (recorded as voltage) with respect to the plunger position. Determination of the zero offset, i.e. the contact distance of the target and degrader foil is shown where first few points are fitted by a linear curve to extrapolate the inverse of the induced charge on the plunger distance.

5.4 Methods of lifetime determination

This section discusses the analysis procedures used to extract the nuclear lifetimes from the RDDS data.

5.4.1 Decay Curve Method

The Decay Curve Method (DCM) can be used to determine the lifetimes knowing the absolute target-degrader distance. This method is used for two purposes in the present work: firstly, to determine the effective lifetime in weak channels where feeding γ-ray transitions are not observed and secondly, to determine precise lifetimes in combination with the $\gamma - \gamma$ coincidence technique (see section 5.4.3). In the case of a single excited level (i) (in Fig. 5.11), the non-normalized decay curve defined in Eq. 5.3 reads:

$$Q_i = N_o e^{(-\frac{t}{\tau})} = N_o e^{(-\frac{x}{v_{in}\tau})} \tag{5.6}$$

where N_o is the initial population, x is the target-degrader distance, v_{in} is the velocity of nuclei decaying before the degrader (discussed in section 5.3.2). When multiple feeding levels are involved (j_k, k $\in \mathbb{N}$ in Fig. 5.11), the lifetime is extracted by solving a corresponding system of differential equations called Bateman equations [Dewald, Möller, and Petkov, 2012]. Solving Bateman equations leads to a more general expression for Q_i that can then be fitted to extract the lifetime. However, in the present work we favored the DDCM method (see section 5.4.2) for cases where the level of interest was fed by higher-lying states (j_k).

5.4.2 Differential Decay Curve Method

The Differential Decay Curve method (DDCM) is an extension of the DCM [Dewald, Harissopulos, and Brentano, 1989; Böhm et al., 1993] which depends on the relative distance between the two plunger positions. DDCM allows the determination of a lifetime value for each plunger distance. The systematic errors related to this method are smaller since it requires no assumptions on the feeding transitions provided that all these transitions are experimentally observed.

In the present experiment a degrader foil was used instead of the stopper to allow the particle identification in VAMOS. The precise velocity determination in VAMOS also reduces the uncertainties as compared to the conventional one with a stopper [Dewald, Harissopulos, and Brentano, 1989]. Using a plunger is essential for the DDCM analysis since it allows the measurement of the decay curve as well as its first derivative.

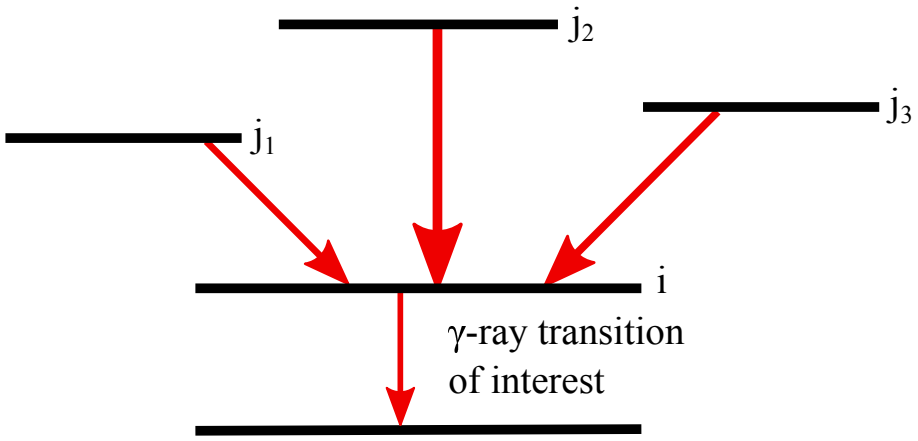

FIGURE 5.9: Level scheme showing multiple levels ($j_{1,2,3}$) feeding the state of interest 'i'

In DDCM, the lifetimes can be mathematically derived in the following way. When multiple levels j feed the state of interest i (see in Fig. 5.11) with n_j and n_i being the number of nuclei in the states j and i, respectively, and b_j being the branching ratio, the differential equation for the level i is given as:

$$\frac{d}{dt}n_i = -\frac{n_i}{\tau_i}(t) + \sum_j \frac{n_j}{\tau_j}(t) \cdot b_j \tag{5.7}$$

where the first term describes the decay from level i with lifetime τ_i and the second term describes the feeding from levels j with lifetimes τ_j. If t_D is the time at which the nucleus crosses the degrader ($t_D = \frac{x}{v_{in}}$, x: target-degrader distance, v_{in}: velocity before the degrader) then the

intensities of the shifted and unshifted transitions deexciting level i are given as:

$$\begin{aligned} I_i^S(x) &= \int_0^{t_D} \frac{n_i(t)}{\tau_i} dt \\ I_i^U(x) &= \int_{t_D}^{+\infty} \frac{n_i(t)}{\tau_i} dt \end{aligned} \tag{5.8}$$

Integral of Eq. 5.7 between t_D and $+\infty$ reads:

$$n_i(\infty) - n_i(t_D) = -I_i^U(x) + \sum_j b_j \cdot I_j^U(x) \tag{5.9}$$

where $n_i(\infty)$=0 and using Eq. 5.3, the derivative of $Q_i(x)$ is given as:

$$\frac{dQ_i(x)}{dx} = \frac{\frac{dI_i^U(x)}{dx}}{I_i^U(x) + I_i^S(x)}$$

where the sum of $I_i^U(x) + I_i^S(x)$ is constant with respect to x and:

$$\begin{aligned} \frac{dI_i^U(x)}{dx} &= \frac{1}{v}\frac{dI_i^U(t_D)}{dt_D} = -\frac{n_i(t_D)}{v\tau_i} \quad \text{(using Eq. 5.8)} \\ \frac{dQ_i(x)}{dx} &= \frac{1}{v\tau_i}\frac{-I_i^U(x) + \sum_j I_j^U(x)}{I_i^U(x) + I_i^S(x)} \quad \text{(using Eq. 5.9)} \\ &= \frac{1}{v\tau_i(x)}\big(- Q_i + \sum \alpha_j b_j \cdot Q_j\big) \quad \Big\{\alpha_j : \ \frac{I_j^U(x)+I_j^S(x)}{I_i^U(x)+I_i^S(x)} \end{aligned}$$

Finally, the lifetime for 'n' distances in the DDCM analysis is calculated using Eq. 5.10

$$\tau_i(x) = -\Big[v\frac{dQ_i(x)}{dx}\Big]^{-1}[Q_i(x) - \sum_j \alpha_j b_j Q_j(x)] \tag{5.10}$$

where:

- ➔ $\frac{dQ_i}{dx}$: First derivative of $Q_i(x)$ determined from the decay curve.
- ➔ v is the mean of the velocity distribution, for nuclei decaying before the degrader (unique for each isotope, presented in table 5.1).
- ➔ b_j: branching ratio from the feeding state towards the state of interest calculated using the transition intensities taken, e.g., from NNDC.
- ➔ α_j: determines the amount of the feeding contribution in the decay curve and is given as:

$$\alpha_j = \frac{I_j}{I_i} \cdot \frac{\epsilon_i}{\epsilon_j} \tag{5.11}$$

  where I_j, I_i are the total measured intensities of feeding and decay transitions, respectively and ϵ_i, ϵ_j are the corresponding γ-ray efficiencies for the decay and feeding transitions, respectively, determined using the efficiency curve 4.10. If α_j is smaller than 100%, the general hypothesis is to assume that the remaining contribution is prompt and does not influence the lifetime.

- ➔ $Q_j(x)$ is the relative intensity of the feeding transition.

The first step in the DDCM analysis is to fit the decay curve using the data points given by Eq. 5.3. The functions used for fitting can be either (1) exponential function with an offset (*expo*), (2) a continuously differentiable piecewise function of second degree polynomials (*piecewise1*) or (3) a continuously differentiable piecewise function of second degree polynomial used to fit the beginning/end of the curve and exponential with offset used to fit the end/beginning of the curve (*piecewise2/piecewise3*). The derivative $\frac{dQ_i}{dx}$ and its error, $\delta\frac{dQ_i}{dx}$, are then calculated directly from the fitting functions (assuming the fit parameters are uncorrelated) before extracting the lifetimes using Eq. 5.10.

Error estimation for lifetimes

The errors on nuclear lifetimes obtained using the DDCM analysis are determined using the standard error propagation formula and are given as:

$$\delta\tau_i = \sqrt{\left(\frac{Q_j}{v\cdot\frac{dQ_i}{dx}}\delta\alpha_j\right)^2 + \left(\frac{\alpha_j}{v\cdot\frac{dQ_i}{dx}}\delta Q_j\right)^2 + \left(\frac{1}{v\cdot\frac{dQ_i}{dx}}\delta Q_i\right)^2 + \left(\frac{\tau_i}{v}\delta v\right)^2 + \left(\frac{\tau_i}{\frac{dQ_i}{dx}}\cdot\delta\frac{dQ_i}{dx}\right)^2} \tag{5.12}$$

where the errors on individual terms are extracted by standard error propagation as exemplified for $\delta\alpha_j$:

$$\delta\alpha_j = \sqrt{\left(\frac{\epsilon_j}{I_i\epsilon_i}\cdot\delta I_j\right)^2 + \left(\frac{I_j}{I_i\epsilon_j}\cdot\delta\epsilon_j\right)^2 + \left(\frac{I_j\epsilon_j}{I_i^2\epsilon_i}\cdot\delta I_i\right)^2 + \left(\frac{I_j\epsilon_j}{I_i\epsilon_i^2}\cdot\delta\epsilon_i\right)^2} \tag{5.13}$$

The first two terms in Eq. 5.12 were summed over all the feeding states 'j'. The uncertainty from the branching ratio was calculated using the standard error propagation. The standard deviation of the velocity distribution in table 5.1 was considered as the uncertainly on the velocity term.

5.4.3 Lifetime measurement using γ-γ coincidences

The advantage of a plunger measurement using the $\gamma-\gamma$ coincidence technique over a singles measurement is that the dependency on the level feeding is removed [Ward et al., 1973]. The uncertainties related to the determination of lifetimes of feeding states and feeding intensities can cause large inaccuracy in the lifetime measurements. The systematic errors are especially large in the case of multiple feeding. The situation becomes worse when dealing with an unobserved side feeding, in which case only a hypothesis can be used on the lifetime of the feeding states. The $\gamma-\gamma$ coincidence technique is illustrated in Fig. 5.10. When considering a coincidence between the feeding and the decay transitions, there are four possible gating scenarios: a) gating on the shifted component of the decay to access the shifted component of the feeding transition, b) gating on the unshifted component of the decay transition to access the shifted and unshifted component of the feeding transition, c) gating on the shifted component of the feeding transition to access the shifted and unshifted component of the decay transition, d) gating on the unshifted component of the feeding transition to access the unshifted component of the decay transition. In the present case the first two options are ineffective since we need to suppress the feeding transitions. Such gating is, however, used to select a proper reaction channel in measurements without recoil identification. To measure the lifetime of the decay, the third option is used, since both shifted and unshifted components are required for lifetime measurements. It has been verified in Ward et al., 1973 that gating on both shifted and unshifted component of the feeding transition will produce unreliable results due to the influence of the γ-ray transitions that are in coincidence with the unshifted component. The gating on the feeding transition (shown in the level scheme in Fig. 5.10) will eliminate the unobserved side feeding if it exists. The biggest

disadvantage of this method is the loss of statistics when using γ-γ coincidence. Both DDCM and DCM procedures can be applied to $\gamma - \gamma$ coincidence data. In the present experiment this method could only be applied to the lifetime measurement of the 4_1^+ state of ^{100,102}Zr and the 4_1^+ and 6_1^+ states of ^{104}Mo. In particular, the lifetime of the 4_1^+ state in ^{104}Mo could be extracted with both DDCM and DCM.

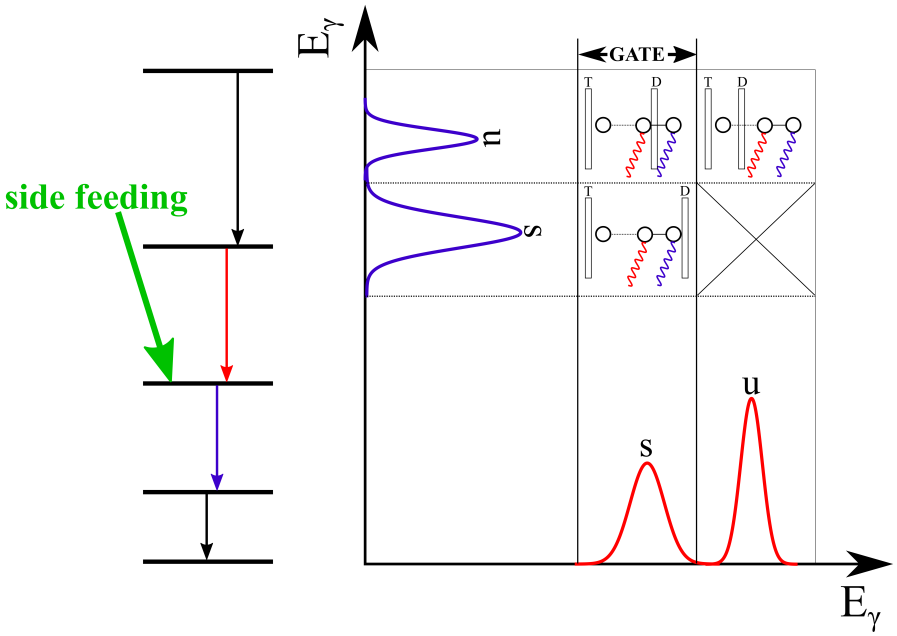

FIGURE 5.10: Outline of the $\gamma - \gamma$ coincidence technique. S and U denotes shifted and unshifted components respectively. T and D are target and degrader, respectively.

5.5 Implementation of DDCM, DCM and $\gamma - \gamma$ coincidence to ^{104}Mo data

There are two important reasons to use ^{104}Mo as a reference isotope for lifetime measurements with DDCM, DCM and $\gamma - \gamma$ coincidence techniques. First, ^{104}Mo is one of the strongest reaction channels. Second, the lifetime of the 4_1^+ state has been measured in three previous experiments with consistent results [Smith et al., 2002; Liang et al., 1991; Mamane et al., 1986]. Here we extract the lifetime of several states of ^{104}Mo using DDCM in singles, DDCM in $\gamma - \gamma$ coincidences as well as DCM in $\gamma - \gamma$ coincidences. In this work we have also used the sum-method (section 5.5.3) to measure lifetimes of weakly populated channels. Here we have tested this method by reproducing the lifetime of the 6_1^+ state of ^{104}Mo.

5.5.1 DDCM

The DDCM analysis employs Eq. 5.10. In the case of ^{104}Mo, the intensities of the shifted and unshifted components could be determined for the decay of the 4_1^+, 6_1^+, 8_1^+ and 10_1^+ states. The DDCM is used for the first three states whereas only the effective lifetime[4] could be measured for the 10_1^+ state using DCM due to low level of statistics. The level scheme of ^{104}Mo, limited to those states, is shown in Fig. 5.11.

[4]Effective lifetime includes the contribution from the feeding transitions

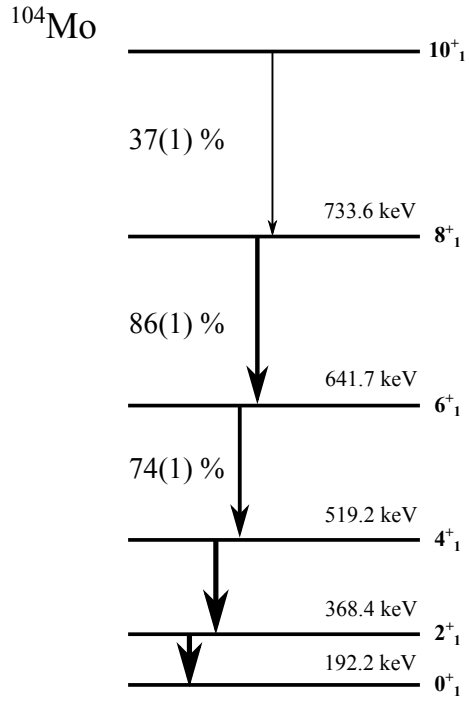

FIGURE 5.11: Level scheme of ^{104}Mo presenting states relevant for the present analysis. α_j for each feeding transition is shown as percentage of the $4_1^+ \longrightarrow 2_1^+$.

The first step for all analysis methods is to fit the shifted and unshifted components in the energy spectrum for both decay and feeding transitions for each plunger distance. We have used two different functions to fit the shifted and unshifted peaks:

- The first function was adapted from the *GF3* program ["Radware"] to take into account the low-energy tail seen in Fig. 5.12. Such a tail is a common feature in Ge detector spectra that arises from incomplete charge collection due to the charges being trapped in the lattice dislocations. The contribution from this tail is prominently observed for strong channels and is hardly visible in weak channels due to low level of statistics. Such a peak with a prominent left tail cannot be fitted with a single Gaussian and therefore the following function was used:

$$\begin{aligned} Y = & \frac{\mathcal{A}}{\sqrt{2\pi}\sigma} \cdot \exp\Big(\Big[-0.5\Big(\frac{x-E_\gamma}{\sigma}\Big)\Big]^2\Big) \\ & + \frac{\mathcal{A}}{(2\rho s)} \cdot \left[\exp\Big(\frac{\sigma}{2s}\Big)^2 \cdot \exp\Big(\frac{x-E_\gamma}{s}\Big) \cdot \operatorname{erfc}\Big(\frac{x-E_\gamma}{\sqrt{2}\sigma} + \frac{\sigma}{\sqrt{2}s}\Big)\right] \\ & + \Gamma \cdot \operatorname{erfc}\Big(\frac{x-E_\gamma}{\sqrt{2}\sigma}\Big) + B \end{aligned} \tag{5.14}$$

where the first term is a Gaussian, the second term is a skewed Gaussian and the third term is a step function modeling the Compton background. The parameters $\mathcal{A}$, E_γ, σ, ρ, s, Γ and B denote the peak area, centroid, standard deviation, the ratio of areas of the normal to skewed Gaussians, the skewness, the step amplitude and the constant background, respectively. In contrast to the *GF3* function, the first two terms are normalized so that the areas can be directly read from the fit parameters (area of the Gaussian and skewed Gaussian are simply $\mathcal{A}$ and $\mathcal{A}/\rho$).

The ratio (ρ) and skewness (s) are first estimated by fitting either the peak of interest in a spectrum obtained by summing those for all plunger distances (sum spectrum) or the nearest peak in the ^{152}Eu calibration spectrum and then fixed for all plunger distances. It was observed that the ratio and skewness are energy dependent. Additionally, the centroid and standard deviation were either fixed or bounded within a specific range after determining their values by fitting the sum spectrum. The boundaries reflect the uncertainty of the fit parameters of the sum spectrum.

The reduced χ^2 obtained for the fit of the shifted and unshifted peaks was smaller using the bounded parameters as compared to the fixed parameters, because the centroid and the standard deviation of the sum-spectrum have uncertainties. The parameters (centroid and standard deviation) were only fixed in a few cases where there was no noticeable difference in the reduced χ^2 square between the fits obtained by fixing parameters and bounding them. With this procedure the number of free parameters used in the function was reduced from 7 to 3.

- A simple double Gaussian is sufficient to fit the shifted and unshifted peaks for cases where the level of statistics is so low that the low-energy tail is not visible. This function was always used for γ-γ coincidence data. It was also used in few cases to measure the lifetimes of 8_1^+ and 10_1^+ states.

Lifetime of the 4_1^+ state

The shifted and the unshifted peaks of the γ-ray transition from the 4_1^+ state are shown in Fig. 5.12a, for plunger distances where the level of statistics is sufficient for fitting both peaks using the function 5.14. Q_i is calculated from the derived peak intensities and plotted as a function of the plunger distance. The slope of the resulting decay curve (Fig. 5.13a) depends primarily on the lifetime of the 4_1^+ state, but also on the lifetime of the 6_1^+ state directly feeding it. Since no additional side feeding was observed in this case, the direct feeding contribution of 74% (α_j) to the 4_1^+ state from the $6_1^+ \longrightarrow 4_1^+$ transition was taken into account and the remaining 26% was assumed to be prompt and not influencing the lifetime.

To obtain the feeding contribution Q_j, the shifted and unshifted peaks of the decay of the 6_1^+ state were fitted in a similar way (Fig. 5.12b). To extract the derivative, $Q_i(x)$ was fitted with the piecewise function (see blue dotted curve in Fig. 5.13a). Lifetimes were extracted individually for each distance using Eq. 5.10 and were plotted as a function of the plunger distance (Fig. 5.13b).

Only certain distances which are located in the sensitive region where the slope of the decay curve is largest are averaged (weighted mean) to obtain the final lifetime. The definition of the sensitive region is discussed in detail in section 4.3 of Grente, 2014 where it has been established that the sensitive range can be defined as:

$$\left|\frac{dQ}{d(log(x))}\right| > \alpha \left|\frac{dQ}{d(log(x))}\right|_{max} \tag{5.15}$$

In our case α was taken as 0.45 which corresponds to at least 4 points in the sensitive region. It can be noticed that due to the piecewise character of the function used to fit the decay curve, its first derivative is continuous. The second derivative is not, forming "irregularities" at the transition points. The lifetime of the 4_1^+ state obtained from singles DDCM is equal to $\tau(4_1^+) = 32.6(20)$ ps.

Lifetime of the 6_1^+ state

The lifetime of the 6_1^+ state was determined in the same way as for the 4_1^+ state (Fig. 5.14a). 86% of direct feeding (α_j) was taken into account in the determination of the lifetime of the 6_1^+ state. The lifetimes obtained for distances outside of the sensitive range are randomly scattered (Fig. 5.14b). Usually a trend in the lifetimes for individual distances can indicate an unobserved side feeding. However, in this case the lifetime distribution does not reflect a side feeding but rather a statistical fluctuation. Though it looks like as if the lifetime in Fig. 5.14b exhibited a trend for small distances, changing the transition point of the piecewise polynomial function scatters the points in the non-sensitive region to different positions without influencing the lifetime. For the state a lifetime of τ= 4.43(16) ps was obtained.

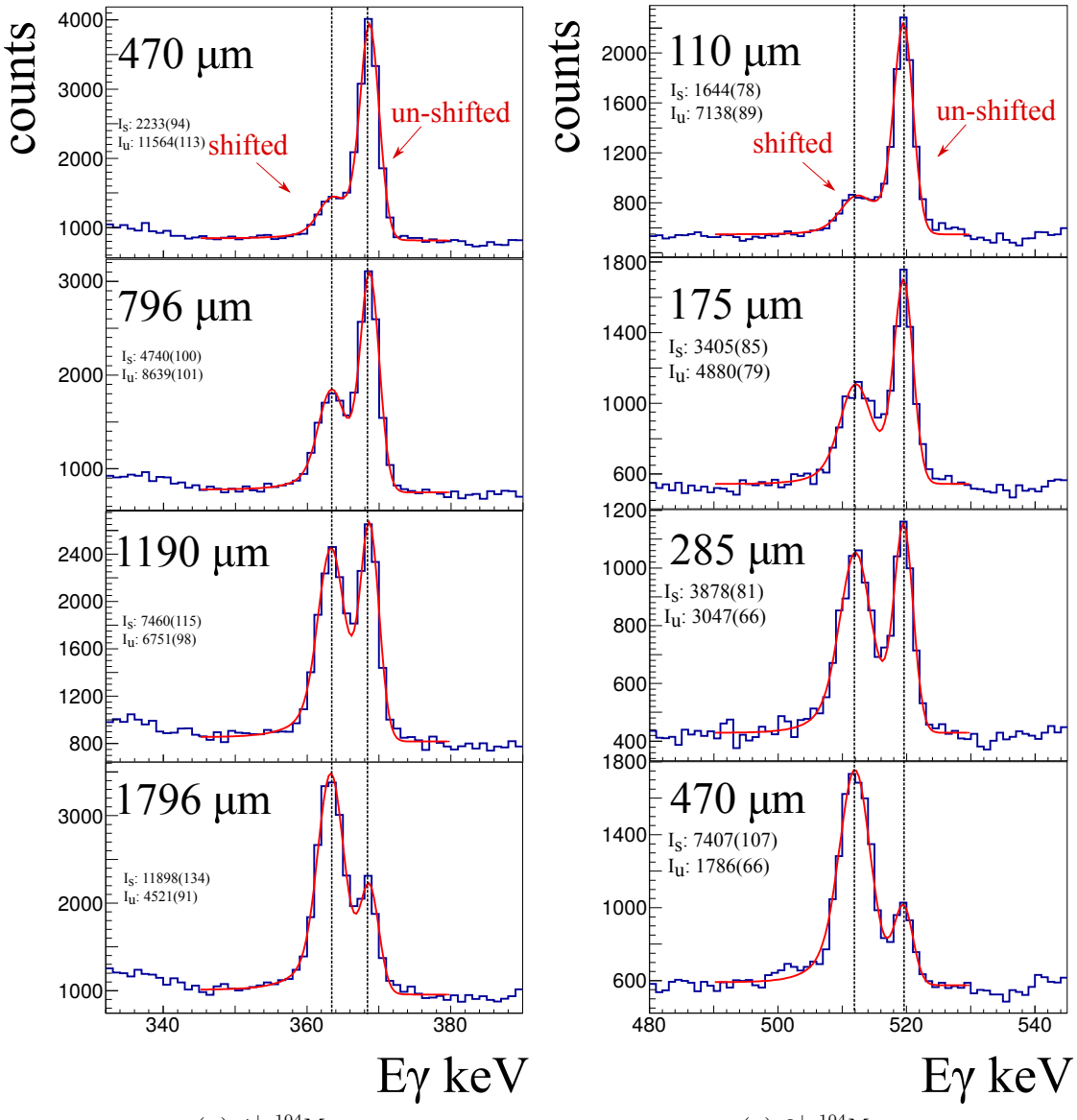

(A) 4_1^+ ^{104}Mo (B) 6_1^+ ^{104}Mo

FIGURE 5.12: (A) and (B) show shifted and unshifted peaks for the transitions deexciting the 4_1^+ and 6_1^+ state in ^{104}Mo, respectively. The areas of the shifted and unshifted peaks from the fits are used for the DDCM and DCM singles analysis.

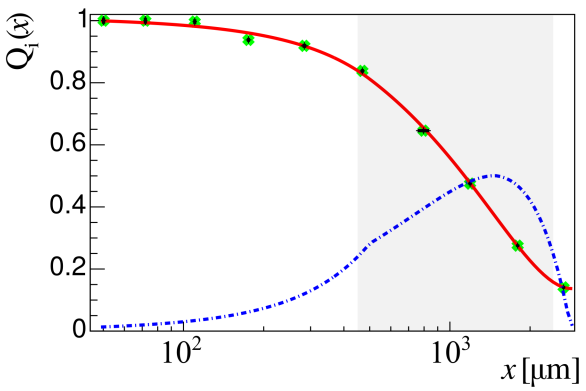

(A)

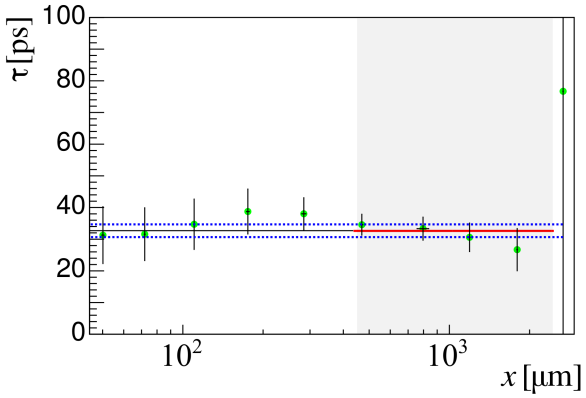

(B)

FIGURE 5.13: (A) Decay curve (solid) plotted using the function *piecewise1* and its derivative (dotted) for the 4_1^+ state in ^{104}Mo. (B) Corresponding lifetimes obtained for individual distances. The solid line denotes the mean lifetime value, while the dotted lines correspond to 1σ uncertainty.

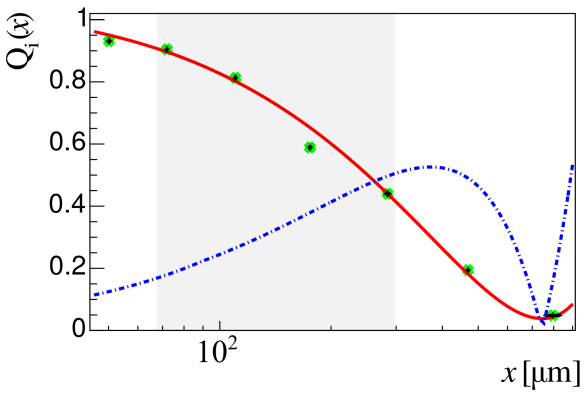

(A)

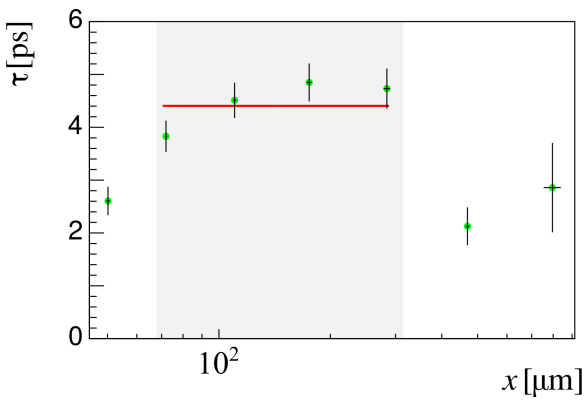

(B)

FIGURE 5.14: (A) Decay curve (solid) using the function *piecewise1* and its derivative (dotted) for the 6_1^+ state in ^{104}Mo. (B) Corresponding lifetimes obtained for individual distances. The solid line denotes the mean lifetime value, while the dotted lines correspond to 1σ uncertainty.

Lifetime of the 8_1^+

The data for the 8_1^+ state is analyzed in the same manner. The level of statistics obtained for ^{104}Mo allowed measuring the Q_j of the feeding from the 10_1^+ state (Fig. 5.15b). The direct feeding of the $10_1^+ \longrightarrow 8_1^+$ transition was determined as $\alpha = 37\%$ and used to obtain the lifetime from the weighted mean of the lifetimes as a function of plunger distance, lying in the sensitive range (Figs. 5.16a and 5.16b). For the 8_1^+ state a lifetime of $\tau = 2.55(27)$ ps was obtained.

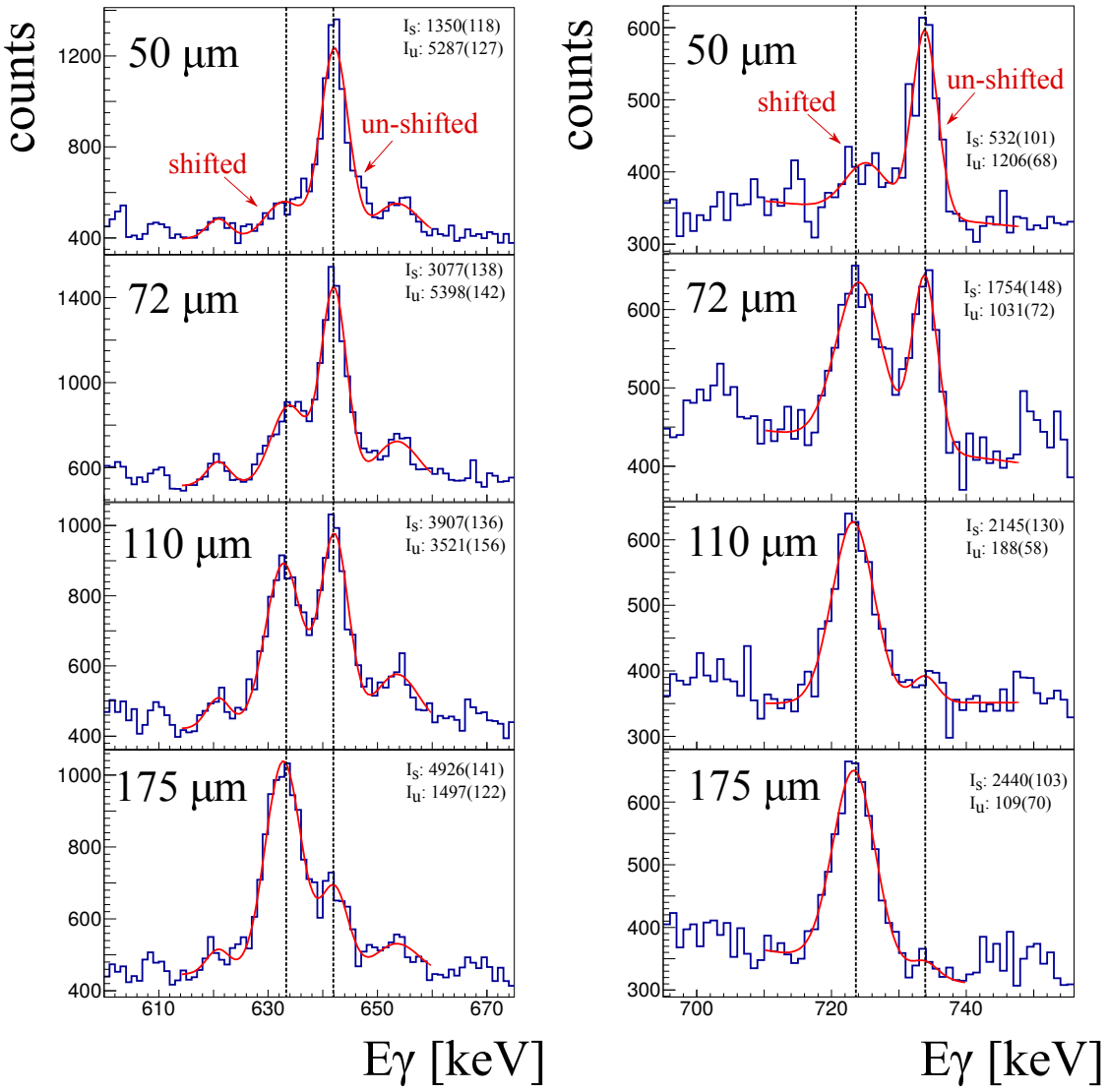

(A) 8_1^+ ^{104}Mo (B) 10_1^+ ^{104}Mo

FIGURE 5.15: (A) and (B) show shifted and unshifted peaks for the transitions deexciting the 8_1^+ and 10_1^+ state in ^{104}Mo, respectively. The areas of the shifted and unshifted peaks are used for the DDCM and DCM singles analysis.

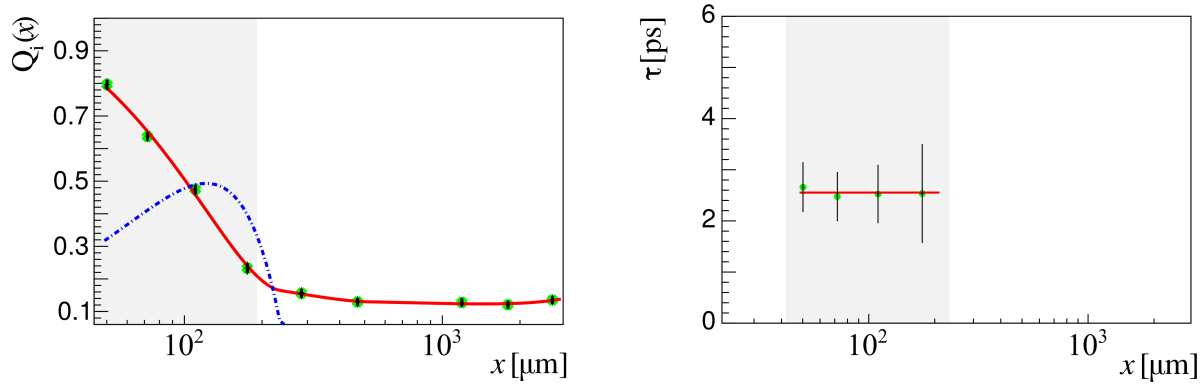

(A) (B)

FIGURE 5.16: (A) Decay curve (solid) using the function *piecewise1* and its derivative (dotted) for the 8_1^+ state in ^{104}Mo. (B) Corresponding lifetimes obtained for individual distances. The solid line denotes the mean lifetime value, while the dotted lines correspond to 1σ uncertainty.

5.5.2 $\gamma - \gamma$ coincidence analysis

The $\gamma - \gamma$ coincidence technique is extremely reliable since it removes the feeding contribution, but requires a high level of statistics as discussed in section 5.4.3. Hence only the lifetimes of the 4_1^+ and 6_1^+ states could be measured using $\gamma - \gamma$ coincidence. Fig 5.17 illustrates the analysis for the 4_1^+ state. It can be seen in Fig. 5.17a that the two peaks are indeed well separated for the most significant distances. The fit for the first distance (470 μm) of the $4_1^+ \longrightarrow 2_1^+$ transition is perhaps the least reliable due to the presence of a high background. Nevertheless, the lifetimes are constant as a function of plunger distance (see Fig. 5.17c).

The lifetimes were extracted using both DCM and DDCM. In DDCM analysis the lifetime of $\tau_{4_1^+} = 35.7(23)$ ps was obtained (Fig. 5.17c). In DCM analysis, the lifetime of $\tau_{4_1^+} = 35.7(40)$ ps was directly given by the fit of the decay curve (Fig. 5.17b). This value is similar to the DDCM result but has a larger uncertainty. The same procedure was repeated to extract the lifetime of the 6_1^+ state. However, in this case the level of statistics is much lower than for the 4_1^+ state. The first point in Fig. 5.18a is influenced strongly by statistical fluctuations. The lifetime obtained for the 6_1^+ via DCM is $\tau = 5.8(19)$ ps. Although the two lifetimes agree within the error, the uncertainty on the lifetime using the γ-γ coincidence data is too large to validate the lifetime obtained from the singles analysis using DDCM.

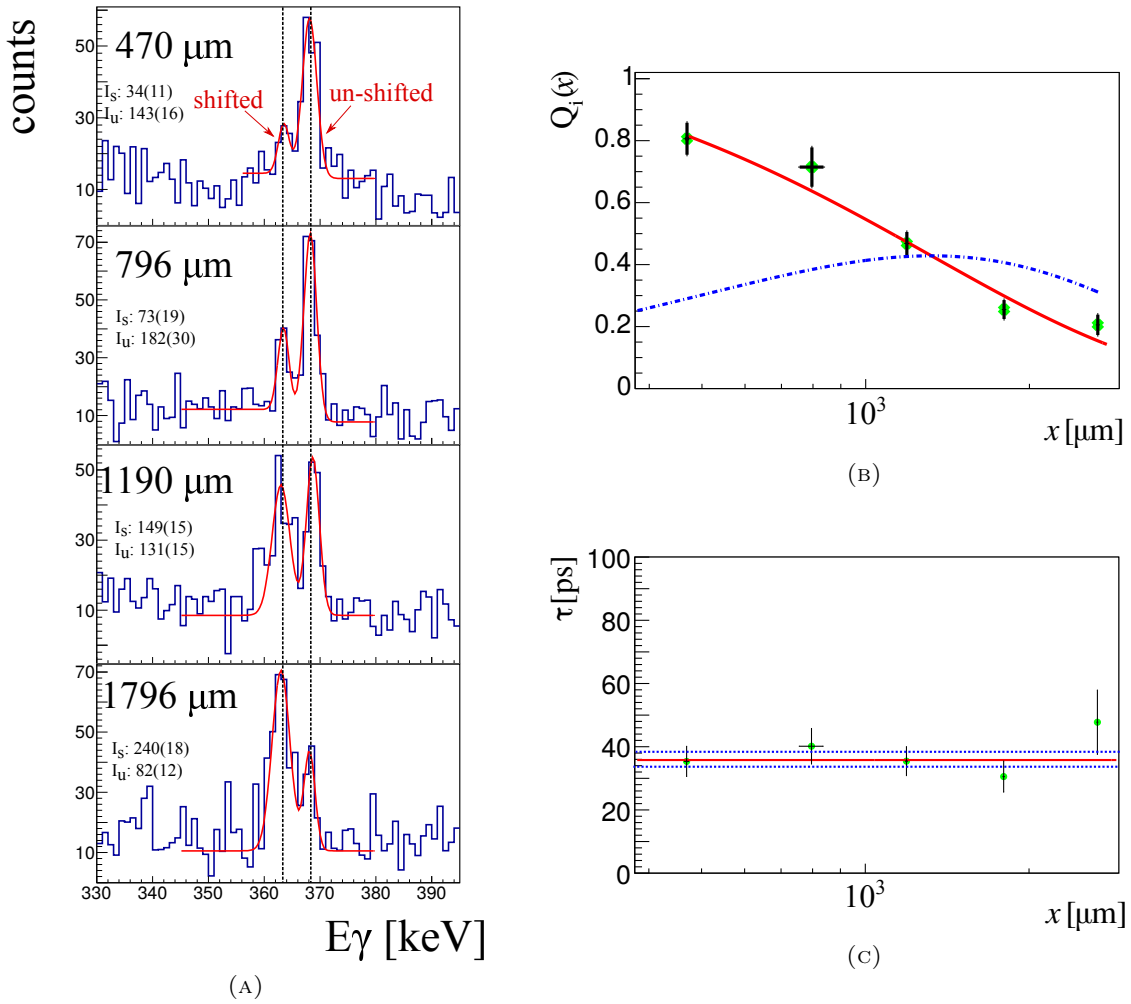

FIGURE 5.17: (A) Shifted and unshifted peaks for the transitions deexciting the 4_1^+ state in ^{104}Mo obtained from $\gamma-\gamma$ coincidence data after gating on the shifted component of the 6_1^+ state, (B) Corresponding decay curve using the function *expo* and its derivative. (C) Lifetimes plotted as a function of plunger distance. The solid line denotes the extracted lifetime, while the dotted lines correspond to 1σ uncertainty.

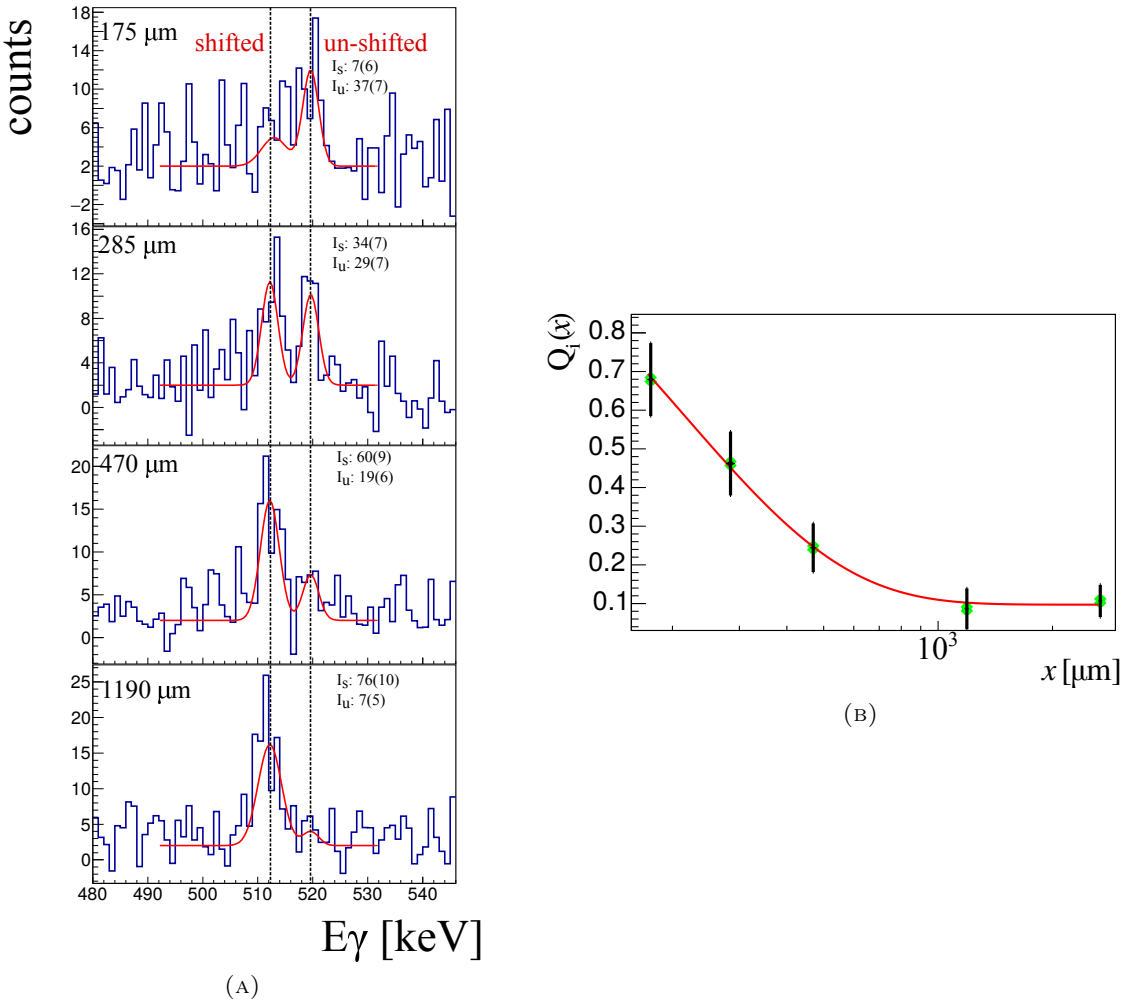

FIGURE 5.18: Shifted and unshifted components of the $6_1^+ \longrightarrow 4_1^+$ transition in ^{104}Mo obtained after gating on the shifted component of the $8_1^+ \longrightarrow 6_1^+$ transition. I_s and I_u represent shifted and unshifted area, respectively. I_s and I_u represent shifted and unshifted area, respectively. (B) corresponding decay curve using the function *expo*

5.5.3 Sum method

The sum method was extensively used by Litzinger et al., 2015 to extract the lifetimes from singles data using a Monte Carlo approach for the feeding transitions. The name suggests that the lifetimes are determined from the Q_i of the summed spectra of all plunger distances rather than from the individual ones. In an ideal case with no feeding contribution, the lifetime resulting from the sum method can be calculated from the solution of the differential Bateman equations as follows:

$$Q_{i_{SUM}} = \frac{\sum_k I_U}{\sum_k I_S + \sum_k I_U} = \sum_k n_k Q_i(x_k) \tag{5.16}$$

where I_U and I_S are the intensities of unshifted and shifted components, respectively and n_k denotes the normalization factor for distances k. Using Eq. 5.6 $Q_{i_{SUM}}$ can be expressed in terms of the plunger distance (x_k), lifetime (τ) and velocity (v_{in}) as:

$$Q_{i_{SUM}} = \sum_k n_k e^{\frac{-x_k}{v_{in}\tau}} = f(\tau) \tag{5.17}$$

In the present work we have used this method mostly in combination with $\gamma-\gamma$ coincidences especially for cases where the level of statistics was too low to extract $Q_i(x)$ from the spectra corresponding to individual distances. This method can also be used with singles data for transitions where the level of statistics is low (like the decay of 10^+_1 state) to obtain the effective lifetimes of these states.

6^+_1 state

The lifetimes of the 6^+_1 state in ^{104}Mo was determined using the sum method from γ-γ coincidence data (see Fig. 5.19). The red curve is plotted as a function of τ using the relation 5.17. The experimental value of $Q_{i_{SUM}}$ for five distances was 0.202 and the lifetime was obtained by finding the corresponding τ on the X axis (shown in blue). $\delta f(\tau)$ was obtained through propagation of uncertainty knowing the errors on n_i, x_i and v_{in}. The $Q^{-1\sigma}_{i_{SUM}}$ and $Q^{+1\sigma}_{i_{SUM}}$ are then extrapolated on the τ axis to obtain the uncertainties of the lifetime, $\delta\tau^-$ and $\delta\tau^+$, respectively. The total error along the Y axis of plot 5.19 (shown by dashed blue lines) is $\sqrt{\delta f(\tau)^2+\delta Q^2_{i_{SUM}}}$).

The resulting lifetime is $\tau_{6^+_1}$ = 5.3(5) ps which agrees rather well with the results obtained from the DCM using $\gamma-\gamma$ coincidence.

10^+_1 state

The effective lifetime of the 10^+_1 state was obtained using the sum method since both shifted and unshifted peaks were not observed sufficiently at many distances (see Fig. 5.15b). The information on Q_j was necessary to extract the lifetime of the 8^+_1 state. Fig. 5.20a illustrates the sum-method procedure applied to obtain the effective lifetime of the 10^+_1 equal to $\tau_{10^+_1} = 1.65^{+17}_{-16}$ ps. The procedure was extended one step further to obtain Q_j for individual distances from the effective lifetime by using the following expression:

$$Q_j(x_k) = e^{\frac{-x_k}{v_{in}\cdot\tau}}; \tag{5.18}$$

The lifetime obtained from this method was very similar to the one from DCM ($\tau_{10^+_1}$ = 1.65(10) ps) using the points obtained from Eq. 5.18.

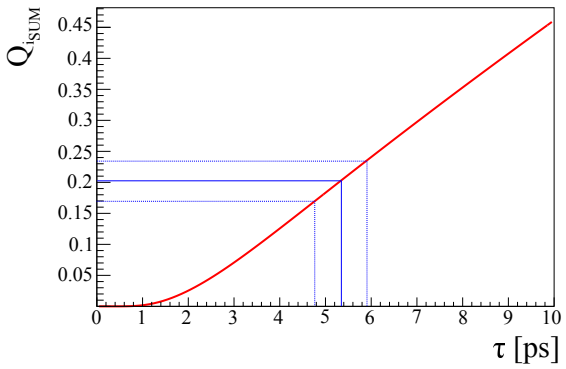

FIGURE 5.19: Illustration of the analysis performed for the 6^+_1 state in ^{104}Mo using the sum-method for $\gamma-\gamma$ coincidence data. The solid line and dashed lines crossing the τ axis represent the lifetime and the error on the lifetime, respectively.

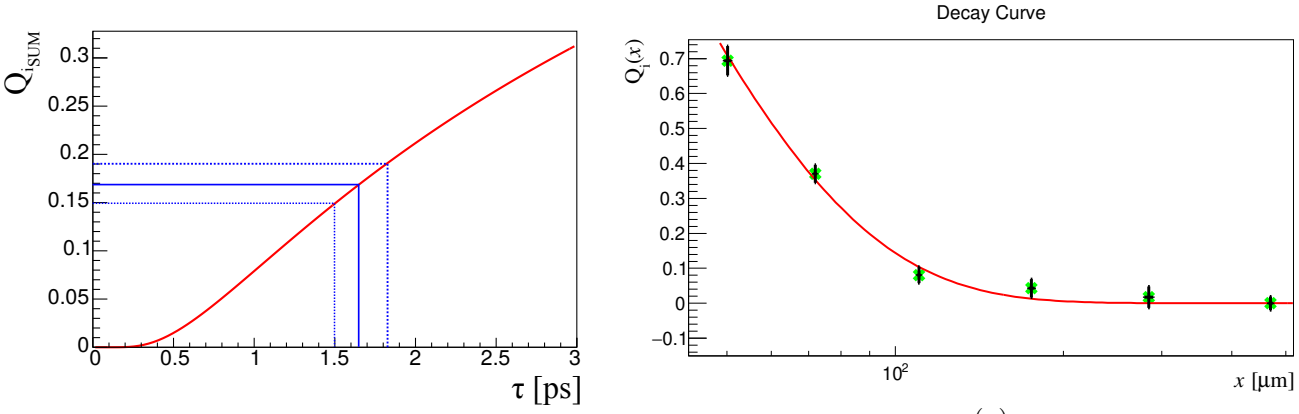

(A) (B)

FIGURE 5.20: (A) Illustration of the analysis performed for the 10^+_1 state in ^{104}Mo using the sum method for singles data. The solid line and dashed lines crossing the τ axis represent the lifetime and the error on the lifetime, respectively. (B) Decay curve for the 10^+_1 state using the function *expo*

Summary of results obtained for the lifetimes in ^{104}Mo

Table 5.3 summarizes the results obtained using different methods for all states in ^{104}Mo that could be studied in the present experiment. It can be seen that the results obtained for the 4^+_1 state from the DDCM using singles spectra and from the DCM using $\gamma-\gamma$ coincidence agree within the errors. Disagreement in the lifetime of the 6^+_1 state between the singles (DDCM) and $\gamma-\gamma$ coincidence (DDCM) data is probably due to overestimation of the feeding from the 8^+_1 state. Nevertheless, there is a good agreement between the DCM and the sum method[5] for the 6^+_1 state using data from the $\gamma-\gamma$ coincidences.

States	DDCM	DCM	$\gamma-\gamma$ DDCM	$\gamma-\gamma$ DCM	Sum method
4^+_1	32.6(20)	-	35.7(23)	35.7(40)	-
6^+_1	4.43(16)	-	-	5.8(19)	5.32(54)
8^+_1	2.55(27)	-	-	-	-
10^+_1	-	*0.85(9)	-	-	$*1.65^{+17}_{-16}$

TABLE 5.3: Lifetimes in ^{104}Mo extracted using different methods. All the lifetimes are in ps. For the 10^+_1 state, an effective lifetime has been determined.

[5]The sum method in this case is applied on γ-γ coincidence data to obtain the lifetime of the 6^+_1 state.

Chapter 6

Lifetime results

This chapter describes the lifetime measurement results of the present experiment in the Zr, Mo and Ru chains obtained using the different methods discussed in chapter 5. The first step towards lifetime measurement is the calculation of Q_i using Eq. 5.3. The shifted and unshifted peaks are fitted and their respective areas are evaluated in order to calculate Q_i for each plunger distance. The shifted and unshifted peaks and the fitted curves are shown only for the complicated case of ^{98}Zr (Fig. 6.2), where several side feeding transitions are involved, and for the cases for which the lifetime is determined using γ-γ coincidence data (4_1^+ in ^{100,102}Zr and ^{108}Ru). The fitted peaks for the remaining isotopes are shown in appendix A. DDCM is the main method used to extract lifetimes from the singles data. DCM is used to obtain the lifetimes of the states for which the level of statistics in the feeding transitions is insufficient. The sum method is used to determine effective lifetimes for transitions with low statistics. It is simultaneously used to determine the feeding contribution (Q_j) to the state of interest for cases where the level of statistics is not sufficient to obtain Q_j for individual distances. The γ-γ coincidence method is used whenever statistically possible.

For each lifetime obtained using the DDCM method, a decay curve (e.g. Fig. 6.3a) and a lifetime plot[1] (e.g. Fig. 6.3b) are presented. In an ideal case the lifetimes corresponding to the individual distances do not evolve as a function of the distance. However, in some cases the lifetime values can decrease or increase systematically as a function of the plunger distance. This could be either due to an overestimation or underestimation of the feeding contribution to the state of interest resulting probably due to contamination in the energy peak of the feeding transition or of the decay transition.

In the DCM method, the lifetime is given directly by the fit of the decay curve (e.g. Fig. 6.8). The level scheme is shown only for the complicated case of ^{98}Zr but not for the rest of the isotopes (since we do not observe feeding from non-yrast states). All the lifetimes measured for a given isotope are summarized at the end of each section.

6.1 ^{98}Zr

The lifetime of the 2_1^+ state could be measured in ^{98}Zr using the RDDS techniques as it is short lived (few picoseconds) unlike other isotopes for which the lifetime of the 2_1^+ state is too long to be measured with the plunger technique. The level scheme of ^{98}Zr presenting the transitions relevant for this analysis is shown in Fig. 6.1. The 2_1^+ state is fed by four transitions that could be observed in the present data and that account for 60.5 % of the total feeding contribution. The rest of the feeding is assumed to be prompt. The lifetime of the 2_1^+ is corrected for the effect of all four feeding transitions by measuring their respective lifetime values and $Q_j(x)$ (5.10). The

[1] Individual lifetime values as a function of plunger distance

$4_1^+ \longrightarrow 2_1^+$ transition at 620 keV accounts for 45 % of the feeding of the 2_1^+ state and its lifetime was determined using DDCM as shown in Fig. 6.4a and 6.4b. The lifetime of the 3_1^- state was obtained using DDCM as seen in Fig. 6.7. It can be noticed in Fig. 6.7b that the uncertainty on the mean lifetime value is almost 25 % which is due to low statistics as seen in Fig. 6.2d.

The lifetimes of the 2_2^+ and 4_2^+ states could only be determined using the sum method as seen in Fig. 6.6a and 6.6b respectively. After considering all four feeding transitions the lifetime of the 2_1^+ is determined using Eq. 5.10. The decay curve and the corresponding lifetime as a function of plunger distance are shown in Fig. 6.3a and 6.3b, respectively. The relatively large error at the plunger distance 1190 μm observed in the decay curve (Fig. 6.3a) comes from the uncertainties in the fitting of the shifted and unshifted 1223 keV peak for this distance (Fig. 6.2a). There is a slight increase in the lifetimes of the 2_1^+ state as a function of the plunger distance (as seen in Fig. 6.3b), which probably means that one of the transitions feeding the 2_1^+ state is slightly contaminated and hence overestimated. Despite this small effects the errors on the individual lifetimes are compatible with the mean lifetime value. The lifetimes of the 4_1^+ and 6_1^+ states are determined using DDCM as shown in Fig. 6.4 and 6.5, respectively. The increasing trend observed in the lifetimes of the 4_1^+ state at individual distances (see Fig. 6.4b) is probably due to a contamination from the $0_2^+ \longrightarrow 2_1^+$ transition at 636 keV which actually overlaps with the shifted component of the 647 keV peak of the $6_1^+ \longrightarrow 4_1^+$ transition. The same contamination may be slightly affecting the lifetime of the 6_1^+ state itself (Fig. 6.5b).

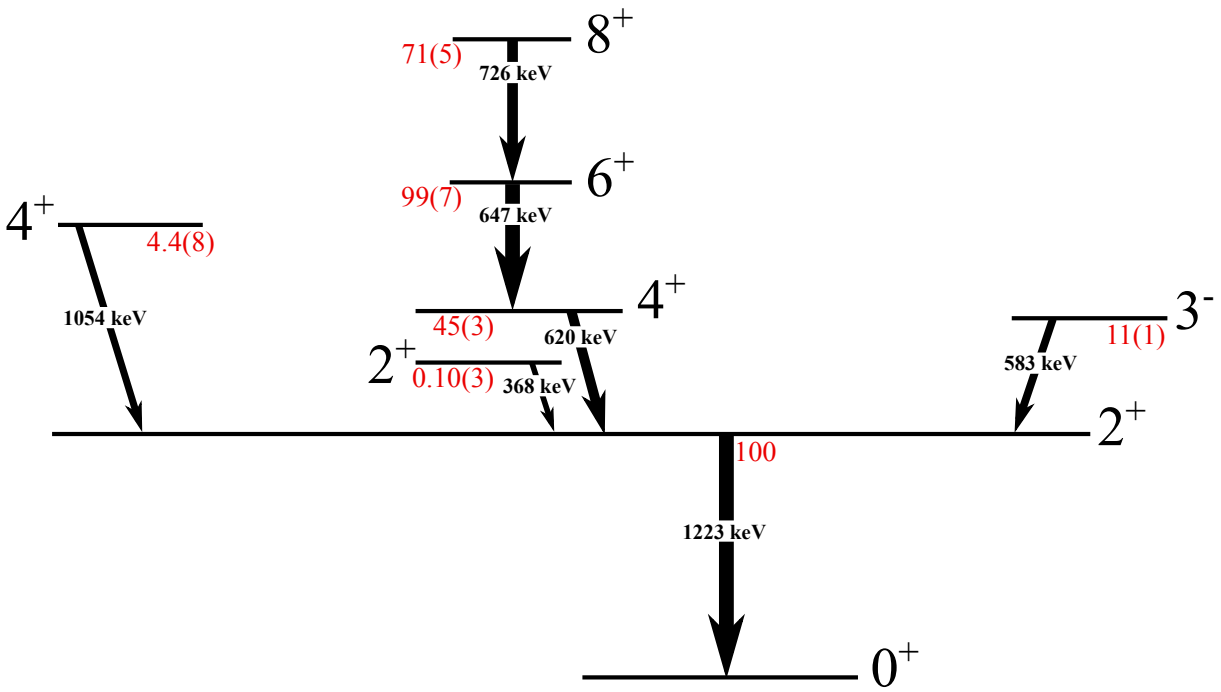

FIGURE 6.1: Level scheme of ^{98}Zr. The percentage of feeding transition contributing to the corresponding decay is shown in red.

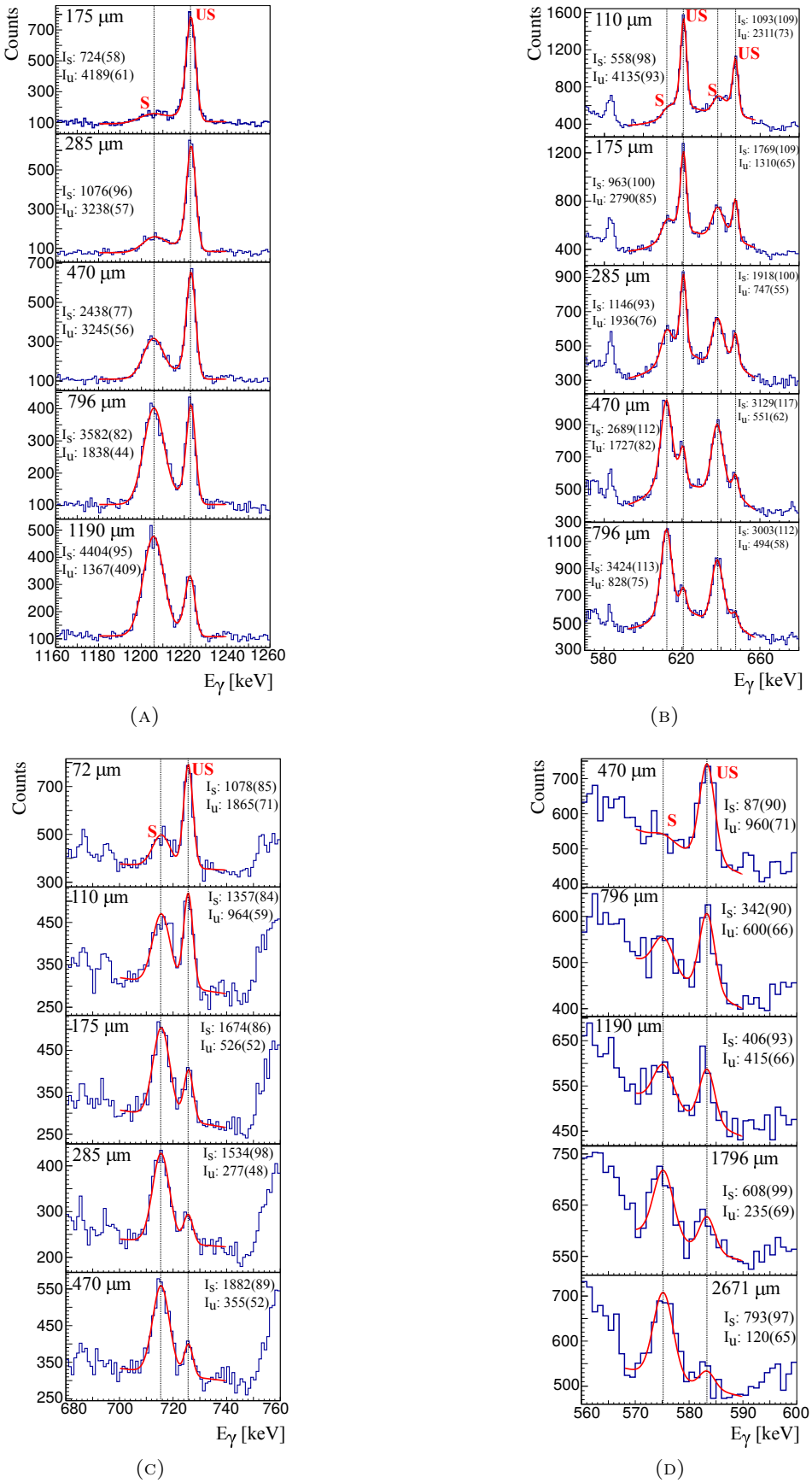

FIGURE 6.2: Shifted and unshifted peaks for the 1233 keV transition deexciting the 2_1^+ state (A), the 620 keV and 647 keV transitions deexciting the 4_1^+ and 6_1^+ states, respectively (B), the 726 keV transition deexciting the 8_1^+ state (C) and the 583 keV transition deexciting the 3^- state (D). I_s and I_u represent shifted and unshifted area, respectively.

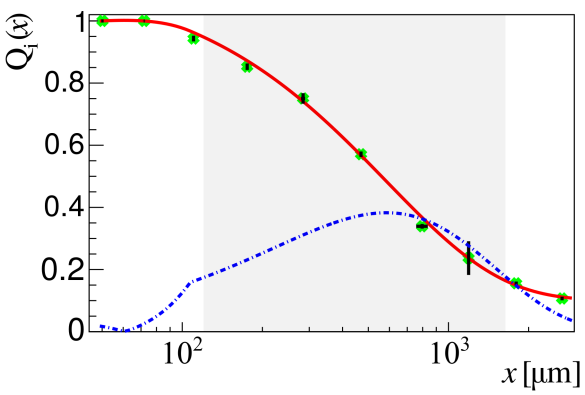

(A)

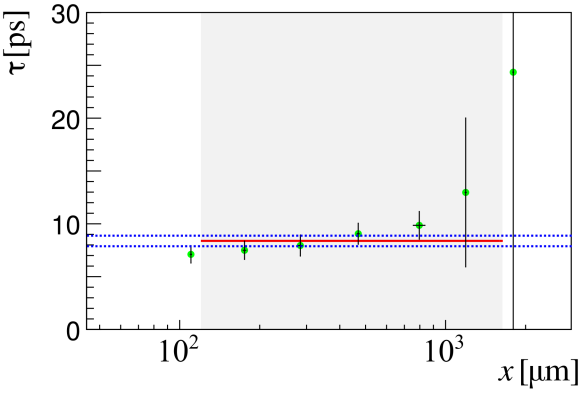

(B)

FIGURE 6.3: (A) Decay curve (solid) fitted using the function *piecewise2* and its derivative (dotted) for the 2_1^+ state in ^{98}Zr. (B) Corresponding lifetimes obtained for individual distances. The solid line indicates the mean lifetime value, while the dotted lines correspond to the 1σ uncertainty.

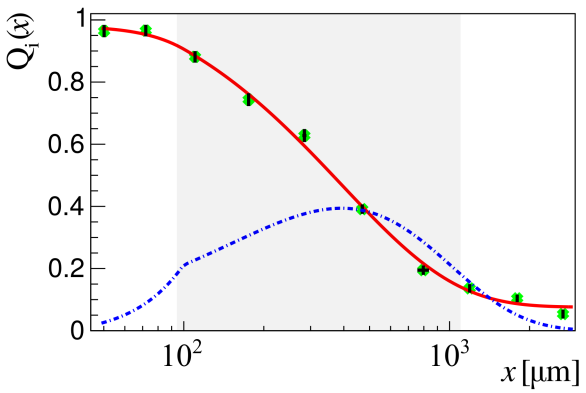

(A)

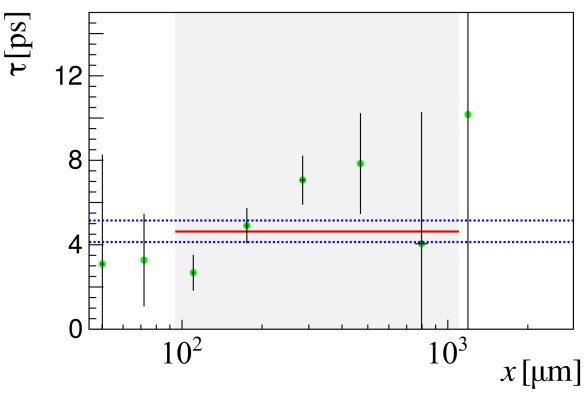

(B)

FIGURE 6.4: (A) Decay curve (solid) fitted using the function *piecewise2* and its derivative (dotted) for the 4_1^+ state in ^{98}Zr. (B) Corresponding lifetimes obtained for individual distances. The solid line indicates the mean lifetime value, while the dotted lines correspond to the 1σ uncertainty.

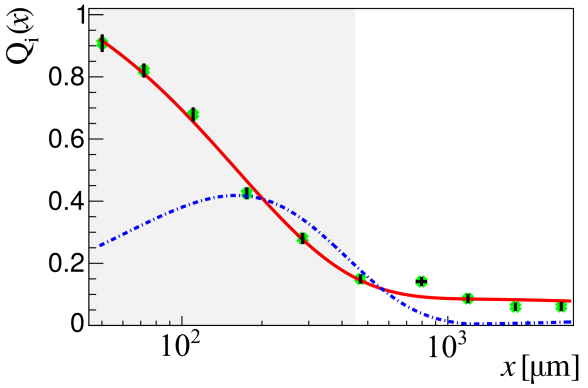

(A)

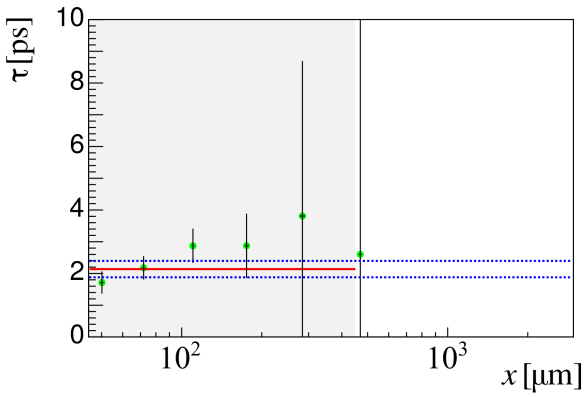

(B)

FIGURE 6.5: (A) Decay curve (solid) fitted using the function *piecewise3* and its derivative (dotted) for the 6_1^+ state in ^{98}Zr. (B) Corresponding lifetimes obtained for individual distances. The solid line indicates the mean lifetime value, while the dotted lines correspond to the 1σ uncertainty.

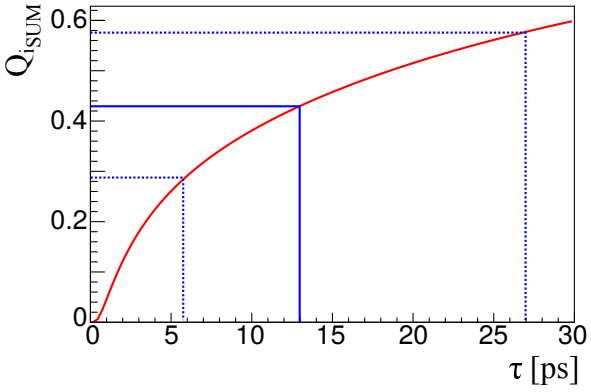

(A)

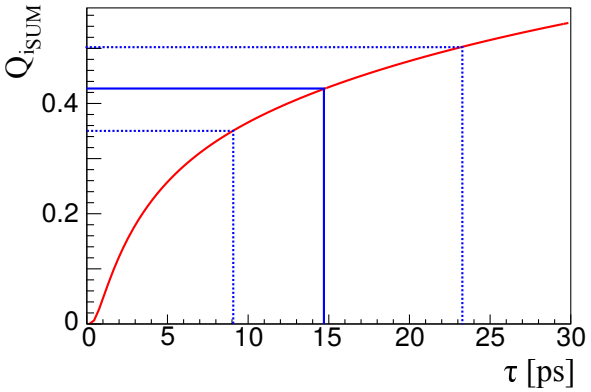

(B)

FIGURE 6.6: (A) Effective lifetime for the 2_2^+ state in ^{98}Zr obtained using the sum method. (B) Effective lifetime for the 4_2^+ state in ^{98}Zr obtained using the sum method.

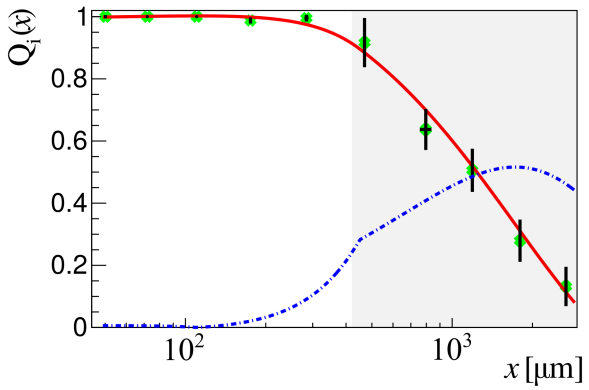

(A)

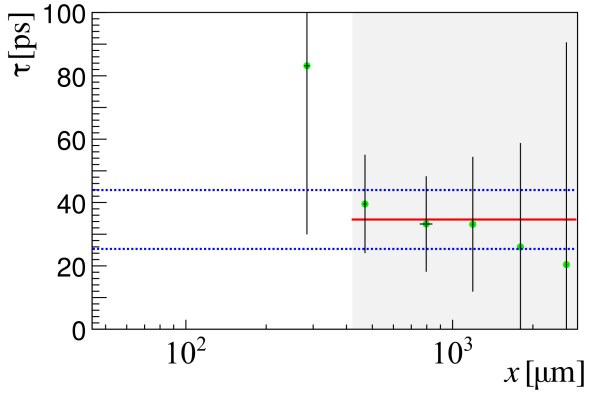

(B)

FIGURE 6.7: (A) Decay curve (solid) fitted using the function *piecewise1* and its derivative (dotted) for the 3_1^- state in ^{98}Zr. (B) Corresponding lifetimes obtained for individual distances. The solid line indicates the mean lifetime value, while the dotted lines correspond to the 1σ uncertainty.

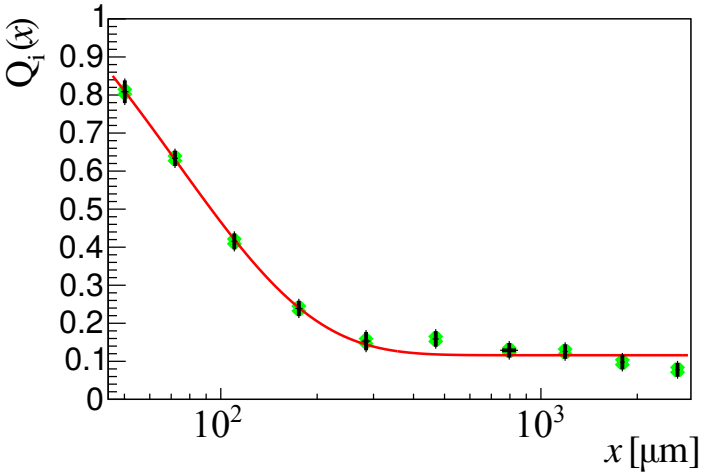

FIGURE 6.8: Decay curve fitted using the function *piecewise1* for the 8_1^+ state in ^{98}Zr for which the lifetime is calculated using Eq. 5.6.

State	Transition [keV]	DDCM	Sum method	DCM
2_1^+	1223	8.3(5)	-	-
4_1^+	620	4.6(5)	-	-
3_1^-	583.2	*35(9)	-	-
2_2^+	368	-	$^*13^{+14}_{-7}$	-
4_2^+	1054	-	$^*15^{+8}_{-6}$	-
6_1^+	647	2.13(21)	-	-
8_1^+	726	-	-	*1.95(19)

TABLE 6.1: Lifetimes in ^{98}Zr determined using the different methods discussed in the text. All the lifetimes are in ps. The lifetimes for the 2_2^+ and 4_2^+ states have asymmetric errors. The values marked with a * are effective lifetimes only.

6.2 ^{100}Zr

In ^{100}Zr, the lifetimes of the 4_1^+, 6_1^+ and 8_1^+ states were determined using DDCM whereas only an effective lifetime could be obtained for the 10_1^+ state using the sum method. The lifetime analysis for the 4_1^+ state is shown in Fig. 6.9. It can be seen in Fig. 6.9b that the lifetime values determined for the individual plunger distance are constant as a function of the distance, as it is expected for DDCM if the feeding is correctly accounted for. The DCM method using γ-γ coincidence data was also employed to determine the lifetime of the 4_1^+ state and the result of τ = 41(5) ps agrees with the one obtained using DDCM with γ-ray singles data.

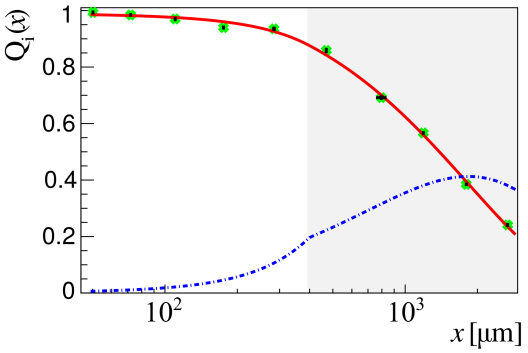

(A)

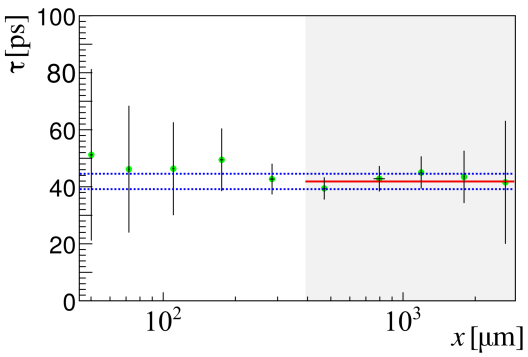

(B)

FIGURE 6.9: (A) Decay curve (solid) fitted using the function *piecewise2* and its derivative (dotted) for the 4_1^+ state in ^{100}Zr. (B) Corresponding lifetimes obtained for individual distances. The solid line indicates the mean lifetime value, while the dotted lines correspond to the 1σ uncertainty.

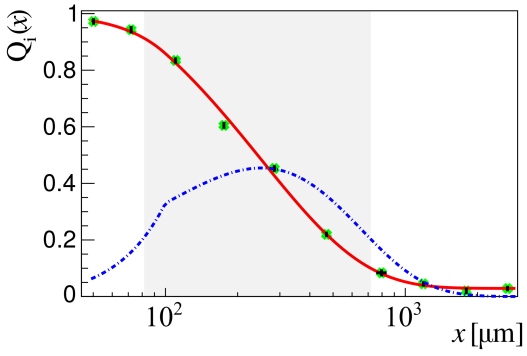

(A)

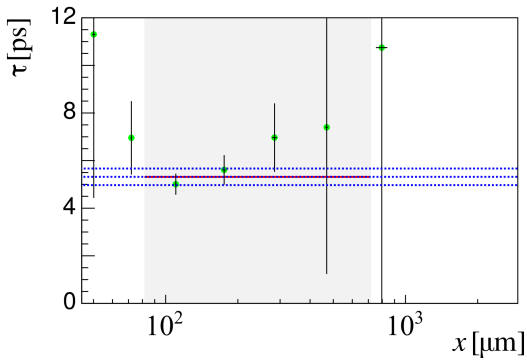

(B)

FIGURE 6.10: (A) Decay curve (solid) fitted using the function *piecewise2* and its derivative (dotted) for the 6_1^+ state in ^{100}Zr. (B) Corresponding lifetimes obtained for individual distances. The solid line indicates the mean lifetime value, while the dotted lines correspond to the 1σ uncertainty.

For the 6_1^+ state a slight increase was observed in the individual lifetimes as a function of the plunger distance as seen in Fig. 6.10b. The individual errors are however compatible with the average lifetime of τ = 5.3(3) ps. The lifetime of the 8_1^+ state was determined using two different approaches to obtain the $Q_j(x)$ of the feeding transition. First, by using the sum method for the 10_1^+ state to calculate its lifetime ($\tau = {}^*1.58^{+11}_{-10}$) and the corresponding $Q_j(x)$. Second, by using the literature lifetime of the 10_1^+ state (1.08(12) ps, [NNDC]) to extract $Q_j(x)$ using Eq. 5.18. The former case is shown in Fig. 6.12c where a lifetime of 1.60(8) ps was obtained whereas the

latter case is shown in Fig. 6.12d and led to a lifetime of 1.91(9) ps. The lifetime of the 8_1^+ state was taken as 1.60(8) ps.

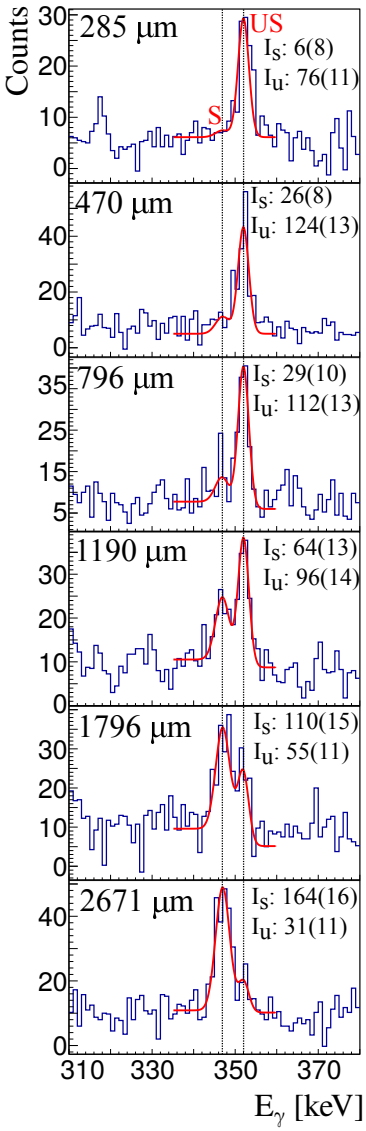

(A)

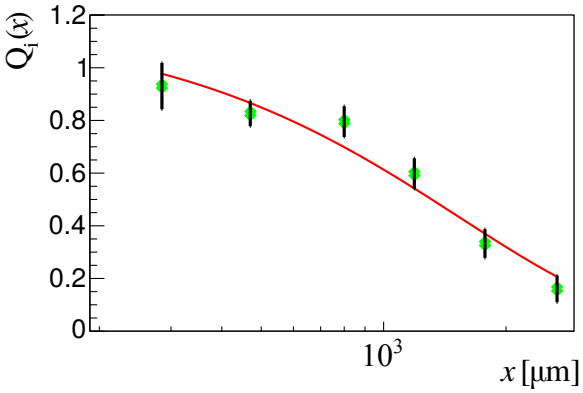

(B)

FIGURE 6.11: (A) Shifted and unshifted peaks for the 352 keV transition deexciting the 4_1^+ state of ^{100}Zr, obtained from $\gamma - \gamma$ coincidence data after gating on the shifted component of the 6_1^+ state. (B) Corresponding decay curve (fitted using the function *expo*) used to calculate the lifetime via Eq. 5.6. I_s and I_u represent shifted and unshifted area, respectively.

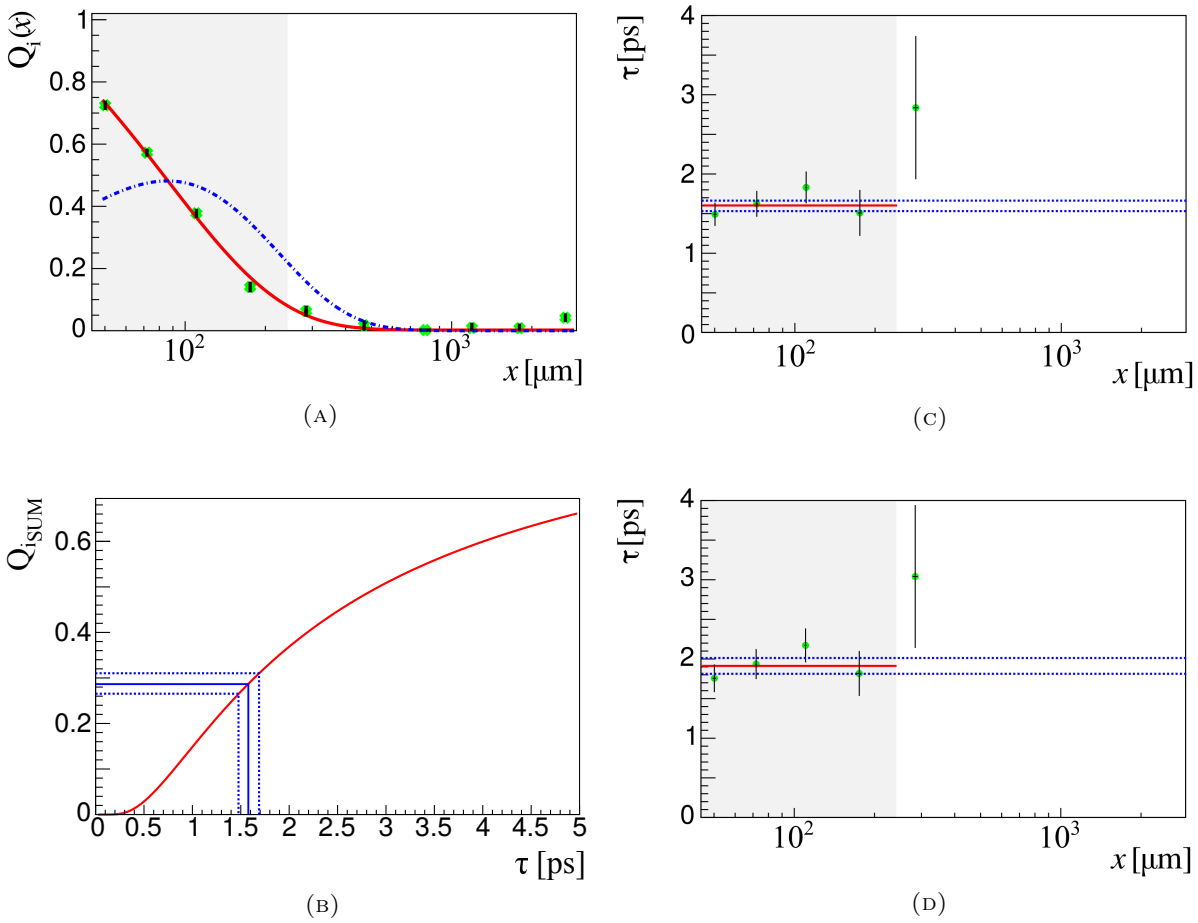

FIGURE 6.12: (A) Decay curve (solid) fitted using the function *expo* and its derivative (dotted) for the 8_1^+ state in ^{100}Zr. (B) Effective lifetime measured using the sum method for the 10_1^+ state in ^{100}Zr. (C) Lifetimes of the 8_1^+ state obtained for individual distances using DDCM, where Q_j (10_1^+) is calculated using the sum method. (D) same as (C) except the Q_j for the 10_1^+ contribution is calculated using the lifetime from the literature ["NNDC"]. In both (C) and (D), The solid line indicates the mean lifetime value, while the dotted lines correspond to the 1σ uncertainty.

State	Transition [keV]	DDCM	Sum method	γ-γ DCM
4_1^+	352	41.8(24)	-	41(5)
6_1^+	497	5.3(3)	-	-
8_1^+	626	1.60(8)	-	-
10_1^+	739	-	$^*1.58^{+11}_{-10}$	-

TABLE 6.2: Lifetimes in ^{100}Zr determined using the different methods discussed in the text. All the lifetimes are in ps. The lifetime of the 10_1^+ state has asymmetric errors. The values marked with a * are effective lifetimes.

6.3 ^{102}Zr

In ^{102}Zr, the lifetimes of the 4_1^+, 6_1^+ and 8_1^+ states were obtained using DDCM whereas for the 10_1^+ state the sum method was used. The lifetime analysis for the 4_1^+ and 6_1^+ states is shown in Figs. 6.13 and 6.14, respectively. The lifetime plots for both states feature a slight increasing trend with respect to the plunger distance in the sensitivity region (as seen in Fig. 6.13b and Fig. 6.14b). However this trend stays within the uncertainties. The DCM method using γ-γ coincidence data was also employed to determine the lifetime of the 4_1^+ state (see Fig. 6.15). The lifetime result of $\tau = 41(7)$ ps from the coincidence data is compatible within the error with the value of $tau = 46(4)$ ps obtained from DDCM analysis applied on singles data. The lifetime of the 8_1^+ state was determined by evaluating the $Q_j(x)$ feeding contribution from the $10_1^+ \longrightarrow 8_1^+$ transition (See Fig. 6.16). Only an effective lifetime of $\tau = 1.31^{+14}_{-13}$ was obtained for the 10_1^+ state using the sum method since the 12_1^+ state was not observed.

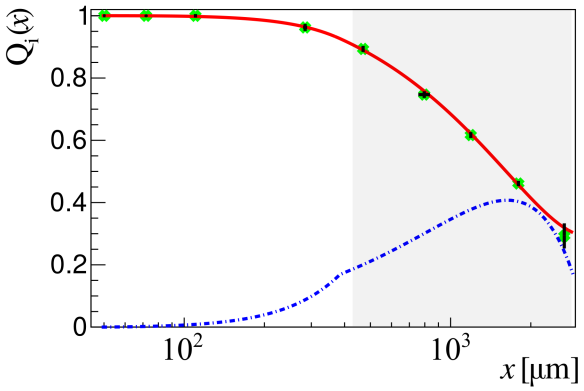

(A)

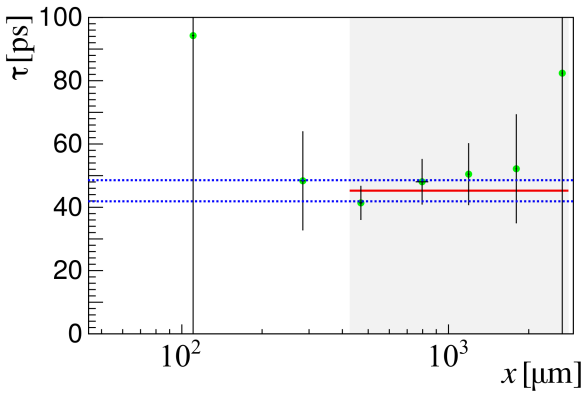

(B)

FIGURE 6.13: (A) Decay curve (solid) fitted using the function *piecewise1* and its derivative (dotted) for the 4_1^+ state in ^{102}Zr. (B) Corresponding lifetimes obtained for individual distances. The solid line indicates the mean lifetime value, while the dotted lines correspond to the 1σ uncertainty.

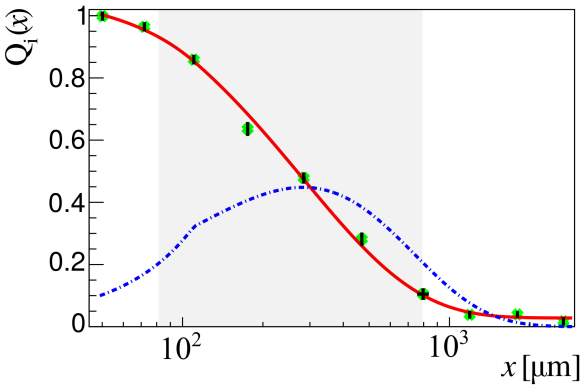

(A)

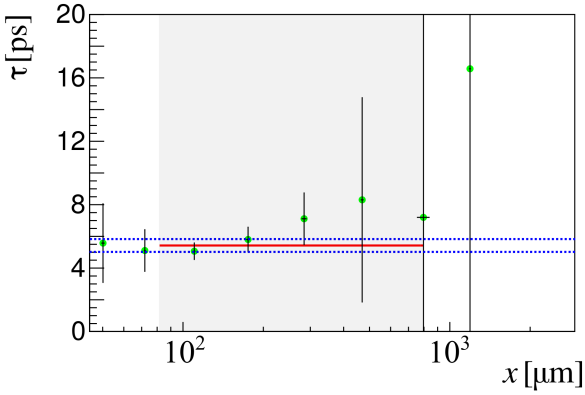

(B)

FIGURE 6.14: (A) Decay curve (solid) fitted using the function *piecewise2* and its derivative (dotted) for the 6_1^+ state in ^{102}Zr. (B) Corresponding lifetimes obtained for individual distances. The solid line indicates the mean lifetime value, while the dotted lines correspond to the 1σ uncertainty.

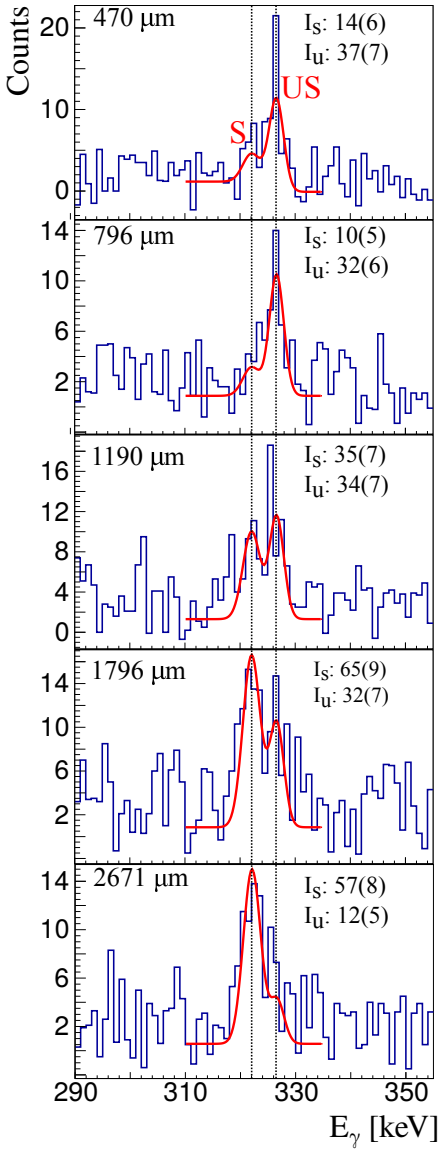

(A)

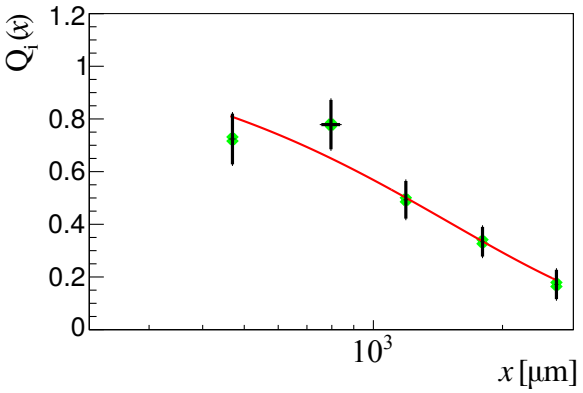

(B)

FIGURE 6.15: (A) Shifted and unshifted peaks for the 326 keV transition deexciting the 4_1^+ state of ^{102}Zr, obtained from $\gamma - \gamma$ coincidence data after gating on the shifted component of the 6_1^+ state. (B) Corresponding decay curve (fitted using the function *expo*) used to calculate the lifetime via Eq. 5.6. I_s and I_u represent shifted and unshifted area, respectively.

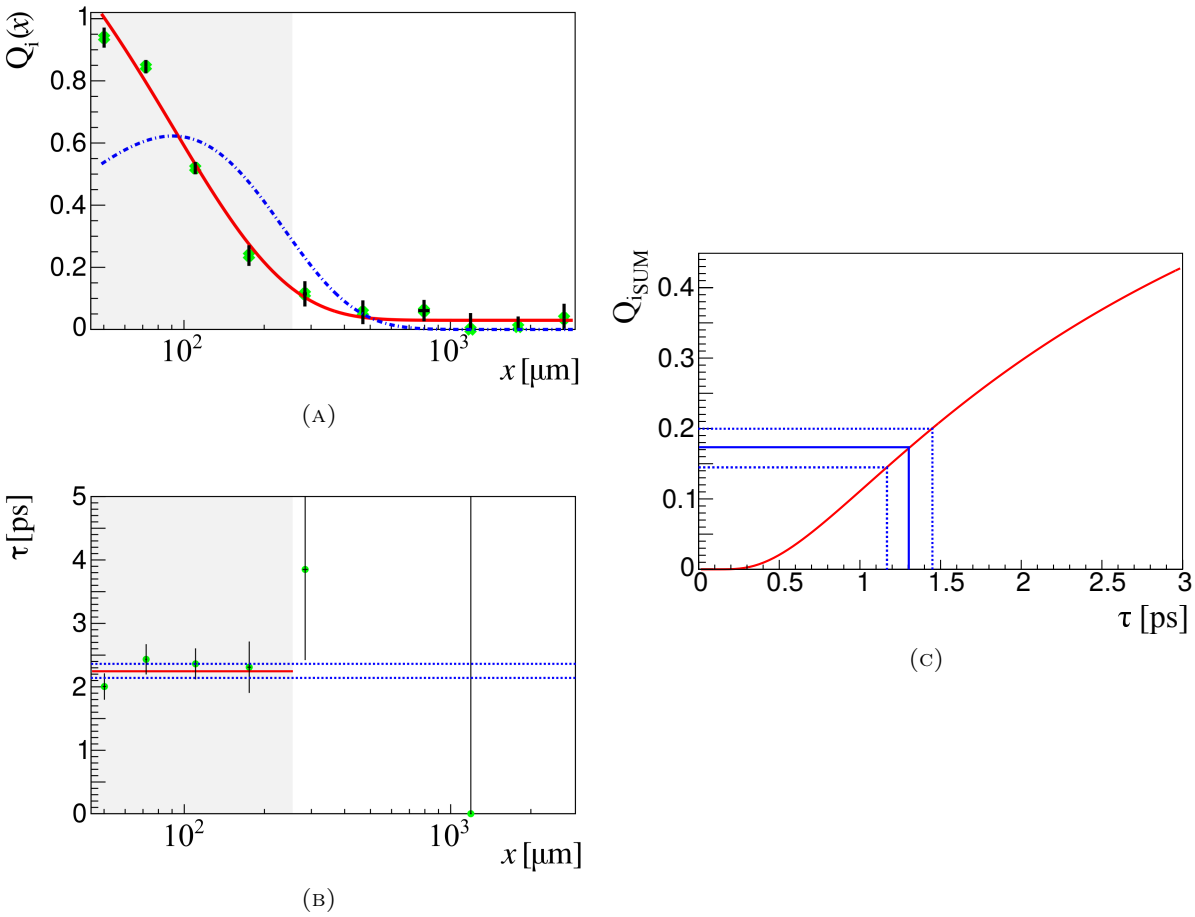

(A)

(B)

(C)

FIGURE 6.16: (A) Decay curve (solid) fitted using the function *expo* and its derivative (dotted) for the 8_1^+ state in ^{102}Zr. (B) Corresponding lifetimes obtained for individual distances. The solid line indicates the mean lifetime value, while the dotted lines correspond to the 1σ uncertainty. (C) Effective lifetime for the 10_1^+ state in ^{102}Zr obtained using the sum method.

State	Transition [keV]	DDCM	Sum method	γ-γ DCM
4_1^+	326	46(4)	-	41(7)
6_1^+	486	5.4(4)	-	-
8_1^+	630	2.24(12)	-	-
10_1^+	756	-	$^*1.31^{+14}_{-13}$	-

TABLE 6.3: Lifetimes in ^{102}Zr determined using the different methods discussed in the text. All the lifetimes are in ps. The lifetime of the 10_1^+ state has asymmetric errors. The values marked with a * are effective lifetimes only.

6.4 ^{104}Zr

^{104}Zr is the weakest channel of all the Zr isotopes where a lifetime analysis could be performed in the present experiment. The lifetimes of the 4_1^+ and 6_1^+ states were determined using DDCM, whereas the lifetime of the 8_1^+ state was obtained using the sum method. The lifetime analysis of the 4_1^+ state is shown in Fig. 6.17. The lifetimes calculated at individual distances increase strongly as a function of the plunger distance as seen in Fig. 6.17b (but mostly outside the region of sensitivity). This kind of trend suggests that either the state of interest is contaminated or the feeding is overestimated. Therefore the lifetime calculated for the 4_1^+ state is only an upper limit.

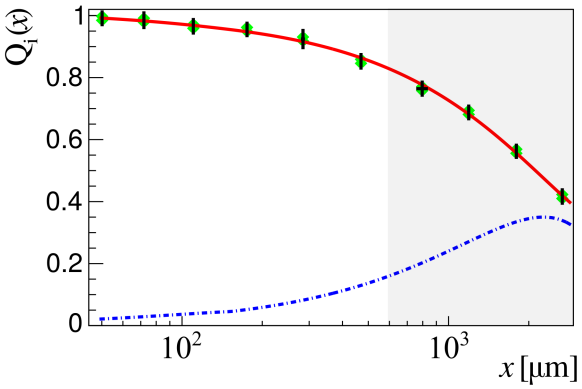

(A)

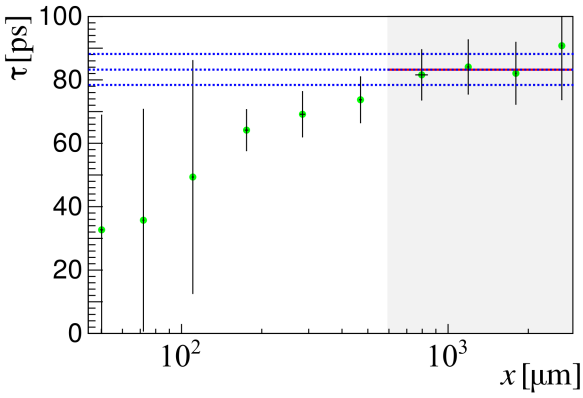

(B)

FIGURE 6.17: (A) Decay curve (solid) fitted using the function *piecewise1* and its derivative (dotted) for the 4_1^+ state in ^{104}Zr. (B) Corresponding lifetimes obtained for individual distances. The solid line indicates the mean lifetime value, while the dotted lines correspond to the 1σ uncertainty.

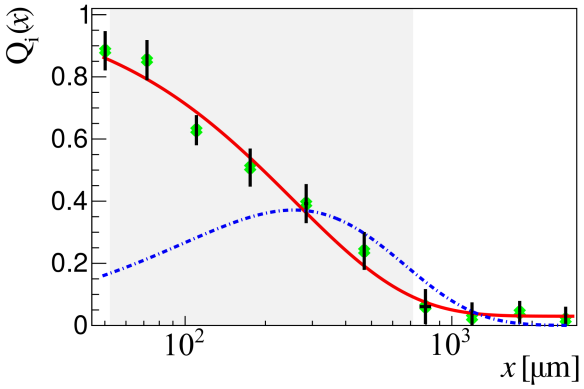

(A)

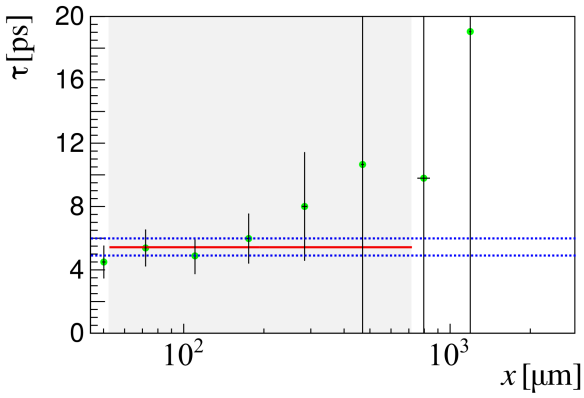

(B)

FIGURE 6.18: (A) Decay curve (solid) fitted using the function *piecewise2* and its derivative (dotted) for the 6_1^+ state in ^{104}Zr. (B) Corresponding lifetimes obtained for individual distances. The solid line indicates the mean lifetime value, while the dotted lines correspond to the 1σ uncertainty.

The lifetime of the 6_1^+ state does not evolve significantly as a function of the plunger distance as seen in Fig. 6.18. The slight increase for three distances (from 175 μm to 470 μm) could also be due to statistical fluctuations in the spectrum of ^{104}Zr. The lifetime of the 8_1^+ state is obtained using the sum method as seen in Fig 6.19. Due to the non linearity of the function defining $Q_{i_{SUM}}$, the extrapolation of $Q_{i_{SUM}}^{-1\sigma}$ and $Q_{i_{SUM}}^{+1\sigma}$ on the τ axis produces asymmetric errors.

Since the $10^+_1 \longrightarrow 8^+_1$ transition was not observed in this case, the lifetime of the 8^+_1 state is only an effective value.

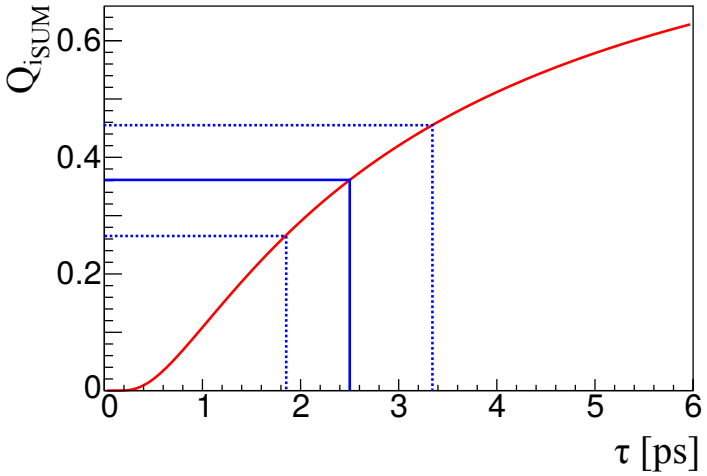

FIGURE 6.19: Effective lifetime obtained for the 8^+_1 state in ^{104}Zr using the sum method.

State	Transition [keV]	DDCM	Sum method
4^+_1	312	*83(5)	-
6^+_1	474	5.5(5)	-
8^+_1	624	-	$*2.5^{+8}_{-6}$

TABLE 6.4: Lifetimes in ^{104}Zr determined using the different methods discussed in the text. All the lifetimes are in ps. The lifetime of the 8^+_1 state has asymmetric errors. The values marked with a * are effective lifetimes only.

6.5 ^{100}Mo

The lifetimes of the 4_1^+ and 6_1^+ states in ^{100}Mo are determined using DDCM as seen in Figs. 6.20 and 6.21 whereas the lifetime of the 8_1^+ state was obtained using the sum method as seen in Fig 6.22. There is an increasing trend in the lifetime values as a function of the plunger distance for the 4_1^+ state (see Fig. 6.20b) which could be due to overestimation of the feeding transition. The spectrum (see appendix A) in the vicinity of the 711 keV peak of the $6_1^+ \longrightarrow 4_1^+$ transition is affected by contaminant transitions $4_2^+ \longrightarrow 2_1^+$ at 707 keV, and $2_4^+ \longrightarrow 2_1^+$ at 702.7 keV. Apart from influencing the $Q_j(x)$, these contaminants also influence the total intensity of the feeding transition required for the calculation of α_j. The aforementioned contamination could also affect the lifetime of the 6_1^+ state. In addition, the $2_3^+ \longrightarrow 0_1^+$ transition at energy 768.77 keV contaminates the shifted peak (at 768.9 keV) of the feeding transition of the 6_1^+ state.

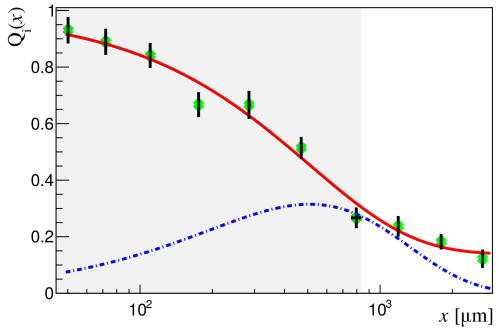

(A)

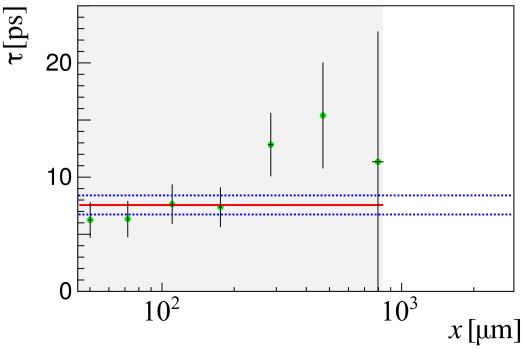

(B)

FIGURE 6.20: (A) Decay curve (solid) fitted using the function *piecewise2* and its derivative (dotted) for the 4_1^+ state in ^{100}Mo. (B) Corresponding lifetimes obtained for individual distances. The solid line indicates the mean lifetime value, while the dotted lines correspond to the 1σ uncertainty.

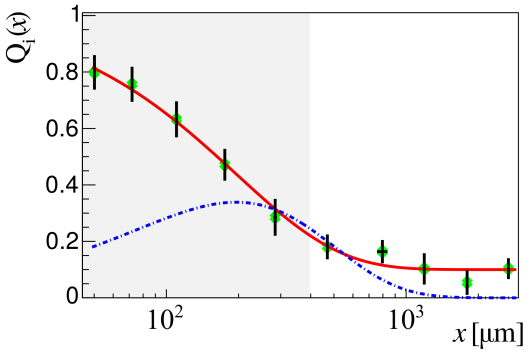

(A)

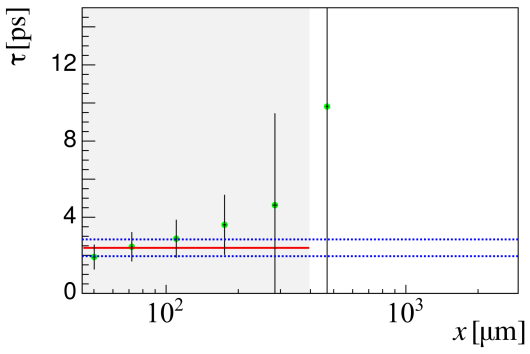

(B)

FIGURE 6.21: (A) Decay curve (solid) fitted using the function *piecewise2* and its derivative (dotted) for the 6_1^+ state in ^{100}Mo. (B) Corresponding lifetimes obtained for individual distances. The solid line indicates the mean lifetime value, while the dotted lines correspond to the 1σ uncertainty.

In the case of the 4_1^+ state, five out of six lifetime values in the sensitivity range still lie within the 1σ uncertainty (see Fig. 6.20b), Therefore, the mean lifetime value of $\tau = 7.6(8)$ ps can be considered as an intrinsic lifetime. The lifetime determined for the 6_1^+ state is also considered as an intrinsic lifetime despite the slight increasing trend of the individual lifetimes as a function of

the plunger distance (see Fig. 6.21b). Only an effective lifetime was obtained for the 8_1^+ state since the 10_1^+ state was not observed.

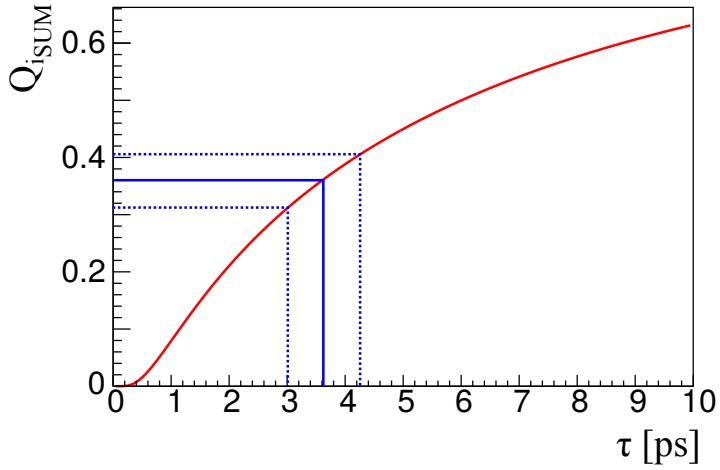

FIGURE 6.22: Effective lifetime obtained for the 8_1^+ state in ^{100}Mo using the sum method.

State	Transition [keV]	DDCM	Sum method
4_1^+	600	7.6(8)	-
6_1^+	711	2.4(4)	-
8_1^+	780	-	$^*3.6^{+6}_{-5}$

TABLE 6.5: Lifetimes in ^{100}Mo determined using the different methods discussed in the text. All the lifetimes are in ps. The lifetime of the 8_1^+ state has asymmetric errors. The values marked with a * are effective lifetimes only.

6.6 ^{102}Mo

The lifetimes of the 4_1^+ and 6_1^+ states in ^{102}Mo were determined using DDCM as shown in Fig. 6.24 and 6.25, respectively and that of the 8_1^+ state was obtained using the sum method (see Fig. 6.26). The lifetimes of the 4_1^+ state of ^{102}Mo do not behave smoothly as a function of the plunger distance as seen in Fig. 6.24b. This behavior is most likely due to the side feeding from the $5^- \longrightarrow 4_1^+$ transition. The energy peak corresponding to this transition could be observed in coincidence with the $4_1^+ \longrightarrow 2_1^+$ transition, however, due to the low level of statistics its lifetime could not be determined. The lifetime of the 5^- state is also not known in the literature and therefore the corresponding $Q_j(x)$ cannot be estimated and properly accounted for when estimating the lifetime of the 4_1^+ state. The $\gamma - \gamma$ coincidence data did not have sufficient statistics to obtain the lifetime of the 4_1^+. However, there was sufficient statistics in the sum spectrum for the relevant distances to measure its lifetime using sum method in γ-γ coincidence. Relevant distances are the ones that lie in the sensitivity range of the decay curve. As per Fig 6.24a, those distances were from 470 μm to 2671 μm (highlighted in grey area) and their sum spectrum using $\gamma - \gamma$ coincidence data is shown in Fig. 6.23a. The lifetime obtained with both methods are summarized in table 6.6 and are in good agreement.

The decay curve of the 6_1^+ state was particularly challenging to fit, mostly due to a strange structure for distances above 796 μm. This may be due to the presence of a contamination ($2_4^+ \longrightarrow 0_1^+$ at 446.2 keV) lying close to the $6_1^+ \longrightarrow 4_1^+$ transition at 447 keV, and perhaps the structure at the end of the decay curve (in Fig. 6.25a) reflects its lifetime. This decay curve could still be analyzed because the points in the sensitivity range are well fitted. Even though the lifetime plotted as a function of the plunger distance does not evolve with the distance, the possible side feeding from the 5^- to the 4_1^+ state could only result in a effective lifetime of $\tau = 6.9(3)$ ps (see Fig. 6.25b). From the decay curve of the 8_1^+ state shown in Fig. 6.26 an effective lifetime of $\tau = 3.65^{+31}_{-28}$ could be obtained.

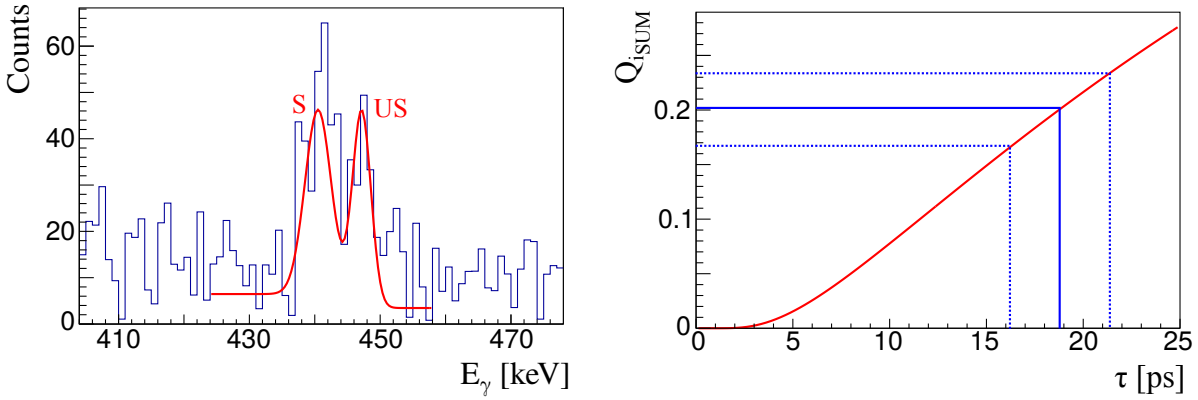

(A) (B)

FIGURE 6.23: (A) Shifted and unshifted peaks for the sum of five distances (from 470 μm to 796 μm) using $\gamma - \gamma$ coincidence data in ^{102}Mo after gating on the shifted component of the 6_1^+ state. I_s and I_u represent shifted and unshifted area, respectively. (B) The lifetime measured using sum-method for the 4_1^+ state using $\gamma - \gamma$ coincidence data.

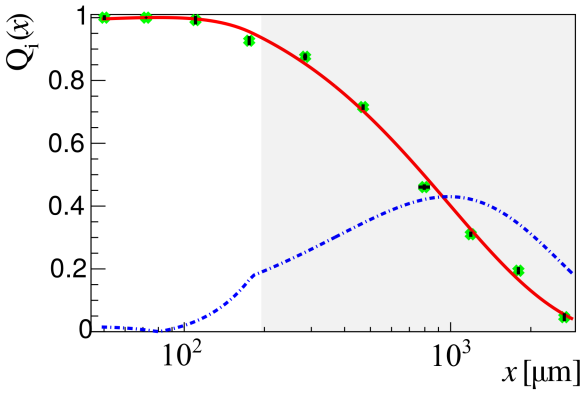

(A)

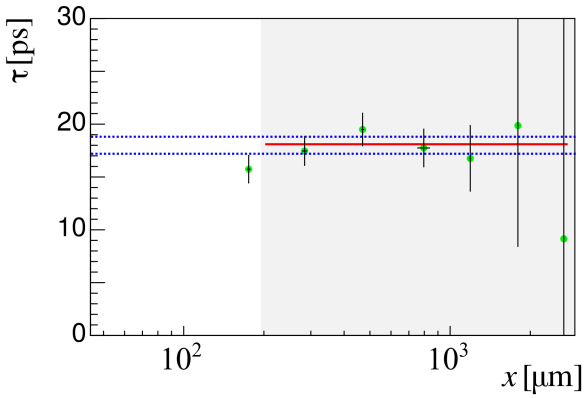

(B)

FIGURE 6.24: (A) Decay curve (solid) fitted using the function *piecewise2* and its derivative (dotted) for the 4_1^+ state in ^{102}Mo. (B) Corresponding lifetimes obtained for individual distances. The solid line indicates the mean lifetime value, while the dotted lines correspond to the 1σ uncertainty.

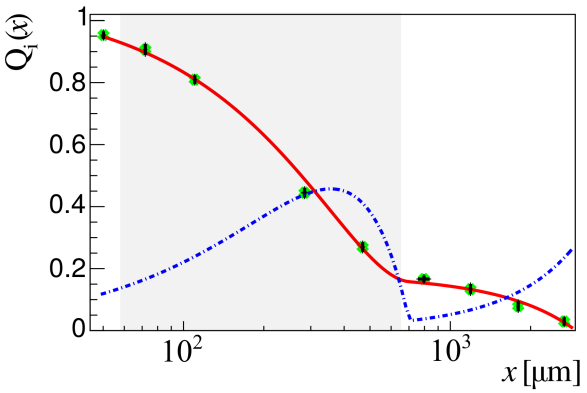

(A)

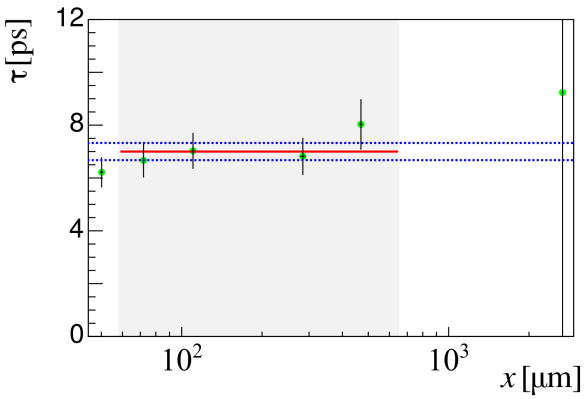

(B)

FIGURE 6.25: (A) Decay curve (solid) fitted using the function *piecewise1* and its derivative (dotted) for the 6_1^+ state in ^{102}Mo. (B) Corresponding lifetimes obtained for individual distances. The solid line indicates the mean lifetime value, while the dotted lines correspond to the 1σ uncertainty.

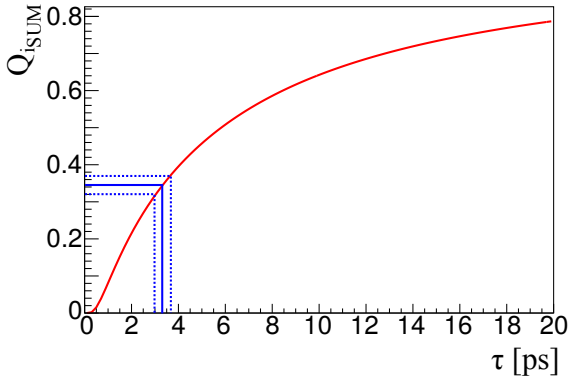

FIGURE 6.26: Effective lifetime measured in ^{102}Mo for the 8_1^+ state using the sum method.

State	Transition [keV]	DDCM	Sum method	γ-γ (Sum method)
4_1^+	447	18.0(8)	-	18.9(25)
6_1^+	584	*6.9(3)	-	
8_1^+	690	-	$^*3.65^{+31}_{-28}$	

TABLE 6.6: Lifetimes in ^{102}Mo determined using the different methods discussed in the text. All the lifetimes are in ps. The lifetime of the 8_1^+ state has asymmetric errors. The values marked with a * are effective lifetimes only.

6.7 ^{106}Mo

The lifetimes in ^{106}Mo were determined for the 4_1^+, 6_1^+ and 8_1^+ states using DDCM as shown in Figs. 6.27, 6.28 and 6.29, respectively. Only effective lifetimes could be determined for the 8_1^+ state, as the 10_1^+ state was not observed in the present data. The variations of the lifetimes as a function of the plunger distance for the 4_1^+ and 6_1^+ states, presented in Figs. 6.27b and 6.28b, respectively, do not seem to follow a specific trend. Therefore, mean values of $\tau(4_1^+) = 48.6(15)$ ps and $\tau(6_1^+) = 5.0(2)$ ps could be extracted and are considered as intrinsic lifetimes.

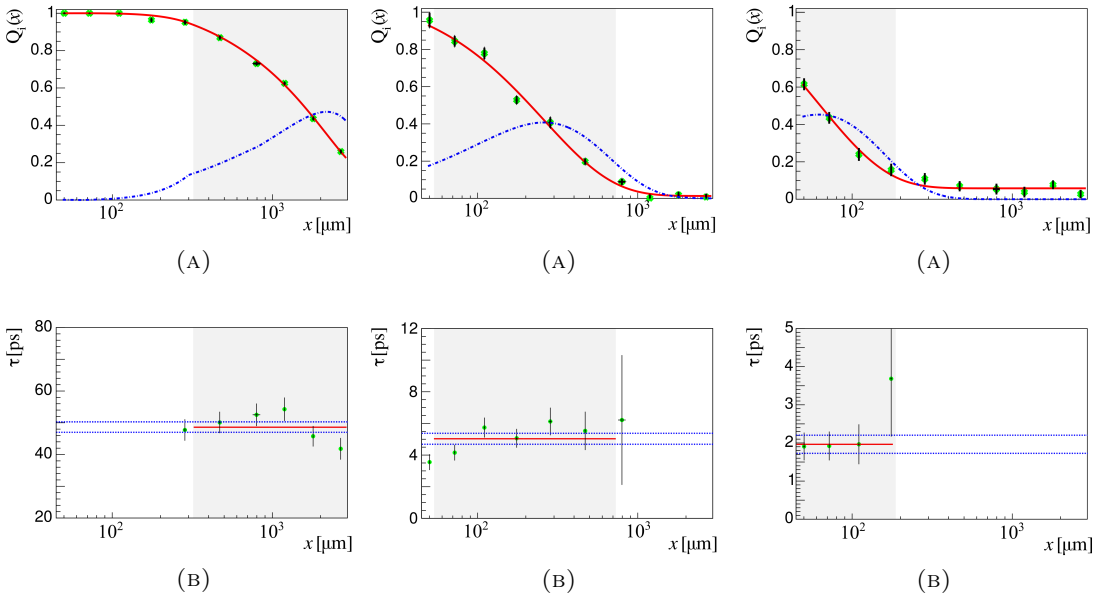

FIGURE 6.27: (A) Decay curve (solid) fitted using the function *piecewise1* and its derivative (dotted) for the 4_1^+ state in ^{106}Mo. (B) Corresponding lifetimes obtained for individual distances. The solid line indicates the mean lifetime value, while the dotted lines correspond to the 1σ uncertainty.

FIGURE 6.28: (A) Decay curve (solid) fitted using the function *expo* and its derivative (dotted) for the 6_1^+ state in ^{106}Mo. (B) Corresponding lifetimes obtained for individual distances. The solid line indicates the mean lifetime value, while the dotted lines correspond to the 1σ uncertainty.

FIGURE 6.29: (A) Decay curve (solid) fitted using the function *expo* and its derivative (dotted) for the 8_1^+ state in ^{106}Mo. (B) Corresponding lifetimes obtained for individual distances. The solid line indicates the mean lifetime value, while the dotted lines correspond to the 1σ uncertainty.

Transition	Transition energy [keV]	DDCM
$4_1^+ \longrightarrow 2_1^+$	350	48.6(15)
$6_1^+ \longrightarrow 4_1^+$	511	5.0(2)
$8_1^+ \longrightarrow 6_1^+$	655	*1.96(22)

TABLE 6.7: Lifetimes in ^{106}Mo determined using the different methods discussed in the text. All the lifetimes are in ps. The lifetime of the 8_1^+ state has asymmetric errors. The values marked with a * are effective lifetimes only.

6.8 ^{108}Mo

The lifetimes in ^{108}Mo could only be determined for the 4_1^+ and 6_1^+ states as shown in Figs. 6.30 and 6.31, respectively. There is no systematic (increasing or decreasing) trend in the lifetime values as a function of the plunger distance in either the decay of the 4_1^+ (Fig. 6.30b state or of the 6_1^+ (Fig. 6.31b) state. However, because there is no feeding subtracted from the 6_1^+ state, the lifetime of $\tau = 7.5(4)$ ps is still considered as an effective value.

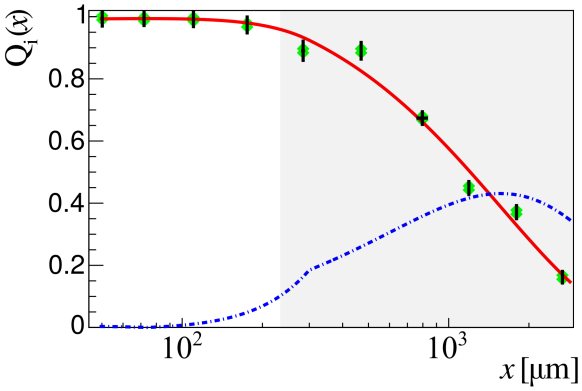

(A)

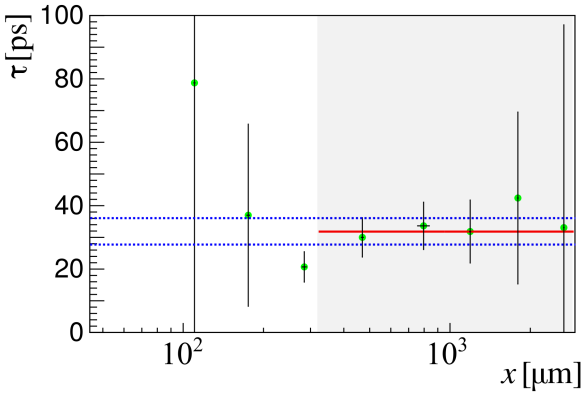

(B)

FIGURE 6.30: (A) Decay curve (solid) fitted using the function *piecewise2* and its derivative (dotted) for the 4_1^+ state in ^{108}Mo. (B) Corresponding lifetimes obtained for individual distances. The The solid line indicates the mean lifetime value, while the dotted lines correspond to the 1σ uncertainty.

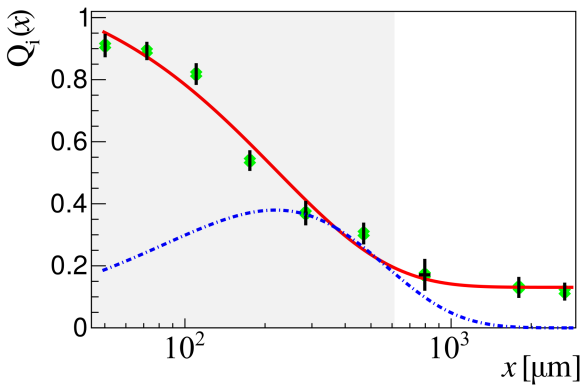

(A)

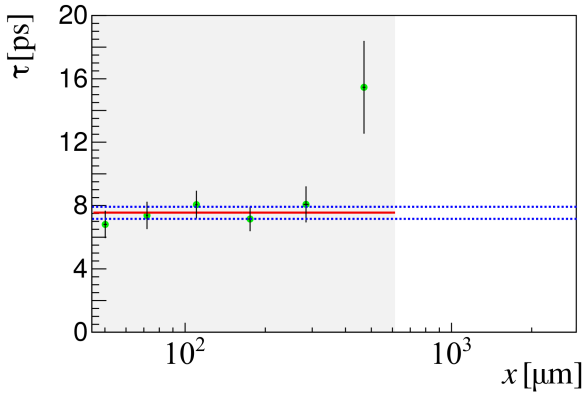

(B)

FIGURE 6.31: (A) Decay curve (solid) fitted using the function *expo* and its derivative (dotted) for the 6_1^+ state in ^{108}Mo. (B) Corresponding lifetimes obtained for individual distances. The The solid line indicates the mean lifetime value, while the dotted lines correspond to the 1σ uncertainty.

Transition	Transition energy [keV]	DDCM
$4_1^+ \longrightarrow 2_1^+$	371	31.8(42)
$6_1^+ \longrightarrow 4_1^+$	527	*7.5(4)

TABLE 6.8: Lifetimes in ^{108}Mo determined using the different methods discussed in the text. All the lifetimes are in ps. The lifetime of the 6_1^+ state has asymmetric errors. The values marked with a * are effective lifetimes only.

6.9 ^{106}Ru

The lifetimes in ^{106}Ru could only be determined for the 4_1^+ and 6_1^+ states as shown in Figs. 6.32 and 6.33, respectively. There is no systematic increase or decrease in the lifetime as a function of the plunger distance in either the decay of 4_1^+ (see Fig. 6.32b) or of 6_1^+ (see Fig. 6.33b) states and a mean value of $\tau(4_1^+) = 13.8(5)$ ps and $\tau(4_1^+) = 3.7(2)$ ps is obtained . Only an effective lifetime could be determined for the 8_1^+ state, since there was no feeding observed for the 10_1^+ state. The effective lifetime of the 8_1^+ state was measured using DDCM, sum method and DCM method. There is an agreement between the DCM and the DDCM method, however the results from these methods do not agree with the sum method. The result from the DDCM method is used to calculate B(E2) value for the 8_1^+ state.

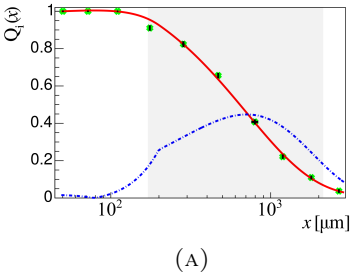

(A)

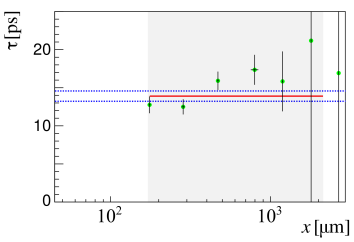

(B)

FIGURE 6.32: (A) Decay curve (solid) fitted using the function *piecewise2* and its derivative (dotted) for the 4_1^+ state in ^{106}Ru. (B) Corresponding lifetimes obtained for individual distances. The The solid line indicates the mean lifetime value, while the dotted lines correspond to the 1σ uncertainty.

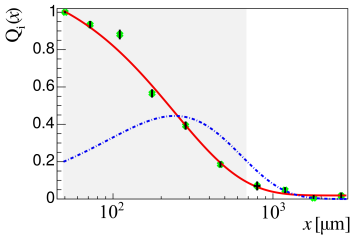

(A)

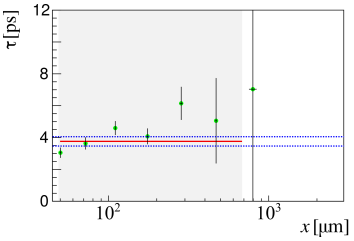

(B)

FIGURE 6.33: (A) Decay curve (solid) fitted using the function *piecewise2* and its derivative (dotted) for the 6_1^+ state in ^{106}Ru. (B) Corresponding lifetimes obtained for individual distances. The The solid line indicates the mean lifetime value, while the dotted lines correspond to the 1σ uncertainty.

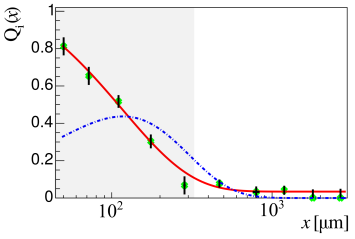

(A)

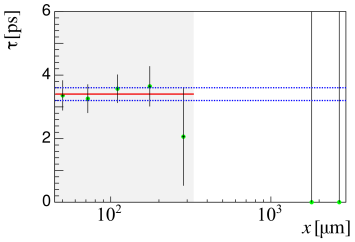

(B)

FIGURE 6.34: (A) Decay curve (solid) fitted using the function *expo* and its derivative (dotted) for the 8_1^+ state in ^{106}Ru. (B) Corresponding lifetimes obtained for individual distances. The The solid line indicates the mean lifetime value, while the dotted lines correspond to the 1σ uncertainty.

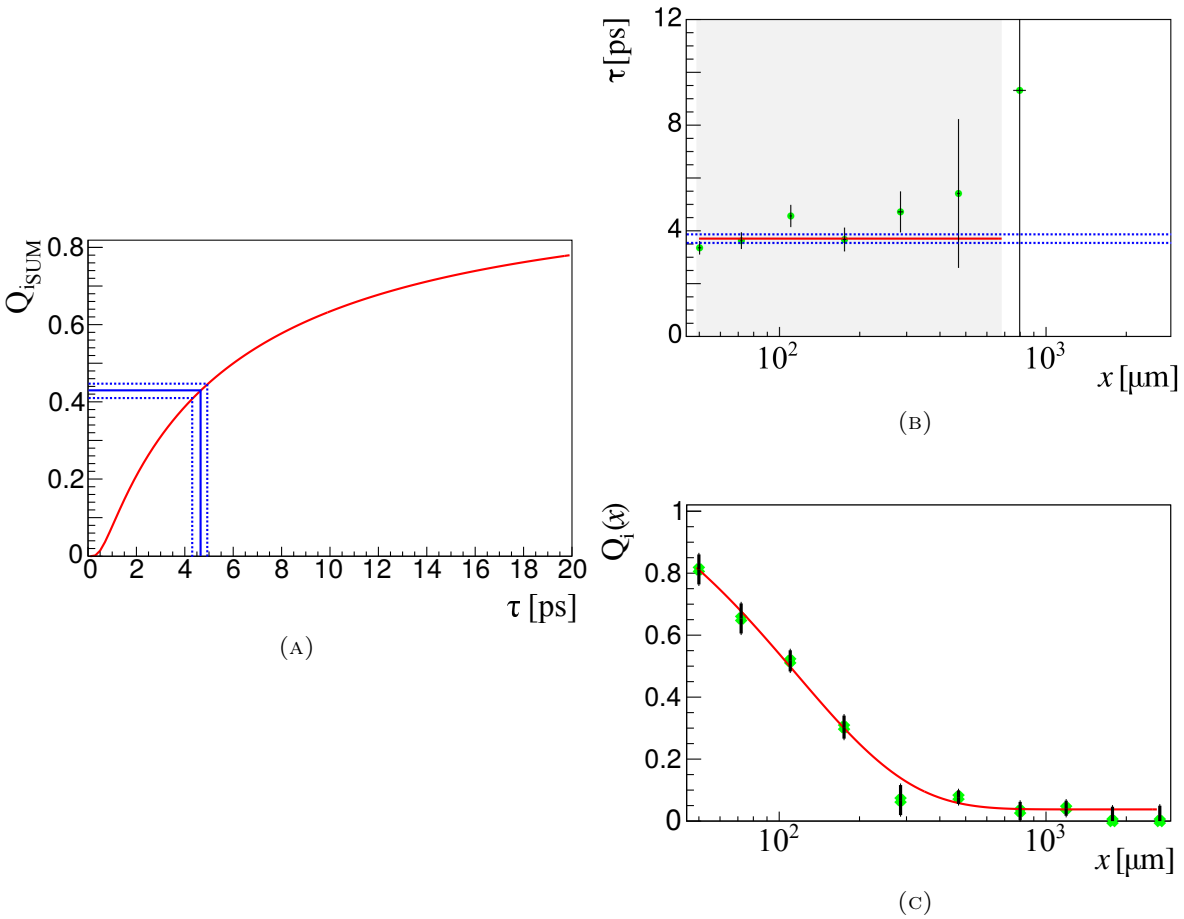

(A) (B) (C)

FIGURE 6.35: (A) Effective lifetime measured using sum-method in ^{106}Ru for the $8_1^+ \longrightarrow 6_1^+$ transition. (B) Lifetimes obtained for individual distances in 6_1^+ state using DDCM, where Q_j (8_1^+) is calculated using sum-method. The The solid line indicates the mean lifetime value while the dotted lines correspond to the 1σ uncertainty. (C) Decay curve (fitted using the function *expo*) for the 8_1^+ state in which the lifetime is calculated using Eq. 5.6.

Transition	Transition energy [keV]	DDCM	Sum Method	DCM
4_1^+	445	13.8(5)	-	-
6_1^+	581	3.7(2)	-	-
8_1^+	678	*3.4(2)	$*4.64^{28}_{27}$	*3.1(4)

TABLE 6.9: Lifetimes in ^{106}Ru determined using the different methods discussed in the text. All the lifetimes are in ps. The lifetime of the 8_1^+ state has asymmetric errors. The values marked with a * are effective lifetimes only.

6.10 ^{108}Ru

The lifetimes in ^{108}Ru was measured for the 4_1^+ state using DDCM method from both singles (see Fig. 6.36) and γ-γ coincidence data (see Fig. 6.39). Both results i.e, $\tau = 24.2(10)$ ps from the singles and $\tau = 27.9$ (52) ps from γ-γ coincidence are in agreement within the errors. The lifetime of the 6_1^+ state as $\tau = 4.5(3)$ ps could only be measured using DDCM as seen in Fig. 6.37. Due to the lack of statistics, 10_1^+ state could not be observed, hence only an effective lifetime of $\tau = 2.15(14)$ ps was obtained for the 8_1^+ state using DDCM (see Fig. 6.38).

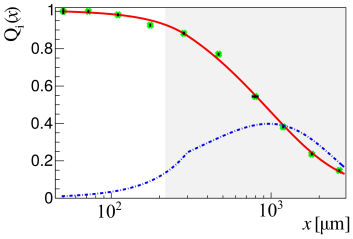

(A)

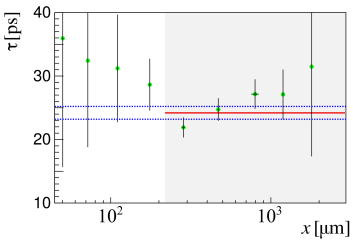

(B)

FIGURE 6.36: (A) Decay curve (solid) fitted using the function *piecewise2* and its derivative (dotted) for the 4_1^+ state in ^{108}Ru. (B) Corresponding lifetimes obtained for individual distances. The The solid line indicates the mean lifetime value, while the dotted lines correspond to the 1σ uncertainty.

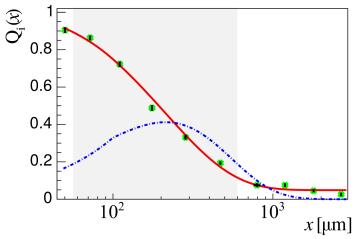

(A)

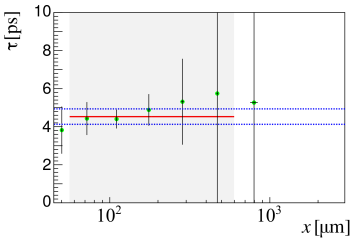

(B)

FIGURE 6.37: (A) Decay curve (solid) fitted using the function *piecewise2* and its derivative (dotted) for the 6_1^+ state in ^{108}Ru. (B) Corresponding lifetimes obtained for individual distances. The The solid line indicates the mean lifetime value, while the dotted lines correspond to the 1σ uncertainty.

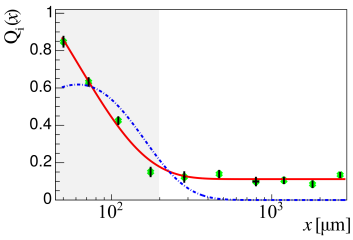

(A)

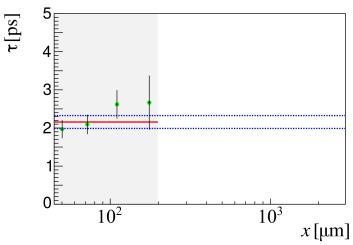

(B)

FIGURE 6.38: (A) Decay curve (solid) fitted using the function *expo* and its derivative (dotted) for the 8_1^+ state in ^{108}Ru. (B) Corresponding lifetimes obtained for individual distances. The The solid line indicates the mean lifetime value, while the dotted lines correspond to the 1σ uncertainty. The trend indicates towards unobserved feeding.

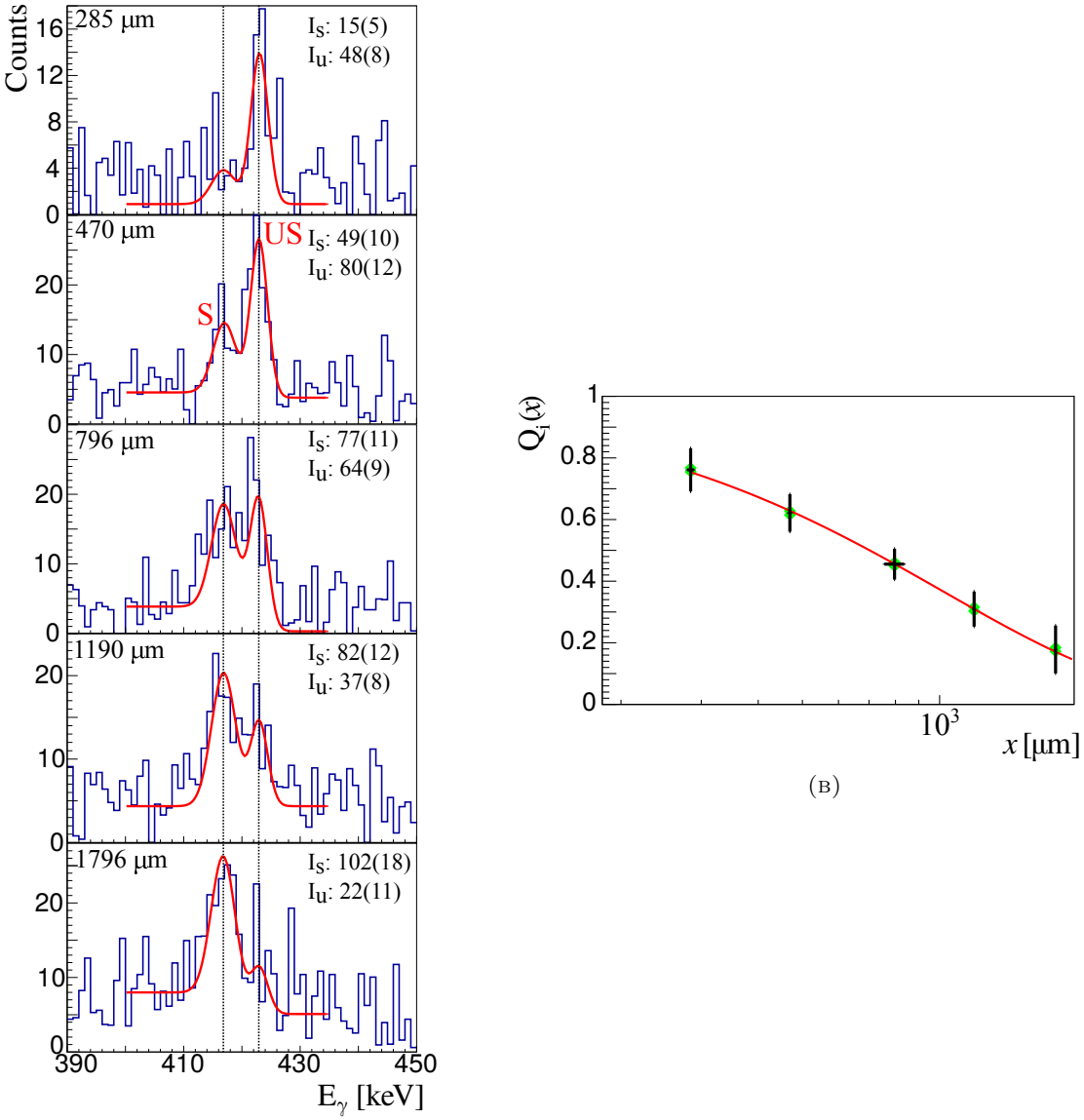

(A) (B)

FIGURE 6.39: (A) Shifted and unshifted peaks for the transitions deexciting the 4_1^+ state (423 keV) of ^{108}Ru, obtained from $\gamma-\gamma$ coincidence data (after gating on the shifted component of the 6_1^+ state), I_s and I_u represent shifted and unshifted area, respectively. (B) Corresponding decay curve (fitted using the function *expo*) in which the lifetime is calculated using Eq. 5.6.

Transition	Transition [keV]	DDCM	γ-γ DCM
$4_1^+ \longrightarrow 2_1^+$	423	24.2(10)	27.9(52)
$6_1^+ \longrightarrow 4_1^+$	575	4.5(3)	-
$8_1^+ \longrightarrow 6_1^+$	701	*2.15(14)	-

TABLE 6.10: Lifetimes in ^{108}Ru determined using the different methods discussed in the text. All the lifetimes are in ps. The lifetime of the 8_1^+ state has asymmetric errors. The values marked with a * are effective lifetimes only.

6.11 ^{110}Ru

The lifetimes in ^{110}Ru were measured for the 4_1^+ (Fig. 6.40) and the 6_1^+ (Fig. 6.41) state using DDCM. The lifetime of $\tau(4_1^+) = 22.0(10)$ ps and $\tau(4_1^+) = 3.1(3)$ ps was obtained. Due to the lack of statistics, 10_1^+ state could not be observed, hence only an effective lifetime of $\tau = 4.1(2)$ ps was obtained for the 8_1^+ state using DDCM (see Fig. 6.42).

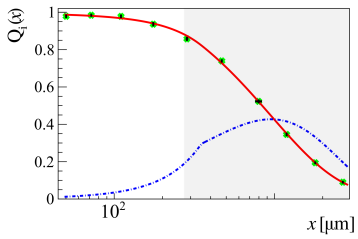

(A)

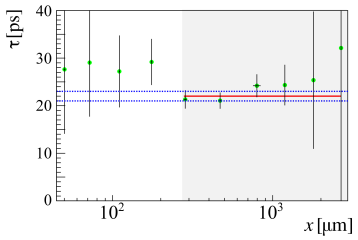

(B)

FIGURE 6.40: (A) Decay curve (solid) fitted using the function *piecewise2* and its derivative (dotted) for the 4_1^+ state in ^{110}Ru. (B) Corresponding lifetimes obtained for individual distances. The The solid line indicates the mean lifetime value, while the dotted lines correspond to the 1σ uncertainty.

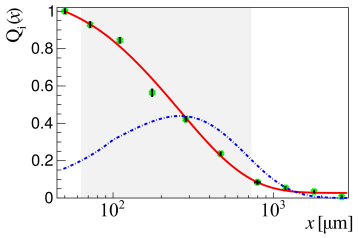

(A)

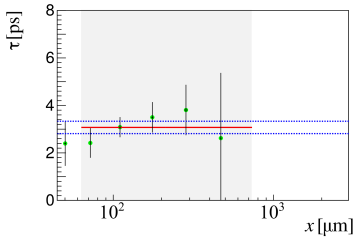

(B)

FIGURE 6.41: (A) Decay curve (solid) fitted using the function *piecewise2* and its derivative (dotted) for the 6_1^+ state in ^{110}Ru. (B) Corresponding lifetimes obtained for individual distances. The The solid line indicates the mean lifetime value, while the dotted lines correspond to the 1σ uncertainty.

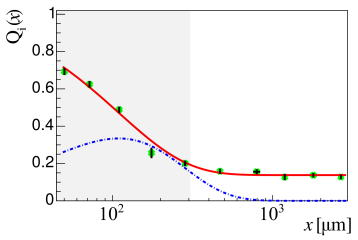

(A)

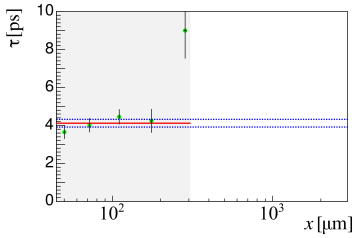

(B)

FIGURE 6.42: (A) Decay curve (solid) fitted using the function *expo* and its derivative (dotted) for the 8_1^+ state in ^{110}Ru. (B) Corresponding lifetimes obtained for individual distances. The The solid line indicates the mean lifetime value, while the dotted lines correspond to the 1σ uncertainty.

Transition	Transition energy [keV]	DDCM
$4_1^+ \longrightarrow 2_1^+$	422	22.0(10)
$6_1^+ \longrightarrow 4_1^+$	576	3.1(3)
$8_1^+ \longrightarrow 6_1^+$	705	*4.1(2)

TABLE 6.11: Lifetimes in ^{110}Ru determined using the different methods discussed in the text. All the lifetimes are in ps. The lifetime of the 8_1^+ state has asymmetric errors. The values marked with a * are effective lifetimes only.

6.12 ^{112}Ru

The lifetimes in ^{112}Ru were determined for the 4_1^+ (Fig. 6.43) and the 6_1^+ (Fig. 6.44) state using DDCM. The lifetime of $\tau(4_1^+) = 26.4(22)$ ps and $\tau(6_1^+) = 2.9(5)$ ps was obtained. Due to the lack of statistics, 10_1^+ state could not be observed, hence only an effective lifetime of $\tau = 4.1(2)$ ps was obtained for the 8_1^+ state using DDCM (see Fig. 6.45).

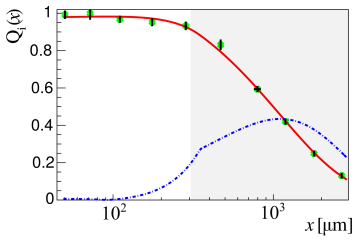

(A)

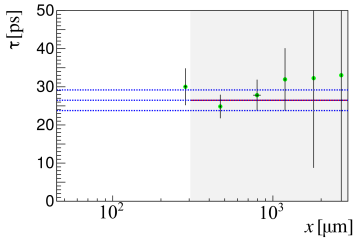

(B)

FIGURE 6.43: (A) Decay curve (solid) fitted using the function *piecewise2* and its derivative (dotted) for the 4_1^+ state in ^{112}Ru. (B) Corresponding lifetimes obtained for individual distances. The The solid line indicates the mean lifetime value, while the dotted lines correspond to the 1σ uncertainty.

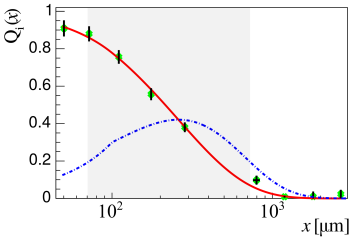

(A)

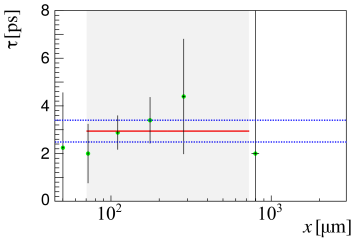

(B)

FIGURE 6.44: (A) Decay curve (solid) fitted using the function *piecewise2* and its derivative (dotted) for the 6_1^+ state in ^{112}Ru. (B) Corresponding lifetimes obtained for individual distances. The The solid line indicates the mean lifetime value, while the dotted lines correspond to the 1σ uncertainty.

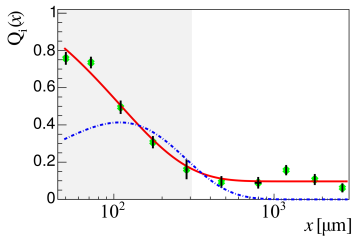

(A)

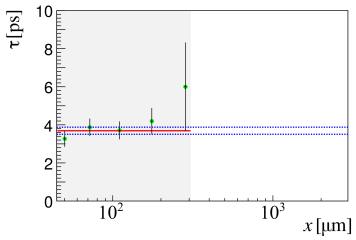

(B)

FIGURE 6.45: (A) Decay curve (solid) fitted using the function *expo* and its derivative (dotted) for the 8_1^+ state in ^{112}Ru. (B) Corresponding lifetimes obtained for individual distances. The The solid line indicates the mean lifetime value, while the dotted lines correspond to the 1σ uncertainty.

Transition	Transition energy [keV]	DDCM
$4_1^+ \longrightarrow 2_1^+$	408	26.4(22)
$6_1^+ \longrightarrow 4_1^+$	545	2.9(5)
$8_1^+ \longrightarrow 6_1^+$	650	*3.6(2)

TABLE 6.12: Lifetimes in ^{112}Ru determined using the different methods discussed in the text. All the lifetimes are in ps. The lifetime of the 8_1^+ state has asymmetric errors. The values marked with a * are effective lifetimes only.

6.13 Summary

In the following tables the results obtained in the current experiment for the Zr, Mo and Ru isotopes (see table 6.13, 6.14, and 6.15, respectively) are summarized as half-life values and compared to those obtained in a previous GANIL experiment using EXOGAM [Grente, 2014; Singh et al., 2018]. Almost half of our lifetime values are slightly longer than the one measured with EXOGAM in Grente, 2014. A specific reason for this behavior is difficult to understand. However, due to the better resolution of AGATA over EXOGAM, the lifetime results obtained from AGATA analysis are statistically more reliable. The rest of our lifetime agrees (within the errors) with the EXOGAM results.

Our lifetime values are also compared with the evaluated literature values from "NNDC" and from some selected more recent experiments. While in most cases our new results agree with the previous experiments, there are a few notable exceptions: In ^{98}Zr the new results differ from the one obtained with EXOGAM which is most likely due to the much better statistics in the AGATA experiment (see Fig. 3.20). Another significant reason for the discrepancy between the two results could be in the measurement of the lifetimes of the side-feeding states since the decay curve from our experiment looks rather similar to the one in Singh et al., 2018. Thanks to the better efficiency and statistics in AGATA experiment, the effective lifetimes for all the significant feeding to the 2^+ state of ^{98}Zr could be measured, unlike in Singh et al., 2018. In ^{100}Zr a large variation is observed for the lifetime of the 4_1^+ state. Our new result is confirmed by a coincidence analysis and agrees well with a recent fast timing measurement [Ansari et al., 2017].

For the Mo isotopes, the lifetime results from our experiment are compared with the one from Ralet et al., 2017, where a relativistic version of the Doppler-shift-attenuation method (DSAM) was employed. Although the results from the two experiments agree within the error, the error in the lifetime of the DSAM is too large to draw a clear conclusion about the equivalence of the two methods.

Our lifetime results agree very well with the literature ["NNDC"] for the Ru isotopic chain except for the 4_1^+ state in ^{108}Ru. In this case, our new value for ^{108}Ru is the first direct measurement since the literature value from "NNDC" is an average of the 4_1^+ states in ^{108}Ru and ^{110}Ru.

Isotope	Transition	EXP ($T_{1/2}$ [ps])	Exp (α_j)	EXOGAM ($T_{1/2}$ [ps])	Lit (NNDC) ($T_{1/2}$ [ps])	Lit* ($T_{1/2}$ [ps])
$^{98}_{40}Zr_{58}$	$2_1^+ \longrightarrow 0_1^+$	5.8(3)	-	†2.6(5)	$<$ 0.2 ns	$<$4
	$4_1^+ \longrightarrow 2_1^+$	3.2(3)	0.45(3)	†5.1(10)	28(12)	$<$10
	$3^- \longrightarrow 2_1^+$	*24.2(62)	0.11(1)	-	-	
	$2_2^+ \longrightarrow 2_1^+$	*9.0(73)	0.0010(3)	-	-	
	$4_2^+ \longrightarrow 2_1^+$	*10.3(49)	0.044(8)	-	-	
	$6_1^+ \longrightarrow 4_1^+$	1.48(14)	0.99(7)	†1.8(6)	-	
	$8_1^+ \longrightarrow 6_1^+$	*1.35(13)	0.71(5)	-	-	
$^{100}_{40}Zr_{60}$	$4_1^+ \longrightarrow 2_1^+$	28.9(16)	-	18.1(14)	37(3)	25.6(27)
	$6_1^+ \longrightarrow 4_1^+$	3.6(2)	0.88(1)	3.1(3)	4.9(11)	8.3(34)
	$8_1^+ \longrightarrow 6_1^+$	1.21(17)	0.55(1)	-	1.73(17)	1.77(12)(17)‡
	$10_1^+ \longrightarrow 8_1^+$	*1.09(7)	0.60(2)	-	0.75(9)	0.75(4)(7)‡
$^{102}_{40}Zr_{62}$	$4_1^+ \longrightarrow 2_1^+$	31.7(25)	-	32.1(34)	-	31.8(48)
	$6_1^+ \longrightarrow 4_1^+$	3.7(3)	0.79(1)	4.7(5)	-	$<$8.3
	$8_1^+ \longrightarrow 6_1^+$	1.55(8)	0.63(1)	-	1.39(21)	1.39(16)(14)‡
	$10_1^+ \longrightarrow 8_1^+$	*0.90(9)	0.45(1)	-	0.53(10)	0.53(6)(5)‡
$^{104}_{40}Zr_{64}$	$4_1^+ \longrightarrow 2_1^+$	*57.6(33)	-	-	-	
	$6_1^+ \longrightarrow 4_1^+$	3.7(5)	0.56(2)	-	-	
	$8_1^+ \longrightarrow 6_1^+$	*1.73(52)	0.65(8)	-	-	1.32(15)(14)‡

TABLE 6.13: Table summarizes the lifetime measurement results of the present experiment from Zr isotopic chain, compared with the previous measurement. Experimental lifetimes marked with a * contains only effective value. The EXOGAM values are from Grente, 2014. The Literature values marked with a † are adopted from Singh et al., 2018, the one marked with a ‡ are taken from Smith et al., 2012 and the one marked with a $\star$ are taken from Ansari et al., 2017. Lit (NNDC) are the evaluated lifetimes from "NNDC".

Isotope	Transition	Exp ($T_{1/2}$ [ps])	Exp (α_j)	EXOGAM ($T_{1/2}$ [ps])	Lit (NNDC) ($T_{1/2}$ [ps])	Lit$^{\bullet}$ ($T_{1/2}$ [ps])
$^{100}_{42}Mo_{58}$	$4^+_1 \longrightarrow 2^+_1$	5.1(5)	-	-	3.8(2)	4.8^{+17}_{-12}
	$6^+_1 \longrightarrow 4^+_1$	1.65(28)	0.75(4)	-	1.20(17)	
	$8^+_1 \longrightarrow 6^+_1$	*2.5(4)	0.78(5)	-	0.58(9)	
$^{102}_{42}Mo_{60}$	$4^+_1 \longrightarrow 2^+_1$	12.5(6)	-	9.4(10)	12.5(25)	19.2^{+72}_{-56}
	$6^+_1 \longrightarrow 4^+_1$	*4.85(24)	0.66(1)	3.4(6)		2.2(5)
	$8^+_1 \longrightarrow 6^+_1$	*2.5(2)	0.62(1)	-	1.8(3)	1.84(26)(19)‡
$^{104}_{42}Mo_{62}$	$4^+_1 \longrightarrow 2^+_1$	22.6(14)	-	18.6(9)	26.1(8)	22.0^{+92}_{-70}
	$6^+_1 \longrightarrow 4^+_1$	3.0(1)	0.74(1)	2.8(2)	4.73(15)	3.6^{+11}_{-8}
	$8^+_1 \longrightarrow 6^+_1$	1.76(19)	0.86(1)	-	2.22(11)	2.0^{+5}_{-4}
	$10^+_1 \longrightarrow 8^+_1$	*1.14(3)	0.37(1)	-	1.08(7)	0.98(9)‡
$^{106}_{42}Mo_{64}$	$4^+_1 \longrightarrow 2^+_1$	33.6(10)	-	28.0(13)	25.4(51)	21.7^{+92}_{-71}
	$6^+_1 \longrightarrow 4^+_1$	3.5(2)	0.54(1)	3.1(3)	4.2(18)	
	$8^+_1 \longrightarrow 6^+_1$	*1.36(15)	0.81(1)	-	1.77(24)	1.76(16)(18)‡
$^{108}_{42}Mo_{66}$	$4^+_1 \longrightarrow 2^+_1$	19.9(34)	-	23.3(51)		20.5^{+79}_{-64}
	$6^+_1 \longrightarrow 4^+_1$	*5.2(3)	0.96(3)	-	-	

TABLE 6.14: Table summarizes the lifetime measurement results of the present experiment from Mo isotopic chain, compared with the previous measurement. Experimental lifetimes marked with a * contains only effective value. The EXOGAM values are from Grente, 2014. The Literature values marked with a $^{\bullet}$ are adopted from Ralet et al., 2017 except the one marked with a ‡ which are taken from Smith et al., 2012. Lit (NNDC) are the evaluated lifetimes from "NNDC".

Isotope	Transition	EXP ($T_{1/2}$ [ps])	Exp (α_j)	EXOGAM ($T_{1/2}$ [ps])	Lit (NNDC) ($T_{1/2}$ [ps])
$^{106}_{44}Ru_{62}$	$4^+_1 \longrightarrow 2^+_1$	9.6(4)	-	-	-
	$6^+_1 \longrightarrow 4^+_1$	2.5(1)	0.75(1)	-	-
	$8^+_1 \longrightarrow 6^+_1$	*2.4(2)	0.67(2)	-	-
$^{108}_{44}Ru_{64}$	$4^+_1 \longrightarrow 2^+_1$	16.7(7)	-	13.6(9)	13.4(10)
	$6^+_1 \longrightarrow 4^+_1$	3.1(2)	0.78(1)	2.9(3)	-
	$8^+_1 \longrightarrow 6^+_1$	*1.49(10)	0.51(1)	-	1.68(27)(17)‡
$^{110}_{44}Ru_{66}$	$4^+_1 \longrightarrow 2^+_1$	15.2(7)	-	15.1(9)	15.4(17)
	$6^+_1 \longrightarrow 4^+_1$	2.1(2)	0.72(2)	3.2(5)	2.4(10)
	$8^+_1 \longrightarrow 6^+_1$	*2.85(13)	1.0	-	1.46(17)(15)‡
$^{112}_{44}Ru_{68}$	$4^+_1 \longrightarrow 2^+_1$	18.3(15)	-	14.6(21)	-
	$6^+_1 \longrightarrow 4^+_1$	2.0(3)	0.82(2)	-	-
	$8^+_1 \longrightarrow 6^+_1$	*2.5(2)	0.93(6)	-	1.84(28)

TABLE 6.15: Table summarizes the lifetime measurement results of the present experiment from Ru isotopic chain, compared with the previous measurement. *Contains only effective lifetimes or upper limit. The EXOGAM values are from Grente, 2014. The Literature values are adopted from "NNDC" except the one marked with a ‡ which are taken from Smith et al., 2012.

Chapter 7

Interpretation and Conclusion

We have obtained lifetimes of excited states in the isotopes $^{98-104}$Zr, $^{100-108}$Mo and $^{106-112}$Ru. These lifetimes are used to extract the B(E2) values (using Eq. 2.17) which are summarized in tables from 7.1 to 7.3 and are compared to the literature values. In addition to NNDC we have also compared our results with selected, more recent experimental B(E2) values.

Isotope	Transition	Present Experiment B(E2; ↓) [e^{2}b^2]	Literature B(E2; ↓) [e^{2}b^2]
$^{98}_{40}$Zr$_{58}$	$2^+_1 \longrightarrow 0^+_1$	0.0035(2)	0.0078(17)†
	$2^+_1 \longrightarrow 0^+_2$	0.034(4)	0.076(16)†
	$4^+_1 \longrightarrow 2^+_1$	0.188(19)	0.118(24)†
	$4^+_1 \longrightarrow 2^+_2$	0.272(68)	0.180(36)†
	$6^+_1 \longrightarrow 4^+_1$	0.336(33)	0.275(95)†
	$8^+_1 \longrightarrow 6^+_1$	$\geq$ 0.208*	-
	$3^- \longrightarrow 2^+_1$	$\geq$ 0.034*	-
	$2^+_2 \longrightarrow 2^+_1$	$\geq$ 0.926*	-
	$4^+_2 \longrightarrow 2^+_1$	$\geq$ 0.004*	-
$^{100}_{40}$Zr$_{60}$	$4^+_1 \longrightarrow 2^+_1$	0.357(20) 0.360(45)$^{\gamma\gamma}$	0.279(3)
	$6^+_1 \longrightarrow 4^+_1$	0.505(29)	0.379(85)
	$8^+_1 \longrightarrow 6^+_1$	0.532(27)	0.341(33)
$^{102}_{40}$Zr$_{62}$	$4^+_1 \longrightarrow 2^+_1$	0.453(37) 0.526(93)$^{\gamma\gamma}$	0.471(72)*
	$6^+_1 \longrightarrow 4^+_1$	0.552(41)	$\geq$ 0.248*
	$8^+_1 \longrightarrow 6^+_1$	0.366(20)	0.409(62)
$^{104}_{40}$Zr$_{64}$	$4^+_1 \longrightarrow 2^+_1$	0.325(18)	-
	$6^+_1 \longrightarrow 4^+_1$	0.619(56)	-
	$8^+_1 \longrightarrow 6^+_1$	$\geq$ 0.343*	-

TABLE 7.1: Summary of the reduced transition probabilities (B(E2)) determined in the present experiment for the Zr isotopes, compared with the previous measurements. Experimental B(E2) values marked with a $^{\gamma\gamma}$ are obtained from the $\gamma - \gamma$ coincidence data, and the ones marked with a * correspond to lower limits. The branching ratio to calculate the B(E2) values for the transitions to the non-yrast states are taken from Khan et al., 1977. The literature values marked with a † are taken from Singh et al., 2018 and the ones marked with a * are taken from Ansari et al., 2017. The remaining literature values are calculated from the evaluated lifetimes from "NNDC".

Isotope	Transition	Experiment B(E2; ↓) [e^{2}b^2]	Literature B(E2; ↓) [e^{2}b^2]
$^{100}_{42}$Mo$_{58}$	$4^+_1 \longrightarrow 2^+_1$	0.141(13)	0.190(10)
	$6^+_1 \longrightarrow 4^+_1$	0.188(32)	0.259(37)
	$8^+_1 \longrightarrow 6^+_1$	$\geq$0.078*	0.337(52)
$^{102}_{42}$Mo$_{60}$	$4^+_1 \longrightarrow 2^+_1$	0.252(11)	0.252(50)
	$6^+_1 \longrightarrow 4^+_1$	$\geq$0.173*	0.373(82)$^\bullet$
	$8^+_1 \longrightarrow 6^+_1$	$\geq$0.142*	0.199(33)
$^{104}_{42}$Mo$_{62}$	$4^+_1 \longrightarrow 2^+_1$	0.365(22) 0.333(37)$^{\gamma\gamma}$	0.316(10)
	$6^+_1 \longrightarrow 4^+_1$	0.486(18) 0.371(122)$^{\gamma\gamma}$	0.316(10)
	$8^+_1 \longrightarrow 6^+_1$	0.293(31)	0.235(12)
$^{106}_{42}$Mo$_{64}$	$4^+_1 \longrightarrow 2^+_1$	0.312(10)	0.414(83)
	$6^+_1 \longrightarrow 4^+_1$	0.466(19)	0.384(165)
	$8^+_1 \longrightarrow 6^+_1$	$\geq$ 0.345*	0.265(36)
$^{108}_{42}$Mo$_{66}$	$4^+_1 \longrightarrow 2^+_1$	0.400(68)	-
	$6^+_1 \longrightarrow 4^+_1$	$\geq$0.267*	-

Table 7.2: Summary of the reduced transition probabilities (B(E2)) determined in the present experiment for the Mo isotopes, compared with the previous measurements. Experimental B(E2) values marked with a $^{\gamma\gamma}$ are obtained from the $\gamma-\gamma$ coincidence data, and the ones marked with a * correspond to lower limits. The literature values marked with a $^\bullet$ are taken from Ralet et al., 2017. The remaining literature values are calculated from the evaluated lifetimes from citeNNDC.

Isotope	Transition	Experiment B(E2; ↓) [e^{2}b^2]	Literature B(E2; ↓) [e^{2}b^2]
$^{106}_{44}$Ru$_{62}$	$4^+_1 \longrightarrow 2^+_1$	0.338(12)	
	$6^+_1 \longrightarrow 4^+_1$	0.332(18)	
	$8^+_1 \longrightarrow 6^+_1$	$\geq$0.168*	
$^{108}_{44}$Ru$_{64}$	$4^+_1 \longrightarrow 2^+_1$	0.247(10) 0.214(40)$^{\gamma\gamma}$	0.309(23)
	$6^+_1 \longrightarrow 4^+_1$	0.286(19)	-
	$8^+_1 \longrightarrow 6^+_1$	0.223(15)	-
$^{110}_{44}$Ru$_{66}$	$4^+_1 \longrightarrow 2^+_1$	0.273(12)	0.270(30)
	$6^+_1 \longrightarrow 4^+_1$	0.415(40)	0.37(15)
	$8^+_1 \longrightarrow 6^+_1$	0.114(6)	-
$^{112}_{44}$Ru$_{68}$	$4^+_1 \longrightarrow 2^+_1$	0.270(23)	-
	$6^+_1 \longrightarrow 4^+_1$	0.583(101)	-
	$8^+_1 \longrightarrow 6^+_1$	$\geq$0.195*	0.264(40)

Table 7.3: Summary of the reduced transition probabilities (B(E2)) determined in the present experiment for the Ru isotopic chain, compared with the previous measurements. Experimental B(E2) values marked with a $^{\gamma\gamma}$ are obtained from the $\gamma-\gamma$ coincidence data, and the one marked with a * correspond to lower limits. The literature values are calculated from the evaluated lifetimes from "NNDC".

7.1 Comparison with theoretical models

The B(E2) values are compared with the predictions of two Hartree Fock Bogoliubov (HFB) based models with the Gogny D1S effective interaction using the Symmetry Conserving Configuration Mixing (SCCM) method [Robledo, Rodríguez, and Rodríguez-Guzmán, 2018] and the 5-Dimension Collective Hamiltonian (5DCH) method [Delaroche et al., 2010] to calculate energy spectra and reduced transition probabilities. The B(E2) values for the Zr isotopes are also compared with the results of the Monte-Carlo Shell Model (MCSM) calculations [Togashi et al., 2016].

Zr isotopes

The shape evolution in the Zr isotopes can be interpreted using the predictions from the HFB+SCCM model for $^{98-104}$Zr. Fig 7.1 shows the PES after particle number projection on the left and the square of the collective wave function after projection on spin and parity illustrating the first 0^+ state on the right. The PES predicts a shape evolution from a minimum towards oblate deformation in ^{98}Zr, through a case of shape coexistence in ^{100}Zr with minima both at prolate and oblate deformations, towards a well defined minimum at large prolate deformation in all heavier isotopes. This behavior is also reflected in the collective wavefunction of the 0_1^+ state, with strong mixing in the ground state of ^{100}Zr. This shape evolution is experimentally supported by the decrease in excitation energy of the first 2^+ state (see Fig. 2.4a). The shape coexistence scenario in ^{100}Zr is confirmed by the observation of low lying 0^+ state [Khan et al., 1977].

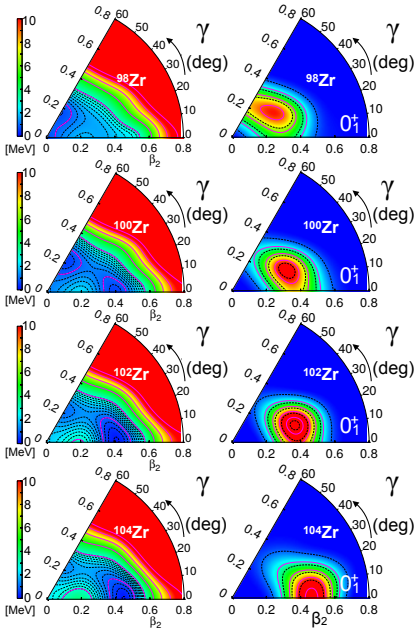

FIGURE 7.1: Illustration of the shape evolution from $^{98-104}$Zr using SCCM+HFB model. Potential energy surface after particle-number projected energy as a function of the quadrupole deformation parameters (β_2, γ) (left panel). The square of the collective wave-function after SCCM configuration mixing for the 0_1^+ state. (right panel)

Our experimental results confirm (see Fig. 7.2) the dramatic change in the B(E2; $2_1^+ \longrightarrow 0_1^+$) transition probability between N=58 and N =60, implying a shape change from the spherical ^{98}Zr to the deformed ^{100}Zr. In ^{98}Zr, the B(E2) value measured for the $2_1^+ \longrightarrow 0_2^+$ transition

is much enhanced as compared to the one in $2_1^+ \longrightarrow 0_1^+$ transition. This suggests that the 0_1^+ state is spherical in nature whereas the 0_2^+ state is deformed, indicating strongly towards shape coexistence. This is in agreement with the MCSM calculation where the B(E2; $2_1^+ \longrightarrow 0_2^+$) is shown to be rather larger than the small B(E2; $2_1^+ \longrightarrow 0_1^+$). Also, the large B(E2) value for the transition to the 2_2^+ state as compare to the 2_1^+ suggests that the former is more deformed than the latter.

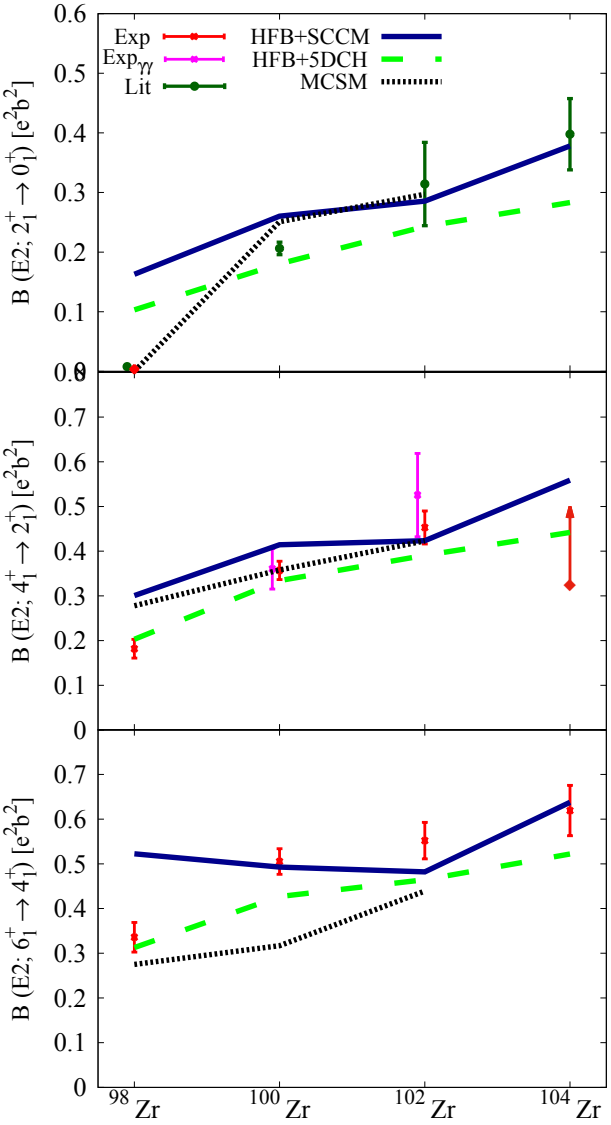

FIGURE 7.2: B(E2) values plotted as a function of neutron number from $^{98-104}$Zr isotopes.

For N > 60, the collectivity continues to increase with increasing neutron number. The B(E2; $4_1^+ \longrightarrow 2_1^+$) value in ^{98}Zr indicates increase in collectivity with increasing spin. A similar picture is emerging from the B(E2; $6_1^+ \longrightarrow 4_1^+$) transition probabilities in the Zr isotopes. Although there is no dramatic shape change for the state 6_1^+ at N =58, the collectivity increases slowly with the addition of neutrons. When comparing the experimental results with the three theoretical models, the MCSM reproduces the collective behavior best as inferred from Fig. 7.2. To be precise in terms of B(E2) values, the differences between the MCSM predictions and experimental B(E2) are noticeable for the $4_1^+ \longrightarrow 2_1^+$ transition in ^{98}Zr and the $6_1^+ \longrightarrow 4_1^+$ transition in $^{100-102}$Zr, whereas, for the $4_1^+ \longrightarrow 2_1^+$ transition in $^{100-102}$Zr, the B(E2) values are well reproduced by the

MCSM and a close agreement is concurred for the $6_1^+ \longrightarrow 4_1^+$ transition in ^{98}Zr.

Unlike the MCSM, the HFB-based models do not predict a drastic shape change from spherical to deformed for the first excited 2^+ state when going from ^{98}Zr to ^{100}Zr. Although, the HFB+5DCH model reproduces very well the reduced transition probability of the decay of 4_1^+ and 6_1^+ states of ^{98}Zr, the collectivity for the heavier Zr isotopes in the decay of the 6_1^+ state is slightly underestimated by this model. The model shows a similar rise in B(E2) as a function of the neutron number (for the decay of the 4_1^+ and decay of the 6_1^+ states) as measured in our experiment, while agreeing very well for the B(E2; $4_1^+ \longrightarrow 2_1^+$) values in ^{100}Zr. The HFB+SSCM model also overestimates the collectivity for the decay of the 4_1^+ and 6_1^+ states in ^{98}Zr. However, it reproduces the trend rather well for all B(E2) values measured for the isotopes heavier than ^{98}Zr.

Fig. 7.3 shows the comparison of the transitional quadrupole moments (Q_t) calculated from the measured B(E2) using the Eq. 2.18. It can be seen in Fig. 7.3 that the two HFB-based models predict the trend very well for $^{98-104}$Zr isotopes, except for the sharp onset of deformation from spherical ^{98}Zr to deformed ^{100}Zr. The HFB+SCCM predicts oblate deformation in ^{98}Zr and shape coexistence in ^{100}Zr (Fig. 7.1). No clear conclusion can be drawn for the 4_1^+ state in ^{104}Zr and 8_1^+ state in ^{98,102,104}Zr) since only an upper limit on the lifetime could be obtained.

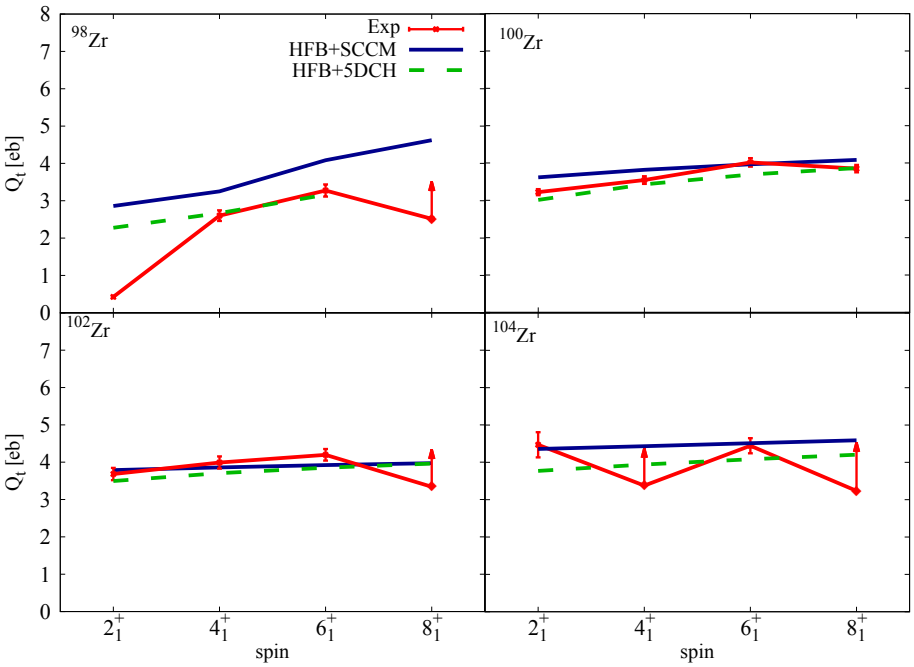

FIGURE 7.3: Transitional quadrupole moment (Q_T) shown for $^{98-104}$Zr compared with the Q_T obtained from the two BMF models.

Mo isotopes

The collective behavior of the Mo isotopes has been studied by examining the PES (left panel) and collective wave function (right panel) of the 0_1^+ state of $^{100-108}$Mo obtained from the HFB+SCCM calculations (see Fig. 7.4). The PES indicates towards gamma instability in $^{100-102}$Mo. However, beyond ^{102}Mo, oblate and prolate-triaxial minimum appear in the PES. One minimum in all $^{104-108}$Mo isotopes leans towards oblate deformation, whereas the other one is more prolate in ^{104}Mo and gradually shifts towards triaxial in ^{108}Mo. The collective wave function of the first 0^+ state in Fig. 7.4 shows a triaxial maximum for all Mo isotopes.

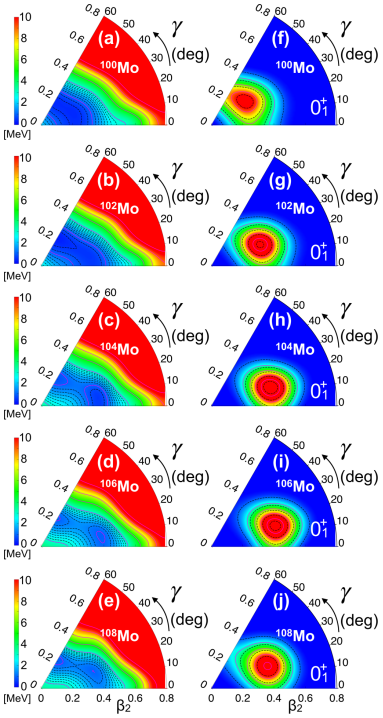

FIGURE 7.4: Illustration of the shape evolution from $^{100-108}$Mo using SCCM+HFB model. Potential energy surface after particle-number projected energy as a function of the quadrupole deformation parameters (β_2, γ) (left panel). The square of the collective wave-function after SCCM configuration mixing for the 0_1^+ state (right panel).

A smooth onset of collectivity and an increase in deformation is observed experimentally as seen in the evolution of the 2_1^+ excitation energy as a function of neutron number for the Mo isotopes (see Fig. 2.4a). An increase in triaxial softness can be conjectured by the lowering of the 2_2^+ energy in the Mo isotopes shown in Fig. 7.5. The low-lying 0_2^+ state in ^{100}Mo at 695 keV could be an indication of shape-coexistence phenomenon.

The lifetimes of the 2_1^+ states in the Mo isotopic chain are too long for the RDDS measurement, therefore, we only discuss the higher spin states. For the 4_1^+ states in the Mo isotopes (see Fig. 7.6), the collectivity increases from N = 58 to N = 66, however the growth is not as strong as for the 4_1^+ states in Zr isotopes. For the 6_1^+ state, the collectivity is rather constant from ^{100}Mo to ^{102}Mo but increases significantly beyond N = 60. No conclusion about the deformation can be drawn beyond ^{106}Mo because only an effective lifetime has been determined for the 6_1^+ state in ^{108}Mo.

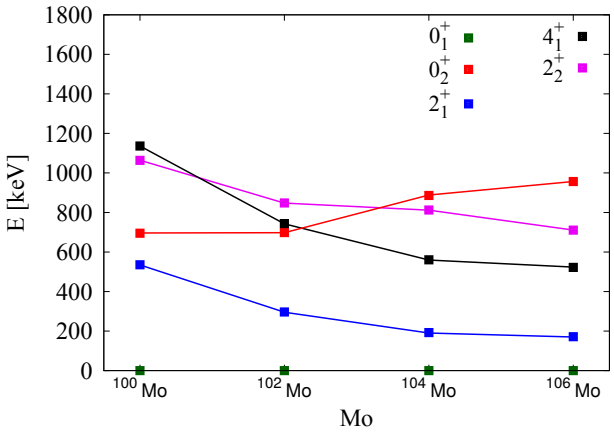

FIGURE 7.5: Evolution of the level energies in the isotopes $^{100-108}$Mo

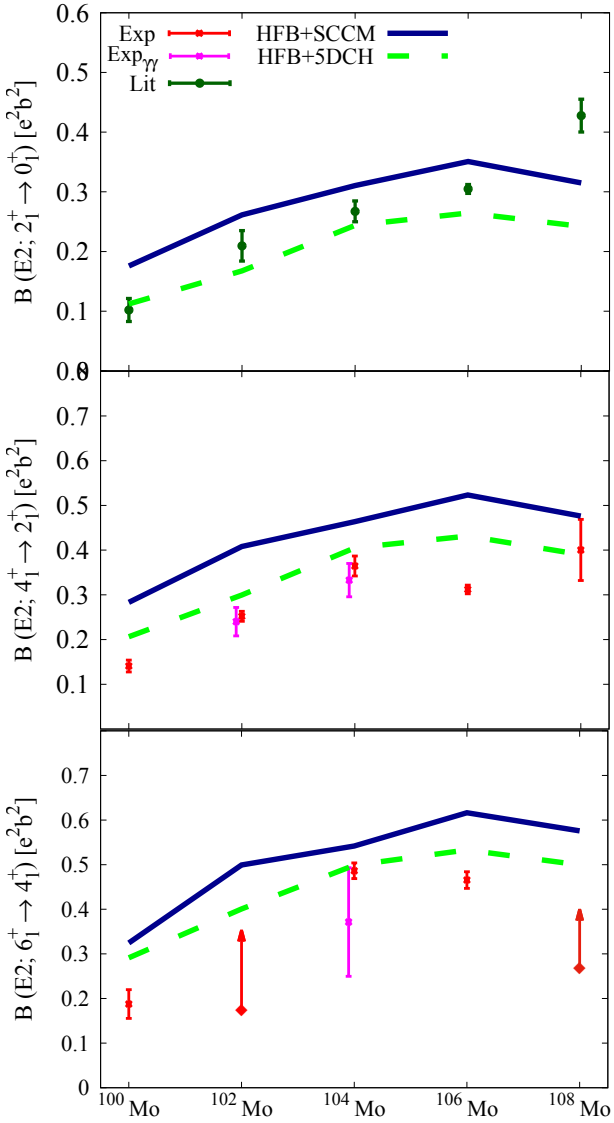

FIGURE 7.6: B(E2) values plotted as a function of neutron number from $^{100-108}$Mo isotopes.

The two HFB based models predict a similar rise in reduced transition probability for the decay of both 4_1^+ and 6_1^+ states. The disagreement with the experiment for the 6_1^+ state in ^{106}Mo could be the result of an underestimation of the B(E2) value in our experiment, since the literature B(E2) value of 0.414(83) (see table 7.2) agrees very well with the model. In general the HFB+SCCM model predicts lower B(E2) values than the HFB+5DCH model.

Ru isotopes

The collectivity in the Ru isotopes ($^{106-114}$Ru) is investigated using the predictions from the HFB+SCCM calculations (see Fig. 7.7). Looking at the PES one sees a gradual transition from a more oblate deformation in ^{106}Ru, passing through a triaxial minimum for $^{108-112}$Ru, towards a more prolate deformation in ^{114}Ru. The collective wave function after projection on spin and parity, shown in the right panel of Fig. 7.7 have their maxima at pure triaxial configurations for all Ru isotopes.

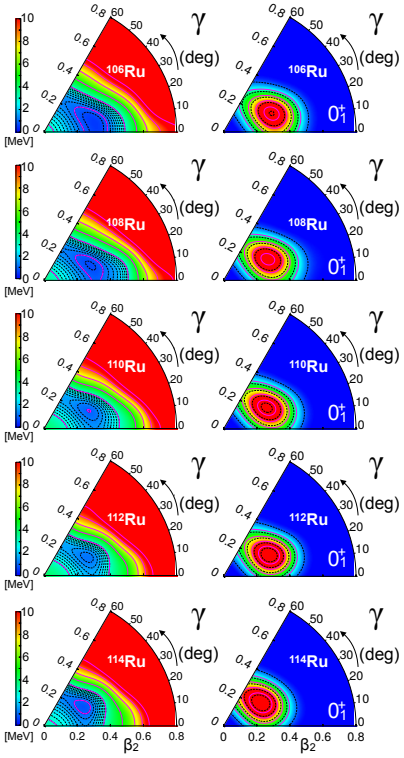

FIGURE 7.7: Illustration of the shape evolution in $^{106-114}$Ru using SCCM+HFB model. Potential energy surface after particle-number projected energy as a function of the quadrupole deformation parameters (β_2, γ) (left panel). The square of the collective wave-function after SCCM configuration mixing for the 0_1^+ state. (right panel)

The deformation in the Ru isotopes is almost constant (as seen in Fig. 7.8) because the energy of the 2_1^+ and 4_1^+ changes very little with increasing mass. The importance of triaxiality increases particularly above ^{108}Ru where the 2_2^+ becomes lower than the 4_1^+ which is a clear indication for triaxiality. This has been partially confirmed for ^{110}Ru in the Coulomb excitation experiment [Doherty et al., 2017].

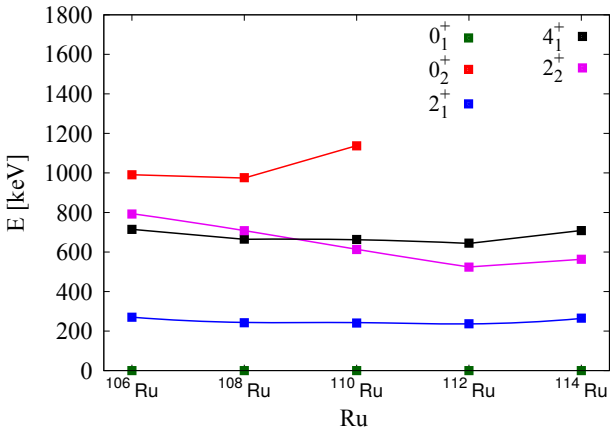

FIGURE 7.8: Evolution of the level energies for the isotopes $^{106-114}$Ru

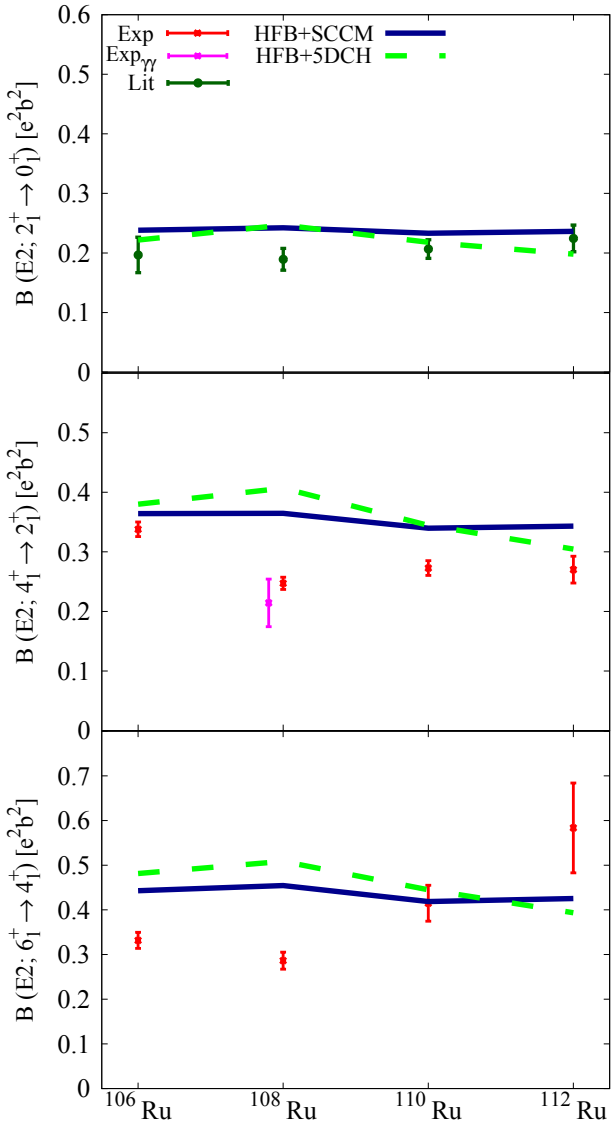

FIGURE 7.9: B(E2) values plotted as a function of neutron number from $^{106-112}$Ru isotopes.

The B(E2) values in Ru isotopes in Fig. 7.9 shows that the evolution of the deformation is smoother as compared to both the Mo and the Zr isotopes. The HFB+SCCM and HFB+5DCH models predicts a rather constant collectivity for the Ru isotopes which in most cases is slightly larger than the experimental values. The collectivity seems slightly overestimated in the case of the 6_1^+ state of ^{112}Ru, since for the rest of the isotopes the experimental values lay below those calculated using the two theoretical models. The agreement in B(E2) values between both singles and gamma-gamma data in 4^+ and 6^+ ^{104}Mo, puts more confidence in the experimental results as compare to the theoretical predictions, especially in case of HFB+SCCM.

7.2 Conclusion

We have measured lifetimes of the the 4_1^+, 6_1^+ and 8_1^+ states in $^{98-104}$Zr, $^{100-108}$Mo and $^{106-112}$Ru isotopes. Effective lifetimes were also measured for the 10_1^+ state for the strongest channels ($^{100-102}$Zr, ^{104}Mo). In general our results have a better precision and agree well with the previously measured lifetimes. However, it is still necessary to analyze the systematic error more carefully which could not be done in the present work due to time constraints. Such errors could arise for cases with a hidden peak under the shifted or unshifted distribution. Another systematic error could also arise from the velocity distribution, since the ratio $\frac{E_S}{E_U}$ which has been used to determine the velocity of the fission fragments before the degrader, is most likely not constant for all angles covered by AGATA (see Eq. 5.4).

An RDDS analysis using $\gamma - \gamma$ coincidence data was possible for the first time under these experimental conditions, i.e. where the fission fragments were identified on an event-by-even basis. The good agreement between these results and the ones obtained from singles data give confidence that the latter are also reliable as long as the feeding contributions can be correctly extracted. We have also performed the first direct measurement of all the "significant" side-feedings of the 2_1^+ state of ^{98}Zr. By measuring new effective lifetimes for the 3^-, 2_2^+, and 4_2^+ states in ^{98}Zr a more precise (and reliable) lifetime of the 2_1^+ state could be obtained. These differences are most likely responsible for the discrepancy in the lifetime of the 2_1^+ state in ^{98}Zr between this experiment using AGATA and the previous one using EXOGAM [Singh et al., 2018]. The effective lifetime of the 8_1^+ state of ^{98}Zr has also been measured for the first time. We also have obtained a new lifetime of the 6_1^+ state in ^{104}Zr, 8 neutrons from stability, and a new effective lifetimes of the 4_1^+ state in the same isotope.

Apart from measuring a new effective lifetime of the 6_1^+ state of ^{108}Mo, we have improved the precision of the lifetimes of the Mo isotopes as compared to those measured previously. For instance, with the RDDS technique, we have a higher precision for the lifetimes in Mo isotopes as compared to the DSAM technique at relativistic energies.

We have measured new lifetime values for the 4_1^+ and 6_1^+ state in ^{106}Ru and for the 6_1^+ state in ^{112}Ru. As these are the lightest and the heaviest Ru isotope for which lifetimes could be determined in the present study, the higher efficiency and position sensitivity of AGATA plays a significant role here as compared to the EXOGAM analysis.

One of the significant findings from the present experiment is the confirmation of the dramatic shape change from ^{98}Zr to ^{100}Zr in their first excited 2_1^+ state which is in good agreement with the predictions of MCSM. The obtained B(E2) values for the transitions to the non-yrast states suggest, deformed structure in the 0_2^+ state in contrast to the spherical 0_1^+ state, indicating towards shape coexistence, and enhanced deformation in the 2_2^+ state as compare to the 2_1^+ state.

Another conclusion from the present work is that the collectivity increases more rapidly as a function of neutron number for the Zr isotopes as compared to the Mo and Ru isotopes.

Future prospects

In order to obtain a comprehensive picture of all neutron-rich nuclei presented in Fig. 2.4, the data on more isotopes need to be analyzed, which could not be possible in the present work due to time constraint. Lifetime measurements using the fast-timing method provides sensitivity to longer-lived states which could not be determined in the present work. Such an analysis could give a lifetime of the first excited 2_1^+ states as well as verify the lifetimes of some of the longer-lived 4_1^+ states in the isotopes of interest.

Other experimental techniques complementary to that described here can also be used to deepen the experimental knowledge of these nuclei. For instance, Coulomb excitation experiments, now possible at CARIBU (CAlifornium Rare Isotope Breeder Upgrade) facility at the Argonne National Laboratory, can offer new perspectives on the shape evolution from mass 100-110. It should be noted that the measured lifetimes may serve as an important constraint in the analysis of data from Coulomb-excitation experiments. Coulomb-excitation cross sections depend on many electromagnetic matrix elements, therefore a knowledge of precise B(E2) values enables the determination of parameters that have a smaller influence on cross sections, such as spectroscopic quadrupole moments.

This kind of experiment could be performed again with more AGATA detectors (larger than 1π array), which would lead to a significantly higher efficiency and statistics and would allow to extend the γ-γ coincidence technique to more exotic isotopes in order to increase the precision and the reliability of the lifetime results.

Appendix A

Fission fragment γ-ray spectra

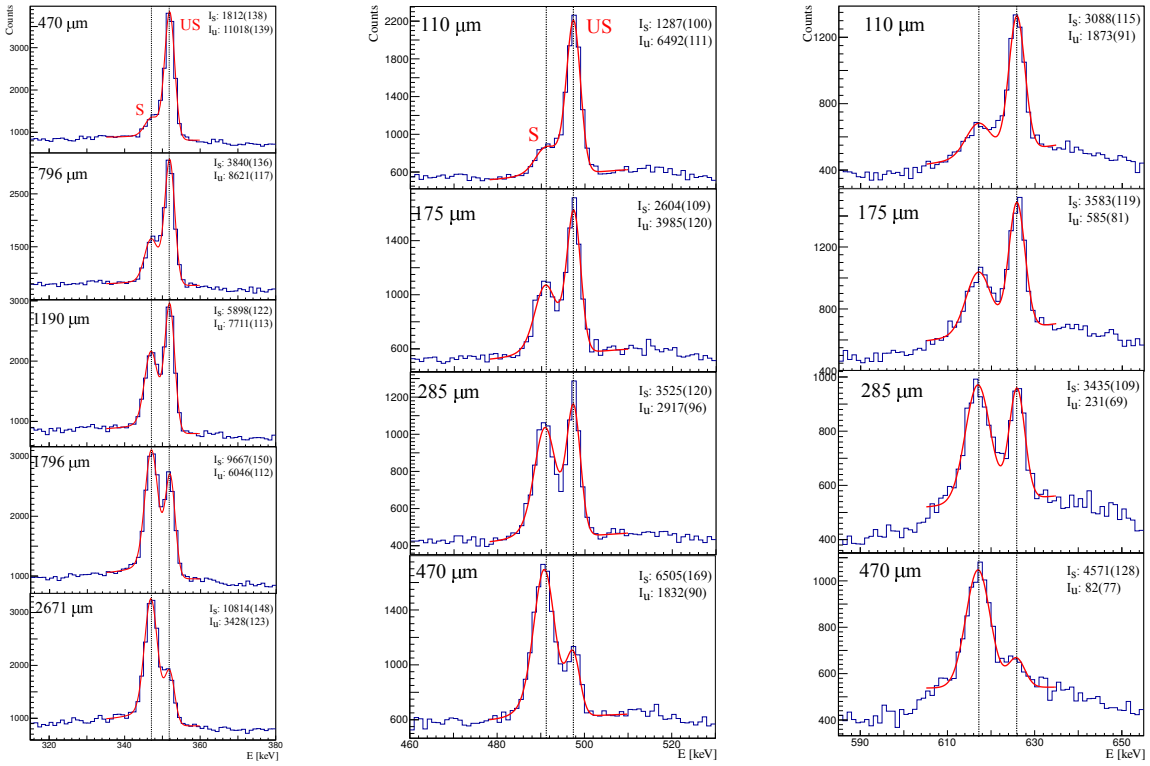

(A) (B) (C)

FIGURE A.1: Shifted and unshifted peaks for the 4_1^+ state in ^{100}Zr shown in (A), the 6_1^+ state in ^{100}Zr shown in (B) and the 8_1^+ state in ^{100}Zr shown in (C). I_s and I_us mean shifted and unsifted area, respectively for all the peaks.

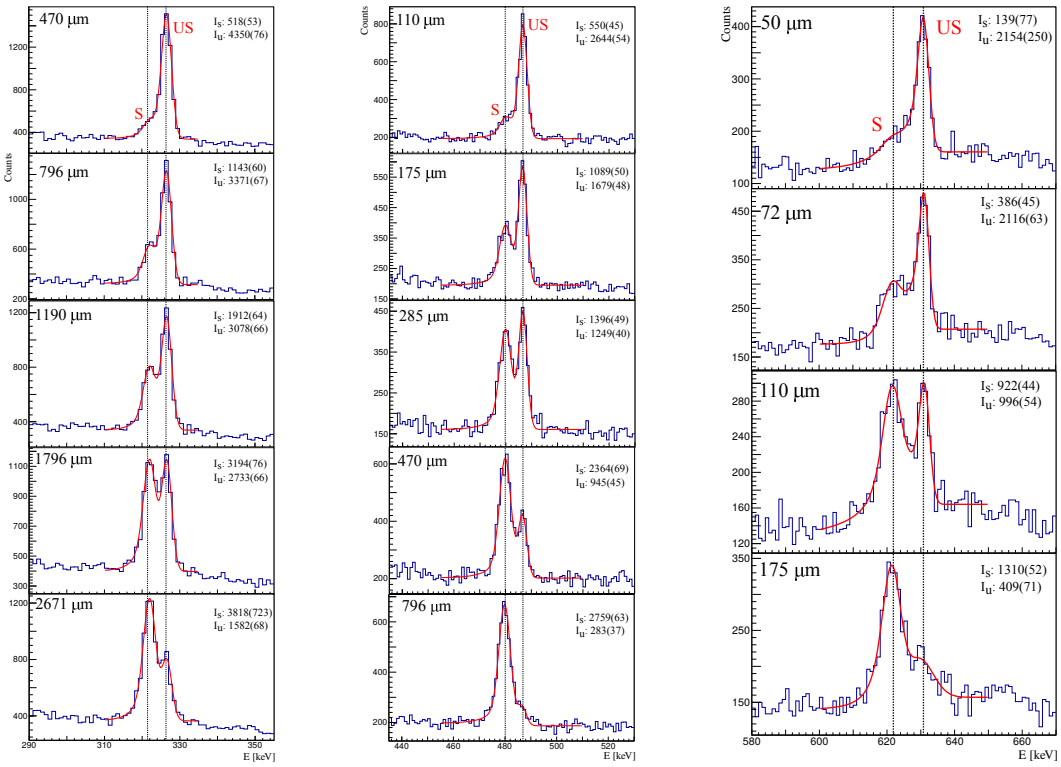

(A) (B) (C)

FIGURE A.2: Shifted and unshifted peaks for the 4_1^+ state in ^{102}Zr shown in (A), the 6_1^+ state in ^{102}Zr shown in (B) and the 8_1^+ state in ^{102}Zr shown in (C)

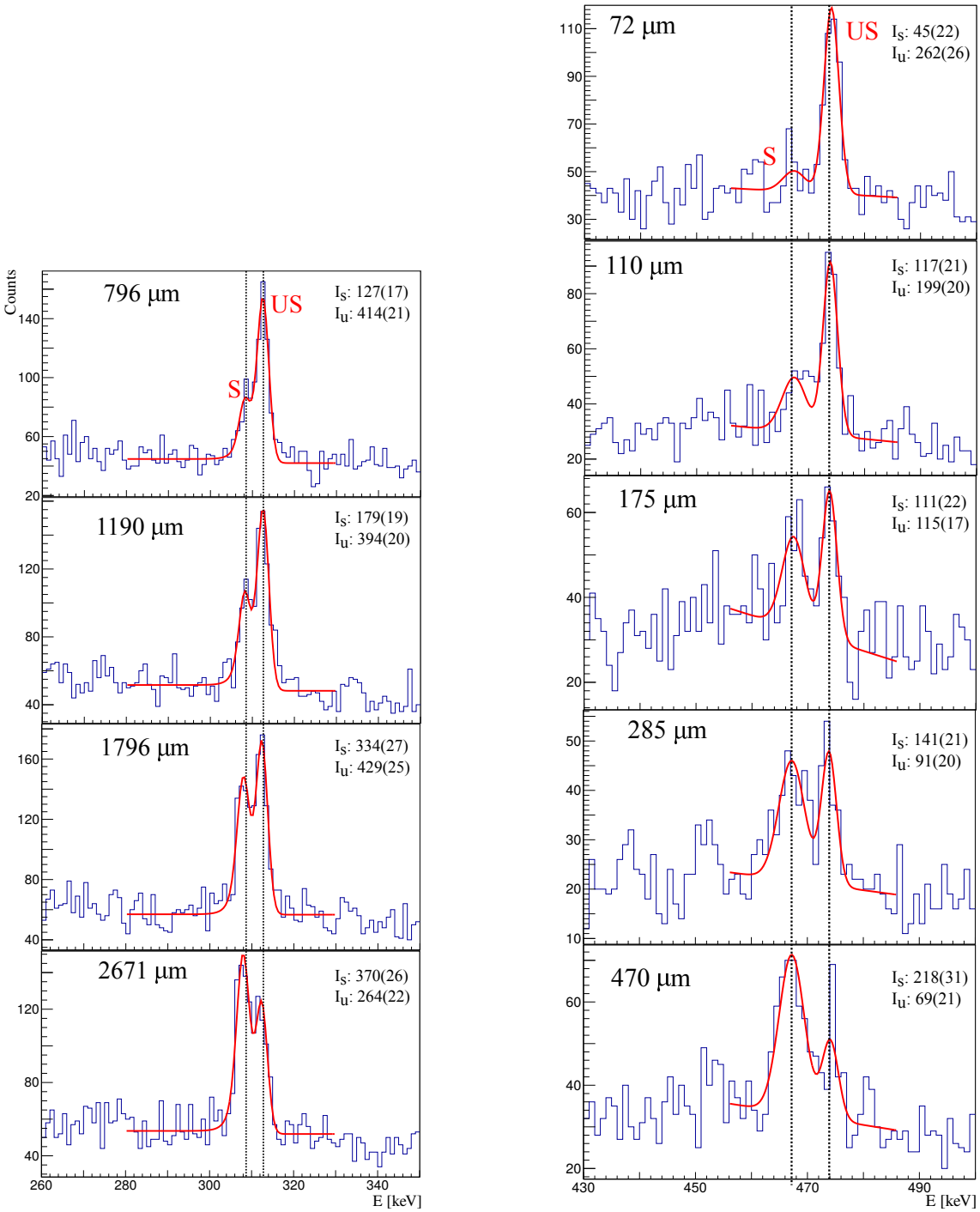

(A) (B)

FIGURE A.3: Shifted and unshifted peaks for the 4_1^+ state in ^{104}Zr shown in (A) and the 6_1^+ state in ^{104}Zr shown in (B)

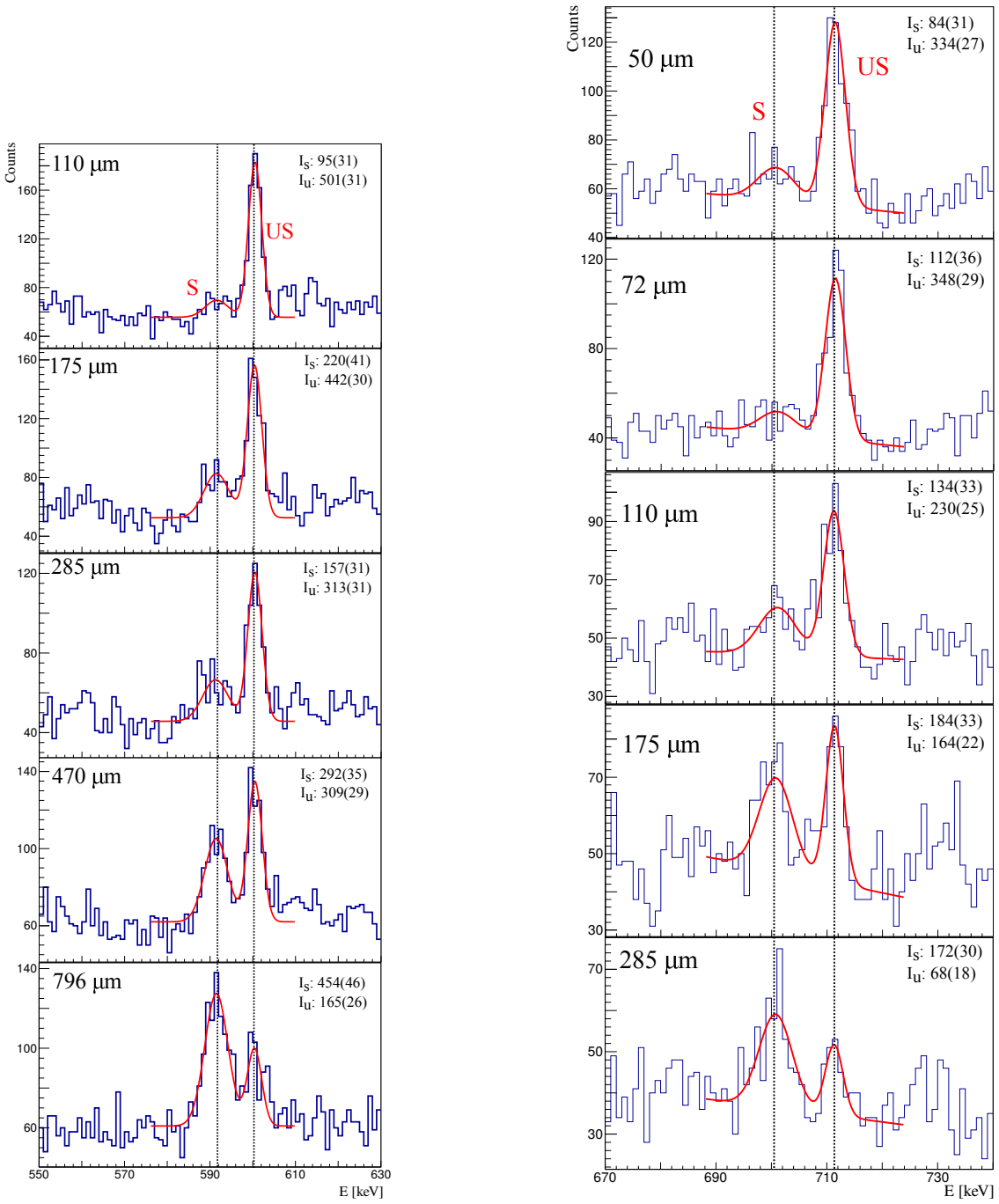

(A) (B)

FIGURE A.4: Shifted and unshifted peaks for the 4_1^+ state in ^{100}Mo shown in (A) and the 6_1^+ state in ^{100}Mo shown in (B)

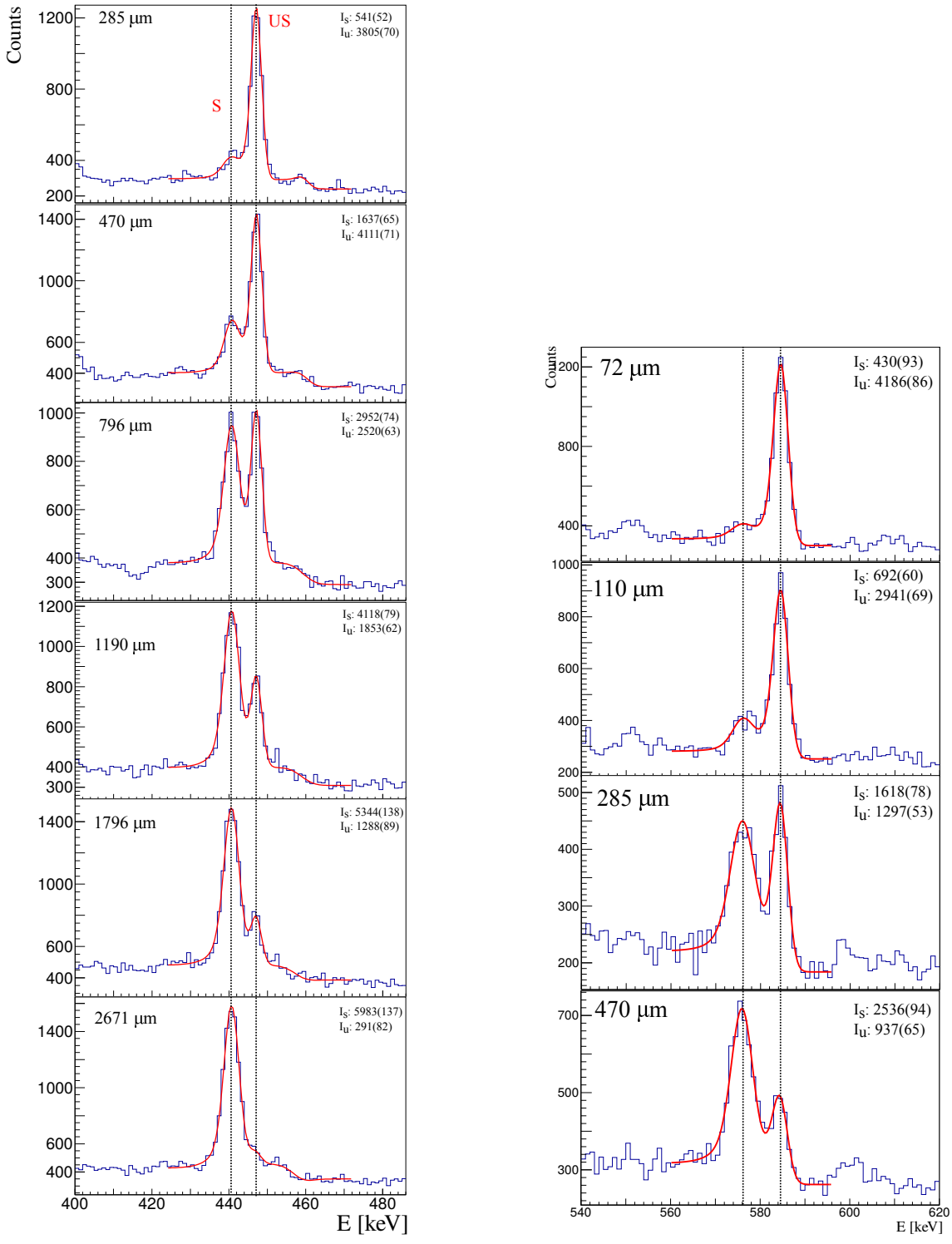

(A) (B)

FIGURE A.5: Shifted and unshifted peaks for the 4_1^+ state in ^{102}Mo shown in (A) and the 6_1^+ state in ^{102}Mo shown in (B)

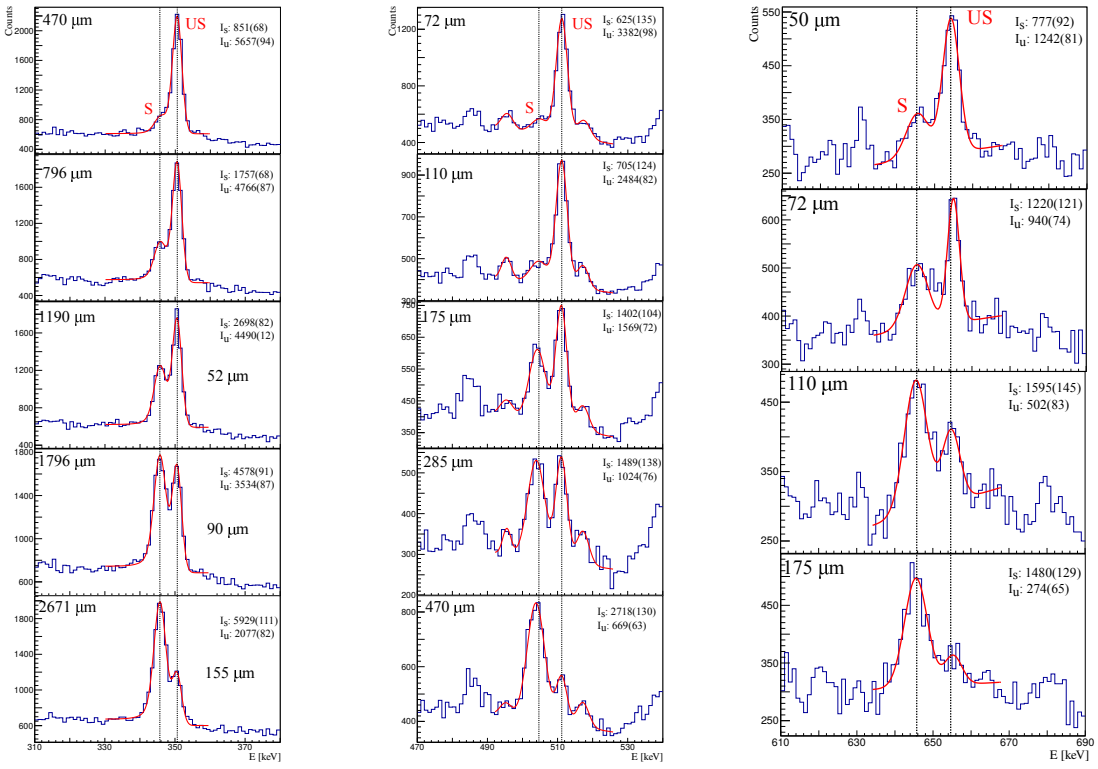

(A) (B) (C)

FIGURE A.6: Shifted and unshifted peaks for the 4_1^+ state in ^{106}Mo shown in (A), the 6_1^+ state in ^{106}Mo shown in (B) and the 8_1^+ state in ^{106}Mo shown in (C)

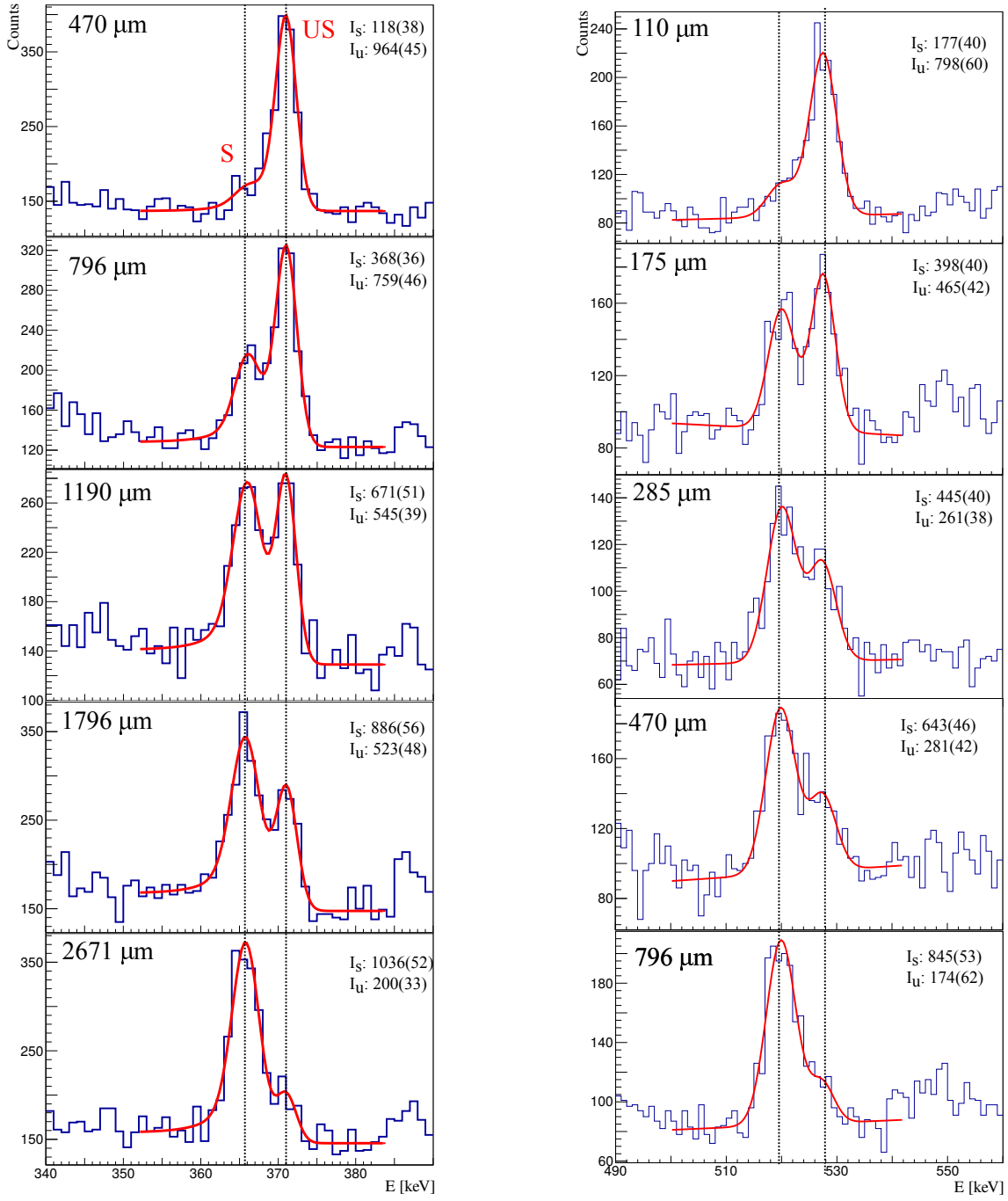

(A) (B)

FIGURE A.7: Shifted and unshifted peaks for the 4_1^+ state in ^{108}Mo shown in (A) and the 6_1^+ state in ^{108}Mo shown in (B)

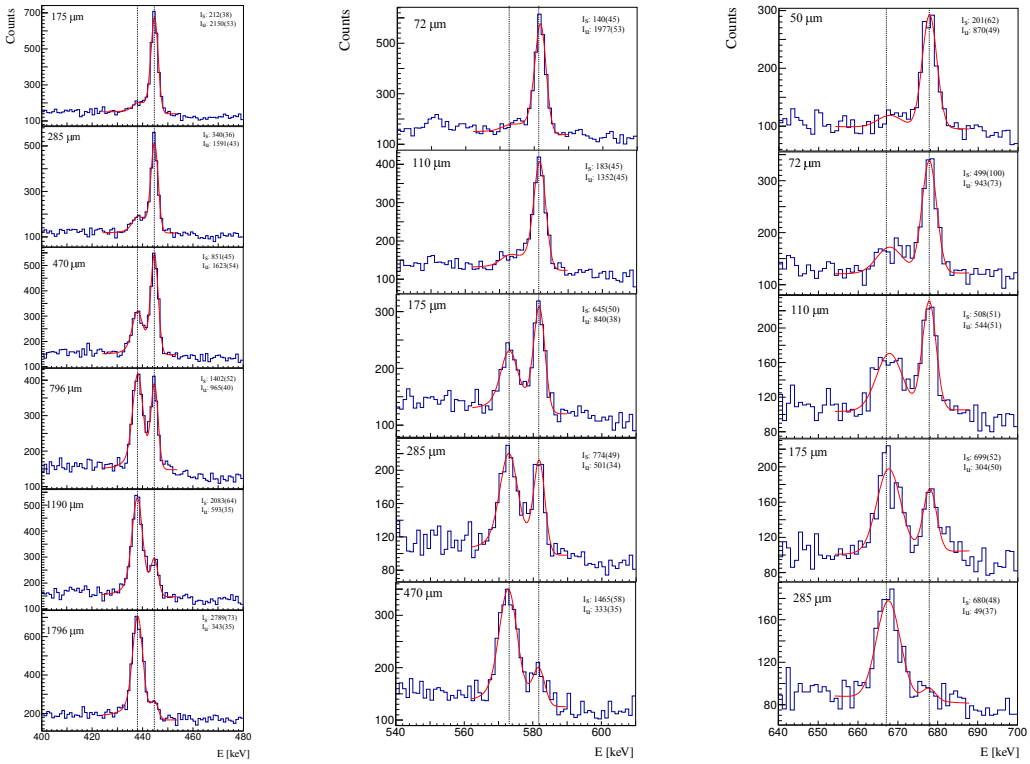

(A) (B) (C)

FIGURE A.8: Shifted and unshifted peaks for the 4_1^+ state in ^{106}Ru shown in (A), the 6_1^+ state in ^{106}Ru shown in (B) and the 8_1^+ state in ^{106}Ru shown in (C)

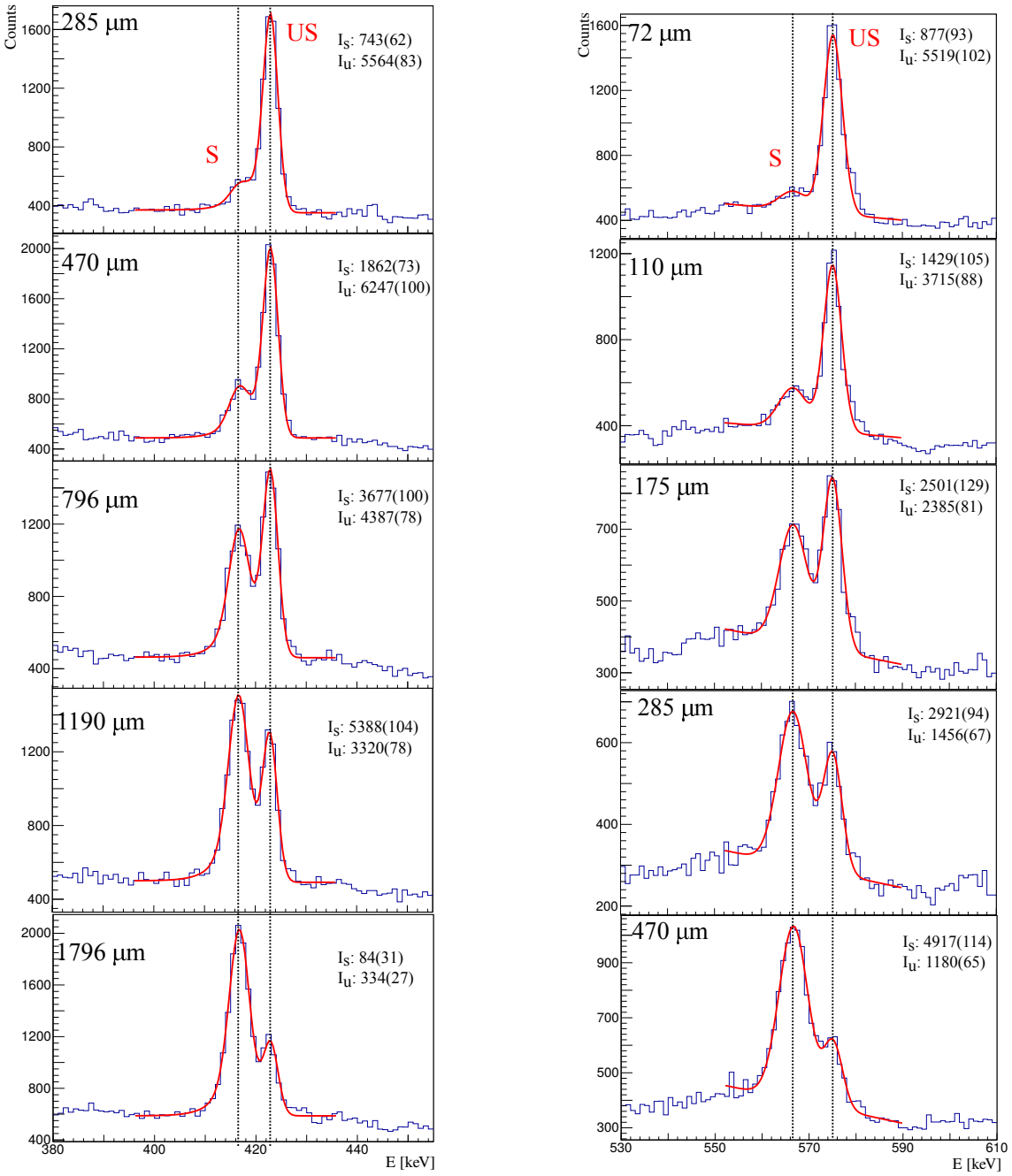

(A) (B)

FIGURE A.9: Shifted and unshifted peaks for the 4_1^+ state in ^{108}Ru shown in (A) and the 6_1^+ state in ^{108}Ru shown in (B)

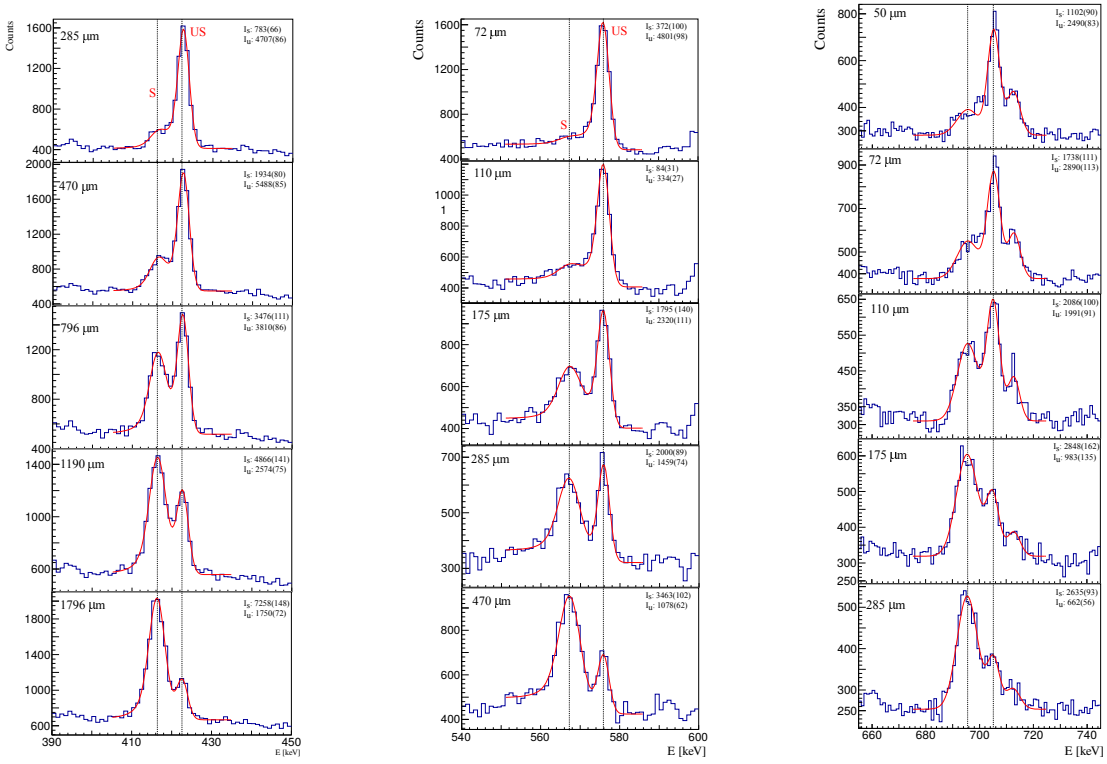

(A) (B) (C)

FIGURE A.10: Shifted and unshifted peaks for the 4_1^+ state in ^{110}Ru shown in (A), the 6_1^+ state in ^{110}Ru shown in (B) and the 8_1^+ state in ^{110}Ru shown in (C)

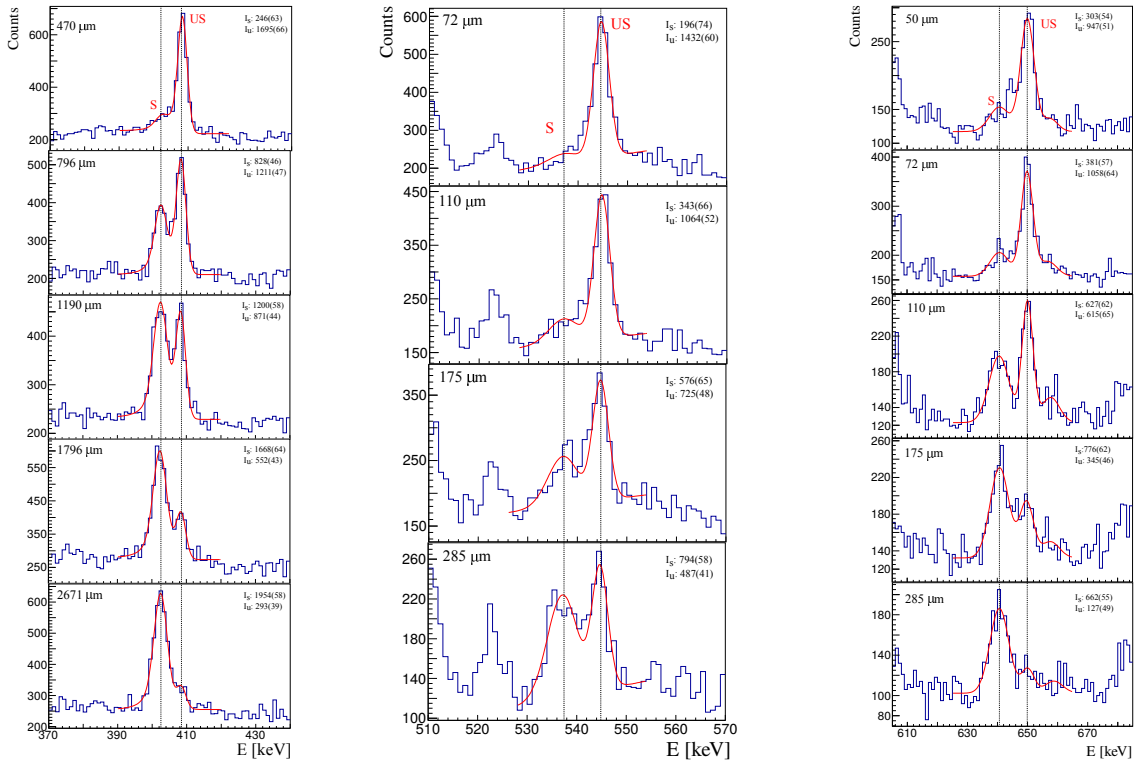

(A) (B) (C)

FIGURE A.11: Shifted and unshifted peaks for the 4_1^+ state in ^{112}Ru shown in (A), the 6_1^+ state in ^{112}Ru shown in (B) and the 8_1^+ state in ^{112}Ru shown in (C)

Appendix B

Résumé en francais

B.1 Introduction

Cette thèse présente de nouveaux résultats expérimentaux sur la durée de vie des états excités du Zr, du Mo et du Ru riches en neutrons. Ces isotopes apportent des informations systématiques sur l'évolution de la déformation et de la collectivité nucléaires à proximité de la transition de forme à N=60. Les forces de transition mesurées sont comparées à celles obtenues par un modèle en couche Monte-Carlo et par des calculs au-delà du champ moyen. La majeure partie de ce travail de thèse a consisté à mesurer la durée de vie des niveaux de basse énergie dans des isotopes pairs-pairs du Zr, du Mo et du Ru, et d'en extraire les valeurs de B(E2) qui peuvent être comparées aux prédictions théoriques.

Les noyaux riches en neutrons dans la région de masse A∼100 sont été le sujet de recherches en structure nucléaire depuis de nombreuses années. La figure 2.4a montre l'énergie d'excitation du premier état 2_1^+ en fonction du nombre de neutrons pour les isotopes pairs des Sr, Zr, Mo, Ru, Pd et Cd. En passant de N = 58 à N = 60, il y a un changement radical dans l'énergie d'excitation de l'état 2^+, notamment pour les isotopes Sr, Zr et Mo. Ce type de comportement peut être lié à un changement de la déformation nucléaire : les noyaux avec N<60 ont une forme plutôt sphérique, alors que ceux au-delà de N = 60 sont fortement déformés. Une mesure de la probabilité de transition réduite est une mesure plus directe de la déformation nucléaire. La figure 2.4b montre les valeurs B(E2 ; $2_1^+ \longrightarrow 0_1^+$) en fonction du nombre de neutrons, du Sr au Cd. L'apparition de la collectivité est plutôt douce du Ru au Cd, alors que la collectivité s'installe plus rapidement au-delà de N = 58 pour les isotopes Sr, Zr et Mo.

Cet îlot de déformation quadripolaire apparaissant au-delà de N=60 dans la région de masse A∼100 a été observé pour la première fois dans les années 1960 par Johansson, 1965 dans une étude des rayons γ émis par des fragments de fission. Peu après, Cheifetz et al., 1970 ont identifié des états excités et mesuré des durées de vie dans des noyaux de masse A∼100 en utilisant la fission spontanée du ^{252}Cf, rapportant un comportement de type rotationnel des isotopes pairs-pairs riches en neutrons Zr, Mo, Ru et Pd, conformément aux prévisions théoriques [Arseniev, Sobiczewski, and Soloviev, 1969; Sheline, Ragnarsson, and Nilsson, 1972].

B.2 Expérience

Cette thèse décrit l'analyse et les résultats d'une expérience de spectroscopie γ, qui a été réalisée au GANIL en juin 2017. Le but de l'expérience était de créer des produits de fission qui se désexcitent en vol afin de mesurer la durée de vie des états excités. Durant l'expérience, un faisceau de $^{238}_{92}$U était accéléré par le cyclotron CSS1 [Lehérissier et al., 2004] à 6,2 MeV/u et dirigé vers une cible de $^{9}_{4}$Be. La réaction de fusion produisait des noyaux composés $^{247}_{96}$Cm avec une énergie d'excitation de 45 MeV, puis ceux-ci fissionnaient. Grâce au couplage de deux spectromètres

hautement sophistiqués, cette expérience a permis de mesurer des durées de vie de niveaux nucléaires allant de quelques picosecondes à plusieurs centaines de picosecondes.

La spectroscopie γ après fission est particulièrement intéressante, car les réactions de fission produisent des fragments du côté riche en neutrons de la vallée de la stabilité. En revanche, elle apporte son lot de difficultés, puisque de nombreux fragments différents sont produits, qui décroissent à leur tour par émission de transitions γ contaminantes, souvent superposées aux transitions étudiées. Les transitions γ des isotopes d'intérêt ont pu être séparées de celles correspondant à la désexcitation d'autres produits de réaction grâce à l'utilisation du spectromètre de masse de haute précision VAMOS, qui a permis d'identifier les isotopes en fonction de leur numéro atomique Z, de leur masse A et de leur état de charge Q.

Le détecteur AGATA, qui pour cette expérience était constitué de 35 détecteurs germanium hautement segmentés, a été placé en amont de la cible. La cible a été placée à l'intérieur d'un mécanisme dit "plunger" qui, en combinaison avec AGATA et VAMOS, a permis la mesure d'états excités de courte durée. La réaction fusion-fission était en cinématique inverse, ce qui a permits de produire des fragments de fission ayant une vitesse de recul élevée ($\approx$10% de la vitesse de la lumière). Ceci a induit d'importants décalages Doppler qui se sont révélés cruciaux pour les mesures des états à courte durée de vie. Les détecteurs germanium d'AGATA ont été placés en sens inverse (à des angles de $\sim$ 135° à 175° de l'axe du faisceau) afin de maximiser le décalage Doppler. La cible était entourée des 24 détecteurs au bromure de lanthane ($LaBr_3$) du réseau FATIMA placés à 90° du faisceau pour mesurer la durée de vie des états de "longue vie" allant de quelques dizaines à quelques centaines de ps en utilisant la méthode dite du "fast-timing".

En utilisant différentes combinaisons de spectromètres présents dans la configuration, nous avons pu déterminer des durées de vie allant de $\sim$ 1 ps à $\sim$ 1 ns : en combinant VAMOS, AGATA et le dispositif de plunger, nous avons pu mesurer des durées de vie allant jusqu'à quelques ps, tandis que la combinaison VAMOS et FATIMA permet d'atteindre $\sim$ 1 ns. Les schémas du montage expérimental sont illustrés dans la figure 3.1. Dans cette thèse, seule la mesure de la durée de vie des états à courte durée de vie à l'aide de la technique du plunger est discutée.

B.2.1 Mesure de la distance de recul par décalage Doppler

Le principe de la méthode RDDS (Recoil Distance Doppler Shift) est illustré par la figure 5.2. Si un noyau recule hors de la cible, il peut se désexciter en vol. L'avantage du dispositif de plunger est que la distance entre la cible et le dégradeur peut être modifiée afin de changer le nombre de noyaux se désexcitant avant ou après le dégradeur (Fig. 5.2b). Dans les deux cas, l'énergie des rayons γ émis en vol sera modifiée par l'effet Doppler.

La vitesse d'un noyau après le dégradeur est mesurée au plan focal de VAMOS (comme indiqué à la section 3.1). Cette vitesse est utilisée pour corriger l'effet Doppler (Eq. 5.1) événement par événement. Par conséquent, l'énergie des rayons γ émis par le noyau en recul peut être déterminée avec précision lorsque la désintégration survient après le dégradeur. Ainsi, les énergies corrigées forment dans le spectre en énergie un pic situé au niveau de l'énergie originale/absolue de la transition γ (position non modifiée). Cependant, lorsque le noyau se désintègre avant le dégradeur, l'énergie est décalée de la valeur initiale en raison de la perte d'énergie dans le dégradeur, représentée par le pic gauche de la figure 5.2a (position décalée). Cette différence en énergie entre les rayons γ émis avant le dégradeur et ceux émis après permet de calculer leurs proportions respectives. Le ratio avant/après dépend de la vitesse des noyaux, de la position du dégradeur, et enfin de la durée de vie de l'état excité à l'origine de la transition étudiée. La mesure de ce rapport (Q_i dans ce travail de thèse) permet donc de déduire la durée de vie.

Mise en œuvre de la technique RDDS

Dans l'analyse RDDS, l'évolution de Q_i, donnée par Eq. 5.3, est étudiée en fonction de la position du plunger. La courbe de désintégration correspondante peut être ajustée par minimisation du χ^2 en utilisant les équations de Bateman [Bateman, 1843] ou une autre fonction appropriée. Pour obtenir $Q_i(x)$, les pics décalés et non décalés doivent être bien séparés dans le spectre en énergie. Leur séparation dépend de la résolution en énergie des détecteurs germanium ainsi que de leur résolution spatiale, qui influence la détermination précise de l'angle d'émission et donc la correction Doppler. La séparation dépend également de l'écart de vitesse dû à la perte d'énergie dans la cible et dans le dégradeur. Dans la présente expérience, la correction de la diaphonie et la correction des dommages neutroniques, détaillées dans le chapitre 4, étaient cruciales pour obtenir une bonne résolution en énergie, et ainsi séparer les deux pics.

B.2.2 Méthode différentielle de courbe de décroissance

La méthode DDCM (Differential Decay Curve Method) est une extension de la DCM [Dewald, Harissopulos, and Brentano, 1989; Böhm et al., 1993], mais celle-ci dépend de la position relative du dispositif de plunger et non de sa position absolue. La DDCM permet de déterminer une valeur de durée de vie pour chaque position du plunger. Les erreurs systématiques liées à cette méthode sont plus faibles, cette dernière ne nécessitant aucune hypothèse sur les transitions qui alimentent la transition étudiée, à condition que toutes ces transitions-mères soient observées expérimentalement. Dans la méthode DCM, la durée de vie est donnée directement par l'ajustement de la courbe de décroissance (par exemple Fig. 6.8).

Dans cette expérience, nous avons utilisé un dégradeur laissant passer les produits de fission au lieu de les arrêter afin permettre leur identification dans VAMOS en aval du plunger. La détermination précise de la vitesse dans le spectromètre VAMOS réduit également les incertitudes par rapport à la méthode classique où les noyaux de recul sont arrêtés [Dewald, Harissopulos, and Brentano, 1989]. L'utilisation d'un pluger est essentielle pour l'analyse DDCM, car elle permet de mesurer décroissance du ratio $Q_i(x)$ en fontion de la position du dégradeur, ainsi que de sa première dérivée. L'estimation de la dérivée à une position est faite en ajustant une courbe de décroissance aux $Q_i(x)$ et la dérivant. L'erreur sur la dérivée est également calculée à partir de la fonction ajustée, en supposant que les paramètres d'ajustement sont non corrélés. Les durées de vie associées à chaque position sont alors déterminées en utilisant Eq. 5.10. La durée de vie de l'état est alors prise comme la moyenne des temps de vie aux positions les plus sensibles (voir chapitre 5).

Le chapitre 6 décrit les résultats des mesures de durée de vie de la présente expérience dans les chaînes du Zr, du Mo et du Ru obtenus à l'aide des différentes méthodes décrites au chapitre 5. La DDCM est la principale méthode utilisée pour extraire les durées de vie des données sans condition de coïncidence. La DCM est utilisée pour obtenir les durées de vie des états dont les transitions-mères ont une statistique insuffisante. La méthode de la somme est utilisée pour déterminer des durées de vie effectives pour les transitions dont la statistique est faible. Celle-ci est également utilisée dans le cas de transitions-mères faibles. Les données de coïncidences γ-γ sont utilisées chaque fois que c'est statistiquement possible.

Pour chaque durée de vie obtenue à l'aide de la méthode DDCM, une courbe de décroissance (par exemple Fig. 6.3a) et un graphique de durée de vie (valeurs individuelles de la durée de vie en fonction de la position du plunger) (par exemple Fig. 6.3b) sont présentés. Dans un cas idéal, les durées de vie correspondant aux distances individuelles n'évoluent pas en fonction de la distance. Cependant, dans certains cas, les valeurs de durée de vie peuvent diminuer ou augmenter systématiquement en fonction de la position du plungeur. Cela pourrait être dû soit à

une surestimation, soit à une sous-estimation de la contribution d'une transition-mère résultant probablement d'une contamination dans le spectre en énergie du pic de la transition-mère ou de celui de la transition étudiée.

B.2.3 Comparaison avec des modèles théoriques

Les valeurs B(E2) sont comparées aux prédictions de deux modèles basés sur Hartree Fock Bogoliubov (HFB) avec l'interaction effective de Gogny D1S utilisant la méthode SCCM (Symmetry Conserving Configuration Mixing) [Robledo, Rodríguez, and Rodríguez-Guzmán, 2018] et la méthode 5DCH (5-Dimensional Collective Hamiltonian) [Delaroche et al., 2010] pour calculer le spectre en énergie et les probabilités réduites de transition. Les valeurs de B(E2) pour les isotopes de Zr sont également comparées aux résultats des calculs du modèle en couche de Monte-Carlo (MCSM) [Togashi et al., 2016].

Nos résultats expérimentaux confirment (voir Fig. 7.2) le changement drastique de probabilité de transition B(E2 ; $2_1^+ \longrightarrow 0_1^+$) entre N=58 et N=60, impliquant un changement de forme entre le ^{98}Zr sphérique et le ^{100}Zr déformé. Pour le ^{98}Zr, la valeur de B(E2) mesurée pour la transition $2_1^+ \longrightarrow 0_2^+$ est beaucoup plus élevée que celle de la transition $2_1^+ \longrightarrow 0_1^+$. Cela laisse à penser que l'état $0k_1$ est de nature sphérique alors que l'état 0_2^+ est déformé, indiquant une probable coexistence de formes. Ceci est en accord avec le calcul MCSM qui prédit un grand B(E2 ; $2_1^+ \longrightarrow 0_2^+$) et un petit B(E2 ; $2_1^+ \longrightarrow 0_1^+$). De plus, la grande valeur B(E2) de la transition vers l'état $4_1^+ \longrightarrow 2_2^+$ par rapport à $4_1^+ \longrightarrow 2_1^+$ suggère que le premier est plus déformé que le second.

Pour N $>$ 60, la collectivité continue d'augmenter avec le nombre de neutrons. La valeur de B(E2 ; $4_1^+ \longrightarrow 2_1^+$) du ^{98}Zr indique une augmentation de la collectivité avec le spin. Une image similaire se dégage des probabilités de transition B(E2 ; $6_1^+ \longrightarrow 4_1^+$) dans les isotopes Zr. Bien qu'il n'y ait pas de changement de forme drastique pour l'état $6k_1$ à N =58, la collectivité augmente lentement avec le nombre de neutrons. Après comparaison des résultats expérimentaux avec les trois modèles théoriques, il se trouve que le MCSM reproduit au mieux le comportement collectif déduit de la Fig. 7.2. Pour être plus précis, la différence entre les valeurs expérimentales de B(E2) et leur prédiction par le MCSM sont notables pour la transition $4_1^+ \longrightarrow 2_1^+$ du ^{98}Zr et les transitions $6_1^+ \longrightarrow 4_1^+$ des $^{100-102}$Zr, alors que pour les transitions $4_1^+ \longrightarrow 2_1^+$ des $^{100-102}$Zr, les valeurs de B(E2) sont bien reproduites par le MCSM et la transition $6_1^+ \longrightarrow 4_1^+$ en ^{98}Zr est en parfait accord avec ce modèle.

On observe expérimentalement un début de collectivité ainsi qu'une augmentation de la déformation, comme on peut le voir dans l'évolution de l'énergie d'excitation de l'état 2_1^+ en fonction du nombre de neutrons pour les isotopes du Mo (voir figure 2.4a). La diminution de l'énergie des états 2_2^+ dans les isotopes du Mo montrés sur la figure 7.5 peut laisser supposer une diminution de la rigidité triaxiale. L'état 0_2^+ du ^{100}Mo à 695 keV pourrait être une indication du phénomène de coexistence de formes. La collectivité des états 4_1^+ des isotopes du Mo (voir Fig. 7.6) augmente entre N = 58 et N = 66, mais pas aussi fortement que pour les états 4_1^+ des isotopes du Zr. En ce qui concerne les états 6_1^+, la collectivité est presque inchangée en passant du ^{100}Mo au ^{102}Mo, mais augmente significativement au delà de N = 60. Aucune conclusion ne peut être tirée sur la déformation des isotopes du Mo après le ^{106}Mo, car seule une durée de vie effective a pu être déterminée pour l'état 6_1^+ du ^{108}Mo.

Les valeurs de B(E2) des isotopes du Ru (voir figure 7.9) montrent que l'évolution de la déformation est moins soudaine que pour les isotopes Mo et Zr. Les modèles HFB+SCCM et HFB+5DCH prévoient une collectivité plutôt constante pour les isotopes du Ru. Cette collectivité dans la plupart des cas, est légèrement supérieure aux valeurs expérimentales. La collectivité

semble légèrement surestimée dans le cas de l'état 6_1^+ du ^{112}Ru, puisque pour le reste des isotopes, les valeurs expérimentales étaient inférieures à celles calculées par les deux modèles théoriques. L'accord des valeurs de B(E2) entre les données sans condition de coïncidence et les données $\gamma - \gamma$ pour les états 4^+ et 6^+ du ^{104}Mo nous permet d'accorder plus de confiance aux résultats expérimentaux qu'aux prévisions théoriques, surtout dans le cas du modèle HFB+SCCM.

B.3 Résultat et conclusion

Les résultats obtenus au cours de cette expérience pour les isotopes du Zr, du Mo et du Ru sont résumés respectivement dans les tableaux 6.13, 6.14 et 6.15, et comparés à ceux obtenus dans une précédente expérience au GANIL utilisant le détecteur γ EXOGAM [Grente, 2014; Singh et al., 2018]. Nous avons mesuré les durées de vie des états 4_1^+, 6_1^+ et 8_1^+ pour les isotopes $^{98-104}$Zr, $^{100-108}$Mo et $^{106-112}$Ru. Des durées de vie effectives ont également été mesurées pour l'état 10_1^+ pour les canaux les plus forts ($^{100-102}$Zr, ^{104}Mo). En général, nos résultats concordent bien avec les durées de vie précédemment mesurées, mais sont plus précis.

Une analyse RDDS utilisant des données de coïncidence $\gamma - \gamma$ a été possible pour la première fois dans ces conditions expérimentales, c'est-à-dire lorsque les fragments de fission ont été identifiés événement par événement. La bonne concordance entre ces résultats et ceux obtenus à partir des données sans condition de coïncidence nous assurent que ces derniers sont fiables tant que les contributions des transitions-mères sont correctement considérées. Nous avons également effectué la première mesure directe de toutes les transitions latérales "significatives" vers l'état 2_1^+ du ^{98}Zr. En mesurant les nouvelles durées de vie effectives des états 3^-, 2_2^+ et 4_2^+ du ^{98}Zr, nous avons pu obtenir une durée de vie plus précise (et fiable) de l'état 2_1^+. Ces différences sont très probablement responsables de l'écart de durée de vie de l'état 2_1^+ du ^{98}Zr entre cette expérience utilisant AGATA et la précédente utilisant EXOGAM [Singh et al., 2018]. La durée de vie effective de l'état 8_1^+ du ^{98}Zr a également été mesurée pour la première fois. De plus, nous avons obtenu une nouvelle durée de vie pour l'état 6_1^+ du ^{104}Zr, à 8 neutrons de la vallée de la stabilité, ainsi qu'une nouvelle durée de vie effective de l'état 4_1^+ de ce même isotope.

En plus de mesurer une nouvelle durée de vie effective de l'état 6_1^+ du ^{108}Mo, nous avons amélioré la précision des durées de vie des isotopes du Mo par rapport à celles mesurées précédemment. Par exemple, avec la technique RDDS, nous avons une plus grande précision sur les durées de vie des isotopes du Mo par rapport à la technique DSAM aux énergies relativistes.

Nous avons mesuré de nouvelles valeurs de durée de vie pour les états 4_1^+ et 6_1^+ du ^{106}Ru ainsi que pour l'état 6_1^+ du ^{112}Ru. Comme il s'agit des isotopes du Ru le plus léger et le plus lourd étudiés dans ce travail de thèse, l'efficacité et la sensibilité en position élevées d'AGATA comparées à celles d'EXOGAM ont joué ici un rôle important. De plus, une valeur de durée de vie effective a été mesurée pour la première fois pour l'état 8_1^+ en ^{106}Ru .

L'une des découvertes significatives de cette expérience est la confirmation du changement de forme spectaculaire entre le ^{98}Zr et le ^{100}Zr dans leur premier état excité 2_1^+, ce qui très proche des prédictions de MCSM. Les valeurs de B(E2) obtenues pour les transitions vers les états non-yrast suggèrent une structure déformée de l'état 0_2^+ par opposition à l'état sphérique 0_1^+, indiquant une coexistence de formes, et une déformation accrue de l'état 2_2^+ par rapport à l'état 2_1^+. Une autre conclusion de ce travail est que la collectivité augmente plus rapidement en fonction du nombre de neutrons pour les isotopes du Zr que pour les isotopes du Mo et du Ru. Ce comportement des isotopes étudiés est cohérent avec un caractère de rotor rigide (au-delà de N = 60) pour la plupart

des isotopes du Zr, de triaxialité dans les isotopes du Mo et de "γ-softness" dans les isotopes du Ru.

Perspectives d'avenir

Afin d'obtenir une image complète de tous les noyaux riches en neutrons présentés dans la Fig. 2.4, les données d'un certain nombre d'isotopes doivent encore être analysées, ce qui n'a pas été possible au cours de cette thèse par manque de temps. Les mesures de la durée de vie à l'aide de la méthode "fast-timing" permettent d'être sensible à des états dont la durée de vie est plus longue et n'a pu être mesurée dans le cadre de ce travail. Une telle analyse permettrait de mesurer la durée de vie des premiers états excités 2_1^+ ainsi que de vérifier la durée de vie de certains des états 4_1^+ à longue vie parmis les isotopes étudiés.

D'autres techniques expérimentales complémentaires à celles décrites ici peuvent également être utilisées pour approfondir la connaissance expérimentale de ces noyaux. Par exemple, les expériences d'excitation de Coulomb, maintenant possibles à l'installation CARIBU (CAlifornium Rare Isotope Breeder Upgrade) de l'ANL (Argonne National Laboratory), peuvent offrir de nouvelles perspectives sur l'évolution de la forme dans les noyaux de masse 100-110. Il convient de noter que les durées de vie mesurées peuvent constituer une contrainte importante dans l'analyse de données des expériences d'excitation de Coulomb. Les sections efficaces d'excitation de Coulomb dépendent de nombreux éléments de la matrice électromagnétique, c'est pourquoi la connaissance de valeurs de B(E2) précises permet de déterminer les paramètres qui ont une influence moindre sur les sections efficaces, tels que les moments quadrupolaires.

Cette expérience ou une du même type pourraient être réalisées à nouveau avec plus de détecteurs dans AGATA (qui a été limité à seulement 1π d'angle solide pour ce travail), ce qui conduirait à une efficacité de détection et à un échantillon statistique bien plus élevés. Cela permettrait d'étendre la technique de coïncidence γ-γ aux isotopes les plus exotiques afin d'augmenter la précision et la fiabilité des résultats de durée de vie.

Bibliography

Akkoyun, S. et al. (2012). "AGATA—Advanced GAmma Tracking Array". In: *Nuclear Instruments and Methods in Physics Research Section A: Accelerators, Spectrometers, Detectors and Associated Equipment* 668, pp. 26 –58. ISSN: 0168-9002. DOI: https://doi.org/10.1016/j.nima.2011.11.081. URL: http://www.sciencedirect.com/science/article/pii/S0168900211021516.

Alexander, T. K. and K. W. Allen (1965). "LIFETIMES OF THE 16O 6.13-MeV LEVEL AND THE 17O 0.871-MeV LEVEL". In: *Canadian Journal of Physics* 43.9, pp. 1563–1573. DOI: 10.1139/p65-148. URL: https://doi.org/10.1139/p65-148.

Alexander, T.K. and A. Bell (1970). "A target chamber for recoil-distance lifetime measurements". In: *Nuclear Instruments and Methods* 81.1, pp. 22 –26. ISSN: 0029-554X. DOI: https://doi.org/10.1016/0029-554X(70)90604-X. URL: http://www.sciencedirect.com/science/article/pii/0029554X7090604X.

Ansari, S. et al. (2017). "Experimental study of the lifetime and phase transition in neutron-rich ^{98,100,102}Zr". In: *Phys. Rev. C* 96 (5), p. 054323. DOI: 10.1103/PhysRevC.96.054323. URL: https://link.aps.org/doi/10.1103/PhysRevC.96.054323.

Arseniev, D.A., A. Sobiczewski, and V.G. Soloviev (1969). "Equilibrium deformations of neutron-rich nuclei in the A $\approx$ 100 region". In: *Nuclear Physics A* 139.2, pp. 269 –276. ISSN: 0375-9474. DOI: https://doi.org/10.1016/0375-9474(69)91109-9. URL: http://www.sciencedirect.com/science/article/pii/0375947469911099.

Barrientos, D. et al. (2015). "Performance of the Fully Digital FPGA-Based Front-End Electronics for the GALILEO Array". In: *IEEE Transactions on Nuclear Science* 62.6, pp. 3134–3139. ISSN: 0018-9499. DOI: 10.1109/TNS.2015.2480243.

Bateman, H. (1843). "The solution of a system of differential equations occurring in the theory of radioactive transformations". In: *In Proceeding of the Cambridge Philosophical Society, Mathematical and Physical Sciences* 15, p. 423. URL: http://citebank.org/node/122715.

Bettermann, L. et al. (2010). "Lifetime measurement of excited states in the shape-phase-transitional nucleus ^{98}Zr". In: *Phys. Rev. C* 82 (4), p. 044310. DOI: 10.1103/PhysRevC.82.044310. URL: https://link.aps.org/doi/10.1103/PhysRevC.82.044310.

Birkenbach, B. et al. (2010). "Installation and usage of the narval emulator". In: URL: https://www.agata.org/sites/default/files/howtos/NarvalEmuHowTo.pdf.

Bizzeti, P. G. et al. (1967). "Measurement of the lifetime of the first excited state in17O and17F". In: *Zeitschrift für Physik* 201.3, pp. 295–300. ISSN: 0044-3328. DOI: 10.1007/BF01326818. URL: https://doi.org/10.1007/BF01326818.

Bohr and Mottelson (1953). "Collective and individual-particle aspects of nuclear structure". In: *Mat-fys Medd* 27 (16), pp. 1–174. URL: https://cds.cern.ch/record/213298/files/p1.pdf.

Boston, A.J. et al. (2009). "Performance of an AGATA asymmetric detector". In: *Nuclear Instruments and Methods in Physics Research Section A: Accelerators, Spectrometers, Detectors and Associated Equipment* 604.1, pp. 48 –52. ISSN: 0168-9002. DOI: https://doi.org/10.1016/j.nima.2009.01.228. URL: http://www.sciencedirect.com/science/article/pii/S0168900209001132.

Bruyneel, B., B. Birkenbach, and P. Reiter (2016). "Pulse shape analysis and position determination in segmented HPGe detectors: The AGATA detector library". In: *The European*

Physical Journal A 52.3, p. 70. ISSN: 1434-601X. DOI: 10.1140/epja/i2016-16070-9. URL: https://doi.org/10.1140/epja/i2016-16070-9.

Bruyneel, B. et al. (2013). "Correction for hole trapping in AGATA detectors using pulse shape analysis". In: *The European Physical Journal A* 49.5, p. 61. ISSN: 1434-601X. DOI: 10.1140/epja/i2013-13061-4. URL: https://doi.org/10.1140/epja/i2013-13061-4.

Bruyneel, Bart, Peter Reiter, and Gheorghe Pascovici (2006). "Characterization of large volume HPGe detectors. Part II: Experimental results". In: *Nuclear Instruments and Methods in Physics Research Section A: Accelerators, Spectrometers, Detectors and Associated Equipment* 569.3, pp. 774 –789. ISSN: 0168-9002. DOI: https://doi.org/10.1016/j.nima.2006.08.129. URL: http://www.sciencedirect.com/science/article/pii/S0168900206015178.

Bruyneel, Bart et al. (2009a). "Crosstalk corrections for improved energy resolution with highly segmented HPGe-detectors". In: *Nuclear Instruments and Methods in Physics Research Section A: Accelerators, Spectrometers, Detectors and Associated Equipment* 608.1, pp. 99 –106. ISSN: 0168-9002. DOI: https://doi.org/10.1016/j.nima.2009.06.037. URL: http://www.sciencedirect.com/science/article/pii/S0168900209012455.

Bruyneel, Bart et al. (2009b). "Crosstalk properties of 36-fold segmented symmetric hexagonal HPGe detectors". In: *Nuclear Instruments and Methods in Physics Research Section A: Accelerators, Spectrometers, Detectors and Associated Equipment* 599.2, pp. 196 –208. ISSN: 0168-9002. DOI: https://doi.org/10.1016/j.nima.2008.11.011. URL: http://www.sciencedirect.com/science/article/pii/S0168900208015921.

Böhm, G. et al. (1993). "The differential decay curve method for the analysis of Doppler shift timing experiments". In: *Nuclear Instruments and Methods in Physics Research Section A: Accelerators, Spectrometers, Detectors and Associated Equipment* 329.1, pp. 248 –261. ISSN: 0168-9002. DOI: https://doi.org/10.1016/0168-9002(93)90944-D. URL: http://www.sciencedirect.com/science/article/pii/016890029390944D.

Canali, C., G. Ottaviani, and G. Majni (1974). "Hot hole anisotropic effect in silicon and germanium". In: *Solid State Communications* 15.7, pp. 1213 –1216. ISSN: 0038-1098. DOI: https://doi.org/10.1016/0038-1098(74)90053-2. URL: http://www.sciencedirect.com/science/article/pii/0038109874900532.

Casten, R. F. (2015). "More General IBA Calculations Spanning the triangle". In: *Lecture notes*. URL: https://www.ikp.uni-koeln.de/students/casten/day5lecture2.pdf.

Cheifetz, E. et al. (1970). "Experimental Information Concerning Deformation of Neutron Rich Nuclei in the $A \sim 100$ Region". In: *Phys. Rev. Lett.* 25 (1), pp. 38–43. DOI: 10.1103/PhysRevLett.25.38. URL: https://link.aps.org/doi/10.1103/PhysRevLett.25.38.

Cline, D (1986). "Nuclear Shapes Studied by Coulomb Excitation". In: *Annual Review of Nuclear and Particle Science* 36.1, pp. 683–716. DOI: 10.1146/annurev.ns.36.120186.003343. URL: https://doi.org/10.1146/annurev.ns.36.120186.003343.

Clément, E. et al. (2017). "Conceptual design of the AGATA 1π array at GANIL". In: *Nuclear Instruments and Methods in Physics Research Section A: Accelerators, Spectrometers, Detectors and Associated Equipment* 855, pp. 1 –12. ISSN: 0168-9002. DOI: https://doi.org/10.1016/j.nima.2017.02.063. URL: http://www.sciencedirect.com/science/article/pii/S0168900217302590.

Davydov, A.S. and G.F. Filippov (1958). "Rotational states in even atomic nuclei". In: *Nuclear Physics* 8, pp. 237 –249. ISSN: 0029-5582. DOI: https://doi.org/10.1016/0029-5582(58)90153-6. URL: http://www.sciencedirect.com/science/article/pii/0029558258901536.

Dechargé, J. and D. Gogny (1980). "Hartree-Fock-Bogolyubov calculations with the $D1$ effective interaction on spherical nuclei". In: *Phys. Rev. C* 21 (4), pp. 1568–1593. DOI: 10.1103/PhysRevC.21.1568. URL: https://link.aps.org/doi/10.1103/PhysRevC.21.1568.

Delaroche, J. P. et al. (2010). "Structure of even-even nuclei using a mapped collective Hamiltonian and the D1S Gogny interaction". In: *Phys. Rev. C* 81 (1), p. 014303. DOI: 10.1103/PhysRevC.81.014303. URL: https://link.aps.org/doi/10.1103/PhysRevC.81.014303.

Devons, S, G Manning, and D St P Bunbury (1955). "Measurement of γ-Transition Lifetimes by Recoil Methods". In: *Proceedings of the Physical Society. Section A* 68.1, pp. 18–31. DOI: 10.1088/0370-1298/68/1/304. URL: https://doi.org/10.1088%2F0370-1298%2F68%2F1%2F304.

Dewald, A., S. Harissopulos, and P. von Brentano (1989). "The differential plunger and the differential decay curve method for the analysis of recoil distance Doppler-shift data". In: *Zeitschrift für Physik A Atomic Nuclei* 334.2, pp. 163–175. ISSN: 0939-7922. DOI: 10.1007/BF01294217. URL: https://doi.org/10.1007/BF01294217.

Dewald, A., O. Möller, and P. Petkov (2012). "Developing the Recoil Distance Doppler-Shift technique towards a versatile tool for lifetime measurements of excited nuclear states". In: *Progress in Particle and Nuclear Physics* 67.3, pp. 786 –839. ISSN: 0146-6410. DOI: https://doi.org/10.1016/j.ppnp.2012.03.003. URL: http://www.sciencedirect.com/science/article/pii/S0146641012000713.

Doherty, D.T. et al. (2017). "Triaxiality near the 110Ru ground state from Coulomb excitation". In: *Physics Letters B* 766, pp. 334 –338. ISSN: 0370-2693. DOI: https://doi.org/10.1016/j.physletb.2017.01.031. URL: http://www.sciencedirect.com/science/article/pii/S0370269317300497.

Eberth, J. and J. Simpson (2008). "From Ge(Li) detectors to gamma-ray tracking arrays–50 years of gamma spectroscopy with germanium detectors". In: *Progress in Particle and Nuclear Physics* 60.2, pp. 283 –337. ISSN: 0146-6410. DOI: https://doi.org/10.1016/j.ppnp.2007.09.001. URL: http://www.sciencedirect.com/science/article/pii/S0146641007000828.

Eberth, J. et al. (1996). "Encapsulated Ge detectors: Development and first tests". In: *Nuclear Instruments and Methods in Physics Research Section A: Accelerators, Spectrometers, Detectors and Associated Equipment* 369.1, pp. 135 –140. ISSN: 0168-9002. DOI: https://doi.org/10.1016/0168-9002(95)00794-6. URL: http://www.sciencedirect.com/science/article/pii/0168900295007946.

Eberth, J. et al. (2003). "A γ-ray spectrometer with position-sensitive Ge detectors for nuclear structure Studies At REX-ISOLDE". In: *AIP Conference Proceedings* 656.1, pp. 349–356. DOI: 10.1063/1.1556664. URL: https://aip.scitation.org/doi/abs/10.1063/1.1556664.

Farnea, E. et al. (2010). "Conceptual design and Monte Carlo simulations of the AGATA array". In: *Nuclear Instruments and Methods in Physics Research Section A: Accelerators, Spectrometers, Detectors and Associated Equipment* 621.1, pp. 331 –343. ISSN: 0168-9002. DOI: https://doi.org/10.1016/j.nima.2010.04.043. URL: http://www.sciencedirect.com/science/article/pii/S0168900210008922.

Federman, P., S. Pittel, and A. Etchegoyen (1984). "Quenching of the 2p12-2p32 proton spin-orbit splitting in the Sr-Zr region". In: *Physics Letters B* 140.5, pp. 269 –271. ISSN: 0370-2693. DOI: https://doi.org/10.1016/0370-2693(84)90750-0. URL: http://www.sciencedirect.com/science/article/pii/0370269384907500.

Fortunato, L. (2005). "Solutions of the Bohr Hamiltonian, a compendium". In: *The European Physical Journal A - Hadrons and Nuclei* 26.1, pp. 1–30. DOI: 10.1140/epjad/i2005-07-115-8. URL: https://doi.org/10.1140/epjad/i2005-07-115-8.

Georgiev, A., W. Gast, and R. M. Lieder (1994). "An analog-to-digital conversion based on a moving window deconvolution". In: *IEEE Transactions on Nuclear Science* 41.4, pp. 1116–1124. DOI: 10.1109/23.322868.

Goriely, S., N. Chamel, and J. M. Pearson (2013). "Further explorations of Skyrme-Hartree-Fock-Bogoliubov mass formulas. XIII. The 2012 atomic mass evaluation and the symmetry coefficient". In: *Phys. Rev. C* 88 (2), p. 024308. DOI: 10.1103/PhysRevC.88.024308. URL: https://link.aps.org/doi/10.1103/PhysRevC.88.024308.

Grave, X. et al. (2005). "NARVAL a modular distributed data acquisition system with Ada 95 and RTAI". In: p. 5. DOI: 10.1109/RTC.2005.1547454.

Grente, Lucie (2014). "Structure des fragments de fission de masse A = 100 - 110 : mesures de temps de vie et analyses en champ moyen et au-delà". In: *Thèse de doctorat, Université Paris-Sud*.

Ha, T.M.H. et al. (2013). "New setup for the characterisation of the AGATA detectors". In: *Nuclear Instruments and Methods in Physics Research Section A: Accelerators, Spectrometers, Detectors and Associated Equipment* 697, pp. 123 –132. ISSN: 0168-9002. DOI: https://doi.org/10.1016/j.nima.2012.08.111. URL: http://www.sciencedirect.com/science/article/pii/S0168900212010157.

Heyde, Kris and John L. Wood (2011). "Shape coexistence in atomic nuclei". In: *Rev. Mod. Phys.* 83 (4), pp. 1467–1521. DOI: 10.1103/RevModPhys.83.1467. URL: https://link.aps.org/doi/10.1103/RevModPhys.83.1467.

Hill, David Lawrence and John Archibald Wheeler (1953). "Nuclear Constitution and the Interpretation of Fission Phenomena". In: *Phys. Rev.* 89 (5), pp. 1102–1145. DOI: 10.1103/PhysRev.89.1102. URL: https://link.aps.org/doi/10.1103/PhysRev.89.1102.

Hutter, C. et al. (2003). "$B(E2)$ values and the search for the critical point symmetry X(5) in ^{104}Mo and ^{106}Mo". In: *Phys. Rev. C* 67 (5), p. 054315. DOI: 10.1103/PhysRevC.67.054315. URL: https://link.aps.org/doi/10.1103/PhysRevC.67.054315.

Johansson, Sven A.E. (1965). "Gamma de-excitation of fission fragments: (II). Delayed radiation". In: *Nuclear Physics* 64.1, pp. 147 –160. ISSN: 0029-5582. DOI: https://doi.org/10.1016/0029-5582(65)90847-3. URL: http://www.sciencedirect.com/science/article/pii/0029558265908473.

Khan, T. A. et al. (1977). "Theβ-decay of100Y: Discovery of a very low lying 0+ state in100Zr". In: *Zeitschrift für Physik A Atoms and Nuclei* 283.1, pp. 105–120. ISSN: 0939-7922. DOI: 10.1007/BF01434071. URL: https://doi.org/10.1007/BF01434071.

Korichi, A. and T. Lauritsen (2019). "Tracking γ rays in highly segmented HPGe detectors: A review of AGATA and GRETINA". In: *The European Physical Journal A* 55.7, p. 121. ISSN: 1434-601X. DOI: 10.1140/epja/i2019-12787-1. URL: https://doi.org/10.1140/epja/i2019-12787-1.

Lau, Kwong and Jörg Pyrlik (1995). "Optimization of centroid-finding algorithms for cathode strip chambers". In: *Nuclear Instruments and Methods in Physics Research Section A: Accelerators, Spectrometers, Detectors and Associated Equipment* 366.2, pp. 298 –309. ISSN: 0168-9002. DOI: https://doi.org/10.1016/0168-9002(95)00604-4. URL: http://www.sciencedirect.com/science/article/pii/0168900295006044.

Lehérissier, P. et al. (2004). "Status report on ECR ion source operation at GANIL". In: *Review of Scientific Instruments* 75.5, pp. 1488–1491. DOI: 10.1063/1.1690447. URL: https://doi.org/10.1063/1.1690447.

Leo, William R. (1994). "Passage of Radiation Through Matter". In: *Techniques for Nuclear and Particle Physics Experiments: A How-to Approach*. Berlin, Heidelberg: Springer Berlin Heidelberg, pp. 17–68. DOI: 10.1007/978-3-642-57920-2_2. URL: https://doi.org/10.1007/978-3-642-57920-2_2.

Lewin, M. and S. Paul (2014). "A Numerical Perspective on Hartree-Fock-Bogoliubov Theory". In: *Mathematical Modelling and Numerical Analysis* 48 (1). DOI: 10.1051/m2an/2013094.

Liang, M. et al. (1991). "The deformation of the neutron-rich isotopes102Mo and104Mo". In: *Zeitschrift für Physik A Hadrons and Nuclei* 340.2, pp. 223–224. ISSN: 0939-7922. DOI: 10.1007/BF01303836. URL: https://doi.org/10.1007/BF01303836.

Libert, J., M. Girod, and J.-P. Delaroche (1999). "Microscopic descriptions of superdeformed bands with the Gogny force: Configuration mixing calculations in the $A \sim$190 mass region". In: *Phys. Rev. C* 60 (5), p. 054301. DOI: 10.1103/PhysRevC.60.054301. URL: https://link.aps.org/doi/10.1103/PhysRevC.60.054301.

Litzinger, J. et al. (2015). "Transition probabilities in neutron-rich ^{84,86}Se". In: *Phys. Rev. C* 92 (6), p. 064322. DOI: 10.1103/PhysRevC.92.064322. URL: https://link.aps.org/doi/10.1103/PhysRevC.92.064322.

Ljungvall, J. et al. (2012). "The Orsay Universal Plunger System". In: *Nuclear Instruments and Methods in Physics Research Section A: Accelerators, Spectrometers, Detectors and Associated Equipment* 679, pp. 61 –66. ISSN: 0168-9002. DOI: https://doi.org/10.1016/j.nima.2012.03.041. URL: http://www.sciencedirect.com/science/article/pii/S0168900212003427.

Lopez-Martens, A. et al. (2004). "γ-ray tracking algorithms: a comparison". In: *Nuclear Instruments and Methods in Physics Research Section A: Accelerators, Spectrometers, Detectors and Associated Equipment* 533.3, pp. 454 –466. ISSN: 0168-9002. DOI: https://doi.org/10.1016/j.nima.2004.06.154. URL: http://www.sciencedirect.com/science/article/pii/S0168900204014779.

Luo, Y. X. et al. (2014). "First observation of a rotational band and the role of the proton intruder orbital $\pi 1/2^+[431]$ in very neutron-rich odd-odd ^{106}Nb". In: *Phys. Rev. C* 89 (4), p. 044326. DOI: 10.1103/PhysRevC.89.044326. URL: https://link.aps.org/doi/10.1103/PhysRevC.89.044326.

Mamane, G. et al. (1986). "Lifetime measurements of excited levels in prompt fission products of 252Cf". In: *Nuclear Physics A* 454.2, pp. 213 –225. ISSN: 0375-9474. DOI: https://doi.org/10.1016/0375-9474(86)90265-4. URL: http://www.sciencedirect.com/science/article/pii/0375947486902654.

Marel, J van der and B Cederwall (1999). "Backtracking as a way to reconstruct Compton scattered γ-rays". In: *Nuclear Instruments and Methods in Physics Research Section A: Accelerators, Spectrometers, Detectors and Associated Equipment* 437.2, pp. 538 –551. ISSN: 0168-9002. DOI: https://doi.org/10.1016/S0168-9002(99)00801-3. URL: http://www.sciencedirect.com/science/article/pii/S0168900299008013.

Michelagnoli, C. (2013). "The lifetime of the 6.79 MeV state in ^{15}O as a challenge for nuclear astrophysics and γ-ray spectroscopy: a new DSAM measurement with the AGATA Demonstrator array". In: *PhD thesis, University of Padova*.

Nelson, L. et al. (2007). "Characterisation of an AGATA symmetric prototype detector". In: *Nuclear Instruments and Methods in Physics Research Section A: Accelerators, Spectrometers, Detectors and Associated Equipment* 573.1. Proceedings of the 7th International Conference on Position-Sensitive Detectors, pp. 153 –156. ISSN: 0168-9002. DOI: https://doi.org/10.1016/j.nima.2006.11.042. URL: http://www.sciencedirect.com/science/article/pii/S0168900206022479.

Nilsson, S. G. (1955). "Binding states of individual nucleons in strongly deformed nuclei". In: *Kong. Dan. Vid. Sel. Mat. Fys. Med.* 29N16, pp. 1–69.

NNDC. "NNDC". In: *Evaluated Nuclear Structure Data File*. URL: https://www.nndc.bnl.gov/ensdf/EnsdfDispatcherServlet.

Nomura, Kosuke, Noritaka Shimizu, and Takaharu Otsuka (2010). "Formulating the interacting boson model by mean-field methods". In: *Phys. Rev. C* 81 (4), p. 044307. DOI: 10.1103/PhysRevC.81.044307. URL: https://link.aps.org/doi/10.1103/PhysRevC.81.044307.

Otsuka, T and Y Tsunoda (2016). "The role of shell evolution in shape coexistence". In: *Journal of Physics G: Nuclear and Particle Physics* 43.2, p. 024009. DOI: 10.1088/0954-3899/43/2/024009. URL: https://doi.org/10.1088%2F0954-3899%2F43%2F2%2F024009.

Ottaviani, G., C. Canali, and A. A. Quaranta (1975). "Charge Carrier Transport Properties of Semiconductor Materials Suitable for Nuclear Radiation Detectors". In: *IEEE Transactions on Nuclear Science* 22.1, pp. 192–204. ISSN: 0018-9499. DOI: 10.1109/TNS.1975.4327640.

Pascovici, G. et al. (2008). "Low Noise, Dual Gain Preamplifier with Built in Spectroscopic Pulser for Highly Segmented High-purity Germanium Detectors". In: *WSEAS Trans. Cir. and Sys.* 7.6, pp. 470–481. ISSN: 1109-2734. DOI: http://dl.acm.org/citation.cfm?id=1482107.1482110.

Pinston, J. A. et al. (2006). "Triaxiality in ^{105}Mo and ^{107}Mo from the low to intermediate spin region". In: *Phys. Rev. C* 74 (6), p. 064304. DOI: 10.1103/PhysRevC.74.064304. URL: https://link.aps.org/doi/10.1103/PhysRevC.74.064304.

Pullanhiotan, S. et al. (2008). "Improvement in the reconstruction method for VAMOS spectrometer". In: *Nuclear Instruments and Methods in Physics Research Section B: Beam Interactions with Materials and Atoms* 266.19. Proceedings of the XVth International Conference on Electromagnetic Isotope Separators and Techniques Related to their Applications, pp. 4148 – 4152. ISSN: 0168-583X. DOI: https://doi.org/10.1016/j.nimb.2008.05.024. URL: http://www.sciencedirect.com/science/article/pii/S0168583X08006952.

Pullia, A. et al. (2012). "A 12-channel 14/16-bit 100/125-MS/s digitizer with 24-Gb/s optical output for AGATA/GALILEO". In: *2012 IEEE Nuclear Science Symposium and Medical Imaging Conference Record*, pp. 819–823. ISSN: 1082-3654. DOI: 10.1109/NSSMIC.2012.6551218.

Radford, D. C. "Radware". In:

— "Radware". In: URL: https://radware.phy.ornl.gov/info.html.

Ralet, D. et al. (2017). "Lifetime measurement of neutron-rich even-even molybdenum isotopes". In: *Phys. Rev. C* 95 (3), p. 034320. DOI: 10.1103/PhysRevC.95.034320. URL: https://link.aps.org/doi/10.1103/PhysRevC.95.034320.

Raman, S., C.W. Nestor, and P. Tikkanen (2001). In: *Atomic Data and Nuclear Data Tables* 78.1, pp. 1 –128. ISSN: 0092-640X.

Ramo, S. (1939). "Currents Induced by Electron Motion". In: *Proceedings of the IRE* 27.9, pp. 584–585. ISSN: 2162-6634. DOI: 10.1109/JRPROC.1939.228757.

Recchia, F. et al. (2009). "Position resolution of the prototype AGATA triple-cluster detector from an in-beam experiment". In: *Nuclear Instruments and Methods in Physics Research Section A: Accelerators, Spectrometers, Detectors and Associated Equipment* 604.3, pp. 555 –562. ISSN: 0168-9002. DOI: https://doi.org/10.1016/j.nima.2009.02.042. URL: http://www.sciencedirect.com/science/article/pii/S0168900209004124.

Reggiani, L. et al. (1977). "Hole drift velocity in germanium". In: *Phys. Rev. B* 16 (6), pp. 2781–2791. DOI: 10.1103/PhysRevB.16.2781. URL: https://link.aps.org/doi/10.1103/PhysRevB.16.2781.

Rejmund, M. et al. (2011). "Performance of the improved larger acceptance spectrometer: VAMOS++". In: *Nuclear Instruments and Methods in Physics Research Section A: Accelerators, Spectrometers, Detectors and Associated Equipment* 646, pp. 184–191. DOI: 10.1016/j.nima.2011.05.007. URL: http://hal.in2p3.fr/in2p3-00592318.

Robledo, L M, T R Rodríguez, and R R Rodríguez-Guzmán (2018). "Mean field and beyond description of nuclear structure with the Gogny force: a review". In: *Journal of Physics G: Nuclear and Particle Physics* 46.1, p. 013001. DOI: 10.1088/1361-6471/aadebd. URL: https://doi.org/10.1088%2F1361-6471%2Faadebd.

Rodríguez, Tomás R., Alexander Arzhanov, and Gabriel Martínez-Pinedo (2015). "Toward global beyond-mean-field calculations of nuclear masses and low-energy spectra". In: *Physical Review C* 91.4. ISSN: 1089-490X. DOI: 10.1103/physrevc.91.044315. URL: http://dx.doi.org/10.1103/PhysRevC.91.044315.

Roth, J., J. H. Primbsch, and R. P. Lin (1984). "Segmentation and Pulse Shape Discrimination Techniques for Rejecting Background in Germanium Detectors". In: *IEEE Transactions on Nuclear Science* 31.1, pp. 367–371. ISSN: 0018-9499. DOI: 10.1109/TNS.1984.4333279.

Régis, J.-M. et al. (2013). "The generalized centroid difference method for picosecond sensitive determination of lifetimes of nuclear excited states using large fast-timing arrays". In: *Nuclear Instruments and Methods in Physics Research Section A: Accelerators, Spectrometers, Detectors and Associated Equipment* 726, pp. 191 –202. ISSN: 0168-9002. DOI: https://doi.org/10.1016/j.nima.2013.05.126. URL: http://www.sciencedirect.com/science/article/pii/S0168900213007377.

Schlarb, M. et al. (2011). "Pulse shape analysis for γ-ray tracking (Part I): Pulse shape simulation with JASS". In: *The European Physical Journal A* 47.10, p. 132. ISSN: 1434-601X. DOI: 10.1140/epja/i2011-11132-2. URL: https://doi.org/10.1140/epja/i2011-11132-2.

Sheline, R.K., I. Ragnarsson, and S.G. Nilsson (1972). "Shell structure for deformed nuclear shapes". In: *Physics Letters B* 41.2, pp. 115 –121. ISSN: 0370-2693. DOI: https://doi.org/10.1016/0370-2693(72)90440-6. URL: http://www.sciencedirect.com/science/article/pii/0370269372904406.

Sieja, K. et al. (2009). "Shell model description of zirconium isotopes". In: *Phys. Rev. C* 79 (6), p. 064310. DOI: 10.1103/PhysRevC.79.064310. URL: https://link.aps.org/doi/10.1103/PhysRevC.79.064310.

Simpson, J. et al. (2000). "The EXOGAM array: A radioactive beam γ-ray spectrometer". In: *Acta Physica Hungarica, Series A: Heavy Ion Physics* 11, pp. 159–188. ISSN: 1219-7580.

Simpson, J. et al. (2008). *Technical design report*. URL: https://www.agata.org/sites/default/files/reports/TDR_EUJRA.pdf.

Singh, Purnima et al. (2018). "Evidence for Coexisting Shapes through Lifetime Measurements in ^{98}Zr". In: *Phys. Rev. Lett.* 121 (19), p. 192501. DOI: 10.1103/PhysRevLett.121.192501. URL: https://link.aps.org/doi/10.1103/PhysRevLett.121.192501.

Skalski, J., S. Mizutori, and W. Nazarewicz (1997). "Equilibrium shapes and high-spin properties of the neutron-rich A $\approx$ 100 nuclei". In: *Nuclear Physics A* 617.3, pp. 282 –315. ISSN: 0375-9474. DOI: https://doi.org/10.1016/S0375-9474(97)00125-5. URL: http://www.sciencedirect.com/science/article/pii/S0375947497001255.

Skyrme, T.H.R. (1958). "The spin-orbit interaction in nuclei". In: *Nuclear Physics* 9.4, pp. 635 –640. ISSN: 0029-5582. DOI: https://doi.org/10.1016/0029-5582(58)90346-8. URL: http://www.sciencedirect.com/science/article/pii/0029558258903468.

Smith, A G et al. (2002). "Lifetimes of yrast rotational states of the fission fragments 100Zr and 104Mo measured using a differential plunger". In: *Journal of Physics G: Nuclear and Particle Physics* 28.8, pp. 2307–2316. DOI: 10.1088/0954-3899/28/8/316. URL: https://doi.org/10.1088%2F0954-3899%2F28%2F8%2F316.

Smith, A. G. et al. (2012). "Lifetime measurements and nuclear deformation in the $A \approx 100$ region". In: *Phys. Rev. C* 86 (1), p. 014321. DOI: 10.1103/PhysRevC.86.014321. URL: https://link.aps.org/doi/10.1103/PhysRevC.86.014321.

Smith, A.G et al. (2004). In: *Physics Letters B* 591.1–2, pp. 55 –60. ISSN: 0370-2693.

Togashi, Tomoaki et al. (2016). "Quantum Phase Transition in the Shape of Zr isotopes". In: *Phys. Rev. Lett.* 117 (17), p. 172502. DOI: 10.1103/PhysRevLett.117.172502. URL: https://link.aps.org/doi/10.1103/PhysRevLett.117.172502.

Vandebrouck, M. et al. (2016). "Dual Position Sensitive MWPC for tracking reaction products at VAMOS++". In: *Nuclear Instruments and Methods in Physics Research Section A: Accelerators, Spectrometers, Detectors and Associated Equipment* 812, pp. 112 –117. ISSN: 0168-9002. DOI: https://doi.org/10.1016/j.nima.2015.12.040. URL: http://www.sciencedirect.com/science/article/pii/S0168900215016113.

Venturelli, R. and D. Bazzacco (2004). "Adaptive Grid Search as Pulse Shape Analysis Algorithm for γ-Tracking and Results". In: *LNL Annual Report*. URL: http://www.lnl.infn.it/~annrep/read_ar/2004/menus/contributions_frame.htm.

Ward, D. et al. (1973). "Lifetimes for Levels above the "Rotational Phase Change" in ^{158}Er". In: *Phys. Rev. Lett.* 30 (11), pp. 493–496. DOI: 10.1103/PhysRevLett.30.493. URL: https://link.aps.org/doi/10.1103/PhysRevLett.30.493.

Ward, D. et al. (1979). "Measurements of lifetimes and feeding times for high spin states in 156Dy". In: *Nuclear Physics A* 332.3, pp. 433 –454. ISSN: 0375-9474. DOI: https://doi.org/10.1016/0375-9474(79)90012-5. URL: http://www.sciencedirect.com/science/article/pii/0375947479900125.

Warr, N. et al. (2003). "MINIBALL: The first gamma-ray spectrometer using segmented, encapsulated germanium detectors for studies with radioactive beams". In: *The European Physical Journal A - Hadrons and Nuclei* 20.1, pp. 65–66. DOI: 10.1140/epja/i2002-10323-2. URL: https://doi.org/10.1140/epja/i2002-10323-2.

Wiens, Andreas et al. (2010). "The AGATA triple cluster detector". In: *Nuclear Instruments and Methods in Physics Research Section A: Accelerators, Spectrometers, Detectors and Associated Equipment* 618.1, pp. 223 –233. ISSN: 0168-9002. DOI: https://doi.org/10.1016/j.nima.2010.02.102. URL: http://www.sciencedirect.com/science/article/pii/S0168900210003384.

Wigner, E. (1937). "On the Structure of Nuclei Beyond Oxygen". In: *Phys. Rev.* 51 (11), pp. 947–958. DOI: 10.1103/PhysRev.51.947. URL: https://link.aps.org/doi/10.1103/PhysRev.51.947.

Wrzosek-Lipska, K. et al. (2012). "Electromagnetic properties of ^{100}Mo: Experimental results and theoretical description of quadrupole degrees of freedom". In: *Phys. Rev. C* 86 (6), p. 064305. DOI: 10.1103/PhysRevC.86.064305. URL: https://link.aps.org/doi/10.1103/PhysRevC.86.064305.

Zhang, C. L. et al. (2015). "Theoretical study of triaxial shapes of neutron-rich Mo and Ru nuclei". In: *Phys. Rev. C* 92 (3), p. 034307. DOI: 10.1103/PhysRevC.92.034307. URL: https://link.aps.org/doi/10.1103/PhysRevC.92.034307.

Zocca, F. et al. (2009). "A Time-Over-Threshold Technique for Wide Dynamic Range Gamma-Ray Spectroscopy With the AGATA Detector". In: *IEEE Transactions on Nuclear Science* 56.4, pp. 2384–2391. ISSN: 0018-9499. DOI: 10.1109/TNS.2009.2023905.

université PARIS-SACLAY | ÉCOLE DOCTORALE PHENIICS

Titre : Changement de forme de noyaux riches en neutrons dans les chaînes isotopiques du Zr, du Mo et du Ru dans la région de masse A=100

Mots clés : physique nucléaire, structure nucléaire, spectroscopie gamma, temps de vie, déformation et collectivité

Résumé : La forme d'un noyau, ou la déviation de la distribution en masse par rapport à une forme sphérique, est une des propriétés fondamentales du noyau. Elle est gouvernée par des effets à la fois macroscopiques et microscopiques, tels que l'énergie de liaison donnée par le modèle de la goutte liquide ou la structure en couches du noyau, respectivement. L'objectif de cette thèse est l'étude de l'évolution de la forme des noyaux exotiques riches en neutrons dans les chaînes isotopiques allant du Zr (Z=40) au Pd (Z=46). Les noyaux auxquels nous nous intéressons ont tendance à avoir des états excités qui évoluent rapidement en fonction du nombre de neutrons, ce qui peut être interprété comme des variations rapides de la forme du noyau. Des mesures précises de durée de vie constituent un élément clé de l'étude systématique de l'évolution de la déformation nucléaire et du degré de collectivité dans cette région. Des noyaux riches en neutrons dans la région de masse A = 100-120 ont été peuplés par la réaction de fusion-fission d'un faisceau de ^{238}U à 6,2 MeV/u sur une cible de ^{9}Be. Le noyau composé ^{247}Cm était produit à une énergie d'excitation de $\sim$45 MeV avant de fissionner. Le dispositif expérimental utilisé pour cette étude comprenait le spectromètre de masse de haute résolution VAMOS pour l'identification les noyaux en Z et en A, le réseau de 35 détecteurs au germanium AGATA (Advanced γ-ray Tracking Array), pour la spectroscopie de rayons γ, ainsi qu'un mécanisme de "plunger" pour mesurer la durée de vie jusqu'à quelques ps par la méthode RDDS (Recoil Distance Doppler Shift). La combinaison de spectromètres sophistiqués utilisée dans cette expérience a permis de mesurer des durées de vie d'états nucléaires allant de 100 picosecondes à quelques picosecondes. Dans cette thèse, nous exposerons de nouveaux résultats pour les états à courte durée de vie dans les noyaux riches en neutrons A$\sim$100, en mettant l'accent sur les chaînes des Zr, Mo et Ru. Nous discuterons des techniques expérimentales utilisées pour évaluer les durées de vie ainsi que l'interprétation de celles-ci à l'aide de modèles de structures nucléaires récents.

Title : Shape evolution in neutron-rich Zr, Mo and Ru isotopes around mass A=100

Keywords : Nuclear Physics, Nuclear Structure, Gamma Spectroscopy, Lifetime, Deformation and Collectivity

Abstract : The shape of an atomic nucleus, ie. the deviation of its mass distribution from sphericity, is a fundamental property and governed by a delicate interplay of macroscopic and microscopic effects, such as the liquid-drop like binding energy and the nuclear shell structure, respectively. This work focuses on the evolution of nuclear shapes in exotic nuclei, far from the valley of stability, specifically in neutron-rich isotopes of Zr (Z=40), Mo (Z=42) and Ru (Z=44). The nuclei of interest show rapidly evolving patterns of excited states, which can be interpreted as rapid variations of the nuclear shape. Precise lifetime measurements are a key ingredient in the systematic study of the evolution of nuclear deformation and the degree of collectivity in the nuclei of interest. In order to measure the lifetime, neutron-rich nuclei in the mass region of A = 100-120 were populated through the fusion-fission reaction of a ^{238}U beam at 6.2 MeV/u on a ^{9}Be target. The compound nucleus ^{247}Cm was produced at an excitation energy of around 45 MeV before undergoing fission. The setup used for this study comprised the high-resolution mass spectrometer VAMOS in order to identify the fission fragments in Z and A, the Advanced gamma ray Tracking Array AGATA of 35 germanium detectors to perform gamma ray spectroscopy, as well as a plunger mechanism to measure lifetimes down to a few ps using the Recoil Distance Doppler Shift method (RDDS). The sophisticated set of spectrometers used in this experiment allowed measurement of nuclear lifetimes in a range from 100's of picoseconds down to a few picoseconds. In this thesis, new lifetime results for short-lived states in neutron-rich Zr, Mo and Ru isotopes have been reported. The obtained reduced transition strength from the measured lifetime have been interpreted using two Hartree Fock Bogoliubov based models and the Monte Carlo Shell Model (MCSM) calculations.

Université Paris-Saclay
Espace Technologique / Immeuble Discovery
Route de l'Orme aux Merisiers RD 128 / 91190 Saint-Aubin, France